博士論文

Study on Strengths of Steel Cone-to-Cylinder Socket Connections under Axial Compression

（軸圧縮を受ける鋼製円錐－円筒ソケット接合部の耐力に関する研究）

田　啓祥

ABSTRACT

A new type of steel connection, which is named steel cone-to-cylinder socket connection, is developed in the Steel Structure Laboratory of the University of Tokyo to reduce the seismic damage occurred at the pile head of building structures. Strength of the connections under axial compression has been studied since 2005. Four potential failure modes: cylinder edge failure, ring tension failure, cone bending failure, and cone buckling failure were summarized. Several models were created and formulae for predicting the yield strength, full plastic strength, and collapse strength of connections were proposed. However, several issues have not been clarified up to now. Though the simple law of friction proposed by Amonton and Coulomb can be employed to simulate the friction contact between cone and cylinder, how to set the value of the friction coefficient for practical design has not been made clear. The distributions of stress and deformation in the connections have not been investigated. The plastic regions in cylindrical wall, tapered ring, conical wall and lid plate at yield, full plastic and ultimate loads respectively, have not been analyzed. The failure modes need to be reinvestigated in detail, especially for the welded connections with cone buckling failure, because the predicted strength is much greater than the experimental results. Furthermore, the influence of interaction of stress resultants on the failure mechanisms has not been studied.

This thesis is aimed to clarify the failure mechanisms and proposed more precise and easy-to-use formulae for predicting the strength of all the connections. This thesis first estimates effective Finite Element (FE) models by considering the influence of friction coefficient on collapse strength and then clarifies the stress transformation mechanisms. Secondly, the failure mechanisms are judged based on the FE Analysis results and the previous experimental results. Thirdly, the interaction of stress resultants is investigated, and then the complicated equation of Mises' yield condition for revolutional shells under axisymmetric loading is simplified into an explicit and easy-to-use form and validated by

the effective FEA results. Finally, plastic collapse mechanisms are proposed and limit analysis is undertaken by considering the interaction of axial (meridional) stress resultants with hoop stress resultant and axial (meridional) bending moment. More precise and easy-to-use formulae for strength of connections are proposed and validated by comparing them with the previous ones and the relevant experimental and FEA results.

NOMENCLATURE

D	External diameter
E	Young's modulus
L	Length of segment in plastic collapse mechanism
M	Bending moment per unit length in hoop direction
N	Normal stress resultant per unit length in hoop direction
P	Strength under compressive loading
Q	Shear stress resultant per unit length in hoop direction
Δ	Axial deformation
d	Center-to-center diameter
e	True strain
s	True stress
t	Thickness of wall
z	Radially outward distance from the middle surface of walls
w	Deformation in radial or normal direction
ϕ	Rotation angle of plastic hinges
α	Semi-vertex angle of conical shell
β	Confinement factor of tapered ring on maximum strength
γ	Influence factor when the influence of external work by axial force on plastic collapse mechanism is considered.
ε	Engineering strain
η	Eccentricity ratio of axial force
μ	Friction coefficient
ξ	Factor for predicting general yield strength based on full plastic strength
ρ	Factor for predicting collapse strength based on full plastic strength
σ	Engineering stress
τ	Shear stress
χ	Fundamental parameter for predicting full plastic strength
ψ	Factor when the influence of meridional stress resultant on plastic collapse

mechanism is considered

Subscripts

C	Conical shell
P	Cylindrical shell
R	Ring
max	At ultimate load for models with perfectly plastic material
p	Plastic
r	Radial direction
s	Meridional direction of conical shell
t	Normal direction of conical shell
u	Ultimate
x	Axial direction
y	Yield
θ	Hoop (Circumferential) direction

Sign convention

Tension: +ve

Compression: -ve

(But strength under compressive loading: +ve)

Outward radial deflection: +ve

Inward radial deflection: -ve

Shear stress: clock rotation +ve

Bending moment: external surface of shell wall is under tension: +ve

(Terms not shown here are defined in the text and figure)

TABLE OF CONTENTS

CHAPTER 1 INTRODUCTION

1.1 Background

1.1.1 Advantage of Steel Cone-to-Cylinder Socket Connections

A new type of steel connection, which is named steel cone-to-cylinder socket connection, is developed by Kuwamura et al. (2005a) in order to facilitate connecting a circular hollow section member to another cylindrical or different shaped section member. As shown in Fig. 1-1, this connection consists of four parts: a conical shell, a cylindrical shell, a tapered ring and a lid plate. In general, the lid plate is attached in advance to the foot of the conical shell in order to serve as a splice to fix the connected member. Then, the apex part of the conical shell is inserted into the open end of the cylindrical shell. The tapered ring is used to strengthen the cylinder edge, if necessary.

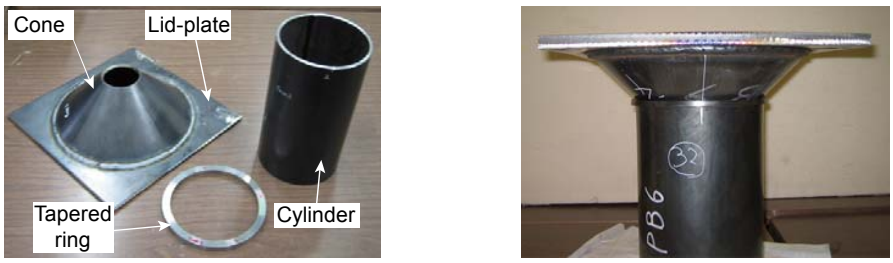

(a) Components (b) Connection

Fig. 1-1 Components of steel cone-to-cylinder socket connections

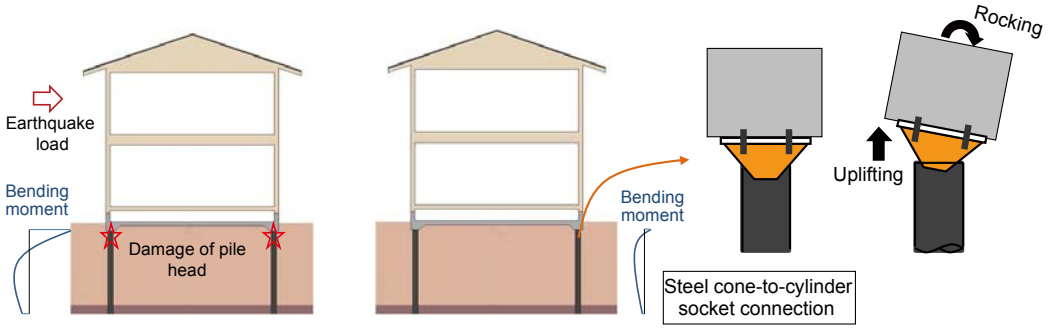

(a) Rigid pile head (b) Proposed new pile head

Fig. 1-2 Major advantage of steel cone-to-cylinder socket connections

Motivation for this connection comes from the seismic damages at pile heads of building structure, which were largely observed in pile foundations in 1995 Kobe Earthquake (Kuwamura and Ito 2009). Past studies (Rutenberg A. et al. 1982; Hayashi Y. et al. 1999; Iwashita K. et al. 2003) have pointed out that the effects of rocking vibration accompanied with uplift motion may reduce the seismic damage to buildings subjected to strong earthquake ground motions. Some kinds of pile head with uplifting and rocking vibration concept have been employed in building structure successfully (Nishimura et al. 2004; Ishizaki et al. 2006). As described in Fig. 1-2(a), the ordinary cylindrical pile head is usually rigid and fixed to foundation beam. It is easy to have a damage or even failure due to the great bending moment induced by horizontal earthquake load. The proposed connection shown in Fig. 1-2(b) can protect the pile head from damage by reducing the bending moment substantially, because it can uplift and rock during earthquake. This is the major advantage of the connections. Another benefit is that field construction can be substantially simplified. After conical wall collapses, it can be replaced easily and quickly.

1.1.2 Research Subject of Steel Cone-to-Cylinder Socket Connections

This socket connection can be not only applied to pile head, but also to some other cases: such as column base, pin-support of truss, and pipeline reducer, as listed in Fig. 1-3. In addition to the applications by considering uplifting and rocking vibration concept, it should be noted that when it is employed in pipeline structure, welding between cone and cylinder is necessary, since the pipeline is usually filled with dangerous chemical, such as oil or gas. Moreover, welded cone-to-cylinder connections, as the most common form of intersections in engineering applications within marine, mechanical and architectural industries, are often found in steel silos and tanks with a conical roof, elevated conical water tanks with a cylindrical shell support and pressure vessels with a conical end closure (Teng 2000).

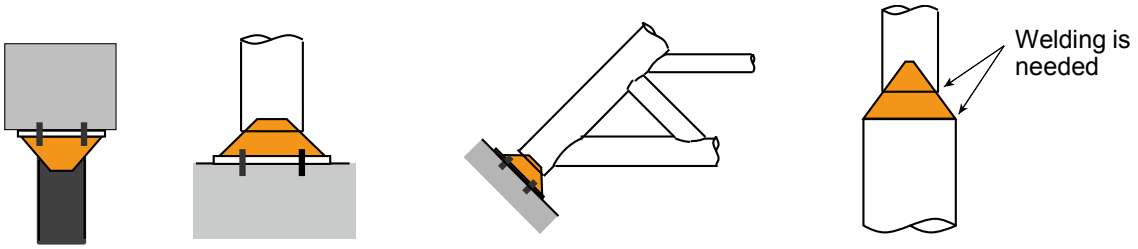

(a) Pile head (b) Column base (c) Truss support (d) Pipeline reducer

Fig. 1-3 Applications of steel cone-to-cylinder socket connection

(a) Metal touch connection (b) Welded connection

Fig. 1-4 Two main kinds of the socket connection

Thus, the socket connections with welding between cone and cylinder are employed from a practical point of view. Furthermore, it is also necessary for comparative research on metal touch socket connections. Finally, steel cone-to-cylinder socket connections are classified to be two main kinds: one is “metal touch connection”, in which cylinder edge will be strengthened by tapered ring if necessary; and the other is “welded connection”, as shown in Fig. 1-4.

In order to make the steel cone-to-cylinder socket connections to be practical, research work has been conducted since 2005, by both experimental study and numerical analysis. The main research subject is to make clear the failure mechanism of the connections under compressive loading and then to predict the strength effectively.

1.2 Previous Research and Unclarified Issues

Kuwamura et al. (2005a) revealed that the connection is strong and stiff enough to be applied to the construction practice of low to middle-rise buildings, based on the results of Feasibility Assessment tests. The potential ultimate modes of this connection were

classified into six cases: cylinder edge failure, ring tension failure, cone edge failure, cone bending failure, cone buckling failure and lid-cone bending failure. The strength of connections under axially uniform compression were mainly studied with bending theory of shells. After the pilot tests, a series of tests with more than 100 specimens were conducted by Tomioka et al. (2005). The strength obtained from experiments was compared with the predicted values by the proposed formulae. The analysis results indicated that

① For connections with cylinder edge failure, the influence of bending of cylindrical wall needs to be considered, especially for predicting collapse strength;

② For connections with ring tension failure, the reinforcement effect of tapered ring on the yield strength of connections would reach the highest limit, even though the thickness of ring in vertical direction increases. It seems that not the whole section of ring plays a role on strengthening the connections;

③ For connections with cone bending failure, large friction coefficient is favorable, because the expansion of the cone due to Poisson's ratio makes the cone sit on the edge of the cylinder;

④ For connections with cone buckling failure, the predicted plastic buckling strength is greater than the collapse strength of experimental results;

⑤ For connections with lid-cone bending failure, the load carrying capacity of conical shell controls the strength of connections;

⑥ In future, the determination of failure mode and friction coefficient is necessary to be reinvestigated (Tomioka 2006).

After then, Kuwamura and Ito (2007) investigated the frictional resistance of a rotating steel cone in contact with the inner edge of a steel cylinder theoretically on the basis of the classical law of friction proposed by Amonton and Coulomb, and suggested that the simple theory works well for the prediction of the frictional rotation resistance of the socket connection. Ito et al. (2008) reinvestigated the cylinder edge failure of the connections by means of FEM and theoretical analysis. It indicated that the previously

proposed model for the yield load is found satisfactory, while the models for the full plastic and ultimate loads are modified to Eason-Shield model (1955) which provides better prediction because the influence of bending in cylindrical wall is considered. Ehara et al. (2007) investigated the influence of initial imperfections of the cylinder and the friction coefficient between cone and cylinder on the stiffness and strength of connections with cylinder edge failure, and suggested that friction coefficient controls the strength and initial imperfection controls the stiffness. Fujimoto and Kuwamura (2009) reinvestigated the yield strength of connections with ring tension failure by considering the rotation of ring and found that the predicted value becomes better than the previous formula for some of the models, while not for other models. Fujimoto and Kuwamua (2010) reinvestigated the yield and ultimate strength of connections with ring tension failure by considering the contact effect of the bottom edge of ring with cylindrical wall and found that the prediction was closer to the experimental results than before. Up to now, the connections with cone bending failure, cone buckling failure and lid-cone bending failure has not been reinvestigated.

The previous research stated above is summarized and the unclarified issues are listed as follow:

① Though the simple law of friction proposed by Amonton and Coulomb can be employed to simulate the friction contact between cone and cylinder, how to determine the values of friction coefficient has not been made clear;

② The distributions of stress and deformation in the connections with ring tension failure, cone bending failure, cone buckling failure and lid-cone bending failure have not been investigated. The plastic regions in cylindrical wall, tapered ring, conical wall and lid plate at yield, full plastic and ultimate loads respectively, have not been analyzed;

③ The influence of axial stress resultant on failure mechanisms has not been studied;

④ The failure modes need to be reanalyzed in detail, especially for connections with cone buckling failure.

1.3 Objective and Scope of this Thesis

This study focuses on the prediction of the strength of steel cone-to-cylinder socket connections under axial compression. The objectives are as follow:

① to find a way to determine the friction coefficient between cone and cylinder for metal touch connections;

② to clarify the failure mechanisms of all the connections;

③ to investigate the interaction among stresses in failure mechanisms;

④ to propose more precise and easy-to-use formulae for predicting the strength of connections.

It should be mentioned that prediction of the stiffness of connections under axial compression is outside the scope of this study. In addition, prediction of the strength of connections under local or eccentric load is also not undertaken. Thus, the lid-cone bending failure will be not analyzed in the following chapters.

1.4 Outline of this Thesis

According to the study plan, this thesis includes the following seven chapters. The configuration of this thesis is shown in Fig. 1-5.

Chapter 1 Introduction

The concept and advantage of steel cone-to-cylinder socket connections are introduced. A comprehensive review of the study related with the steel cone-to-cylinder connections are carried out. The unclarified issues are addressed, and the purpose and scope of the dissertation are presented.

Chapter 2 Discussion on Failure Modes Based on Previous Experimental Results

The whole schedule of the previous experiments is addressed. The strength and ultimate behavior of specimens are analyzed. The failure modes are reinvestigated based

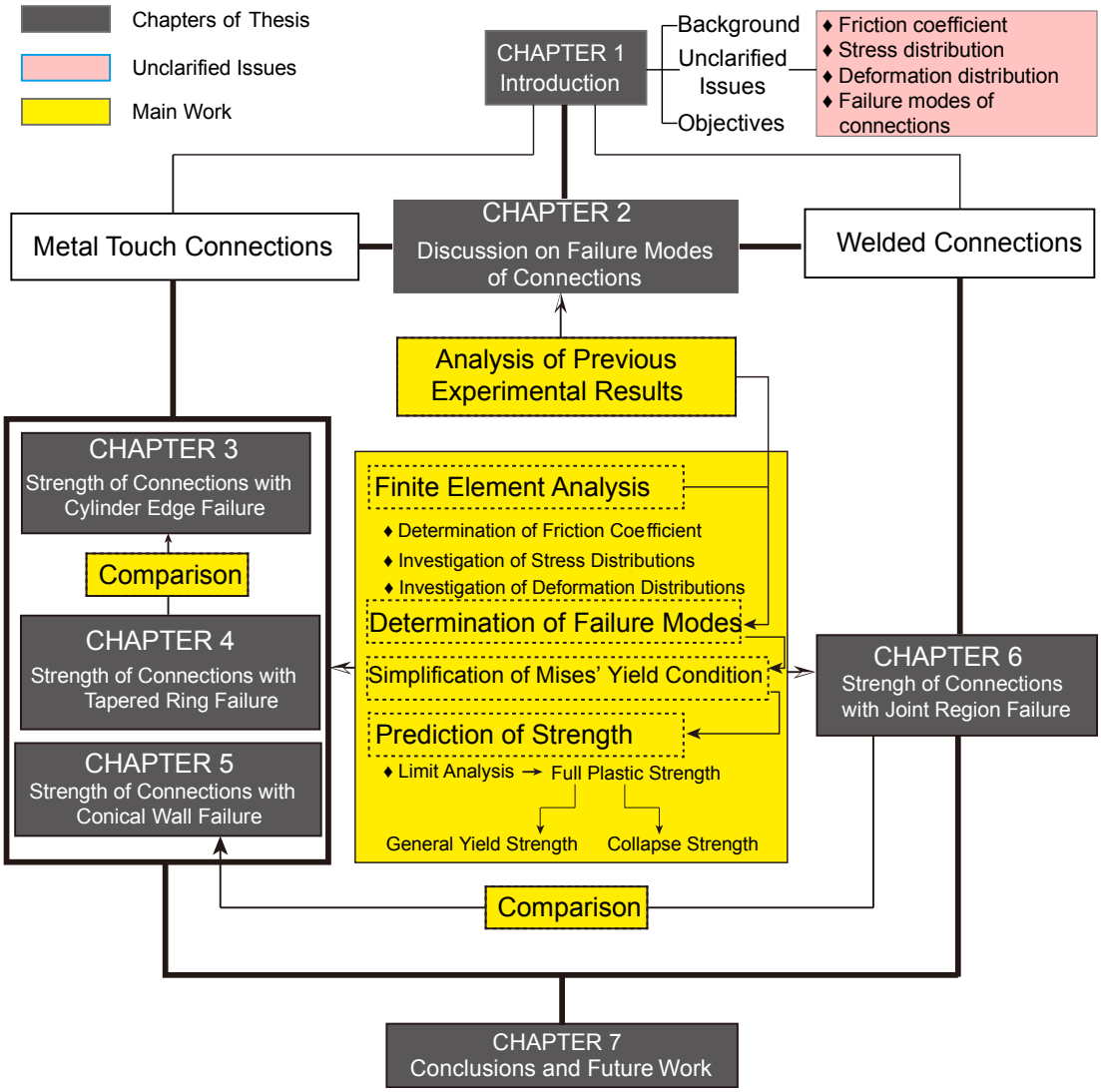

Fig. 1-5 Configuration of this thesis

on the experimental results.

Chapter 3 Strength of Metal Touch Connections with Cylinder Edge Failure

A comprehensive review of the preceding study on cylinder edge failure is addressed. Effective FEA (Finite Element Analysis) is then employed to analyze the friction coefficient between cone and cylinder and investigate the distributions of stresses and deformations of cylinder edge. Based on the FEA results and the preceding experimental results, the failure mode is determined by the proposed criteria. The limitations of the previous mechanical models are presented, and then a new mechanical model is created. Limit analysis is undertaken and the formula for predicting the full plastic strength of models is proposed. Based on the formula for full plastic strength, the prediction of ultimate strength and general yield strength is undertaken.

Chapter 4 Strength of Metal Touch Connections with Tapered Ring Failure

A comprehensive review of the preceding study on the reinforcement effect of rings on strength of cylindrical shells is addressed. FEA is employed to analyze the friction coefficients both between cone and cylinder and between cylinder and ring. And then, the distributions of stress and deformation of tapered ring are investigated. The failure mode is judged by the proposed criterion. The limitations of the previous mechanical model are presented, and then a new mechanical model is created. Limit analysis is undertaken and formula for predicting the full plastic strength of models is proposed. Based on the formula for full plastic strength, the prediction of ultimate strength and general yield strength is undertaken.

Chapter 5 Strength of Metal Touch Connections with Conical Wall Failure

A comprehensive review of conical wall failure under external pressure or along with axial compression is addressed. FEA is employed to analyze the friction coefficient between cone and cylinder. And then, the distributions of stress and deformation of conical wall are investigated. The failure mode is judged by the proposed criteria. The limitations of the previous mechanical model are presented, and then a new mechanical model is created. Limit analysis is undertaken and the formula for predicting the full plastic strength of models is proposed. Based on the formula for full plastic strength, the prediction of ultimate strength and general yield strength is undertaken.

Chapter 6 Strength of Welded Connections with Joint Region Failure

A comprehensive review of prediction of strength of welded cone-to-cylinder connections is addressed. FEA is employed to investigate the distributions of stress and deformation of conical and cylindrical walls. The failure mode is judged by the proposed criteria for plastic collapse. A new mechanical model is created and then limit analysis is undertaken. The formula for predicting the full plastic strength of models is proposed. Based on the formula for full plastic strength, the prediction of ultimate strength and general yield strength is undertaken.

Chapter 7 Conclusions and Future Research

CHAPTER 2 DISCUSSION ON FAILURE MODES BASED ON PREVIOUS EXPERIMENTAL RESULTS

2.1 Introduction

The feasibility of cone-to-cylinder socket connections was verified according to the results of pilot tests under compressive loading (Kuwamura et al. 2005a). Further experimental study including 104 specimens was then performed by Tomioka et al. (2006) to investigate the failure mechanisms of connections. Figure 2-1 gives the set-up of experiments under axial compression. The compressive loading was transformed to the connections through a round loading plate. The axial deformation, which is the shortening of the entire length of a specimen in the loading direction was measured by four laser displacement sensors. For each specimen, the bottom edge of cylindrial shell was metal-touched with foundation and the top edge of conical shell was welded to lid plate. Four kinds of boundary condition between conical wall and cylinder edge were adopted, such as “Metal touch”, “Metal touch + weak ring”, “Metal touch + strong ring” and “Welding”, as shown in Fig. 2-2. For specimens with the boundary of “Metal touch”, the cylindrical shell was designed to be much thinner than conical one in order to make it fail first; For specimens with the boundary of “Metal touch + thin ring”, the cylindrical shell was also designed to be much weaker than conical shell. Tapered ring of various thickness was then employed to investigate its reinforcement effect on the strength of specimens; For specimens with the boundary of “Metal touch + thick ring”, ring was designed to be strong enouch to make sure conical shell fail first; For specimens with the boundary of “Welding”, failure near to the weld region between conical wall and cylinder edge was investigated. The necessary parameters of connections for realizing these objectives are shown in Fig. 2-3. Table 2-1 lists their actually measured data. It should be noted that as

this study focuses on the specimens under axial compression, the information of those under local or eccential compression are omitted.

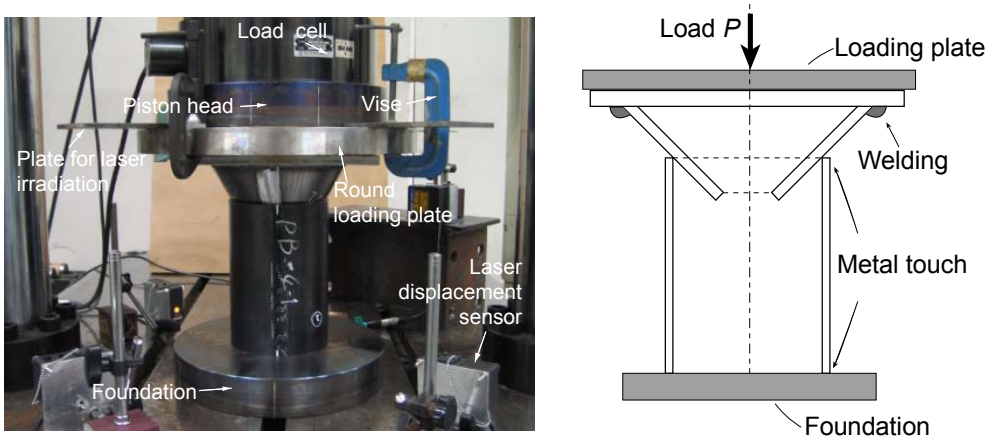

Fig. 2-1 Set-up of experiments under axial compression

(A metal touch connection is taken for example)

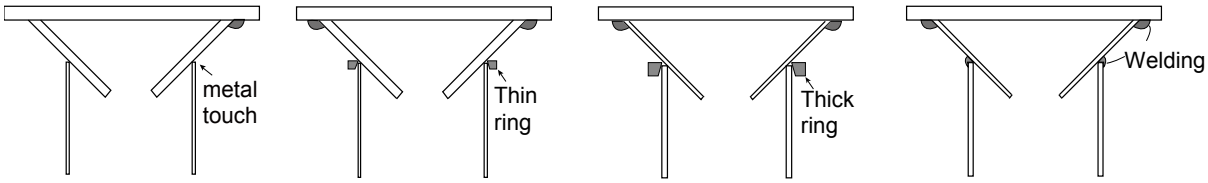

(a) "Metal touch" (b) "Metal touch +thin ring" (c) "Metal touch +thick ring" (d) "Welding"

Fig. 2-2 Boundary conditions between cone and cylinder

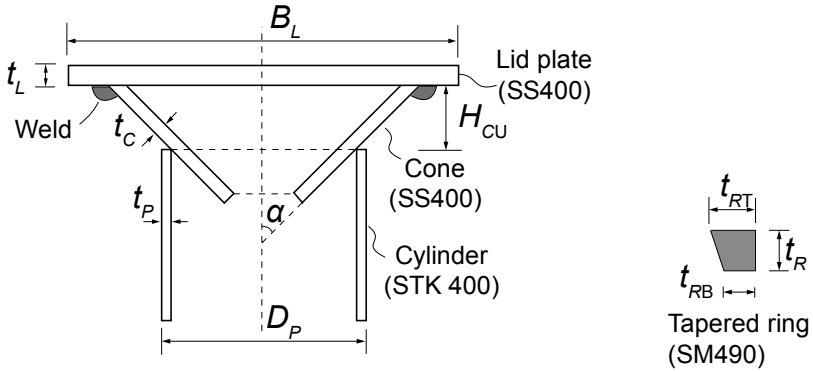

Fig. 2-3 Parameters of specimens

Note: ( ) gives the types of mild steel material

Table 2-1 Actual measurements of all the specimens under axial compression

Boundary condition (cone-cylinder)	Specimen No.	Cone			Cylinder		Lid plate		Tapered ring		
		Semi-angle	Thick-ness	Upper height	External diameter	Thick-ness	Width	Thick-ness	Thick-ness	Top width	Bottom width
		α	t_C	H_{CU}	D_P	t_P	B_L	t_L	t_R	t_{RT}	t_{RB}
		°	mm	mm	mm	mm	mm	mm	mm	mm	mm
"Metal touch"	1	31.97	8.74	50.07	139.80	3.32	239.65	11.62	-	-	-
	2	32.26	8.77	49.17	139.80	4.20	239.05	11.66	-	-	-
	3	32.64	8.67	48.77	140.50	6.03	240.55	11.63	-	-	-
	4	46.81	8.56	47.06	139.80	3.32	279.95	11.67	-	-	-
	5	45.91	8.53	48.27	140.00	4.30	279.70	11.86	-	-	-
	6	46.45	8.53	46.22	140.00	6.06	279.20	11.68	-	-	-
	7	59.26	8.63	50.78	140.05	3.33	358.85	11.60	-	-	-
	8	59.52	8.62	49.67	139.90	4.20	359.15	11.65	-	-	-
	9	59.97	8.64	49.07	140.00	6.03	360.20	11.62	-	-	-
	10	32.72	8.46	49.53	114.50	4.24	219.50	11.65	-	-	-
	11	32.74	8.51	49.85	165.60	5.58	259.40	11.66	-	-	-
	12	47.34	8.50	45.05	114.30	4.23	259.90	11.65	-	-	-
	13	45.69	8.64	50.42	165.50	5.64	299.85	11.64	-	-	-
	14	59.71	8.64	48.79	114.40	4.25	318.40	11.82	-	-	-
	15	60.15	8.66	47.09	165.65	5.62	375.20	11.69	-	-	-
"Metal touch +thin ring"	26	46.28	8.74	47.18	139.85	3.27	239.65	11.62	6.11	5.88	4.57
	27	46.25	8.77	49.16	139.75	3.34	239.05	11.66	9.16	9.07	7.85
	28	45.03	8.67	51.37	139.90	3.28	240.55	11.63	11.99	12.01	10.64
	29	46.64	8.56	47.28	139.75	4.13	279.95	11.67	6.01	5.83	4.60
	30	45.86	8.53	48.88	139.80	4.17	279.70	11.86	9.05	9.04	7.61
	31	45.93	8.53	48.87	139.80	4.15	279.20	11.68	12.00	11.98	10.58
	32	45.67	8.63	49.08	139.90	6.00	358.85	11.60	6.12	6.04	4.56
	33	45.33	8.62	51.87	139.90	6.01	359.15	11.65	9.04	9.07	7.73
	34	46.08	8.64	49.28	139.85	5.99	360.20	11.62	12.00	12.00	10.55
	35	33.38	8.46	51.85	139.85	4.21	219.50	11.65	9.07	9.02	7.72
	36	62.39	8.51	40.46	139.90	4.14	259.40	11.66	9.06	8.99	8.69
	37	49.02	8.50	50.08	114.30	4.24	259.90	11.65	9.07	8.93	7.71
	38	45.94	8.64	48.79	165.30	5.64	299.85	11.64	9.02	8.85	7.38
"Metal touch +thick ring"	43	33.27	3.05	49.33	139.90	4.21	239.50	11.70	12.07	12.01	10.62
	44	33.51	4.24	47.16	139.95	4.23	240.00	11.65	11.99	12.01	10.64
	45	33.10	5.78	49.84	139.85	4.23	239.00	11.75	11.99	11.99	10.61
	46	46.03	3.05	49.80	139.90	4.24	280.00	11.62	11.98	12.02	10.66
	47	46.68	4.27	49.39	139.85	4.21	280.00	11.62	12.01	12.03	10.62
	48	48.01	5.74	48.23	139.95	4.19	280.00	11.63	12.02	12.03	10.62
	49	61.37	3.05	46.32	139.80	4.19	359.00	11.62	12.05	12.05	10.67
	50	60.56	4.25	48.80	139.85	4.20	359.00	11.62	11.98	12.01	10.59
	51	59.58	5.64	50.14	139.90	4.17	359.50	11.62	11.96	11.96	10.69
	52	44.80	4.29	52.48	114.50	4.26	259.50	11.71	12.01	11.98	10.58
	53	46.24	4.20	49.97	165.80	5.62	300.00	11.68	12.04	11.99	10.59
"Welding"	64	30.47	3.20	49.80	139.90	4.31	239.50	12.00	-	-	-
	65	29.54	4.50	49.39	139.90	4.34	239.50	11.68	-	-	-
	66	30.96	6.00	51.53	139.90	4.31	239.50	11.60	-	-	-
	67	46.04	3.20	49.39	139.95	4.32	279.50	11.65	-	-	-
	68	43.96	4.50	49.94	139.90	4.34	280.00	11.68	-	-	-
	69	43.64	6.00	49.92	139.95	4.37	279.50	11.60	-	-	-
	70	59.04	3.20	51.53	139.85	4.31	359.50	11.65	-	-	-
	71	57.38	4.50	49.92	139.90	4.29	359.50	11.63	-	-	-
	72	58.60	6.00	51.53	139.90	4.34	359.50	11.67	-	-	-
	73	44.29	4.50	49.39	114.50	4.27	260.00	11.86	-	-	-
	74	46.05	4.50	49.97	165.20	5.61	299.50	11.68	-	-	-

Note: the specimens of Nos.16~25, 39~42, 54~63 and 75~84 under local or eccentric compression are not included in this table.

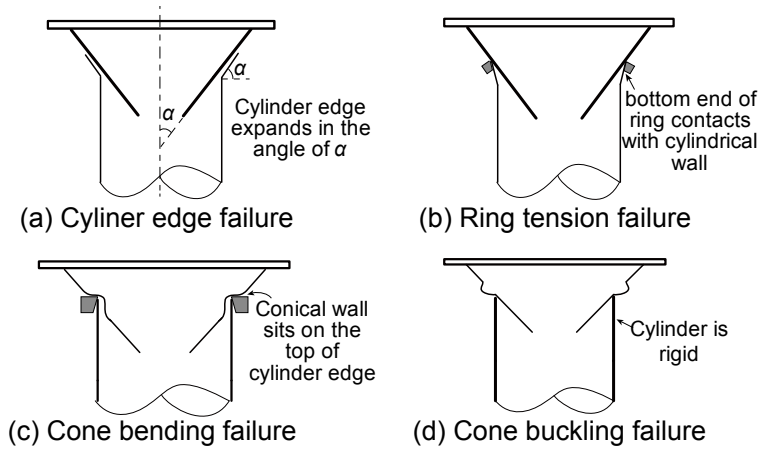

Fig. 2-4 Potential failure modes proposed by previous research

The failure mode of specimens under axial compression was classified into four cases: cylinder edge failure, ring tension failure, and cone bending failure for metal touch connections and cone buckling failure for welded connections, as shown in Fig. 2-4. The strength of connections with all the modes was derived theoretically (Kuwamura et al. 2005b, Fujimoto et al. 2010). It was found that for metal touch connections with cylinder edge failure, strength was predicted by assuming that cylinder edge expands with the same slope of conical wall; For metal touch connections with ring tension failure, the top edge of cylindrical wall was assuemd to be supported by the bottom end of ring; For metal touch connections with conical wall failure, strength was predicted by assuming that friction coefficient between conical wall and cylinder edge to be 1.0, which is a coefficient of static friction. Schey (1983) proposed that the maximum value of kinetic friction coefficient can never exceed $1/\sqrt{3}$ according to von Mises yield criterion even in a strain-hardening material. The assumption that the expansion of conical wall due to Poisson's ratio makes the cone sit on the edge of cylinder needs to be discussed; Lastly, for welded connections with cone buckling failure, strength was predicted by assuming cylindrical wall is rigid. However, the predicted buckling strength of cone was greater than the experimental results. Therefore, these failure modes need to be reinvestigated.

2.2 Material Properties of Connections

To obtain the material properties of all the members in the connections, tensile coupons are manufactured and then coupon test are undertaken. The results of coupon tests are listed in Appendix A. It should be noted that for cylindrical shell and tapered ring, the previous coupon test results (Tomioka 2006) are referred; while for conical shell and lid plate, the new coupon test results are obtained from the connections which still remain.

2.2.1 Cylindrical Shell

The tensile coupons were cut from cold-formed cylindrical shell used in the connection, as shown in Fig. 2-5. For each kind of cylindrical shell, three coupons were manufactured to obtain the average material properties. The effective results are shown in Fig. 2-6. It can be found that not all the results of coupons are employed. The yield plateau does not occur for all the coupons because of the effect of cold forming. The type of average curve is determined by the better result of coupons. The yield stress, tensile tress and relevant strain are listed in Table 2-2. It can be found that the diameter-to-thickness ratio has obvious effect on the yield stress of cold-formed cylindrical shells.

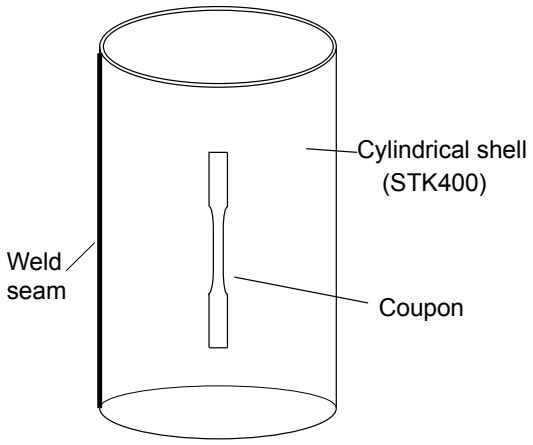

Fig. 2-5 Position of coupons for cylindrical shell

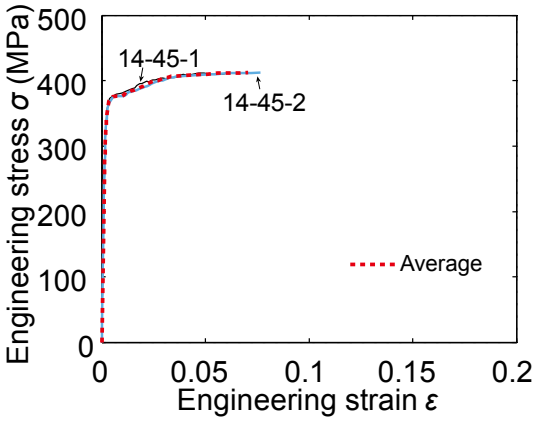

(a) D_P114.3mm×t_P4.5mm

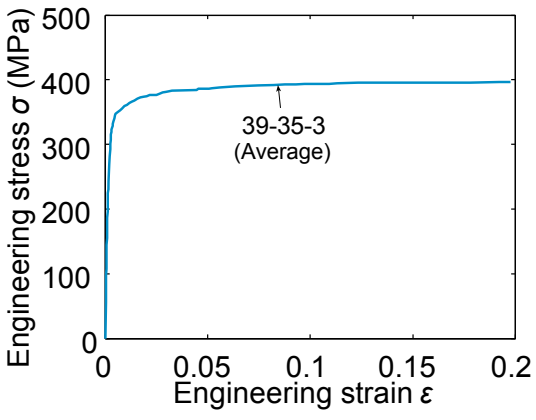

(b) D_P139.8mm×t_P3.5mm

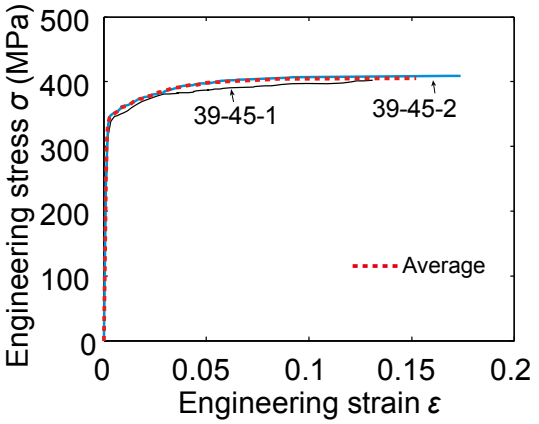

(c) D_P139.8mm×t_P4.5mm

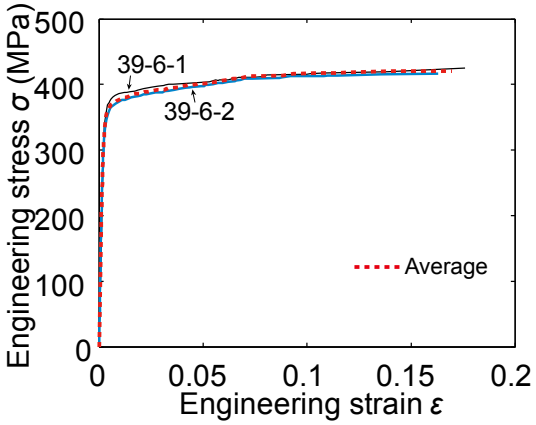

(d) D_P139.8mm×t_P6.0mm

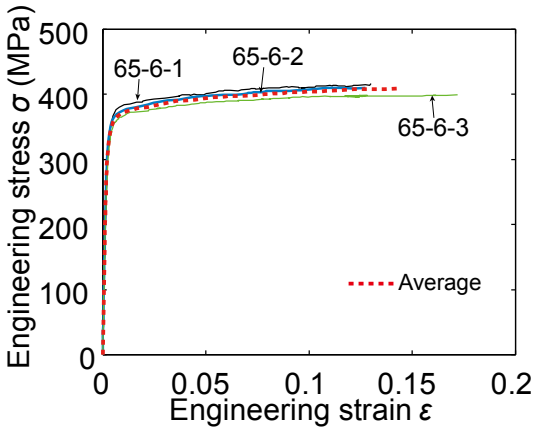

(d) D_P165.2mm×t_P6.0mm

Fig. 2-6 Engineering stress versus engineering strain curves of effective coupons of cylindrical shell

Table 2-2 Measured material properties of steel STK400 used in cylindrical shell

Steel grade	Size ($D_P \times t_P$) mm×mm	No.	t_P mm	σ_{yP} MPa	σ_{uP} MPa	ε_{yP}	ε_{uP}
STK400	114.3×4.5	14-45-1	4.22	373	413	0.0036	0.0648
		14-45-2	4.23	365	413	0.0033	0.0765
		average	**4.23**	**369**	**413**	**0.0034**	**0.0707**
	139.8×3.5	39-35-3	3.30	331	396	0.0037	0.1978
		average	**3.30**	**331**	**396**	**0.0037**	**0.1978**
	139.8×4.5	39-45-1	4.31	339	403	0.0033	0.1230
		39-45-2	4.25	347	409	0.0032	0.1602
		average	**4.28**	**343**	**406**	**0.0033**	**0.1416**
	139.8×6.0	39-6-1	5.61	369	425	0.0040	0.1760
		39-6-2	5.55	353	416	0.0039	0.1632
		average	**5.58**	**361**	**421**	**0.0039**	**0.1696**
	165.2×6.0	65-6-1	5.65	348	417	0.0037	0.1299
		65-6-2	5.67	350	410	0.0037	0.1272
		65-6-3	5.65	331	399	0.0036	0.1719
		average	**5.66**	**343**	**409**	**0.0036**	**0.1430**

Note: σ_y: yield stress, σ_u: tensile stress, ε_y: engineering strain at yield stress and ε_u: engineering strain at ultimate stress.

2.2.2 Conical Shell

The tensile coupons are cut from cold-formed conical shell used in the connection, as shown in Fig. 2-7. For each kind of conical shell, three coupons are manufactured to obtain the average material properties. If the results of former two coupons are well, the last one will be not undertaken. The effective results are shown in Fig. 2-8. The yield plateau does not occur for all the coupons because of the effect of cold forming. The material properties are listed in Table 2-3. It should be noted that the material properties of conical shells with thicknesses of 3.2 and 6.0 mm are not measured. They are assumed to be the same as those of conical shell with thickness of 4.5mm.

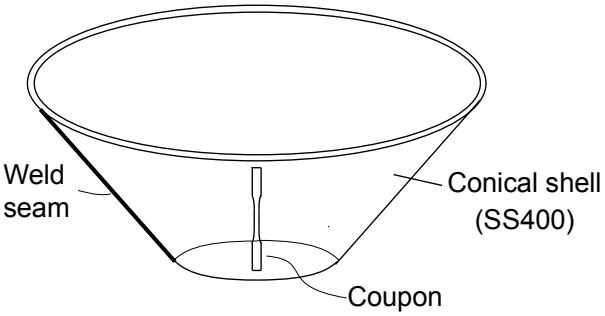

Fig. 2-7 Position of coupons for conical shell

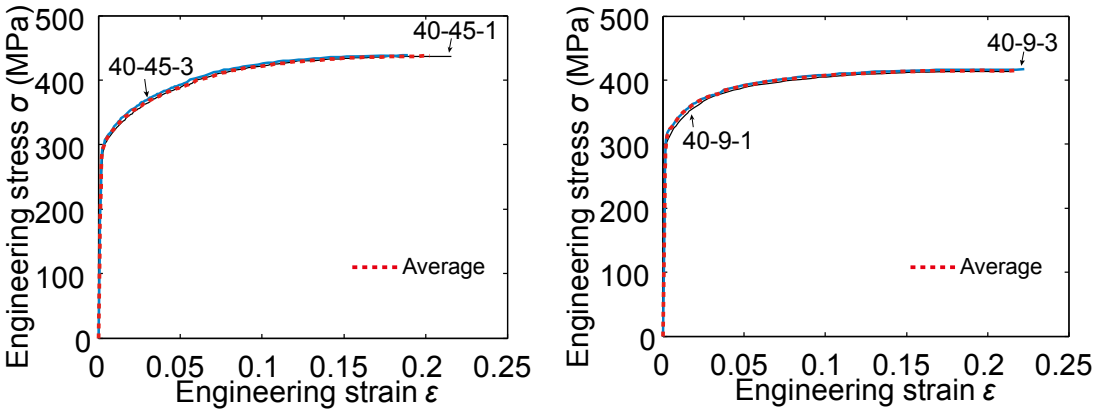

(a) t_C=4.5mm (B) t_C=9.0mm

Fig. 2-8 Engineering stress versus engineering strain curves of effective coupons of conical shell

Table 2-3 Measured material properties of steel SS400 used in conical shell

Steel grade	Size (t_C) mm	No.	t_C mm	σ_{yC} MPa	σ_{uC} MPa	ε_{yC}	ε_{uC}
SS400	4.5	40-45-1	4.20	296	437	0.0034	0.2156
		40-45-3	4.22	302	439	0.0033	0.1891
		average	**4.20**	**299**	**438**	**0.0034**	**0.2024**
	9.0	40-9-1	8.77	312	414	0.0037	0.2135
		40-9-3	8.27	322	417	0.0035	0.2227
		average	**8.52**	**317**	**416**	**0.0036**	**0.2181**

Note: The material properties of conical shells with thicknesses of 3.2 and 6.0 mm were not measured. They are assumed to be the same as those of conical shell with thickness of 4.5mm.

2.2.3 Tapered Ring

The tensile coupons were cut from a plate as shown in Fig. 2-9. The tapered rings are manufactured from the plate. By considering the fabrication process, the thicknesses of

plate were set to be 9mm, 12mm and 16mm, which are all a little greater than those of tapered ring. For each kind of ring, three coupons were manufactured to obtain the average material properties. The results are shown in Fig. 2-10. Not all the results of coupons were employed. The yield plateau occurs for all the coupons. The type of average curve is determined by the better result of coupons. The material properties are listed in Table 2-4. It can be found that the thickness of coupon has little effect on yield stress.

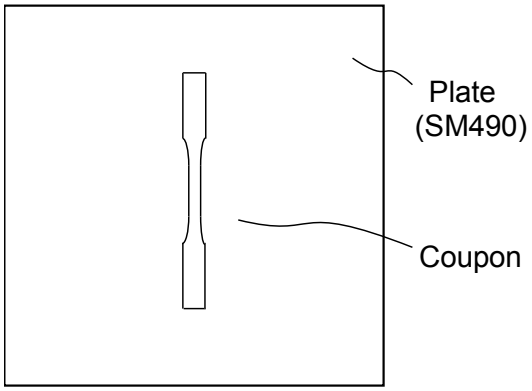

Fig. 2-9 Position of coupon for tapered ring

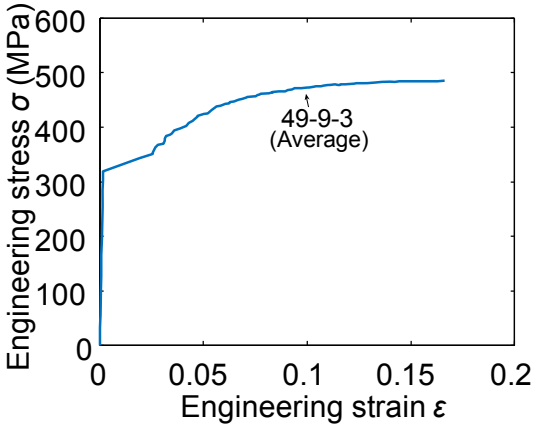

(a) t_R=6mm

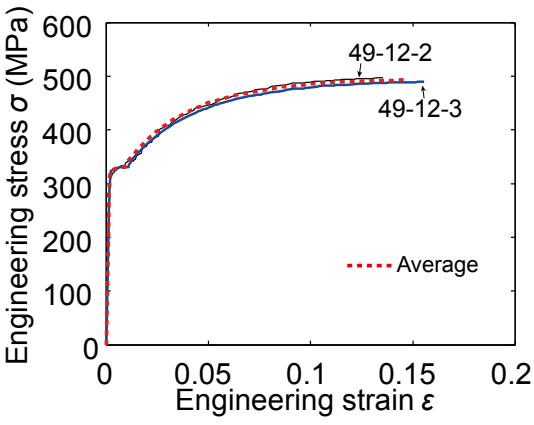

(b) t_R=9mm

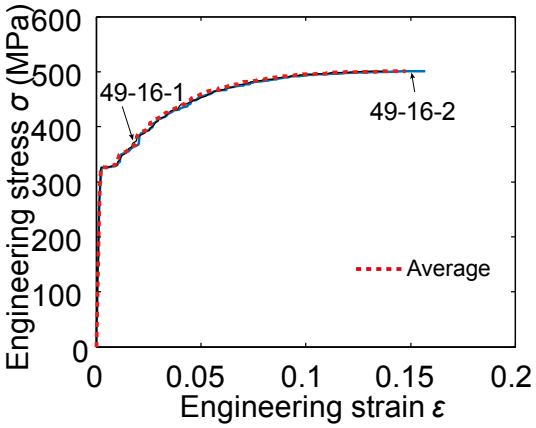

(c) t_R=12mm

Fig. 2-10 Engineering stress versus engineering strain curves of effective coupons of tapered ring

Table 2-4 Measured material properties steel SM490 used in tapered ring

Steel grade	Size (t_R) mm	No.	t_{coupon} mm	σ_{yR} MPa	σ_{uR} MPa	ε_{yR}	ε_{uR}
SM490	6	49-9-3	8.74	319	485	0.0017	0.1661
		average	**8.74**	**319**	**485**	**0.0017**	**0.1661**
	9	49-12-2	11.81	321	497	0.0036	0.1355
		49-12-3	11.81	321	490	0.0022	0.1557
		average	**11.81**	**321**	**494**	**0.0029**	**0.1456**
	12	49-16-1	15.66	321	502	0.0019	0.1386
		49-16-2	15.70	324	501	0.0024	0.1571
		average	**15.68**	**322**	**502**	**0.0022**	**0.1478**

Note: Tapered rings with thicknesses of 6, 9, and 12mm were produced from the plates with thicknesses of 9,12, and 16mm respectively.

2.2.4 Lid Plate

Three coupons parallel to *x* direction and three coupons parallel to *y* direction are cut from the plate used in the connection, as shown in Fig. 2-11. For the coupons in each direction, if the results of former two coupons are well, the last one will be not undertaken. The effective results are shown in Fig. 2-12. The yield plateau occurs for all the coupons. The material properties are listed in Table 2-5. The type of steel of lid plate is the same as that of conical shell. Comparing with the yield stress of conical shell with the thickness of 9mm shown in Table 2-3, the yield stress of lid plate is much smaller. It indicates again

that the effect of cold forming is great for the yield stress of shell structures.

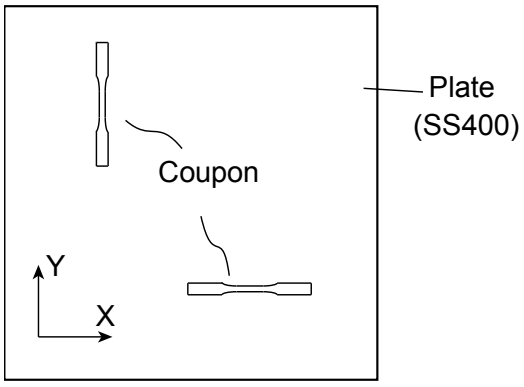

Fig. 2-11 Position of coupon for lid plate

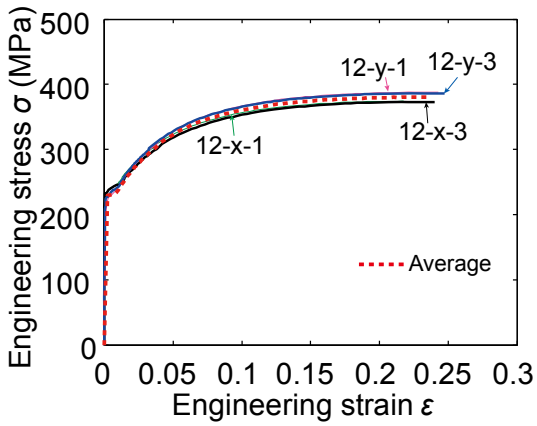

Fig. 2-12 Engineering stress versus engineering strain curves of effective coupons of lid plate (t_L=12mmm)

Table 2-5 Measured material properties steel SS400 used in lid plate

Steel grade	Size (t_L) mm	No.	t_L mm	σ_{yL} MPa	σ_{uL} MPa	ε_{yL}	ε_{uL}
SS400	12	40-12-X-1	11.50	235	374	0.0020	0.2176
		40-12-X-3	11.60	235	373	0.0022	0.2400
		40-12-Y-1	11.50	221	388	0.0022	0.2428
		40-12-Y-3	11.40	227	386	0.0020	0.2474
		average	**11.50**	**230**	**380**	**0.0021**	**0.2370**

2.3 Diameter-to-Thickness Ratios of Cylindrical and Conical Shells

In this study, conical and cylindrical shells are designed to fail in plastic condition. It

is necessary to control their diameter-to-thickness ratios smaller than the limit values of elastic buckling. The classical buckling stress of a smooth-walled perfect cylinder was proposed by Donnell (1933), as shown in Eq. (2-1).

$$\sigma_{crP} = \frac{E_0}{\sqrt{3(1-\nu^2)}} \frac{2t_P}{d_P} \tag{2-1}$$

where, elastic modulus E_0=205,000MPa, ν=0.3.

Then, the elastic buckling stress of a long circular cone was studied by Seide (1956). For the socket connections, assuming the buckle of conical shell is close to the top edge of cylindrical shell, the equation for elastic buckling stress of cone is expressed as

$$\sigma_{crC} = \sigma_{crP} \cos\alpha = \frac{E_0}{\sqrt{3(1-\nu^2)}} \frac{2t_C}{d_P} \cos\alpha \tag{2-2}$$

The design standard for steel structures in Japan (2002) suggests that the limit diameter-to-thickness ratio of cylindrical shell for practical design work is

$$\left(\frac{d_P}{t_P}\right)_{\text{limit\_}P} = \frac{23500}{\sigma_{yP}} \tag{2-3}$$

Based on Eqs. (2-2) and (2-3), the limit diameter-to-thickness ratio of conical shell for practical design work can be expressed as

$$\left(\frac{d_P}{t_C}\right)_{\text{limit\_}C} = \frac{23500}{\sigma_{yC}} \cos\alpha \tag{2-4}$$

The diameter-to-thickness ratios of cylindrical and conical shells in the connections are compared with the limit values shown in Eqs. (2-3) and (2-4), respectively. The results are listed in Table 2-6. It can be found that most of the ratios are much smaller than 1.0, except for specimen Nos. 49 and 70. As these limit diameter-to-thickness ratios are smaller than the theoretical values, all the shells in this study can be thought to fail in plastic condition.

Table 2-6 Comparison of diameter-to-thickness ratios of shells with the limit values

Boundary condition (cone-cylinder)	Specimen No.	Cone			Cylinder			Cylinder	Cone	Cylinder	Cone	Cyliner	Cone
		Semi-angle	Thick-ness	Yield stress	External diameter	Thick-ness	Yield stress	Diameter-to-thickness ratio (*)		Limit diameter-to-thickness ratio (**)		ratio of (*) to (**)	
		α	t_C	σ_{yC}	D_P	t_P	σ_{yP}						
		°	mm	mm	mm	mm	mm	d_P/t_P	d_P/t_C	Eq. (2-3)	Eq. (2-4)		
"Metal touch"	1	31.97	8.74	317	139.80	3.32	331	41.11	14.39	71.00	62.89	0.58	0.23
	2	32.26	8.77	317	139.80	4.20	343	32.29	14.14	68.51	62.69	0.47	0.23
	3	32.64	8.67	317	140.50	6.03	361	22.30	13.97	65.10	62.42	0.34	0.22
	4	46.81	8.56	317	139.80	3.32	331	41.11	14.87	71.00	50.73	0.58	0.29
	5	45.91	8.53	317	140.00	4.30	343	31.56	14.71	68.51	51.58	0.46	0.29
	6	46.45	8.53	317	140.00	6.06	361	22.10	14.30	65.10	51.07	0.34	0.28
	7	59.26	8.63	317	140.05	3.33	331	41.06	14.95	71.00	37.89	0.58	0.39
	8	59.52	8.62	317	139.90	4.20	343	32.31	14.75	68.51	37.60	0.47	0.39
	9	59.97	8.64	317	140.00	6.03	361	22.22	14.31	65.10	37.10	0.34	0.39
	10	32.72	8.46	317	114.50	4.24	369	26.00	11.69	63.69	62.37	0.41	0.19
	11	32.74	8.51	317	165.60	5.58	343	28.68	17.31	68.51	62.36	0.42	0.28
	12	47.34	8.50	317	114.30	4.23	369	26.02	11.77	63.69	50.23	0.41	0.23
	13	45.69	8.64	317	165.50	5.64	343	28.34	17.15	68.51	51.78	0.41	0.33
	14	59.71	8.64	317	114.40	4.25	369	25.92	11.75	63.69	37.40	0.41	0.31
	15	60.15	8.66	317	165.65	5.62	343	28.48	17.33	68.51	36.90	0.42	0.47
"Metal touch +thin ring"	26	46.28	8.74	317	139.85	3.27	331	41.77	14.56	71.00	51.23	0.59	0.28
	27	46.25	8.77	317	139.75	3.34	331	40.84	14.48	71.00	51.26	0.58	0.28
	28	45.03	8.67	317	139.90	3.28	331	41.65	14.67	71.00	52.39	0.59	0.28
	29	46.64	8.56	317	139.75	4.13	343	32.84	14.67	68.51	50.90	0.48	0.29
	30	45.86	8.53	317	139.80	4.17	343	32.53	14.72	68.51	51.63	0.47	0.29
	31	45.93	8.53	317	139.80	4.15	343	32.69	14.72	68.51	51.56	0.48	0.29
	32	45.67	8.63	317	139.90	6.00	361	22.32	14.12	65.10	51.80	0.34	0.27
	33	45.33	8.62	317	139.90	6.01	361	22.28	14.13	65.10	52.12	0.34	0.27
	34	46.08	8.64	317	139.85	5.99	361	22.35	14.11	65.10	51.42	0.34	0.27
	35	33.38	8.46	317	139.85	4.21	343	32.22	14.70	68.51	61.90	0.47	0.24
	36	62.39	8.51	317	139.90	4.14	343	32.79	15.00	68.51	34.36	0.48	0.44
	37	49.02	8.50	317	114.30	4.24	369	25.96	11.79	63.69	48.61	0.41	0.24
	38	45.94	8.64	317	165.30	5.64	343	28.31	17.13	68.51	51.55	0.41	0.33
"Metal touch +thick ring"	43	33.27	3.05	299	139.90	4.21	343	32.23	42.27	68.51	65.71	0.47	0.64
	44	33.51	4.24	299	139.95	4.23	343	32.09	30.18	68.51	65.53	0.47	0.46
	45	33.10	5.78	299	139.85	4.23	343	32.06	21.89	68.51	65.84	0.47	0.33
	46	46.03	3.05	299	139.90	4.24	343	32.00	42.39	68.51	54.57	0.47	0.78
	47	46.68	4.27	299	139.85	4.21	343	32.22	30.09	68.51	53.93	0.47	0.56
	48	48.01	5.74	299	139.95	4.19	343	32.40	22.25	68.51	52.58	0.47	0.42
	49	61.37	3.05	299	139.80	4.19	343	32.37	42.61	68.51	37.66	0.47	1.13
	50	60.56	4.25	299	139.85	4.20	343	32.30	30.44	68.51	38.63	0.47	0.79
	51	59.58	5.64	299	139.90	4.17	343	32.55	22.82	68.51	39.79	0.48	0.57
	52	44.80	4.29	299	114.50	4.26	369	25.88	23.99	63.69	55.77	0.41	0.43
	53	46.24	4.20	299	165.80	5.62	343	28.50	36.11	68.51	54.36	0.42	0.66
"Welding"	64	30.47	3.20	299	139.90	4.31	343	31.46	40.16	68.51	67.74	0.46	0.59
	65	29.54	4.50	299	139.90	4.34	343	31.24	28.29	68.51	68.38	0.46	0.41
	66	30.96	6.00	299	139.90	4.31	343	31.46	21.02	68.51	67.39	0.46	0.31
	67	46.04	3.20	299	139.95	4.32	343	31.40	40.34	68.51	54.56	0.46	0.74
	68	43.96	4.50	299	139.90	4.34	343	31.24	28.44	68.51	56.58	0.46	0.50
	69	43.64	6.00	299	139.95	4.37	343	31.03	21.14	68.51	56.88	0.45	0.37
	70	59.04	3.20	299	139.85	4.31	343	31.45	40.49	68.51	40.44	0.46	1.00
	71	57.38	4.50	299	139.90	4.29	343	31.61	28.64	68.51	42.37	0.46	0.68
	72	58.60	6.00	299	139.90	4.34	343	31.24	21.35	68.51	40.95	0.46	0.52
	73	44.29	4.50	299	114.50	4.27	369	25.81	22.83	63.69	56.26	0.41	0.41
	74	46.05	4.50	299	165.20	5.61	343	28.45	33.52	68.51	54.54	0.42	0.61

2.4 Definitions of Strength and Axial Deformation

In this thesis, the collapse strength, full plastic strength and general yield strength of the connections are studied. The definitions of them and relevant axial deformation are shown in Fig 2-13. For collapse strength P_u, it is defined as the peak load of load-axial deformation curves. For full plastic strength P_p, several methods were proposed by many scholars (Wardenieer 1982; Tateyama et al. 1988; Morita et al. 1989; and Kuwamura et al. 2014). However, unified way cannot be found because the type of connections has obvious influence on the determination of full plastic strength. In this study, P_p is defined as the load where the slope of load versus axial deformation curve reduces to one sixth of the initial stiffness K_0 (Tateyama et al. 1988). For general yield strength P_y, the research on its definition has been undertaken since 1939 (Johnston 1939a, b; Packer et al. 1980; Kurobane et al. 1984, Zhao and Hancock 1991; et al). In this study, P_y is defined as the load where the slope of load versus axial deformation curve reduces to one third of the initial stiffness K_0 (Johnston 1939). This method is recommended in steel structure engineering in Japan (Building Research Institute et al. 2002).

In addition, the theoretical elastic axial deformation of specimen when full plastic strength is reached is defined as $\Delta_{pe.}$ The axial deformation of specimen at ultimate load is defined as $\Delta_{u.}$

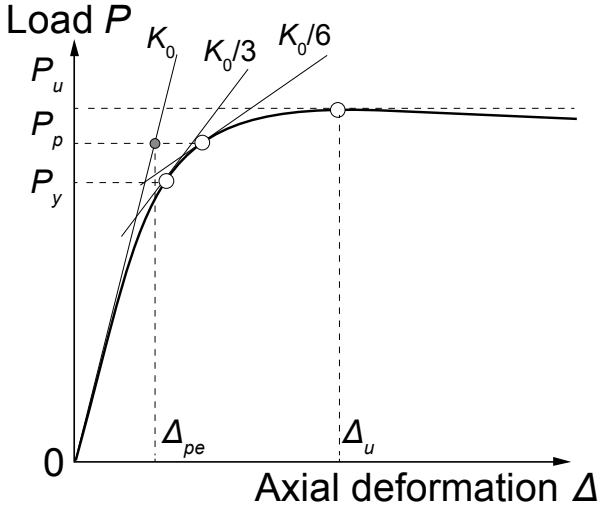

Fig. 2-13 Standard load-axial deformation curves of specimens and definitions of strength and deformation

2.5 Discussion on Failure Modes of Specimens

2.5.1 Specimens with Boundary of "Metal touch"

The behavior of connections with boundary of "Metal touch" after large deformation is shown in Fig. 2-14. It can be found that specimens Nos.1~8 and 10~14 failed like a trumpet, at the top edge of cylinder wall in an axisymmetric type. While, specimens No. 9 failed in conical wall with the shape of depression. In addition, specimen No.15 failed in both conical wall and cylinder edge asymmetrically. Thus, the specimens mainly occurred at cylinder edge.

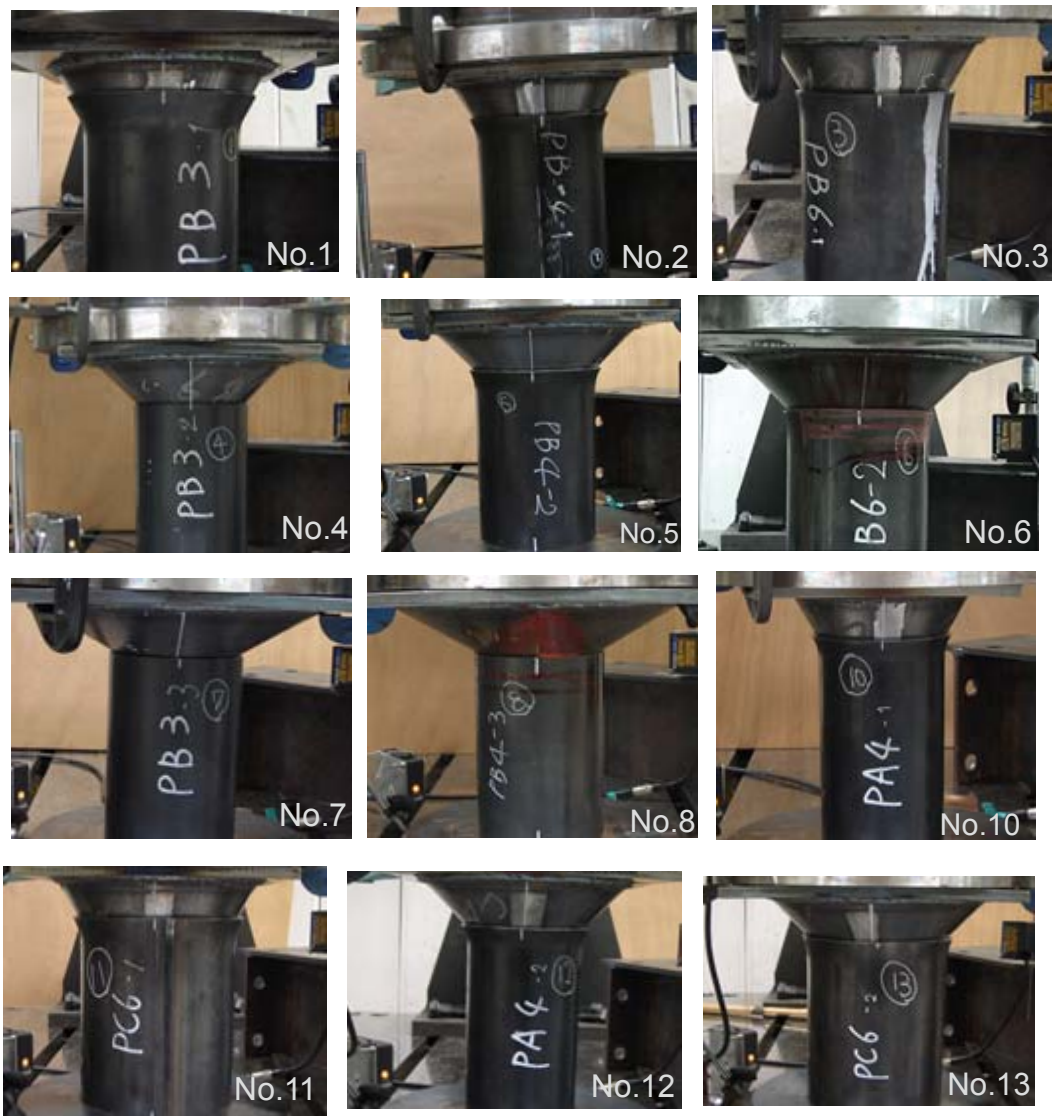

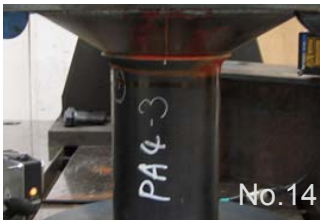

(a) Specimens with cylinder edge failure

(b) Specimens with other failure modes

Fig. 2-14 Behavior of specimens with boundary of "Metal touch" after testing

Table 2-7 Strength of specimens with cylinder edge failure

Specimen No.	Main parameters			General yield strength	Plastic strength	Collapse strength	Δ_u	$P_{u\text{-}EXP}/P_{p\text{-}EXP}$
	Cone	Cylinder						
	Semi-angle	Thick-ness	External diameter					
	α	t_P	D_P	$P_{y\text{-}EXP}$	$P_{p\text{-}EXP}$	$P_{u\text{-}EXP}$		
	°	mm	mm	kN	kN	kN	mm	
1	32.0	3.3	139.8	43.6	48.8	58.8	2.89	1.20
2	32.3	4.2	139.8	94.2	116.4	120.8	2.98	1.04
3	32.6	6.0	140.5	149.5	164.0	174.9	3.72	1.07
4	46.8	3.3	139.8	80.8	102.4	112.1	2.28	1.09
5	45.9	4.3	140.0	129.2	148.2	169.7	2.85	1.15
6	46.5	6.1	140.0	222.7	275.0	336.6	6.12	1.22
7	59.3	3.3	140.1	194.1	207.5	215.1	3.40	1.04
8	59.5	4.2	139.9	264.0	280.8	285.0	2.31	1.01
10	32.7	4.2	114.5	80.0	90.8	99.4	2.67	1.09
11	32.7	5.6	165.6	125.6	137.5	160.2	5.72	1.16
12	47.3	4.2	114.3	140.0	160.0	176.8	2.56	1.11
13	45.7	5.6	165.5	268.2	281.8	302.8	3.54	1.07
14	59.7	4.3	114.4	234.0	242.0	246.9	3.16	1.02

The strength and deformation of specimen Nos.1~8 and 10~14 which failed at cylinder edge are listed in Table 2-15. It can be found that as thickness t_P or semi-vertex angle α increases, the strength of specimens will become larger. By comparing the

strength of specimen No.7 with those of specimen Nos. 1 and 4, it is found that as the value of α increases, the strength become larger, but the ratio of $P_{u\text{-}EXP}$ to $P_{p\text{-}EXP}$ becomes smaller. By comparing the strength of specimen No.6 with those of specimen Nos. 4 and 5, it is found that as the value of t_P increases, not only the strength but also the ratio of $P_{u\text{-}EXP}$ to $P_{p\text{-}EXP}$ become greater.

The ultimate behavior of specimens with cylinder edge failure is sketched in the axisymmetric coordinate system (r, θ, x), as shown in Fig. 2-15. The radial deformation of the top edge of cylinder is defined as w_{ruP}. It can be obtained by

$$w_{ruP} = -\Delta_u \tan\alpha \tag{2-5}$$

Then, the strain in hoop direction can be obtained as

$$\varepsilon_{\theta uP} = \frac{-2\Delta_u \tan\alpha}{D_P - t_P} \tag{2-6}$$

based on the assumption of uniaxial stress state. In order to investigate the failure mode of cylinder edge, it is compared with yield strain ε_{yP}, as shown in Table 2-8. It can be found that their ratios are in the range of 7~29. The $\varepsilon_{\theta uP}$ is larger than ε_{yP}, but still much less than strain at tensile stress ε_{uP}. The top edge of cylindrical wall entered into plastic condition when ultimate load arrived. However, the length of plastic region cannot be obtained because the radial deformation along x direction cannot be measured. For shell structures, out of plane deformation not only induces hoop stress, but also induces bending stress. Whether cylinder edge failure is controlled by hoop tension or by axial bending cannot be judged based on the experimental results.

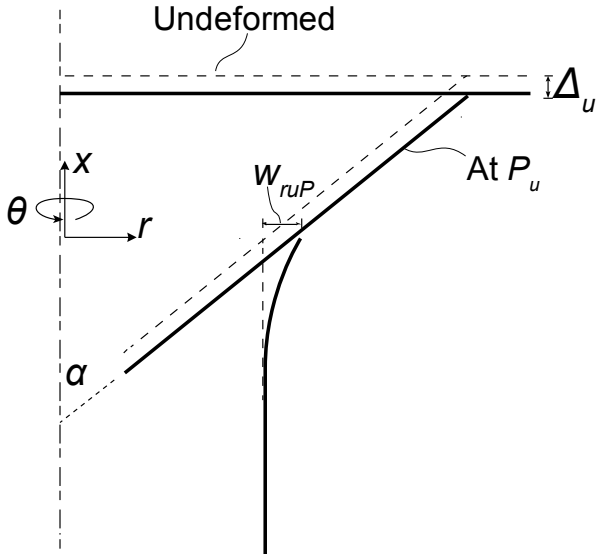

Fig. 2-15 Sketch of ultimate behavior of specimen with cylinder edge failure

Table 2-8 Ultimate radial deformation at the top edge of cylinder for specimens with cylinder edge failure

Specimen No.	Main parameters			Δ_u	w_{ruP}	$\varepsilon_{\theta uP}$	ε_{yP}	$\varepsilon_{\theta uP}/\varepsilon_{yP}$
	Cone	Cylinder						
	Semi-vertex angle	Thickness	External diameter					
	α	t_P	D_P					
	deg.	mm	mm	mm	mm			
1	32.0	3.3	139.8	2.89	1.81	0.0265	0.0037	7.15
2	32.3	4.2	139.8	2.98	1.88	0.0278	0.0033	8.42
3	32.6	6.0	140.5	3.72	2.38	0.0354	0.0039	9.07
4	46.8	3.3	139.8	2.28	2.43	0.0356	0.0037	9.63
5	45.9	4.3	140.0	2.85	2.94	0.0433	0.0033	13.13
6	46.5	6.1	140.0	6.12	6.45	0.0964	0.0039	24.71
7	59.3	3.3	140.1	3.40	5.72	0.0837	0.0037	22.62
8	59.5	4.2	139.9	2.31	3.92	0.0578	0.0033	17.52
10	32.7	4.2	114.5	2.67	1.72	0.0311	0.0034	9.16
11	32.7	5.6	165.6	5.72	3.67	0.0459	0.0036	12.75
12	47.3	4.2	114.3	2.56	2.77	0.0504	0.0034	14.82
13	45.7	5.6	165.5	3.54	3.63	0.0454	0.0036	12.62
14	59.7	4.3	114.4	3.16	5.41	0.0983	0.0034	28.90

2.5.2 Specimens with Boundary of “Metal touch + thin ring”

The ultimate behavior of specimens with boundary of “Metal touch + thin ring” is shown in Fig. 2-16. It can be found that specimen Nos. 26~30, 35 and 37 failed at cylinder edge, specimen Nos. 34 and 36 failed in conical wall with the type of depression, specimen No. 31 failed in “elephant foot buckling” of cylindrical shell, and specimen Nos. 32, 33 and 38 failed asymmetrically. For all the specimens, the tapered ring did not drop when ultimate load arrived.

(a) Specimens with tapered ring failure

(b) Specimens with other failure modes

Fig. 2-16 Ultimate behavior of specimens with boundary of "Metal touch + thin ring"

Table 2-9 Strength and deformations of specimens with boundary of "Metal touch + thin ring" failed at the top edge of cylinder

Specimen No.	Main parameters				General yield strength	Full plastic strength	Collapse strength	Δ_u	$P_{u\text{-}EXP}/P_{p\text{-}EXP}$
	Cone	Cylinder		Ring					
	Semi-angle	Thick-ness	External diameter	Thick-ness					
	α	t_P	D_P	t_R	$P_{y\text{-}EXP.}$	$P_{p\text{-}EXP.}$	$P_{u\text{-}EXP.}$		
	deg.	mm	mm	mm	kN	kN	kN	mm	
26	46.3	3.3	139.9	6.1	160.1	165.2	182.4	2.48	1.10
27	46.3	3.3	139.8	9.2	260.0	287.5	342.3	3.25	1.19
28	45.0	3.3	139.9	12.0	293.3	333.3	420.0	4.73	1.26
29	46.6	4.1	139.8	6.0	230.4	257.0	277.0	2.80	1.08
30	45.9	4.2	139.8	9.1	356.4	417.9	509.0	3.87	1.22
35	33.4	4.2	139.9	9.1	405.0	463.9	530.6	10.08	1.14
37	49.0	4.2	114.3	9.1	338.0	432.0	472.7	5.21	1.09

The strength and deformation of specimens Nos.26~30, 35 and 37 which failed at the top edge of cylindrical wall are listed in Table 2-9. By comparing the strength among specimen Nos.26~28, it can be found that as the thickness t_R of tapered ring increases, the strength of specimens become greater. Meanwhile, the ratio of P_u to P_p also increases.

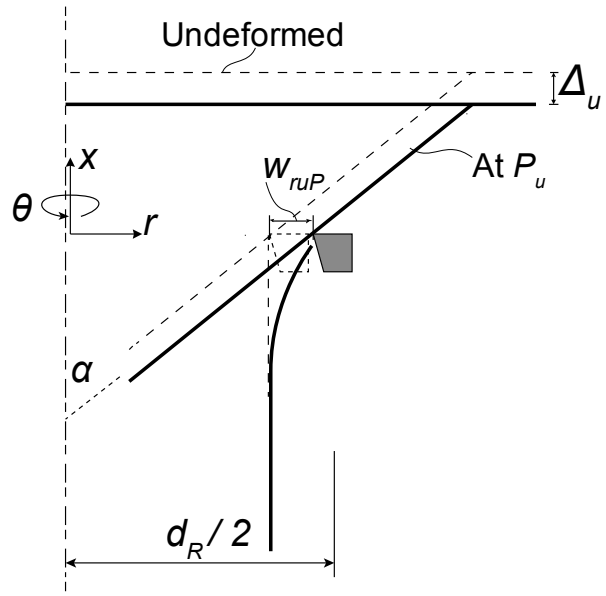

Fig. 2-17 Sketch of ultimate behavior of specimens with boundary of "Metal touch + thin ring" failed at the top edge of cylindrical shell

Table 2-10 Ultimate radial deformations of specimens with boundary of "Metal touch + thin ring" failed at the top edge of cylinder

Specimen No.	Main parameters				w_{ruP}	$\varepsilon_{\theta uR}$	ε_{yR}	$\varepsilon_{\theta uR}/\varepsilon_{yR}$
	Cone	Cylinder		Ring				
	Semi-vertex angle	Thickness	External diameter	Thickness				
	α	t_P	D_P	t_R				
	deg.	mm	mm	mm	mm			
26	46.3	3.3	139.9	6.1	2.59	0.0355	0.0017	20.90
27	46.3	3.3	139.8	9.2	3.41	0.0457	0.0029	15.77
28	45.0	3.3	139.9	12.0	4.73	0.0623	0.0022	28.30
29	46.6	4.1	139.8	6.0	2.96	0.0407	0.0017	23.93
30	45.9	4.2	139.8	9.1	3.99	0.0536	0.0029	18.48
35	33.4	4.2	139.9	9.1	6.64	0.0892	0.0029	30.76
37	49.0	4.2	114.3	9.1	5.99	0.0972	0.0029	33.50

The ultimate behavior of the specimens with boundary of "Metal touch +thin ring" failed at the top edge of cylindrical shell is sketched in Fig. 2-17. In order to investigate the failure mode of tapered ring, its average hoop strain is obtained by

$$\varepsilon_{\theta uR} = \frac{w_{ruP}}{d_R} = \frac{-2\Delta_u \tan\alpha}{d_R} \tag{2-7}$$

It is compared with yield strain ε_{yR} of tapered ring, as shown in Table 2-10. It is found that their ratios are in the range of 15~34. Tapered rings entered into plastic condition as ultimate load arrived. It can be assumed that the specimen with boundary of "Metal touch + thin ring" failed in tapered ring.

2.5.3 Specimens with Boundary of "Metal touch + thick ring"

The ultimate behavior of specimens with boundary of "Metal touch + thick ring" is shown in Fig. 2-18. It can be found that specimen Nos. 43, 44, and 46~53 failed in conical wall, as no obvious deformation was found in cylindrical wall and tapered ring after testing. In addition, specimen No.45 failed asymmetrically. As the typical case, the deformation of conical wall in specimen No. 47 after testing is shown in Fig. 2-19. Obvious bending deformation in the conical wall can be found.

(a) Specimens with conical wall failure

(b) Specimen with asymmetric failure mode

Fig. 2-18 Ultimate behavior of specimens with boundary of "Metal touch + thick ring"

Fig. 2-19 Deformation of conical wall after testing in specimen No. 47

The strength and deformation of specimen Nos. 43, 44, and 46~53 with conical wall failure are listed in Table 2-11. Those of specimen Nos. 9, 34 and 36 which failed in conical wall are also included. By comparing the strength of specimen No.50 with those of specimen Nos. 44 and 47, it is found that as semi-vertex angle α increases, not only the strength of conical wall but also the ratio of $P_{u\text{-}EXP}$ to $P_{p\text{-}EXP}$ become smaller. By comparing the strength of specimen No.48 with those of specimen Nos. 46 and 47, it is found that as thickness t_C increases, not only the strength of conical wall but also the ratio of $P_{u\text{-}EXP}$ to $P_{p\text{-}EXP}$ become greater.

Table 2-11 Strength and deformation of specimens with conical wall failure

Specimen No.	Main parameters					General yield strength	Full plastic strength	Collapse strength	Δ_u	$P_{u\text{-}EXP.}/P_{p\text{-}EXP}$
	Cone		Cylinder		Ring					
	Semi-angle	Thick-ness	Thick-ness	External diameter	Thick-ness					
	α	t_C	t_P	D_P	t_R	$P_{y\text{-}EXP.}$	$P_{p\text{-}EXP.}$	$P_{u\text{-}EXP.}$		
	deg.	mm	mm	mm	mm	kN	kN	kN	mm	
9	60.0	8.6	6.0	140.0		482.6	561.5	601.2	5.35	1.07
34	46.1	8.6	6.0	139.9	12.0	543.8	620.0	872.8	15.46	1.41
36	62.4	8.6	4.1	139.9	9.1	390.9	527.3	625.7	8.92	1.19
43	33.3	3.1	4.2	139.9	12.1	139.1	153.6	234.9	12.00	1.53
44	33.5	4.2	4.2	140.0	12.0	263.0	294.7	389.9	14.12	1.32
46	46.0	3.1	4.2	139.9	12.0	127.5	158.7	178.4	5.81	1.12
47	46.7	4.3	4.2	139.9	12.0	192.6	218.5	274.2	7.62	1.25
48	48.0	5.7	4.2	140.0	12.0	314.8	400.0	510.0	9.13	1.27
49	61.4	3.1	4.2	139.8	12.1	120.9	123.5	125.2	5.42	1.01
50	60.6	4.3	4.2	139.9	12.0	182.8	190.0	194.9	6.98	1.03
51	59.6	5.6	4.2	139.9	12.0	325.0	336.5	352.8	7.37	1.05
52	44.8	4.3	4.3	114.5	12.0	171.1	208.5	251.8	8.68	1.21
53	46.2	4.2	5.6	165.8	12.0	200.0	254.3	309.3	8.02	1.22

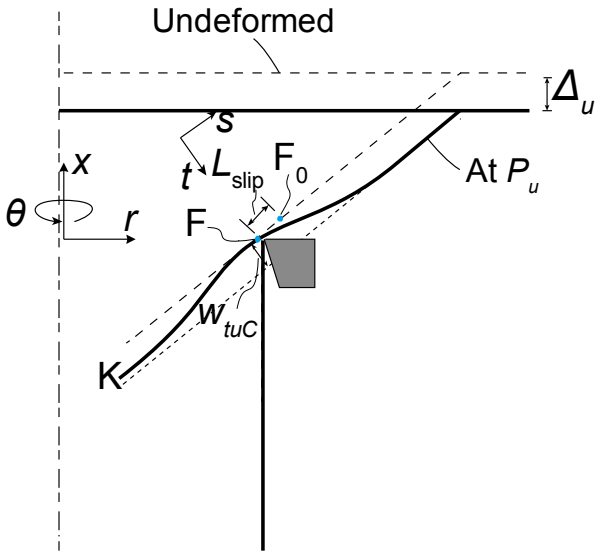

Fig. 2-20 Sketch of ultimate behavior of specimens with conical wall failure

The ultimate behavior of the specimens failed in conical wall is sketched in Fig. 2-20. The section in conical wall which contacts with cylinder edge at ultimate load is set to be Sect. F. It is originally located at section "F_0". The slip of conical wall is defined as L_{slip},

which is equal to the distance from "F_0" to "F". It is quite difficult to be measured in experiments. The normal deformation of Sect. F in t direction is defined as w_{tuC}. It is obtained by the following equation:

$$w_{tuC} = \left(\Delta_u - L_{slip}\cos\alpha\right)\sin\alpha \tag{2-8}$$

If neglecting L_{slip}, w_{tuC} will be simplified as

$$w_{tuC} = \Delta_u \sin\alpha \tag{2-9}$$

Then, hoop strain of Sect. F can be obtained by

$$\varepsilon_{\theta uCF} = \frac{2w_{tuC}}{d_{CF}}\cos\alpha = \frac{2\Delta_u \sin\alpha\cos\alpha}{d_{CF}} \tag{2-10}$$

Table 2-12 Ultimate deformation of specimens with conical wall failure

Specimen No.	Main parameters					Δ_u	w_{tuC}	$\varepsilon_{\theta uC}$	ε_{yC}	$\varepsilon_{\theta uC}/\varepsilon_{yC}$
	Cone		Cylinder		Ring					
	Semi-angle	Thick-ness	Thick-ness	External diameter	Thick-ness					
	α	t_C	t_P	D_P	t_R					
	deg.	mm	mm	mm	mm	mm	mm			
9	60.0	8.6	6.0	140.0		5.35	4.63	0.0346	0.0036	10.17
34	46.1	8.6	6.0	139.9	12.0	15.46	11.14	0.1154	0.0036	33.94
36	62.4	8.6	4.1	139.9	9.1	8.92	7.91	0.0540	0.0036	15.87
43	33.3	3.1	4.2	139.9	12.1	12.00	6.59	0.0812	0.0034	23.88
44	33.5	4.2	4.2	140.0	12.0	14.12	7.79	0.0957	0.0034	28.16
46	46.0	3.1	4.2	139.9	12.0	5.81	4.18	0.0428	0.0034	12.59
47	46.7	4.3	4.2	139.9	12.0	7.62	5.55	0.0561	0.0034	16.50
48	48.0	5.7	4.2	140.0	12.0	9.13	6.79	0.0669	0.0034	19.68
49	61.4	3.1	4.2	139.8	12.1	5.42	4.76	0.0336	0.0034	9.88
50	60.6	4.3	4.2	139.9	12.0	6.98	6.08	0.0440	0.0034	12.94
51	59.6	5.6	4.2	139.9	12.0	7.37	6.35	0.0474	0.0034	13.94
52	44.8	4.3	4.3	114.5	12.0	8.68	6.11	0.0787	0.0034	23.15
53	46.2	4.2	5.6	165.8	12.0	8.02	5.78	0.0500	0.0034	14.70

It is compared with yield strain ε_{yC} of conical wall, as shown in Table 2-12. Their ratios are found to be in the range of 10~34. It indicates that the contact region in conical wall entered into plastic condition as ultimate load arrived. Just like the specimens with cylinder edge failure, the out of plane deformation of conical wall not only induces hoop compression but also induces meridional bending. Thus, whether the failure is controlled by hoop compression or by meridional bending is difficult to be determined by experimental results.

2.5.4 Specimens with Boundary of "Welding"

The ultimate behavior of specimens with boundary of "Welding" is shown in Fig. 2-21. It can be found that specimen Nos. 64, 65, and 67~74 failed near to the joint region between conical wall and cylinder edge. The deformation at cylinder edge is not obvious. In addition, specimen No. 66 failed in "elephant foot buckling" mode near to the bottom edge of cylindrical wall. It is found that the failure of specimens mainly occurred in the welded joint region.

(a) Specimens with joint region failure

(b) Specimen with elephant foot buckling of cylindrical wall

Fig. 2-21 Pictures of specimens with boundary of "Welding" at ultimate load

The strength and deformation of specimens Nos. 64, 65, and 67~74 which failed in joint region are listed in Table 2-13. It can be found that for specimen Nos. 70, 71 and 72, the averages of the ratios of P_u to P_p are similar to those of specimen Nos. 7, 8 and 14 in cylinder edge failure and Nos.49, 50 and 51 in conical wall failure.

The perspective and profile of the specimen after testing are sketched in Fig. 2-22. The hoop strain $\varepsilon_{\theta j}$ of external point j of Sec. J and axial displacement Δ_k of the lowest point k of Sect. K are calculated as follows.

Table 2-13 Strength and deformations of welded specimens with joint region failure

Specimen No.	Main parameters				General yield strength	Plastic strength	Collapse strength	Δ_u	$P_{u\text{-}EXP}/P_{p\text{-}EXP}$
	Cone		Cylinder						
	Semi-angle	Thick-ness	Thick-ness	External diameter					
	α	t_C	t_P	D_P	$P_{y\text{-}EXP}$	$P_{p\text{-}EXP}$	$P_{u\text{-}EXP}$		
	deg.	mm	mm	mm	kN	kN	kN	mm	
64	30.5	3.2	4.3	139.9	365.0	390.0	409.0	1.16	1.05
65	29.5	4.5	4.3	139.9	519.0	547.7	576.7	1.47	1.05
67	46.0	3.2	4.3	140.0	276.9	294.4	305.0	1.06	1.04
68	44.0	4.5	4.3	139.9	418.4	450.0	460.0	1.60	1.02
69	43.6	6.0	4.4	140.0	546.2	581.5	641.4	2.67	1.10
70	59.0	3.2	4.3	139.9	209.7	216.1	220.7	1.53	1.02
71	57.4	4.5	4.3	139.9	291.3	316.1	322.7	1.59	1.02
72	58.6	6.0	4.3	139.9	435.9	460.8	474.7	2.22	1.03
73	44.3	4.5	4.3	114.5	361.8	394.1	409.0	1.48	1.04
74	46.1	4.5	5.6	165.2	413.0	467.5	497.2	1.96	1.06

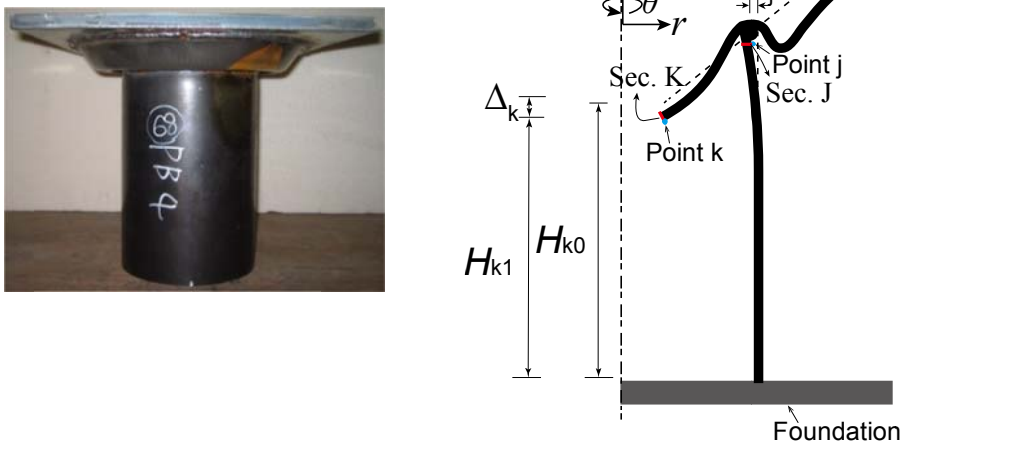

(a) Perspective deformation (b) Longitudinal section

Fig. 2-22 Deformation of specimen No. 68 after testing

The absolute value of hoop strain of section J after testing is obtained by

$$\left|\varepsilon_{\theta J}\right| = -\frac{2w_j}{d_P} = -\frac{L_{j1} - L_{j0}}{L_{j0}} = -\frac{433.2\text{-}439.5}{439.5} = 0.014 > \varepsilon_{yP} = 0.0033 \qquad (2\text{-}11)$$

where, L_{j0}—the measured circumference of cylinder at point j before testing;

L_{j1}—the measured circumference of cylinder at point j after testing.

Then, Δ_k of Sect. K is obtained by

$$\Delta_k = H_{k1} - H_{k0} = 170.7 - 171.88 = -1.18\text{mm} \quad (2\text{-}12)$$

where, H_{k0}—the measured distance from point k to the bottom edge of cylindrical wall before testing.

H_{k1}—the measured distance from point k to the bottom edge of cylindrical wall after testing.

Based on Eqs. (2-11) and (2-12), it can be found that the top edge of cylindrical wall moved along *–r* direction during testing, and entered into plastic condition after testing. In addition, the deformation along *-x* direction occurred in the lowest part of conical wall after testing.

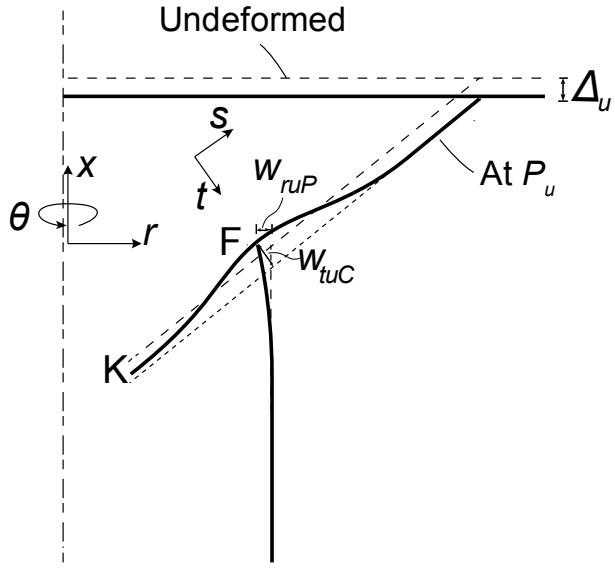

Fig. 2-23 Sketch of ultimate deformation of specimens with boundary of "Welding"

The ultimate behavior of specimens failed in joint region is sketched in Fig. 2-23. The radial deformation of cylinder edge at ultimate load is defined to be w_{ruP}. It is difficult to be measured from experiments. The joint region of cone-to-cylinder is simplified to be Sect. F. Its normal deformation w_{tuC} can be calculated by

$$w_{tuC} = \Delta_u \sin\alpha + w_{ruP} \cos\alpha \tag{2-13}$$

If neglecting w_{ruP}, w_{tuC} will be simplified as

$$w_{tuC} = \Delta_u \sin\alpha \tag{2-14}$$

Then, hoop strain in Sect. F is obtained as

$$\varepsilon_{\theta uC} = \frac{2w_{tuC}}{d_C}\cos\alpha = \frac{2\Delta_u \sin\alpha\cos\alpha}{D_P - t_P} \tag{2-15}$$

It is compared with yield strain ε_{yC} of conical wall, as shown in Table 2-14. It can be found that their ratios are in the range of 2~6. They are much smaller than those in the specimens with conical wall failure listed in Table 2-12, but it have to be said that the joint region of welded connection also entered into plastic as ultimate load arrived.

Table 2-14 Ultimate deformation of welded specimens with joint region failure

Specimen No.	Main parameters				Δ_u	w_{tuC}	$\varepsilon_{\theta uC}$	ε_{yC}	$\varepsilon_{\theta uC}/\varepsilon_{yC}$
	Cone		Cylinder						
	Semi-angle	Thick-ness	Thick-ness	External diameter					
	α	t_C	t_P	D_P					
	deg.	mm	mm	mm	mm	mm			
64	30.5	3.2	4.3	139.9	1.16	0.59	0.0073	0.0034	2.14
65	29.5	4.5	4.3	139.9	1.47	0.73	0.0090	0.0034	2.65
67	46.0	3.2	4.3	140.0	1.06	0.77	0.0076	0.0034	2.23
68	44.0	4.5	4.3	139.9	1.60	1.11	0.0114	0.0034	3.36
69	43.6	6.0	4.4	140.0	2.67	1.84	0.0190	0.0034	5.60
70	59.0	3.2	4.3	139.9	1.53	1.31	0.0096	0.0034	2.83
71	57.4	4.5	4.3	139.9	1.59	1.34	0.0104	0.0034	3.04
72	58.6	6.0	4.3	139.9	2.22	1.90	0.0141	0.0034	4.15
73	44.3	4.5	4.3	114.5	1.48	1.04	0.0130	0.0034	3.81
74	46.1	4.5	5.6	165.2	1.96	1.41	0.0119	0.0034	3.49

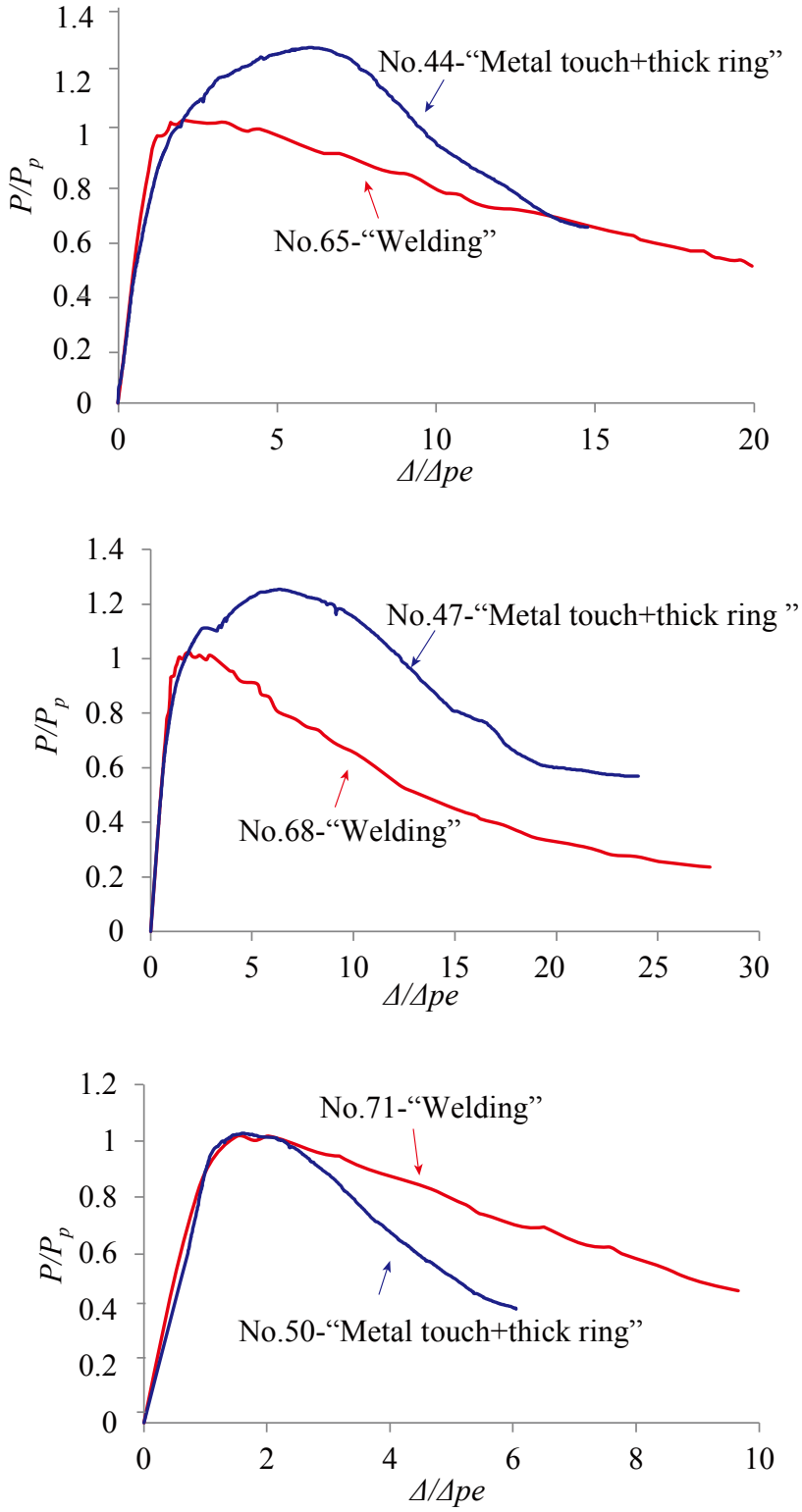

Fig. 2-24 Comparison of Normalized load versus axial deformation relationships between specimens with boundary of "Welding" and those with boundary of "Metal touch + thick ring"

The normalized load versus axial deformation relationships between specimens with the boundary of “Welding” and thosed with the boundary of “Metal touch +thick ring” are compared, as shown in Fig. 2-24. Representative specimen Nos. 65, 68 and 71 and Nos. 44, 47 and 50 are employed. It can be found that strength degradation of specimens with the boundary of “Welding” is not rapider than that of specimens with the boundary of “Metal touch + thick ring”. The failue modes of the two kinds of connections are difficult to be distinguished based on the experimental results.

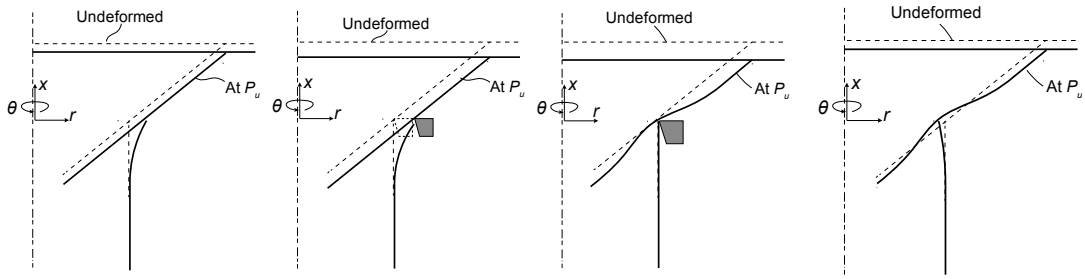

(a) Cylinder edge failure (b) Tapered ring failure (c) Conical wall failure (d) Joint region failure

Fig. 2-25 Proposed failure modes based on failure positions

2.6 Summaries

This chapter focuses on the reinvestigation of the failure modes of experimental specimens. Based on the above analysis, the following conclusions can be obtained.

(1) For specimens with boundary of “Metal touch”, “Metal touch + thin ring” and “Metal touch + thick ring”, failure of connections mainly occurred at cylinder edge, tapered ring and conical wall, respectively. However, the plastic region cannot be measured because of the limitation of the experiments. Thus, the failure mechanisms are difficult to be clarified in detail.

(2) For specimens with boundary of “Welding”, because the top edge of cylindrical wall moved along inward direction and the bottom edge of conical wall moved along downward direction, joint region between conical wall and cylinder edge may have some deformation during loading process. The ratio of collapse strength to full plastic strength is quite small, but similar to some metal touch specimens. Moreover, their

strength degradation is not rapider than that of metal touch specimens. Though the post-failure was mainly observed in the upper part of conical wall, the failure mode could not be determined to be “cone buckling failure” directly.

The failure modes of connections are summaried in Fig. 2-25, based on the failure positions. In the following chapters, Finite Element Analysis will be employed to investigate the stress and deformation distributions. After then, failure mechanisms will be determined

CHAPTER 3 STRENGTH OF METAL TOUCH CONNECTIONS WITH CYLINDER EDGE FAILURE

3.1 Introduction

The strength of cylinder edge failure was first studied by Kuwamura et al. (2005) by means of experiments and theoretical analysis. A simple hoop tension failure mechanism was assumed based on the assumption of uniaxial stress state. The formulae for full plastic strength and ultimate strength were proposed. But the influences of axial bending moment and axial stress resultant on the failure mechanism were not considered. His work was extended by Ito et al. (2008), in which Finite Element Analysis (FEA) was employed to investigate the friction property between cone and cylinder, and stress behaviors in cylindrical walls. The plastic collapse mechanism proposed by Eason and Shield (1955) was employed to consider the effect of axial bending moment on failure mechanism. More precise formulae for strength were proposed. Especially for the cases of high axial stress resultant, previous studies (Tsang and Harding 1984, Zhao and Hancock 1993, Cao et al. 1998, et al) indicated that the interaction of hoop stress resultant or axial bending moment with axial stress resultant has an influence on the failure mechanism. It needs to be analyzed for the connections in this study.

In the first part of this chapter, solid axisymmetric FEA models are first created and validated by comparing their strength and deformation with experimental results. The friction property in the contact region between cone and cylinder is discussed. Then, FEA is undertaken not only for the existing experimental specimens, but also for six newly added models which have relatively larger axial stress resultants. The changing distributions of stress resultants under increasing load are investigated, and the

correlations among stress resultants are analyzed. The ultimate deformation of models is also investigated. Based on the analysis results, the failure mode is determined by the proposed criterion.

In the second part of this chapter, Mises' yield condition in the form of stress resultants for axisymmetrically loaded revolutional shells with perfectly-plastic material is simplified and validated by the effective FEA results. Then, a new plastic collapse mechanism for cylinder edge failure is proposed, in which the correlations of axial stress resultant with axial bending moment and hoop stress resultant are considered. The limit analysis is undertaken and the maximum strength of models with perfectly-plastic material is derived, which corresponds to the full plastic strength of models with actual strain hardening material. The prediction of ultimate strength and general yield strength of models with actual material are then proposed respectively, based on the formula for full plastic strength. The precision of the proposed formulae are examined through comparing them with previous ones and the experimental and FEA results.

3.2 FE Modeling

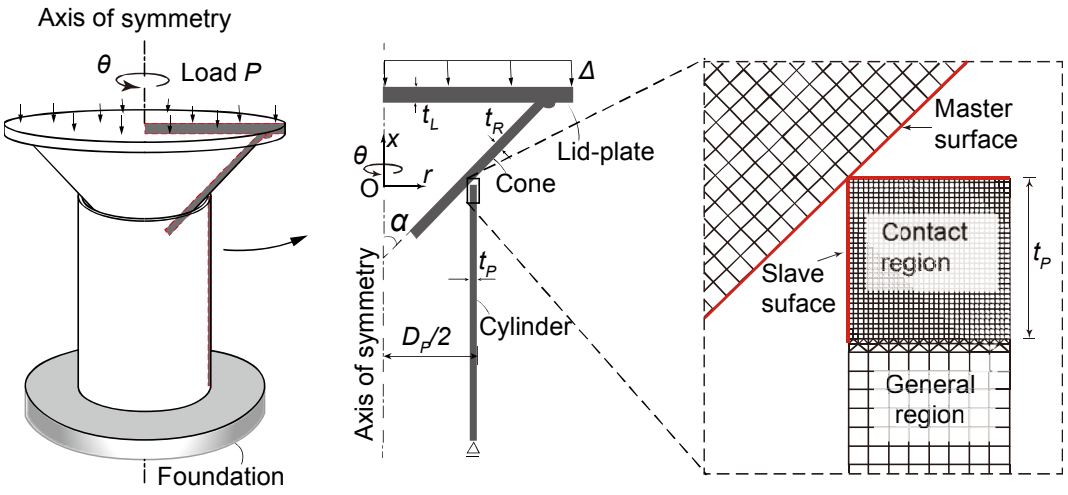

Fig. 3-1 Details of FEA axisymmetric solid model

3.2.1 General

The details of axisymmetric solid model in ABAQUS FE package (Hibbitt et al. 2011) are shown in Fig.3-1. The cylindrical coordinate (r, θ, x) system is chosen. Cylindrical wall is simply supported at the base. Static loading is controlled by displacement Δ. Because both the geometry of specimens and loading are axisymmetric, linear quadrilateral and triangular axisymmetric solid element CAX4R and CAX3 are employed. The contact between cone and cylinder is defined using the CONTACT PAIRS option (surface-to-surface contact). The external surface of conical wall is set to be "Master surface", and the right-angled edges of contact region in cylindrical wall are set to be "Slave surface". The height of contact region is assumed as the thickness t_P of cylindrical wall. Finite sliding and node-to-surface discretization method are adopted. Mesh size in contact region is set to be 1/4 of that in general region to consider the local stress concentration phenomenon. When mesh size in general region is smaller than $t_P/6$, ultimate strength is found to be convergent. As the smallest thickness of cylindrical walls for all the specimens is 3.3 mm, mesh size in general region is set to be a constant of 0.5mm.

The stress-strain curves for the mild steel used in cylindrical walls are shown in Fig. 3-2. Equivalent plastic strain e_p, obtained by Eqs. (3-1)~(3-3), is used for defining the strain hardening behavior of mild steel materials in ABAQUS FE package. The s~e_p curves of cylindrical walls with different diameter-to-thickness ratios are shown in Fig. 3-3. Moreover, the perfectly-elastic plastic materials whose yield stress is equal to that of the actual ones are also employed for the later analysis.

$$s = \sigma(1+\varepsilon) \tag{3-1}$$

$$e = \ln(1+\varepsilon) \tag{3-2}$$

$$e_p = e - s/E_0 \tag{3-3}$$

Herein, s is true stress, e is true strain, σ is engineering stress, ε is engineering strain, e_p is equivalent plastic strain, and E_0 is initial Young's modulus, set to be a constant of

205,000MPa for all the models.

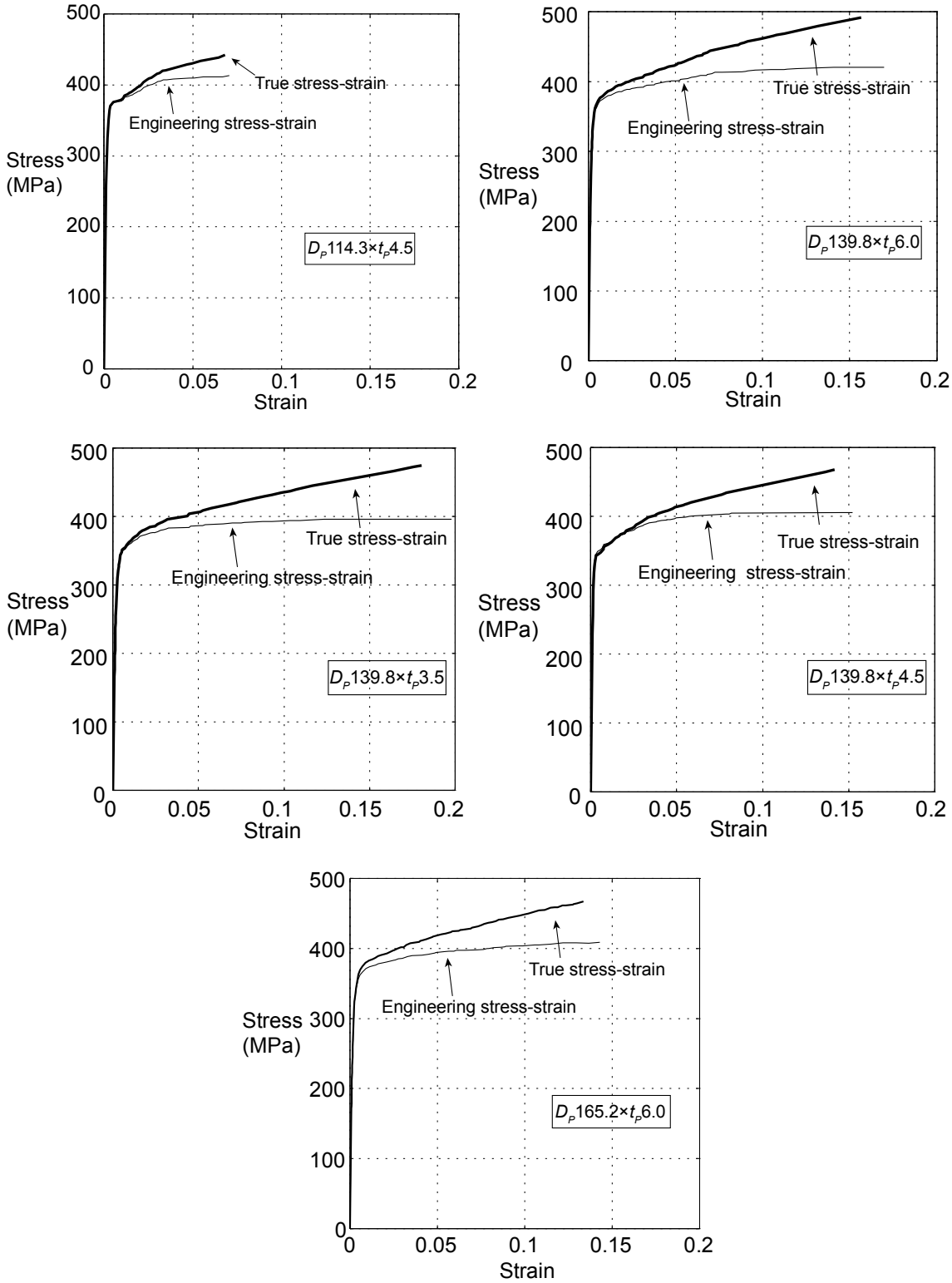

Fig. 3-2 True stress-strain curves for material STK400 used in cylindrical shells

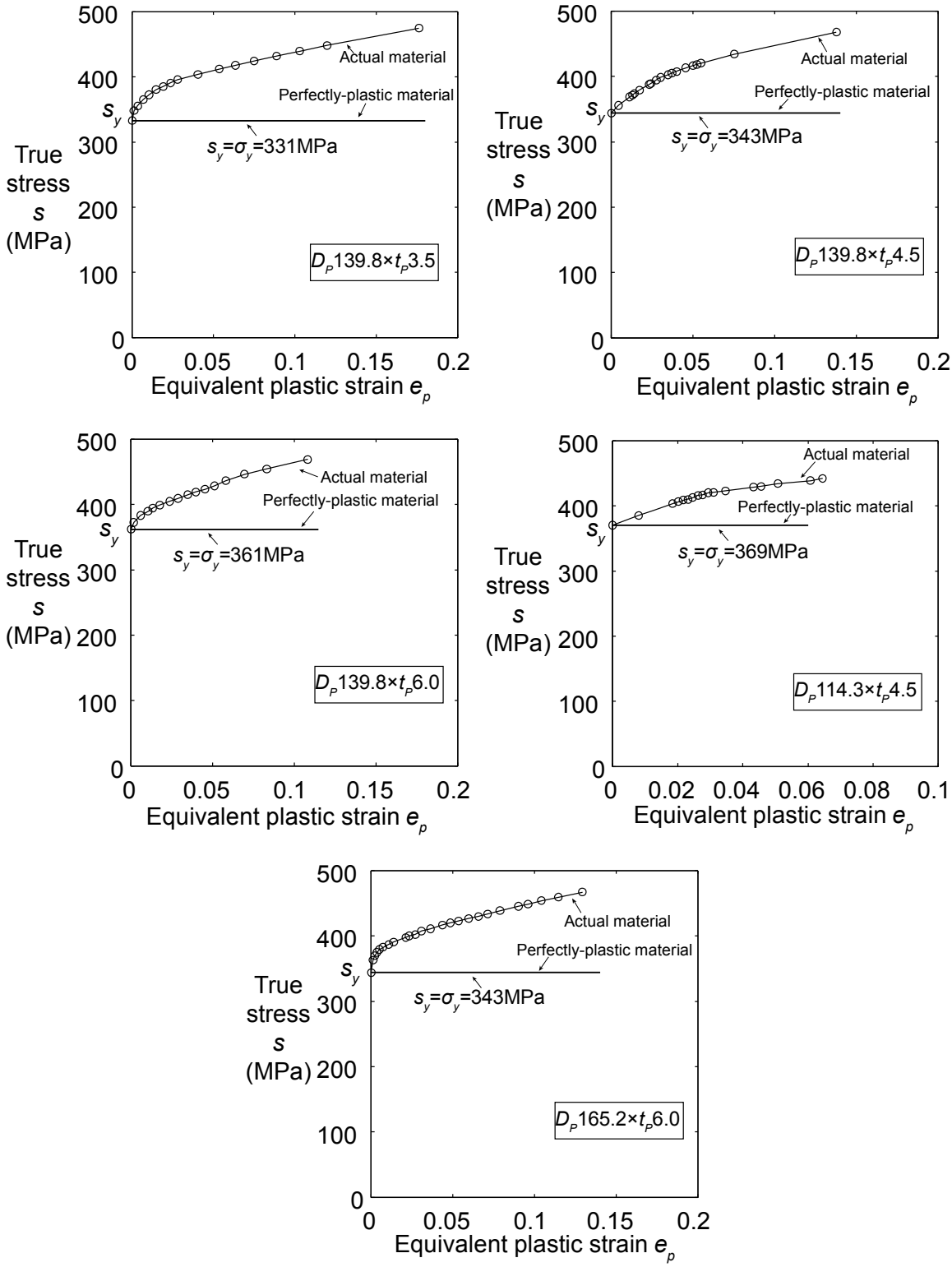

Fig. 3-3 s~e_p curves of cylindrical shells input in ABAQUS

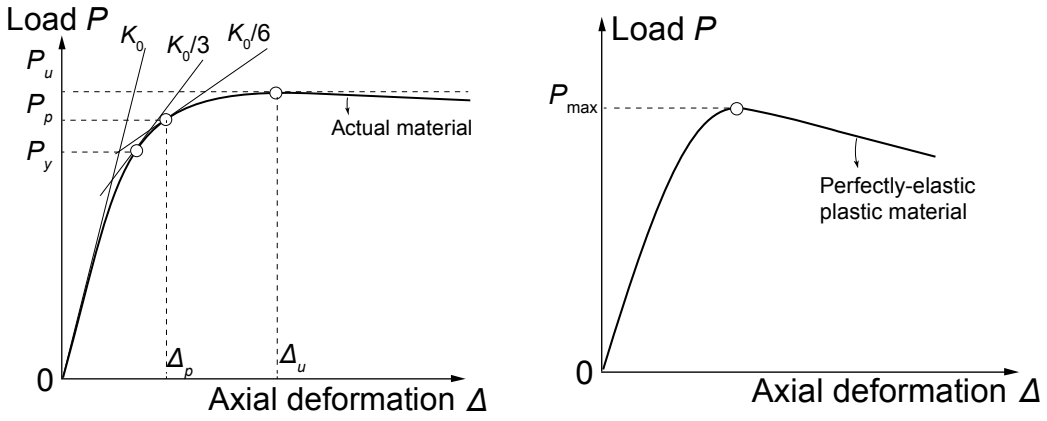

(a) (b)

Fig. 3-4 Definition of strength of FE models

3.2.2 Definitions of Strength of FE Models

As shown in Fig. 3-4(a), for FE models with actual strain hardening materials, the definitions of strength are the same as those introduced in Chapter 2. In addition, for FE models with perfectly-elastic plastic materials, their collapse strength is defined to be "maximum strength P_{max}", as shown in Fig. 3-4(b). The P_{max} is employed to examine the precision of the theoretical prediction of strength based on limit analysis and the full plastic strength P_p of models with actual material.

3.2.3 Effectiveness of FE models

Thomsen et al. (1965) suggested that it is necessary to assume that μ remains constant during the forming operation and its use is necessary to make the theoretical equations amenable to relatively simple analytical solutions. Hence, Amontons-Coulomb's friction law with formulation of Penalty is adopted and friction coefficient μ is assumed to be a constant during the whole deformation process in this study. The variation of collapse strength in FEA along with the increase of μ is shown in Fig. 3-5. It can be seen that the correlation with each other is great. The collapse strength of FE model becomes about equal to that of experimental specimen by calibrating the value of μ. As a result, the values of μ for all the modes are obtained, as shown in Table

3-1. It is found that their average is 0.18 with a Coefficient of Variation (COV) of 0.29. The values of full plastic strength and general yield strength of FE models are then compared with those of experimental specimens by the same value of μ. It is found that the averages of ratios are 1.02 for full plastic strength and 1.04 for general yield strength, with small COV of 0.05 and 0.09, respectively. The strength of cylinder edge failure can be predicted well with a constant value of μ for each model.

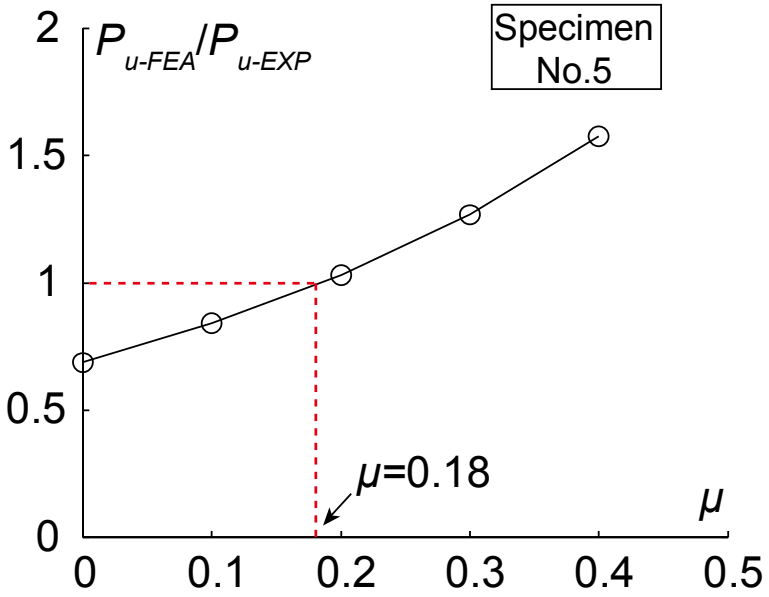

Fig. 3-5 Variation of collapse strength of models with cylinder edge failure along with the increase of friction coefficient between conical wall and cylinder edge

Table 3-1 Comparison of strength between FE models and experimental specimens for models with cylinder edge failure

Model NO.	Experiments			FEA				Comparison		
	Collapse strength	Full plastic strength	General yield strength	COF	Collapse strength	Full plastic strength	General yield strength	$P_{u\text{-}FEA}/P_{u\text{-}EXP}$	$P_{p\text{-}FEA}/P_{p\text{-}EXP}$	$P_{y\text{-}FEA}/P_{y\text{-}EXP}$
	$P_{u\text{-}EXP}$ (kN)	$P_{p\text{-}EXP}$ (kN)	$P_{y\text{-}EXP}$ (kN)	μ	$P_{u\text{-}FEA}$ (kN)	$P_{p\text{-}FEA}$ (kN)	$P_{y\text{-}FEA}$ (kN)			
1	58.8	48.8	43.6	0.09	58.2	52.0	43.5	0.99	1.07	1.00
2	120.8	116.4	94.2	0.27	119.1	108.4	98.8	0.99	0.93	1.05
3	174.9	164.0	149.5	0.15	176.3	162.9	140.3	1.01	0.99	0.94
4	112.1	102.4	80.8	0.16	112.9	102.5	91.1	1.01	1.00	1.13
5	169.7	148.2	129.2	0.18	167.8	157.0	144.4	0.99	1.06	1.12
6	336.6	275.0	222.7	0.22	333.4	317.7	285.8	0.99	1.16	1.28
7	220.1	207.5	194.1	0.23	222.7	214.8	190.9	1.01	1.04	0.98
8	285.0	280.8	264.0	0.19	284.9	277.3	258.4	1.00	0.99	0.98
10	99.4	90.8	80.0	0.17	98.2	88.4	80.7	0.99	0.97	1.01
11	160.2	137.5	125.6	0.13	161.0	146.2	123.3	1.01	1.06	0.98
12	176.8	160.0	140.0	0.20	173.0	167.2	152.2	0.98	1.05	1.09
13	302.8	281.8	268.2	0.21	304.2	286.8	253.6	1.00	1.02	0.95
14	246.9	242.0	234.0	0.14	247.2	240.9	223.8	1.00	1.00	0.96
Avg.				0.18				1.00	1.02	1.04
COV				0.29				0.01	0.05	0.09

Note: μ is friction coefficient in the contact region between cone and cylinder.

Then, the maximum strength $P_{\max}$ of models with perfectly-plastic material is compared with the full plastic strength P_p of models with actual material, as shown in Fig. 3-6. The average of the ratios is 1.00, with a small standard deviation of 0.03. If $P_{\max}$ is assumed as the ideal full plastic strength P_p of models with actual material, it can be found that the method of "K_0/6 slope factor" proposed by Tateyama (1988) is effective to determine the full plastic strength from experimental load versus axial deformation curves.

In addition, the load versus axial deformation curves and ultimate deformation of FE models are compared with the relevant experimental results, as shown in Appendix B.

The effectiveness of all the models is verified.

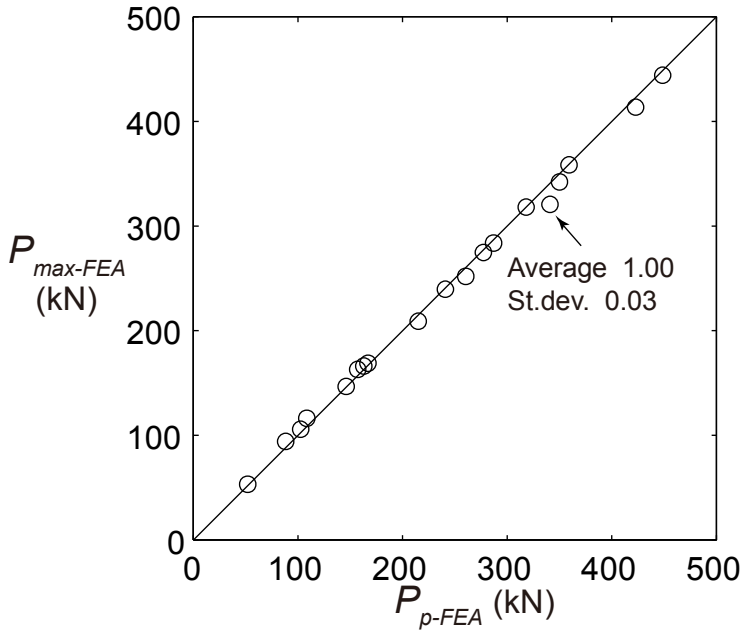

Fig. 3-6 Comparison of maximum strength to full plastic strength for models with cylinder edge failure

3.2.4 Discussion on Friction Coefficient for Practical Design

Friction has an obviously influence on the strength of cylinder edge failure (Ito et al. 2008). Whitehead (1950) suggested that the increase of friction coefficient μ is due to the breakdown of oxide film. Its value is difficult to be derived theoretically in this study. The μ needs to be determined in advance for practical design. The average of μ calibrated in section 3.2.3 is 0.18. But it cannot represent the actual value, because the influence of other factors, for example residual stress, was not considered. Kuwamura and Ito (2007) suggested that friction coefficient μ might be 0.21~0.36 due to the plastic flow of steel materials based on the experimental study.

Thus, it is suggested that μ = 0.20 for models with cylinder edge failure in practical design. The predicted strength by FEA is compared with the experimental result. The results are listed in Table 3-2. It is found that the averages of ratios are 1.05, 1.06 and 1.10, for collapse strength, full plastic strength and general yield strength respectively. The values of COV are not small, but can be acceptable.

Table 3-2 Comparison of strength between FEA and experiment with the assumption of μ= 0.20 for models with cylinder edge failure

Model NO.	Experiments			FEA				Comparison		
	Collapse strength	Full plastic strength	General yield strength	COF	Collapse strength	Full plastic strength	General yield strength	$P_{u\text{-}FEA}/P_{u\text{-}EXP}$	$P_{p\text{-}FEA}/P_{p\text{-}EXP}$	$P_{y\text{-}FEA}/P_{y\text{-}EXP}$
	$P_{u\text{-}EXP}$	$P_{p\text{-}EXP}$	$P_{y\text{-}EXP}$	μ	$P_{u\text{-}FEA}$	$P_{p\text{-}FEA}$	$P_{y\text{-}FEA}$			
	(kN)	(kN)	(kN)		(kN)	(kN)	(kN)			
1	58.8	48.8	43.6	0.20	72.9	61.5	57.1	1.24	1.26	1.31
2	120.8	116.4	94.2		104.9	91.6	86.5	0.87	0.79	0.92
3	174.9	164.0	149.5		195.1	182.2	160.0	1.12	1.11	1.07
4	112.1	102.4	80.8		122.4	112.0	103.1	1.09	1.09	1.28
5	169.7	148.2	129.2		175.3	162.4	155.8	1.03	1.10	1.21
6	336.6	275.0	222.7		320.5	303.2	276.3	0.95	1.10	1.24
7	220.1	207.5	194.1		204.8	197.1	187.0	0.93	0.95	0.90
8	285.0	280.8	264.0		292.7	270.0	255.2	1.03	0.96	0.97
10	99.4	90.8	80.0		104.6	94.1	89.9	1.05	1.04	1.12
11	160.2	137.5	125.6		186.1	167.3	140.0	1.16	1.22	1.11
12	176.8	160.0	140.0		173.0	165.5	158.5	0.98	1.03	1.13
13	302.8	281.8	268.2		298.0	280.5	259.0	0.98	1.00	0.97
14	246.9	242.0	234.0		285.2	275.4	265.5	1.16	1.14	1.13
Avg.								1.05	1.06	1.10
COV								0.10	0.12	0.12

3.3 FE Analysis Results

3.3.1 Definitions of Stress Resultants

The internal forces acting on an infinitesimal body cut out from the cylindrical wall are defined in Fig. 3-7. Hoop stress resultant N_θ, axial stress resultant N_x, axial bending moment M_x, and shear stress resultant Q_x are defined as

$$N_\theta = \int_{-t/2}^{t/2} s_\theta dz;\ N_x = \int_{-t/2}^{t/2} s_x dz;\ M_x = \int_{-t/2}^{t/2} s_x z dz;\ \text{and}\ Q_{rx} = \int_{-t/2}^{t/2} \tau_{rx} dz \qquad (3\text{-}4)$$

Herein, s is true normal stress, τ is shear stress, t is the thickness of cylindrical wall, and z is the radially outward distance from its middle surface. It should be noted that the subscript "$_P$" for cylindrical shell is omitted in the equations (The same hereinafter in this chapter).

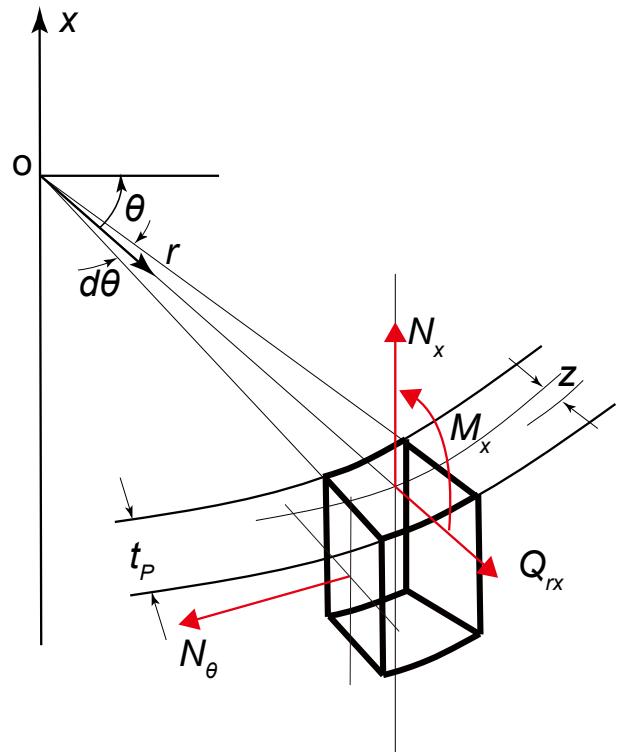

Fig. 3-7 Definition of stress resultants in cylindrical wall

The following dimensionless variables are introduced for the stress resultants.

$$n_x = \frac{N_x}{\sigma_y t};\ n_\theta = \frac{N_\theta}{\sigma_y t};\ m_x = \frac{M_x}{M_{xp0}};\ \text{and}\ q_{rx} = \frac{\sqrt{3}Q_{rx}}{\sigma_y t} \tag{3-5}$$

Where, $M_{xp0} = \sigma_y t^2 / 4$. The σ_y is the yield stress of cylindrical wall and set to be positive both for tension and compression.

3.3.2 Distributions of Stress Resultants

Model No.8 is taken as a typical case to investigate the changing distributions of axial stress resultant n_x, axial bending moment m_x, shear stress resultant q_{rx}, and hoop stress resultant n_θ under general yield load P_y, full plastic load P_p and ultimate load P_u,

respectively. As shown in Fig. 3-8(a), $|n_x|$ increases as load increases. It can be assumed as a constant along x direction at each load. As shown in Fig. 3-8(b), $|m_x|$ also increases as load increases. Section A is defined to be the section where local concentrated deformation in the contact region starts to disappear. The assumption that line elements normal to the middle surface remain normal during the deformation is obeyed below Sect. A. Section B is defined to be the section with peak value of axial bending moment. The $|m_{xu}|$ in Sect. B does not reach 1.0 at P_u. It must be due to the effect of interaction between n_{xu} and m_{xu}. As shown in Fig. 3-8(c), the value of q_{rx} at each load decreases almost in a straight line from Sects. A to B, and becomes close to 0 at Sect. B. The changing distributions of n_θ, as shown in Fig. 3-8(d), are a little difficult to assimilate. Its maximum value does not occur in Sect. A. Moreover, its value in Sect. B at P_u is slightly smaller than that at P_p. The reason might be the effect of interaction of $n_{\theta u}$ with n_{xu} and m_{xu}.

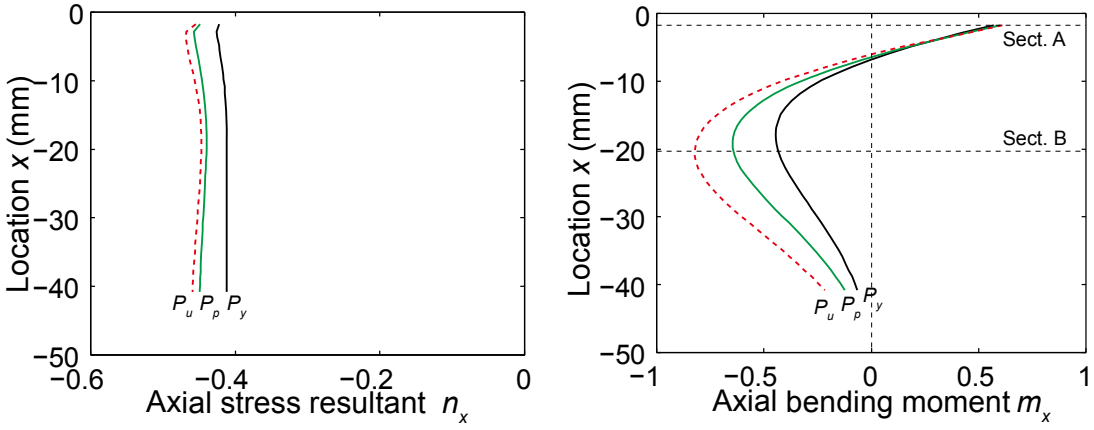

(a) (b)

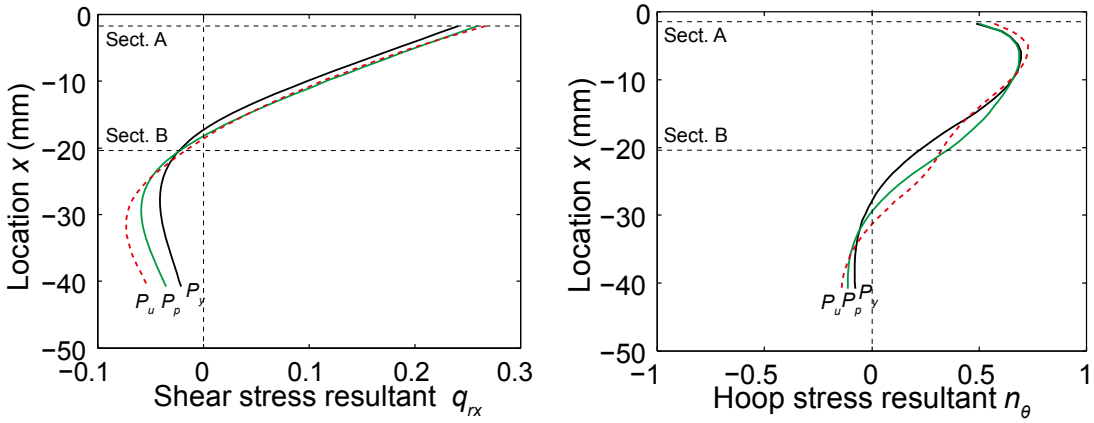

(c) (d)

Fig. 3-8 Changing distribution of stress resultants in the cylindrical wall of model No.8 under increasing load

3.3.3 Correlation of Stress Resultants at Ultimate Load

By setting the friction coefficient μ of model Nos. 7, 8 and 14 to be 0.3 and 0.4 respectively, additional six models, which named Nos.7-μ03, 7-μ04, 8-μ03, 8-μ04, 14-μ03 and 14-μ04, are designed to investigate the influence of high axial stress resultant on the failure mechanism.

The model Nos. 2, 5, 8, 8-μ03 and 8-μ04, with axial stress resultant n_{xu} of -0.20, -0.27, -0.46, -0.61, and -0.78 respectively, are taken as typical cases to analyze the correlation among stress resultants at ultimate load. For the correlation between n_{xu} and $n_{\theta u}$, $n_{\theta u}$ decreases as $|n_{xu}|$ increases for each section, as shown in Fig.3-9(a). The correlation between n_{xu} and m_{xu} is a little different. As shown in Fig. 3-9(b), for the region where m_{xu} is positive, m_{xu} increases as $|n_{xu}|$ increases; while for the region where m_{xu} is negative, $|m_{xu}|$ decreases as $|n_{xu}|$ increases. The detailed results in Sects. A and B for all the models are plotted in Fig. 3-9. It can be found that the stress resultants have high correlation with each other.

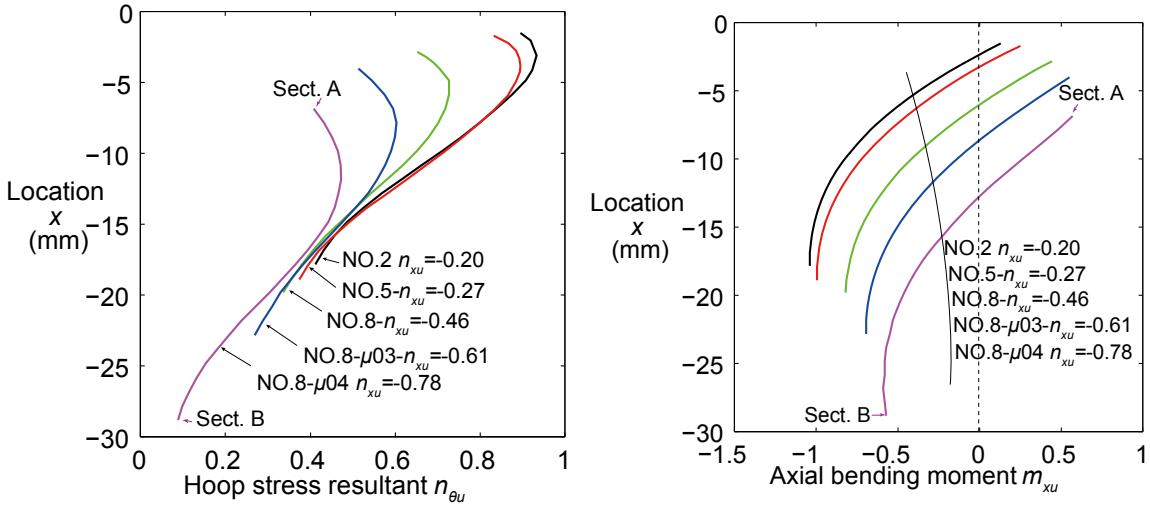

(a) $n_{\theta u}$ (b) m_{xu}

Fig. 3-9 Distribution of ultimate stress resultants in the plastic region of models with actual material

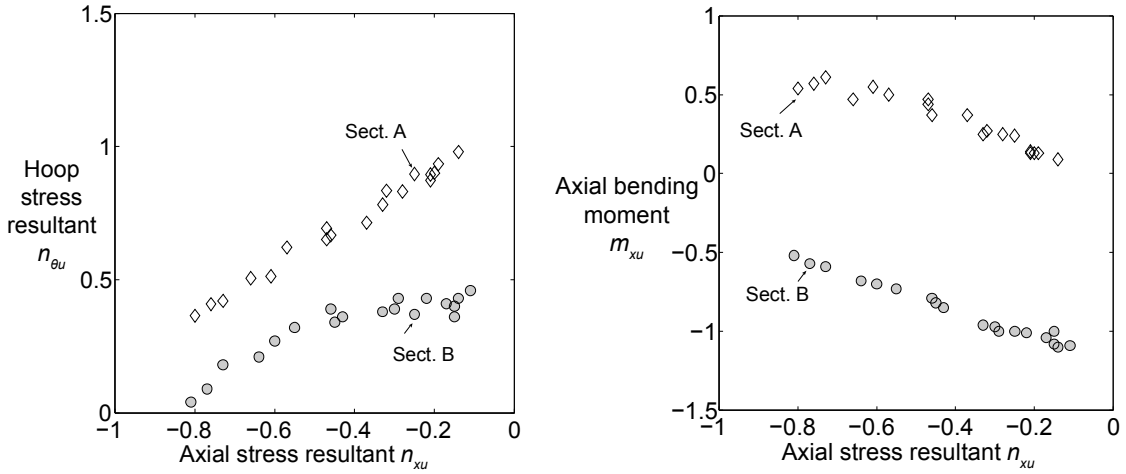

(a) $n_{\theta u}$ *vs.* n_{xu} (b) m_{xu} *vs.* n_{xu}

Fig. 3-10 Correlation among stress resultants at ultimate load in Sects. A and B of all the models with cylinder edge failure

3.3.4 Distributions of Ultimate Deformation

The ultimate behavior of the top edge of cylinder for model No.8 is illustrated in Fig. 3-11. It can be found that the out of plane deformation at ultimate load in the region from Sect. A to Sect. B is quite small.

The ultimate radial deformations in the region AB for model Nos. 2, 5, 8, 8-μ03 and 8-μ04 are shown in Fig. 3-12. It is found that the variation of deformation curves along with the increasing of axial stress resultant is a little complicated. Especially for model

No. 8-μ04, the radial deformation becomes much larger than other models due to the great value of axial stress resultant.

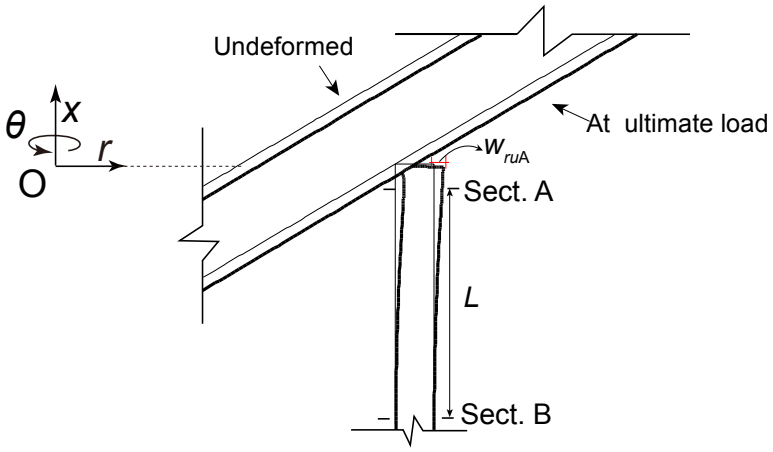

Fig. 3-11 Ultimate deformation of the top edge of cylinder for model No.8

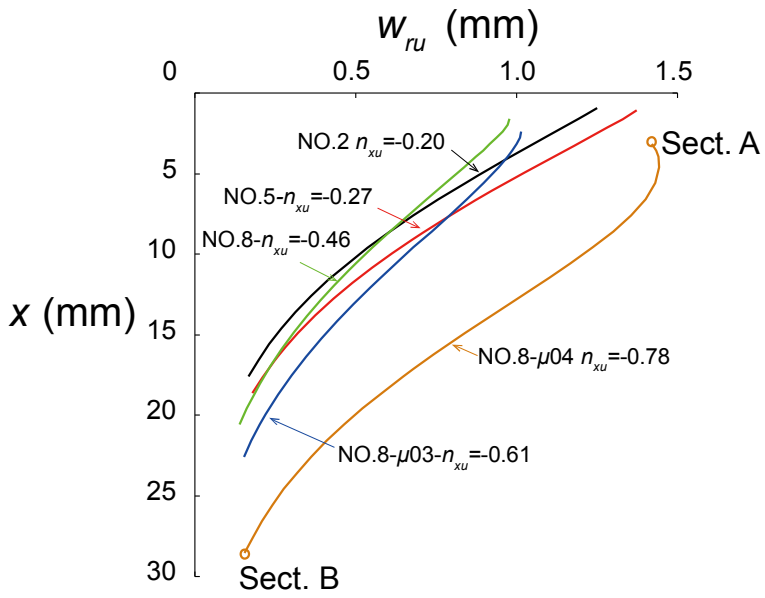

Fig. 3-12 Distribution of ultimate radial deformation in the plastic region of models with actual material

The ϕ_u is defined as the ratio of radial displacement w_{ruA} in sect. A to the length L of region AB. Figure 3-13 plots the ratios ϕ_u for all the FE models. It is seen that for the cases of lower axial stress resultant, ϕ_u decreases in a straight line as $|n_{xu}|$ increases. But for the cases of larger axial stress resultant, such as model Nos. 7-μ04, 8-μ04, 14-μ03

and 14-μ04, ϕ_u increases even though $|n_{xu}|$ increases. Because all the values of ϕ_u are smaller than 0.1, the small deformation theory can be employed in the later analysis.

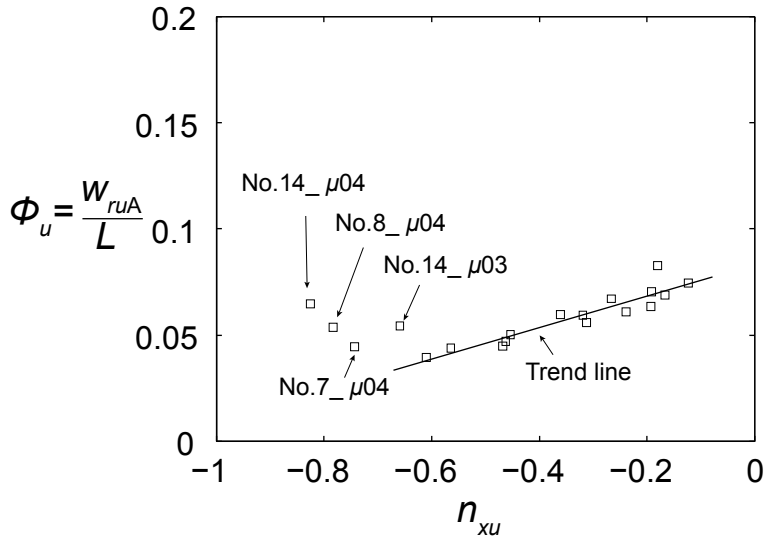

Fig. 3-13 Ratios of w_{ruA} in Sect. A to the length of L along with the increase of $|n_{xu}|$

3.4 Judgement of Failure Mode

3.4.1 Definition of the Criterion of Failure Mode

The ratio of average equivalent stress $\bar{s}_{eq}$ in a section to yield stress σ_y is defined as

$$r = \frac{\bar{s}_{eq}}{\sigma_y} = \frac{\int_{-t/2}^{t/2} s_{eq} dz}{\sigma_y t} \tag{3-6}$$

Herein, equivalent stress s_{eq} can be obtained by

$$s_{eq} = \sqrt{s_x^2 - s_x s_\theta + s_\theta^2 + 3\tau_{rx}} \tag{3-7}$$

If r in the section where axial bending moment m_x reaches the local peak, satisfies that $r_{(m_x = m_{x,peak})} \approx 1.0$, a plastic hinge is assumed to form there. If the number of plastic hinges becomes sufficient and the kinematically admissible state is reached just prior to or at collapse load, the failure is assumed to be governed by “plastic collapse”. It should be

noted that

(1) Because of the strain hardening effect of materials, $r_{(m_s=m_{s,peak})}$ in some section where plastic deformation is great, is possible to exceed 1.0;

(2) Some section with peak meridional bending moment does not enter into plastic range at ultimate load. From the engineering point of view, $r_{u(m_{su}=m_{su,peak})} \geq 0.8$ is acceptable for the determination of plastic hinge.

3.4.2 Failure Mode of Models

Figure 3-14 shows the changing distributions of ratio r at P_y, P_p, and P_u in the cylindrical wall of model No.8. It is found that r increases as the load increases for each section. Finally, r_u in Sect. B becomes very close to 1.0. It indicates that a plastic hinge form there. The region between Sect. B and Sect. A enters into plastic condition at ultimate load. Because of the strain hardening effect of material, the nearer a section gets to Sect. A, the larger is r_u.

The r_u in Sect. B for all the models are listed in Fig. 3-15. It is seen that all the values are close to 1.0. Their average is 1.01, with a small COV of 0.02. Therefore, the failure mode of cylinder edge can be assumed to be controlled by "plastic collapse", as shown in Fig. 3-16.

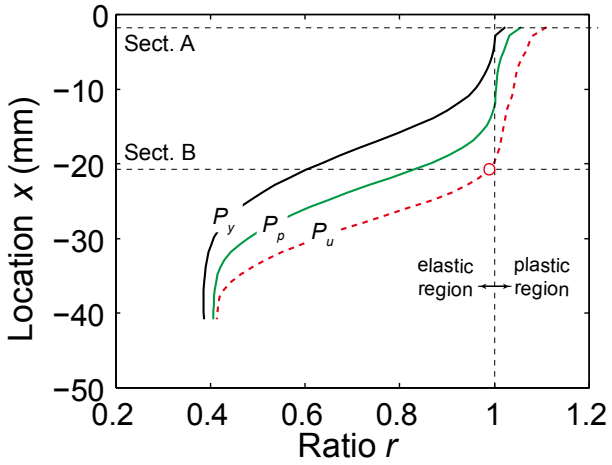

Fig. 3-14 Changing distributions of average equivalent stress in the cylindrical wall of model No.8 under increasing load

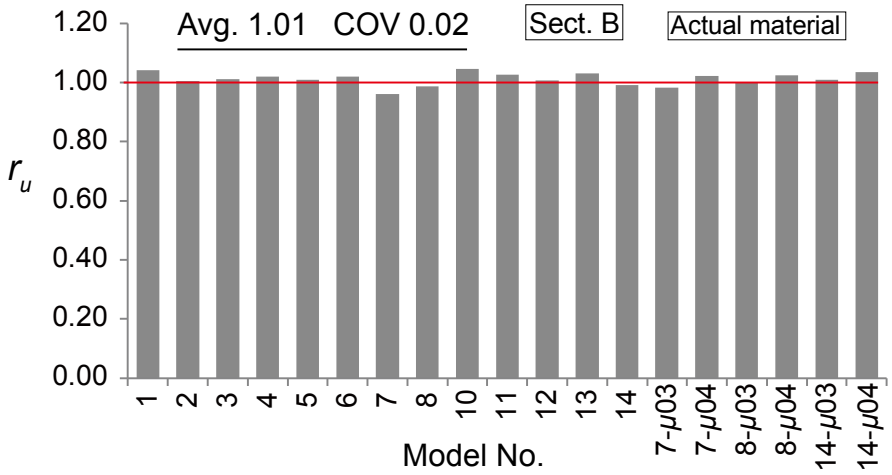

Fig. 3-15 Ratios of average equivalent stress to yield stress at ultimate load in Sect. B of all the models with cylinder edge failure

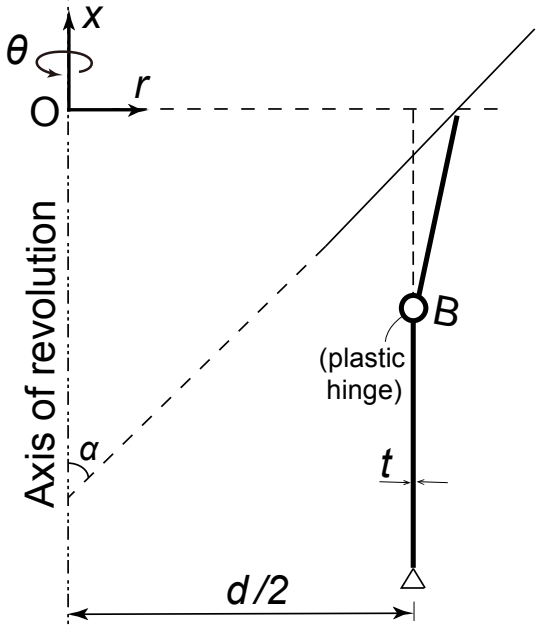

Fig. 3-16 Proposed failure mechanism for models with cylinder edge failure

3.5 Prediction of Strength

3.5.1 Simplification of Mises' Yield Condition for Axisymmetrically Loaded Revolutional Shells with Perfectly-plastic Material

The high correlation among axial stress resultant, hoop stress resultant and axial bending moment in cylindrical walls has been clarified in section 3.3.3. The interaction

equation for stress resultants at ultimate load constitutes the yield condition of cylindrical shells under axisymmetric loading, which has been first published by Drucker (1953). His work was developed by Onat (1955) and Hodge (1961). The latter one is for Perfectly-plastic material obeying Mises' yield criterion and the associated flow rule. The yield surface equations are expressed by stress resultants, in closed parametric form as shown in Eq. (3-8).

$$
\begin{aligned}
n_{x\max} &= \pm\frac{2}{\sqrt{3}}\frac{\cos p-\cos q}{\sin(p-q)} \\
n_{\theta\max} &= \pm\left[-\frac{1}{2}\frac{\cos p\cos q}{\sin(p-q)}\ln\frac{(1+\sin q)}{(1-\sin q)}\frac{(1-\sin p)}{(1+\sin p)}+\frac{\cos p-\cos q}{\sqrt{3}\sin(p-q)}\right] \\
m_{x\max} &= \pm\left[\frac{2}{\sqrt{3}}\frac{\cos^2 p\cos^2 q}{\sin^2(p-q)}\ln\frac{(1+\sin q)}{(1-\sin q)}\frac{(1-\sin p)}{(1+\sin p)}-4\frac{\cos p\cos q(\sin q-\sin p)}{\sqrt{3}\sin^2(p-q)}\right]
\end{aligned}
\tag{3-8}
$$

Herein, the p and q are two parameters, which satisfy either of the following inequalities.

$$
-\frac{\pi}{2}\le p<q\le\frac{\pi}{2}\ ;\qquad \frac{\pi}{2}\le q<p\le\frac{3\pi}{2}
$$

Three special curves on the yield surface were discovered by Hodge (1961). One is given by

$$
m_{x\max}=0;\ n_{\theta\max}=\frac{1}{2}n_{x\max}\pm\sqrt{1-\frac{3}{4}n_{x\max}^2} \tag{3-9}
$$

The other two are given by

$$
n_{\theta\max}=0.5n_{x\max};\ m_{x\max}=\pm\frac{2}{\sqrt{3}}(1-\frac{3}{4}n_{x\max}^2) \tag{3-10}
$$

(1) Simplification of Mises' Yield Condition Equation

The characteristic curves for $n_{x\max}$ = 1.0, 0.8, 0.6 , …, -0.6, -0.8, -1.0 on Mises' yield surface, and the three special curves in Eqs. (3-9) and (3-10) are plotted in Fig. 3-17. It can be seen that the yield surface is antisymmetric with respect to the plane $n_{\theta\max}=0.5n_{x\max}$. The projections of these curves for $n_{x\max}\le 0$ onto the plane $n_{x\max}=0$

are shown in Fig. 3-18. The shape of these curves resembles an ellipse and are symmetric with respect to the plane $m_{x\max} = 0$. The vertexes of these ellipselike curves lie on the curves of Eqs. (3-9) and (3-10). The curves for $n_{x\max} > 0$ are omitted here because of antisymmetry.

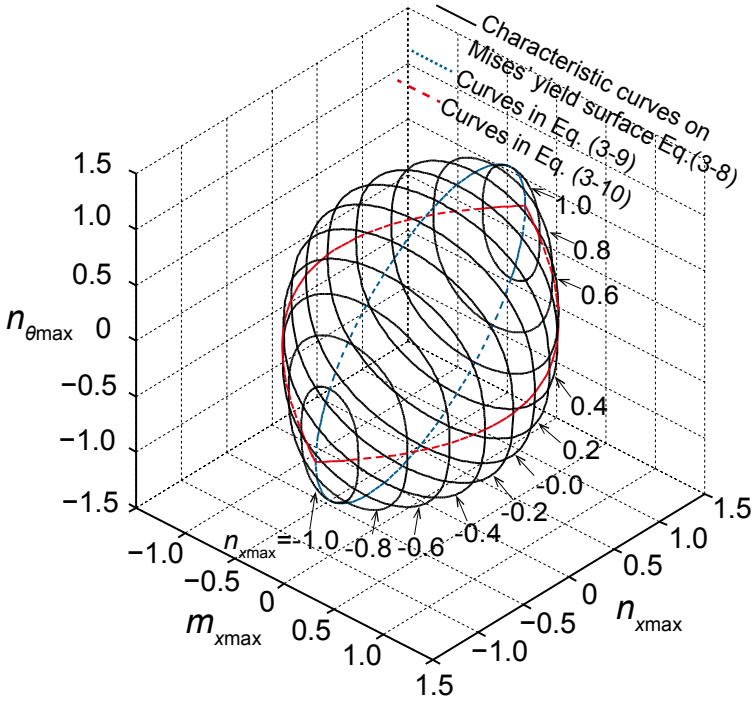

Fig. 3-17 Characteristic curves on Mises' yield surface of axisymmetrically loaded revolutional shells with Perfectly-plastic material

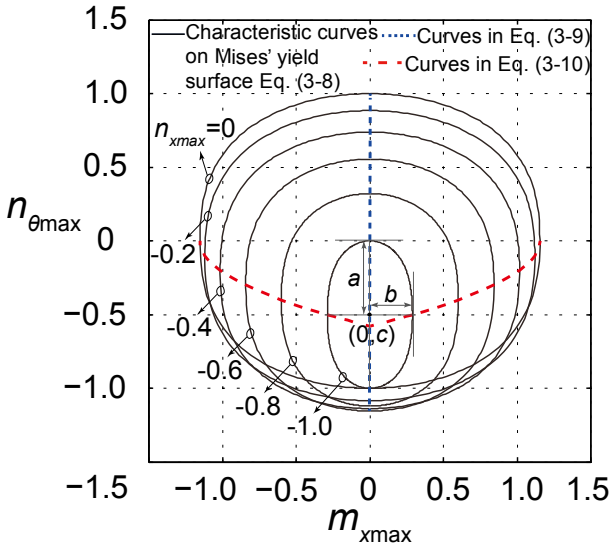

Fig. 3-18 Projections of characteristic curves onto the plane $n_{x\max} = 0$

Denoting the center as (0, c), the semi-major axis in the $n_{\theta\max}$ direction a, and the semi-minor axis in the $m_{x\max}$ direction b, as indicated in Fig. 3-18, these ellipselike curves are assumed to satisfy the form

$$\left|\frac{n_{\theta\max}-c}{a}\right|^{i}+\left|\frac{m_{x\max}}{b}\right|^{j}=1 \tag{3-11}$$

The c is set to be

$$c=0.5n_{x\max} \tag{3-12a}$$

Then, a and b can be obtained based on Eqs. (3-9) and (3-10).

$$a=\left|n_{\theta\max\,(m_{x\max}=0)}\right|-c=\sqrt{1-\frac{3}{4}n_{x\max}^{2}} \tag{3-12b}$$

$$b=\left|m_{x\max\,(n_{\theta\max}=0.5n_{x\max})}\right|=\frac{2}{\sqrt{3}}\left(1-\frac{3}{4}n_{x\max}^{2}\right) \tag{3-12c}$$

The i and j are determined by a curve-fitting approach.

$$i=2.5;\ j=2 \tag{3-13}$$

Consequently, substitutions of Eqs. (3-12) and (3-13) into Eq. (3-11) give the simplified explicit formula for Mises' yield surface.

$$\left|\frac{2n_{\theta\max}-n_{x\max}}{\sqrt{4-3n_{x\max}^{2}}}\right|^{2.5}+\left(\frac{2\sqrt{3}m_{x\max}}{4-3n_{x\max}^{2}}\right)^{2}=1 \tag{3-14}$$

The expression of $m_{x\max}$ can be obtained as

$$m_{x\max}=\pm\frac{2}{\sqrt{3}}\left(1-\frac{3}{4}n_{x\max}^{2}\right)\sqrt{1-\left|\frac{2n_{\theta\max}-n_{x\max}}{\sqrt{4-3n_{x\max}^{2}}}\right|^{2.5}} \tag{3-15}$$

The characteristic curves for $n_{x\max}$=-1.0, -0.8, -0.6, …, 0 in Eq. (3-14) are compared with those in Eq. (3-8). Good agreement can be observed as shown in Fig. 3-19.

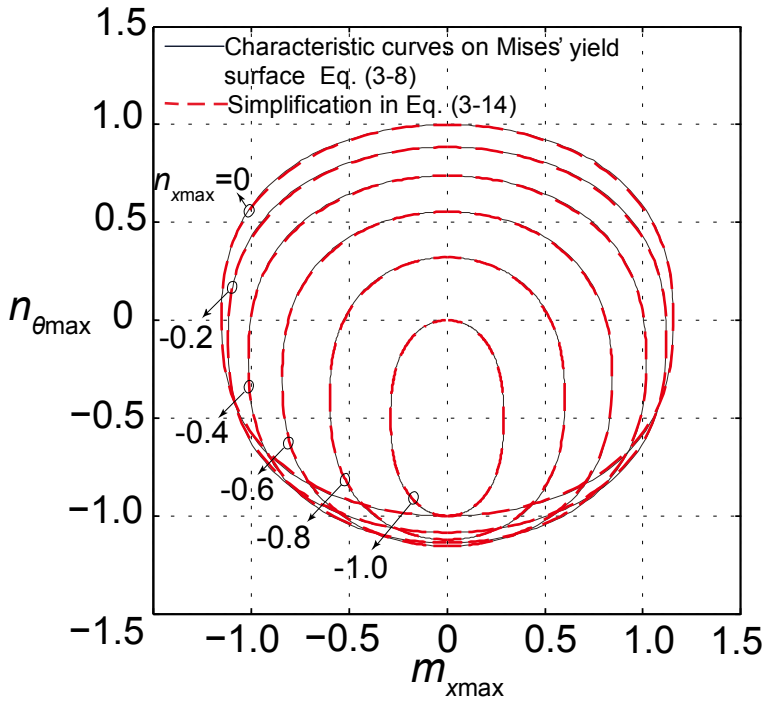

Fig. 3-19 Comparison of the characteristic curves between Mises' yield surface equation and the simplified approximation

(2) Validation of the Simplified Formula by FEA Results

Figure 3-20 shows the comparison between the interaction of $n_{\theta\max}$ with $m_{x\max}$ along with the increase of $|n_{\theta\max}|$ in FEA and the corresponding curves in Eq. (3-14). It can be found that the data of stress resultants in the range $m_{x\max} > 0$ for FEA models with different diameter-thickness ratios all approximately lie on the relevant curves in Eq. (3-14). Whereas, when $m_{x\max} < 0$, they do not. The reason might be the influence of shear stress resultant on yield condition.

Based on the above analysis, the simplified formula in Eq. (3-14) for Mises' yield surface is found to be close to the original one in Eq. (3-8). The proposed formula in Eq. (3-14) is validated by comparing with the stress resultants of FEA models with perfectly-elastic plastic material.

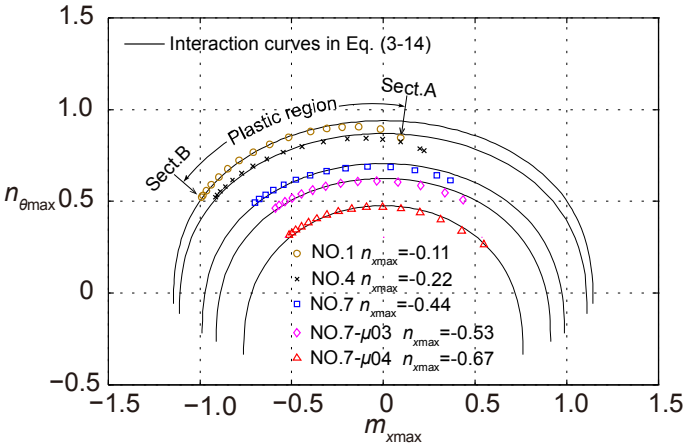

(a) Diameter-to-thickness ratio $d/t \approx 41.0$

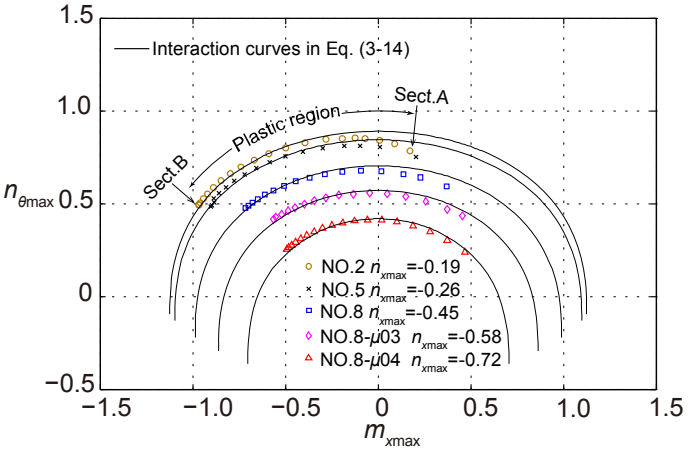

(b) Diameter-to-thickness ratio $d/t \approx 32.0$

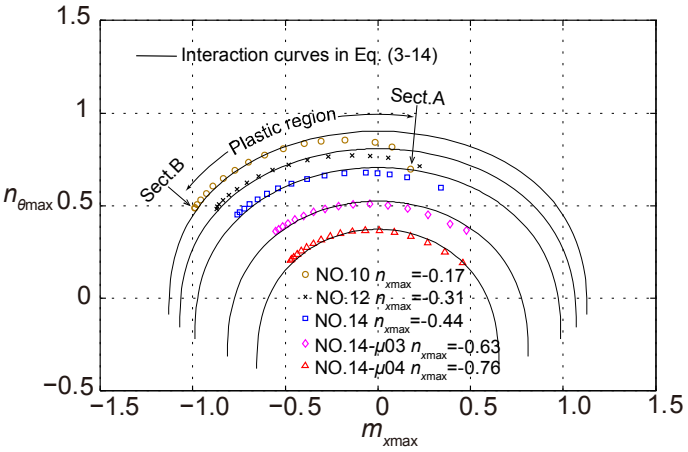

(c) Diameter-to-thickness ratio $d/t \approx 26.0$

Fig. 3-20 Comparison of the simplified interaction of stress resultants with the results of the FE models with perfectly-plastic material

3.5.2 Prediction of Full Plastic Strength

3.5.2.1 Equilibriums in the Cylindrical Wall

Limit analysis is employed to derive the maximum strength of models with perfectly-plastic material. The external forces acted at cylinder edge are shown in Fig. 3-21. Compressive force R and frictional force μR, which are transmitted from conical wall to cylindrical wall, are equivalent to radial force F_r, axial force F_x and axial bending moment $F_x \eta t$ applied at the center of sect. A. It should be noted that they are defined to be applied in 360 degrees in hoop direction. The ηt is the radially outward eccentricity of axial force F_x, in which η means the eccentricity ratio in sect. A. The exact value of η is difficult to be derived from the point of plastic theory of solid mechanics. In this study, it is obtained by

$$\eta = \frac{\int_{-t/2}^{t/2} s_{x\max A} z dz}{t \int_{-t/2}^{t/2} s_{x\max A} dz} \tag{3-16}$$

where, z is the radially outward distance from the middle surface of cylindrical walls.

The values of η are listed in Fig. 3-22. It is found that their average is -0.20 with a COV of 0.12. In this study, η of all the models is assumed to be a constant -0.20.

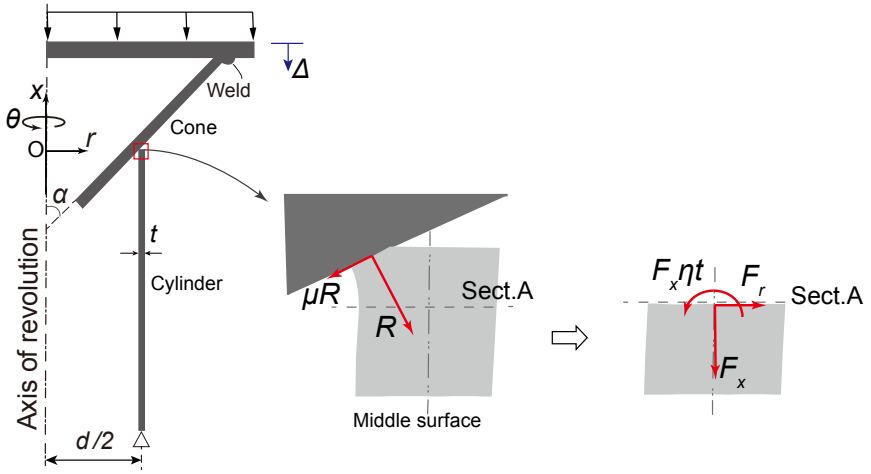

Fig. 3-21 Equivalent external forces at maximum load in cylindrical wall

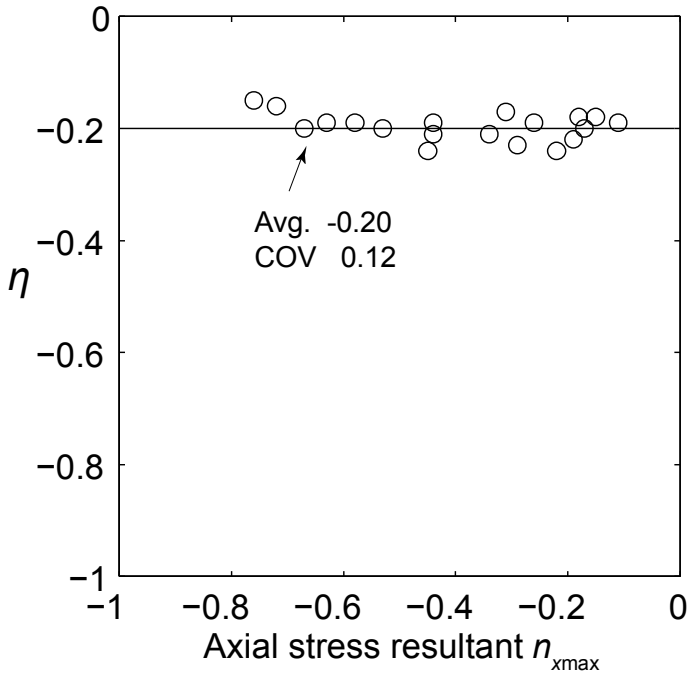

Fig. 3-22 Distribution of eccentricity ratio η along with the increase of $|n_{x\max}|$

The equilibriums for external forces are given by

$$F_x = \mu R\cos\alpha + R\sin\alpha \tag{3-17a}$$

$$F_r = R\cos\alpha - \mu R\sin\alpha \tag{3-17b}$$

Combining Eqs. (3-17a) and (3-17b) by eliminating R, The relationship between F_x and F_r is expressed as

$$F_r = -\frac{1-\mu\tan\alpha}{\tan\alpha+\mu}F_x \tag{3-18}$$

Maximum strength $P_{\max}$ can be given by

$$P_{\max} = -F_x \tag{3-19}$$

In addition, the axial external force is equal to the axial stress resultant numerically.

$$F_x = \pi d \cdot n_{x\max}\sigma_y t \tag{3-20}$$

where, d is the center-to-center diameter of cylinder.

3.5.2.2 Proposed Plastic Collapse Mechanism

Plastic collapse mechanism based on upper bound theory has been employed successfully for estimating the collapse strength of cylindrical shells under radial pressure or along with axial compression (Drucker 1954, Eason and Shield 1955, Onat 1955, Tsang and Harding 1984, et al.). Plastic hinges are assumed to absorb the strain energy done by axial bending moment and the straight segments between plastic hinges are assumed to absorb the strain energy done by hoop stress resultant. Tsang and Harding (1984) considered the influence of axial stress resultant on the failure mechanism. Especially for plastic hinges, they assumed that bending deformation takes places under plane strain condition. But the evidence for the interaction between axial stress resultant and axial bending moment has not been clear.

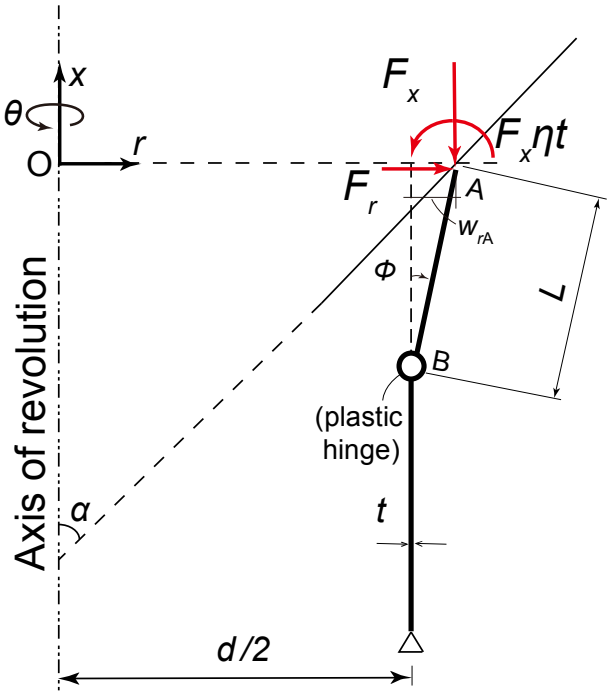

Fig. 3-23 Proposed plastic collapse mechanism for models with cylinder edge failure

For cylinder edge failure in this study, The plastic collapse mechanism shown Fig. 3-23 is assumed. The external forces of $\{F_r, F_x, F_x\eta t\}$ are applied in Sect. A. A plastic hinge with a rotation angle ϕ is assumed to occur in Sect. B. For segment AB, the axial

bending moment $m_{x\max AB}$ is equal to zero because of the assumption that segment AB is in a straight line. Substitution of $m_{x\max AB}=0$ into Eq. (3-14) gives the interaction between axial stress resultant and hoop stress resultant in the segment AB.

$$n_{\theta\max AB}=\frac{1}{2}n_{x\max}+\sqrt{1-\frac{3}{4}n_{x\max}^2} \tag{3-21}$$

where, $n_{\theta\max AB}$ is positive, and $n_{x\max}$ is assumed to be uniform along *x* direction.

For plastic hinge B, $\varepsilon_{\theta\max B}=0$ because of the assumption of rigid-plastic material. Assuming $t \ll L$ and very long (infinite) in hoop direction, plastic hinge B is under cylindrical bending. In this case, plane strain condition can be employed (Save, 1997). It indicates that

$$n_{\theta\max B}=\frac{1}{2}n_{x\max} \tag{3-22}$$

and

$$m_{x\max B}=\frac{2}{\sqrt{3}}(-1+\frac{3}{4}n_{x\max}^2) \tag{3-23}$$

3.5.2.3 Derivation of Virtual Work Equations

Based on the principle of virtual work, the equilibrium of external work $\mathrm{d}W$ and dissipation of internal energy $\mathrm{d}U$ for the whole mechanism in 360 degrees in hoop direction during a virtual change of rotation $\mathrm{d}\phi$ is given by

$$\mathrm{d}U=\mathrm{d}W \tag{3-24}$$

where

$$\mathrm{d}U=\mathrm{d}U_1+\mathrm{d}U_2+\mathrm{d}U_3$$

$$\mathrm{d}W=\mathrm{d}W_1+\mathrm{d}W_2+\mathrm{d}W_3$$

Herein, for internal energy, $\mathrm{d}U_1$ is done by hoop stress resultant $n_{\theta\max}\sigma_y t$, $\mathrm{d}U_2$ is done by axial stress resultant $n_{x\max}\sigma_y t$ and $\mathrm{d}U_3$ is done by axial bending moment

$m_{x\max}\dfrac{1}{4}\sigma_y t^2$; For external work, $\mathrm{d}W_1$ is done by radial force F_r, $\mathrm{d}W_2$ is done by axial force F_x and $\mathrm{d}W_3$ is done by axial bending moment $F_x\eta t$.

The components of $\mathrm{d}U$ and $\mathrm{d}W$ are derived as follows.

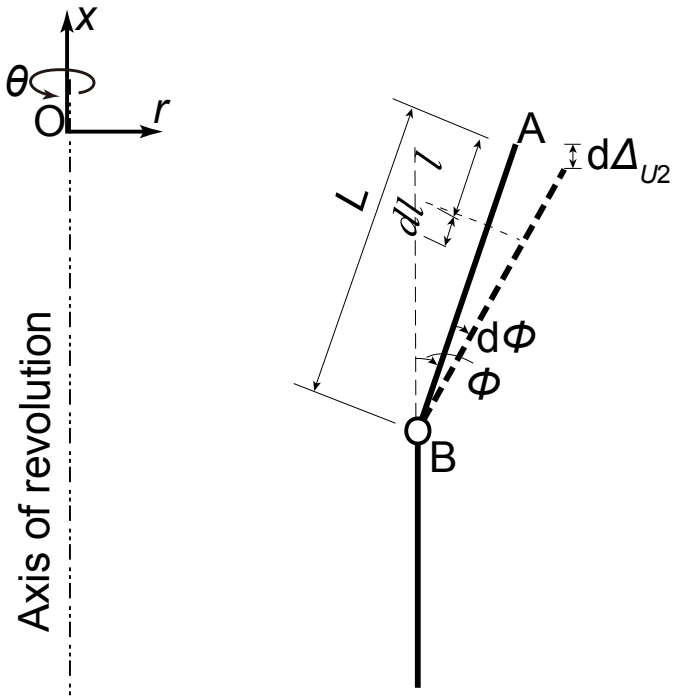

Fig. 3-24 Axial shortening compatible with the circumferential stretching of the segment AB in plastic collapse mechanism

① $\mathrm{d}U_1$

A small segment of length $\mathrm{d}l$ is considered, as shown in Fig. 3-24. Increase in length $\mathrm{d}\Delta_{U1}$ in hoop direction after the virtual change of rotation $\mathrm{d}\phi$ can be derived as

$$\mathrm{d}\Delta_{U1} = (L-l)[\sin(\phi+\mathrm{d}\phi)-\sin\phi] \approx (L-l)\cos\phi\mathrm{d}\phi \tag{3-25}$$

The strain rate in hoop direction is given by

$$\dot{\varepsilon}_{\theta\max} = \frac{(L-l)\cos\phi}{d/2+(L-l)\sin\phi}\mathrm{d}\phi \tag{3-26}$$

This may be approximated to

$$\dot{\varepsilon}_{\theta\max} \approx \frac{(L-l)\cos\phi}{d/2}\mathrm{d}\phi \tag{3-27}$$

The $\mathrm{d}U_1$ during the increase in length in hoop direction for the whole length of the mechanism can be obtained as

$$\begin{aligned}\mathrm{d}U_1 &= \pi d\int_0^L n_{\theta\max\mathrm{AB}}\sigma_y t\dot{\varepsilon}_{\theta\max}\,\mathrm{d}\,l = \pi d\,\frac{n_{\theta\max\mathrm{AB}}\sigma_y t\cos\phi\mathrm{d}\phi}{d/2}\int_0^L (L-l)\mathrm{d}l \\ &= \pi n_{\theta\max\mathrm{AB}}\sigma_y tL^2\cos\phi\mathrm{d}\phi\end{aligned} \tag{3-28}$$

② $\mathrm{d}U_2$

Since the deformations in the plastic failure mechanism except plastic hinge B take place under Mises' yield condition as shown in Eq. (3-29), a flow rule must be adopted to determine the change in the strain rate (Save, 1997).

$$f = n_{x\max}^2 + n_{\theta\max\mathrm{AB}}^2 - n_{x\max}n_{\theta\max\mathrm{AB}} - 1 = 0 \tag{3-29}$$

Thus,

$$\dot{\varepsilon}_{x\max} = \lambda\frac{\partial f}{\partial n_{x\max}} = \lambda(2n_{x\max} - n_{\theta\max\mathrm{AB}}) \tag{3-30}$$

and

$$\dot{\varepsilon}_{\theta\max} = \lambda\frac{\partial f}{\partial n_{\theta\max\mathrm{AB}}} = \lambda(2n_{\theta\max\mathrm{AB}} - n_{x\max}) \tag{3-31}$$

where λ is a positive scalar factor.

Combining Eqs. (3-30) and (3-31) gives

$$\dot{\varepsilon}_{x\max} = \frac{2n_{x\max} - n_{\theta\max\mathrm{AB}}}{2n_{\theta\max\mathrm{AB}} - n_{x\max}}\dot{\varepsilon}_{\theta\max} \tag{3-32}$$

Substituting Eq. (3-27) into Eq. (3-32) and integrating $\dot{\varepsilon}_{x\max}$, the shortening in length $\mathrm{d}\Delta_{U2}$ in the longitudinal direction for the whole length of the mechanism, as shown in Fig. 3-24, is given by

$$\begin{aligned}\mathrm{d}\Delta_{U2} &= \int_0^L \dot{\varepsilon}_{x\max}\mathrm{d}l = \int_0^L \frac{2n_{x\max} - n_{\theta\max\mathrm{AB}}}{2n_{\theta\max\mathrm{AB}} - n_{x\max}}\frac{\cos\phi\mathrm{d}\phi}{d/2}(L-l)\mathrm{d}l \\ &= L^2\frac{2n_{x\max} - n_{\theta\max\mathrm{AB}}}{2n_{\theta\max\mathrm{AB}} - n_{x\max}}\frac{\cos\phi}{d}\mathrm{d}\phi\end{aligned} \tag{3-33}$$

The $\mathrm{d}U_2$ can be obtained by

$$\begin{aligned}\mathrm{d}U_2 &= \pi d n_{x\max}\sigma_y t\mathrm{d}\Delta_{U2} \\ &= \pi n_{x\max}\sigma_y t L^2 \frac{2n_{x\max} - n_{\theta\max AB}}{2n_{\theta\max AB} - n_{x\max}}\cos\phi\mathrm{d}\phi\end{aligned} \tag{3-34}$$

③ $\mathrm{d}U_3$

The $\mathrm{d}U_3$ by axial bending moment $m_{x\max B}\frac{1}{4}\sigma_y t^2$ is obtained by

$$\mathrm{d}U_3 = \pi d \cdot m_{x\max B}\frac{1}{4}\sigma_y t^2\mathrm{d}\phi \tag{3-35}$$

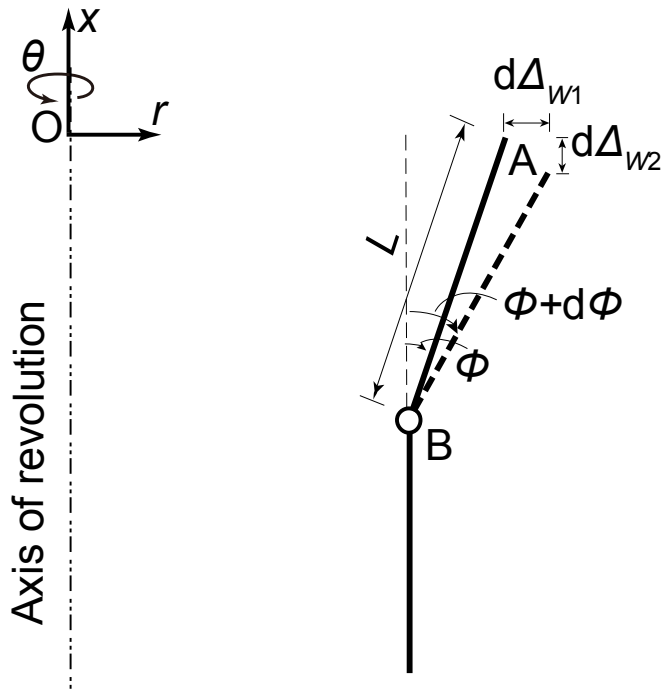

Fig. 3-25 Virtual deformation due to an incremental rotation of the plastic hinge

④ $\mathrm{d}W_1$

After the virtual change of rotation $\mathrm{d}\phi$, the virtual radial deformation by radial force F_r is defined as $\mathrm{d}\Delta_{W1}$ in Fig. 3-25.

$$\mathrm{d}\Delta_{W1} = L\sin(\phi+\mathrm{d}\phi) - L\sin\phi \approx L\cos\phi\mathrm{d}\phi \tag{3-36}$$

Thus, the work $\mathrm{d}W_1$ is obtained by

$$\mathrm{d}W_1 = F_r L \cos\phi \mathrm{d}\phi \tag{3-37}$$

⑤ $\mathrm{d}W_2$

After the virtual change of rotation $\mathrm{d}\phi$, the virtual axial deformation by axial force F_x, excluding the virtual strain deformation $\mathrm{d}\Delta_{U2}$ in Eq. (3-33), is defined as $\mathrm{d}\Delta_{W2}$ in Fig. 3-25.

$$\mathrm{d}\Delta_{W2} = L\cos(\phi + \mathrm{d}\phi) - L\cos\phi \approx -L\sin\phi \mathrm{d}\phi a \tag{3-38}$$

Thus, the work $\mathrm{d}W_2$ can be written as

$$\begin{aligned} \mathrm{d}W_2 &= F_x(\mathrm{d}\Delta_{W2} + \mathrm{d}\Delta_{U2}) \\ &= F_x(-L\sin\phi \mathrm{d}\phi + L^2 \frac{2n_{x\max} - n_{\theta\max \mathrm{AB}}}{2n_{\theta\max \mathrm{AB}} - n_{x\max}} \frac{\cos\phi}{d} \mathrm{d}\phi) \end{aligned} \tag{3-39}$$

⑥ $\mathrm{d}W_3$

The work $\mathrm{d}W_3$ by external axial bending moment is given by

$$\mathrm{d}W_3 = -F_x \eta t \mathrm{d}\phi \tag{3-40}$$

Substituting Eqs. (3-28), (3-34), (3-35), (3-37), (3-39) and (3-40) into Eq. (3-24) and eliminating $\mathrm{d}\phi$ give the general equation that

$$F_r L\cos\phi - F_x L\sin\phi - \eta F_x t = \pi n_{\theta\max \mathrm{AB}} \sigma_y t L^2 \cos\phi - \pi d m_{x\max \mathrm{B}} \frac{1}{4}\sigma_y t^2 \tag{3-41}$$

3.5.2.4 Proposed Formula for Full Plastic Strength

Based on the small deformation theory, $\sin\phi = \phi$, $\cos\phi = 1$. Eq. (3-41) can be simplified to be that

$$F_r L = \pi n_{\theta\max \mathrm{AB}} \sigma_y t L^2 - \pi d m_{x\max \mathrm{B}} \frac{1}{4}\sigma_y t^2 + \eta F_x t + \phi F_x L \tag{3-42}$$

Dividing the both sides of Eq. (3-42) by L and substituting Eq. (3-19) into it, F_r can be expressed as

$$F_r = \pi n_{\theta \max AB} \sigma_y t L + \frac{-\pi d m_{x \max B} \sigma_y t^2 + 4\eta F_x t}{4L} - \phi P_{\max} \tag{3-43}$$

Based on upper bound theorem, F_r can be obtained by $\frac{dF_r}{dL} = 0$. Thus,

$$F_r = \sqrt{-m_{x \max B} + 4\eta n_{x \max}} \sqrt{n_{\theta \max AB}} \cdot \pi \sigma_y t \sqrt{dt} - \phi P_{\max} \tag{3-44}$$

Herein, η is assumed to be a constant of -0.2 as shown in Fig. 3-21, and L is given by

$$L = \sqrt{\frac{-m_{x \max B} + 4\eta n_{x \max}}{4 n_{\theta \max AB}}} \sqrt{dt} \tag{3-45}$$

Substituting $n_{\theta \max AB}$ in Eq. (3-21) and $m_{x \max B}$ in Eq. (3-23) into Eq. (3-45), L is finally obtained as

$$L = \frac{1}{2} \sqrt{\frac{\frac{2}{\sqrt{3}}(1 - \frac{3}{4} n_{x \max}^2) - 0.8 n_{x \max}}{\frac{1}{2} n_{x \max} + \sqrt{1 - \frac{3}{4} n_{x \max}^2}}} \cdot \sqrt{dt} \tag{3-46}$$

The length of plastic region L varies with the increasing of axial stress resultant. Its prediction in Eq. (3-46) is compared with the corresponding results of FE models with perfectly plastic material, as shown in Fig. 3-26. The average of the ratios is 0.99, with a standard deviation 0.08. Good agreement can be found with each other.

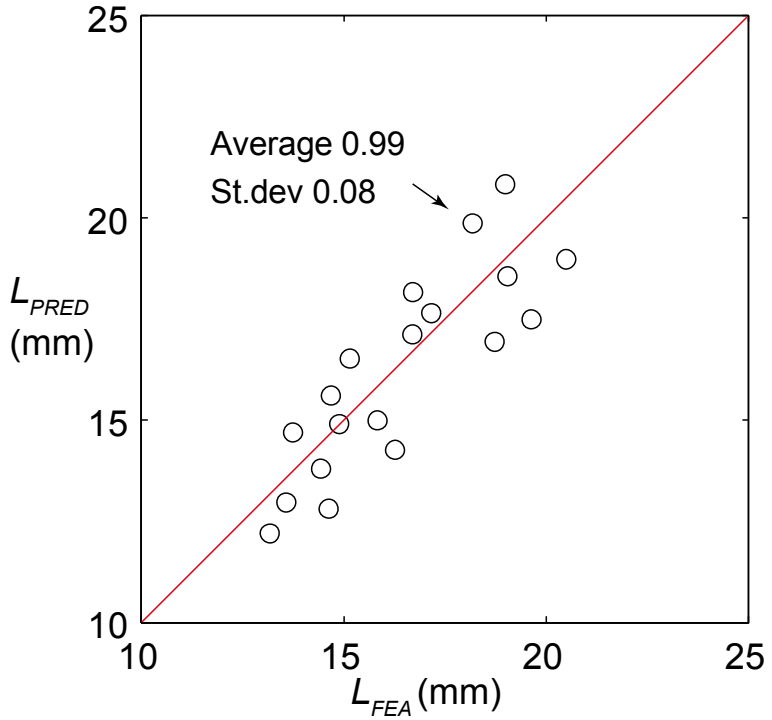

Fig. 3-26 Comparison of the predicted length of plastic region with that of FE models with perfectly plastic material

Substituting Eqs. (3-18), (3-19), (3-20), (3-21) and (3-23) into Eq. (3-44) and dividing the both sides of Eq. (3-44) by $\pi d\sigma_y t$, maximum axial stress resultant $n_{x\max}$ is obtained by the implicit expression as follow:

$$n_{x\max} = -\psi \cdot \gamma \cdot \chi \tag{3-47}$$

where, ψ is a factor in which the interaction of axial stress resultant with hoop stress resultant and axial bending moment in the failure mechanism is considered.

$$\psi = \sqrt{\frac{2}{\sqrt{3}}\left(1-\frac{3}{4}n_{x\max}^2\right)-0.8n_{x\max}}\sqrt{\frac{1}{2}n_{x\max}+\sqrt{1-\frac{3}{4}n_{x\max}^2}} \tag{3-48}$$

The γ is a reduction factor by considering the external work of axial force.

$$\gamma = \frac{\dfrac{1-\mu\tan\alpha}{\tan\alpha+\mu}}{\dfrac{1-\mu\tan\alpha}{\tan\alpha+\mu}+\phi} \tag{3-49}$$

The χ is a parameter including the dimensionless quantities of diameter-to-thickness ratio d/t, friction coefficient μ, and semi-convex angle α. It is the fundamental

parameter for calculating maximum strength.

$$\chi = \sqrt{\frac{t}{d}} \frac{\tan\alpha + \mu}{1 - \mu\tan\alpha} \tag{3-50}$$

The arrays of $(\psi, n_{x\max})$ where $n_{x\max} \in [0, -0.8]$ are plotted in Fig. 3-27. The variation of ψ with $n_{x\max}$ may be closely approximated by the quadratic equation as

$$\psi = -0.87 n_{x\max}^2 - 0.16 n_{x\max} + 1.07 \tag{3-51}$$

The values of ψ for all the models are also plotted. It can be seen that the smallest one is low to about 0.6. The relationship between γ and ϕ for all the FE models is shown in Fig. 3-28. It is found that as ϕ increases, γ almost keeps being constant except for the model Nos. 7_μ04, 8_μ04 and 14_μ04. Because high axial stress resultants make their radial deformations a little more complicated than those of other models. The average of γ is 0.93, with a small COV of 0.04. Thus, it can be simplified to be 0.93 in this study.

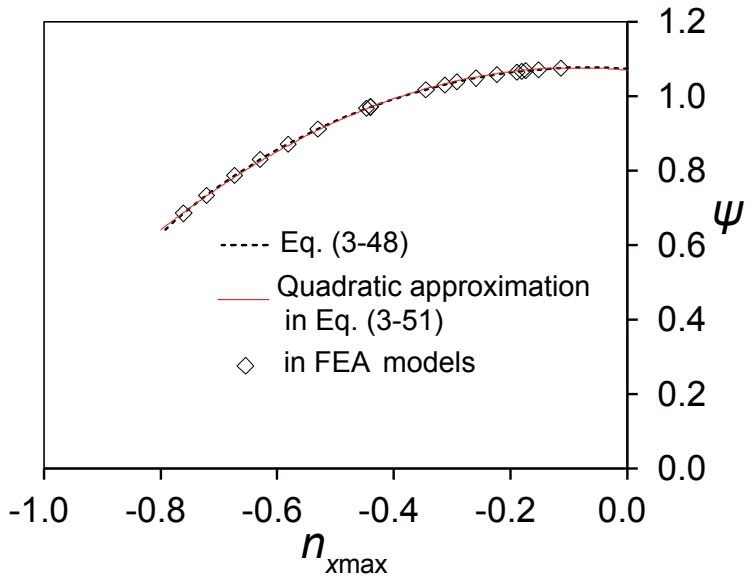

Fig. 3-27 Plot of ψ and the relevant values of FEA models in series I

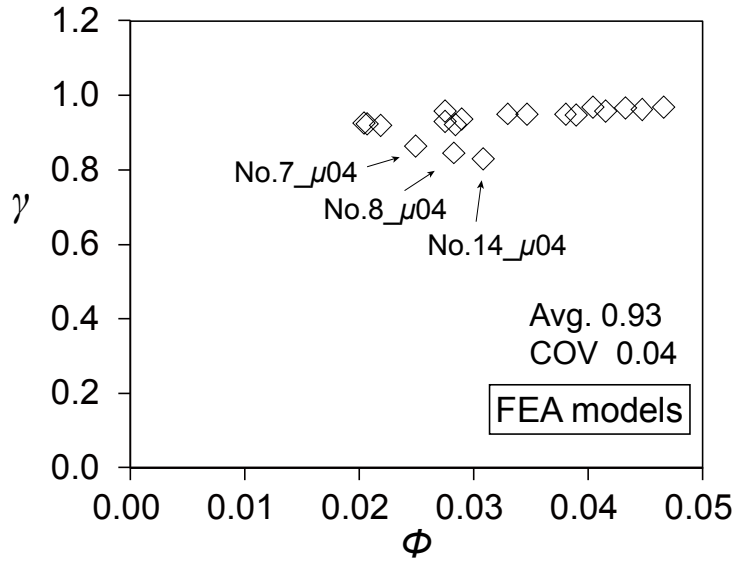

Fig. 3-28 Relationship between γ and ϕ of FEA models in series I

Substituting Eq. (3-51) and $\gamma = 0.93$ into Eq. (3-47), $n_{x\max}$ can be expressed in the following quadratic equation.

$$n_{x\max} = (0.81 n_{x\max}^2 + 0.15 n_{x\max} - 1.00)\chi \tag{3-52}$$

The solution of $n_{x\max}$ is

$$n_{x\max} = \frac{-0.15\chi + 1 - \sqrt{3.26\chi^2 - 0.3\chi + 1}}{1.62\chi} \tag{3-53}$$

Therefore, $P_{\max}$ can be finally expressed as

$$P_{\max} = -n_{x\max}\pi dt\sigma_y = \frac{0.15\chi + 1 + \sqrt{3.26\chi^2 - 0.3\chi + 1}}{1.62\chi}\pi dt\sigma_y \tag{3-54}$$

Comparison of $P_{\max-PRED}$ expressed in Eq. (3-54) with $P_{\max-FEA}$ is shown in Fig. 3-29. The average of the ratios is 1.02 with a quite small COV of 0.02. Formula in Eq. (3-54) can predict well the maximum strength of models with perfectly plastic material. It means that the full plastic strength P_p can be predicted by

$$P_{p-PRED} = \frac{0.15\chi + 1 + \sqrt{3.26\chi^2 - 0.3\chi + 1}}{1.62\chi}\pi dt\sigma_y \tag{3-55}$$

Comparison of P_{p-PRED} with P_{p-FEA} is shown in Fig. 3-30. The average of the ratios is 0.98 with a quite small COV of 0.04. Therefore, full plastic strength of specimens with cylinder edge failure can be predicted well by the proposed formula.

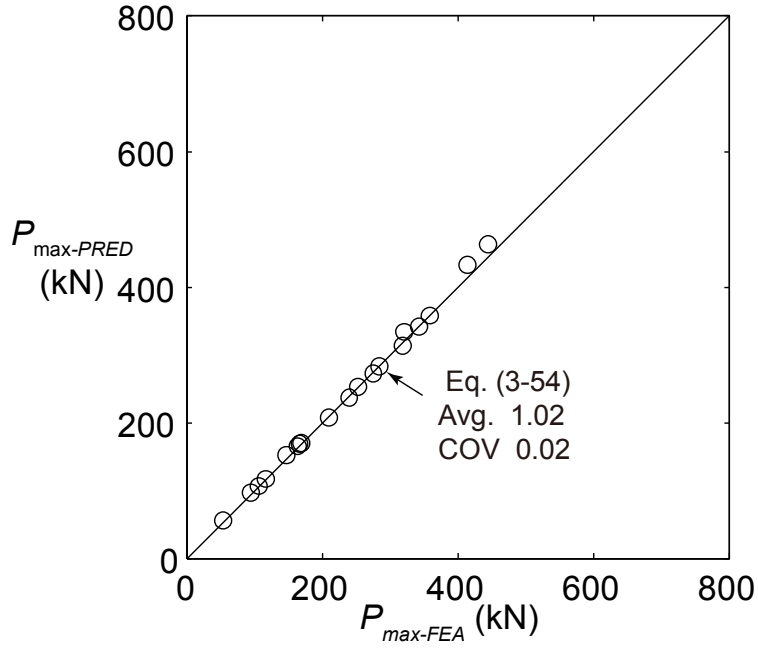

Fig. 3-29 Comparison of predicted maximum strength of models with the relevant FEA results

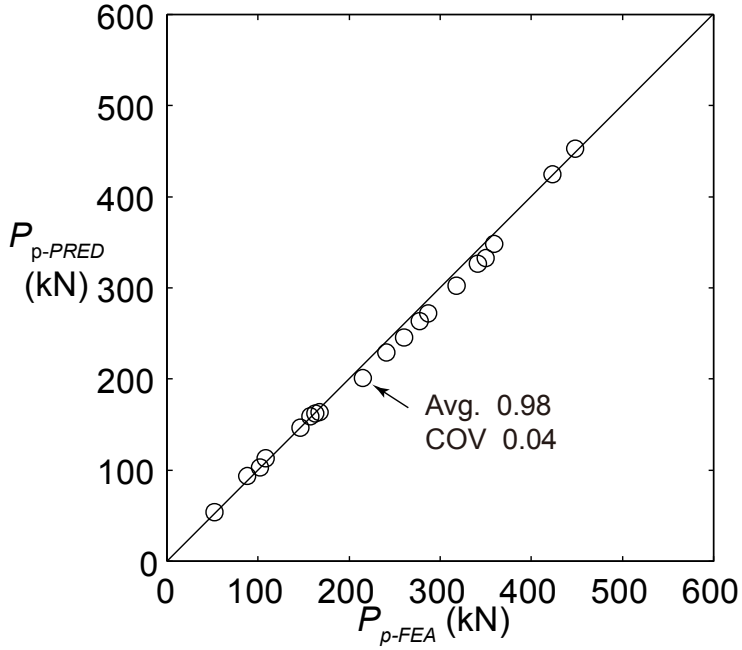

Fig. 3-30 Comparison of predicted full plastic strength of specimens with the relevant effective FEA results

3.5.3 Prediction of Collapse Strength

Because of the strain hardening effect of mild steel material, the strength continues to increase after full plastic strength arrives. A simple way to prediction collapse strength is multiplying full plastic strength by an enhancement factor ρ. Based on the assumption of uniaxial stress state, it is usually assumed to be σ_u/σ_y (Morita 1988) or $(\sigma_y+\sigma_u)/(2\sigma_y)$ (Kuwamura et al. 2015). The latter one is smaller than the former one and gives a little safer prediction of collapse strength. But if the interaction of axial stress resultant with hoop stress resultant and axial bending moment is considered, the stress state in the failure mechanism will become multi-axial. Thus, the two factors of σ_u/σ_y and $(\sigma_y+\sigma_u)/(2\sigma_y)$ are not reasonable to be employed in this study. The factor ρ is assumed to be the average of the ratios of collapse strength to full plastic strength of both experimental specimens and FEA models, which is shown in Fig. 3-31. It is found that the average is 1.08 with a COV of 0.05. Collapse strength P_u is predicted by

$$P_{u\text{-}PRED} = \rho P_{p-PRED} \tag{3-56}$$

where, $\rho = 1.08$.

The predicted collapse strength P_u in Eq. (3-56) and the previous formulae proposed by Kuwamura et al. (2005) and Ito et al. (2008) are compared with those of FEA models. The ratios along with n_{xu} are shown in Fig. 3-32. It can be found that the COV of the new proposed formula in Eq. (3-56) are much smaller than those of previous ones. The precision of Eq. (3-56) is verified.

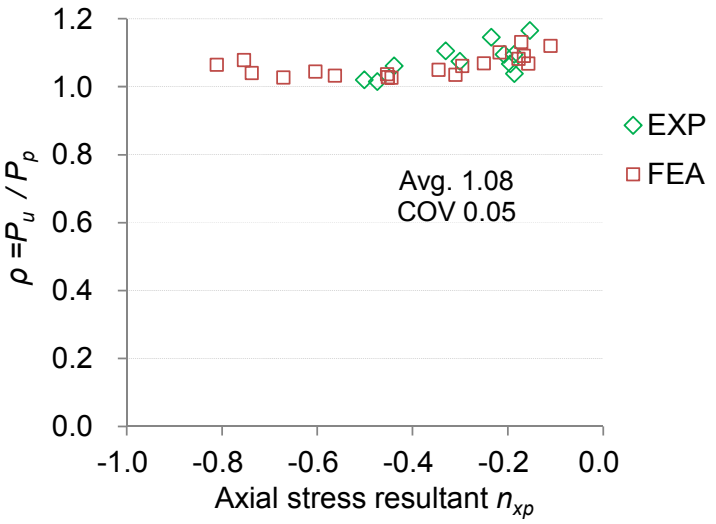

Fig. 3-31 Ratios of collapse strength to full plastic strength for both experimental and FEA specimens

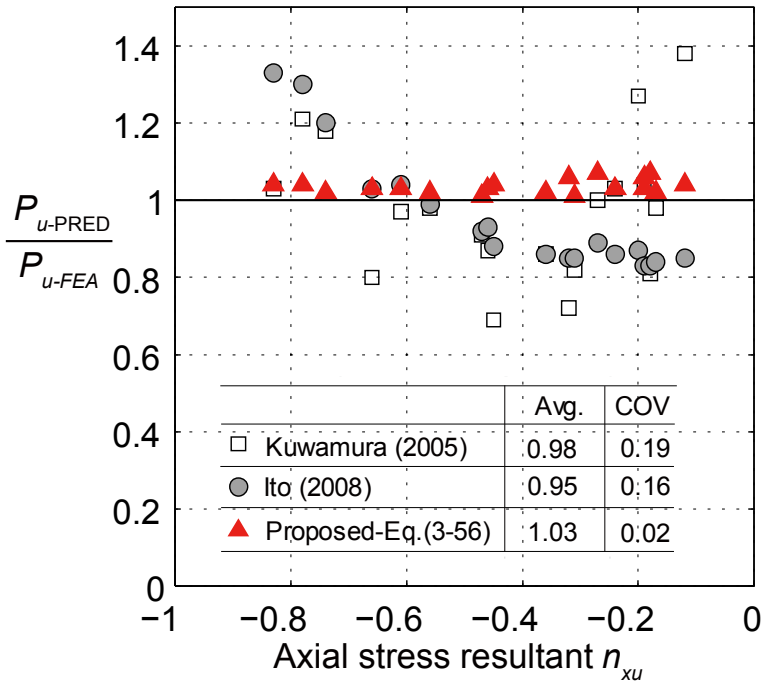

Fig. 3-32 Comparison of collapse strength between the proposed formula and the previous ones

3.5.4 Prediction of General Yield Strength

General yield strength of connections was first studied by Johnston. B.G. (1939b). 106 tests of differently proportioned steel pin-connected plates were undertaken and then the empirical equation for it was proposed. After then, many studies were undertaken on the prediction of general yield strength. However, most of them are based on empirical

method (Kurobane et al. 1984, Kamba et al. 1998, et al.). Moreover, as local region at the top edge of cylindrical wall has entered into plastic before general yield load arrived, Elastic solution from bending theory of shells cannot be applied. In this study, it is predicted based on the formulae for full plastic strength, which was derived precisely by limit analysis. The reduction factor is set to be ξ. It is assumed to be the average of the ratios of P_y to P_p for both experimental specimens and FEA models. The results of the ratios are plotted in Fig. 3-33. It is found that the average is 0.90 with a small COV of 0.05. Therefore, general yield strength P_y is predicted by

$$P_{y-PRED} = \xi P_{p-PRED} \tag{3-57}$$

where, $\xi = 0.90$.

The predicted values of general yield strength are compared with those in FEA, as shown in Fig. 3-34. It can be seen that the average value is 1.01 with a COV of 0.07. The formula in Eq. (3-57) can predict well the general yield strength of models.

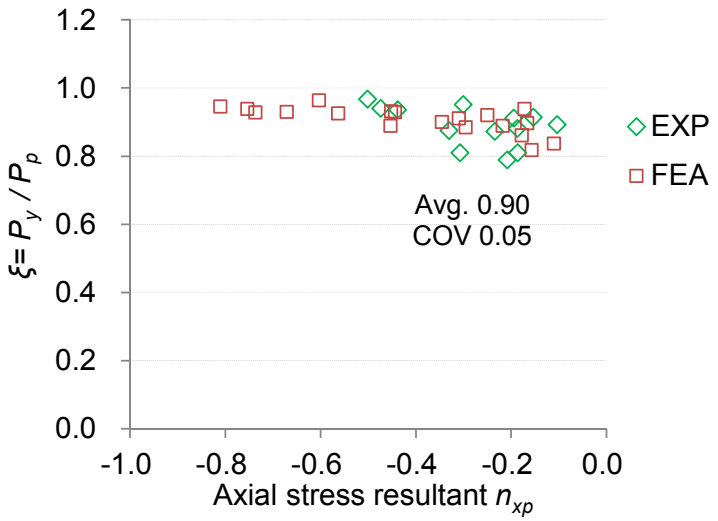

Fig. 3-33 Ratios of P_y to P_p for both experimental and FEA results

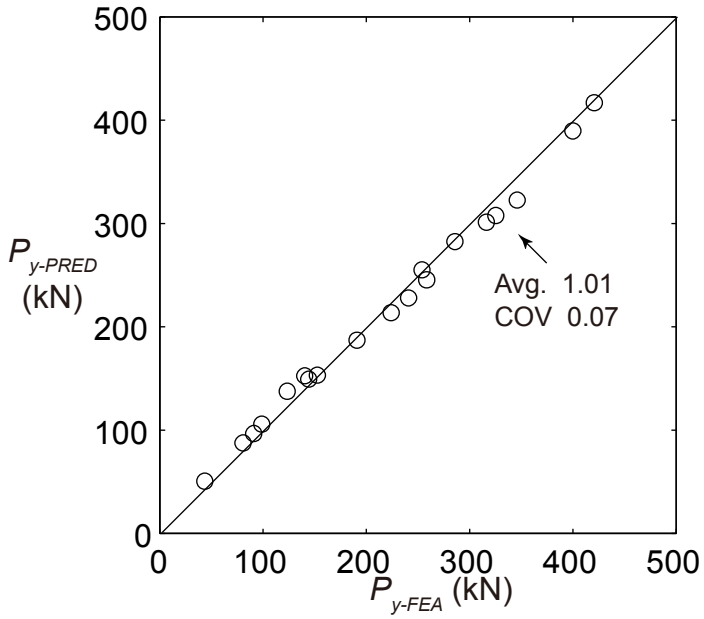

Fig. 3-34 Comparison of the predicted general yield strength of specimens with effective FEA results

3.6 Summaries

This chapter focuses on strength of metal touch connections with cylinder edge failure under axial compression. Based on the above analysis, the following conclusions can be obtained.

(1) The effectiveness of axisymmetric solid model for predicting the strength of the socket connection under axial compression is validated. The friction coefficient between cone and cylinder is assumed to be a constant during the deformation process. For practical design work, it can be assumed to be 0.20;

(2) The correlation among axial stress resultant, hoop stress resultant and axial bending moment in the plastic region of cylindrical wall is found to be significant;

(3) The radial deformation at the top edge of cylindrical wall at ultimate load is found to be very small, by comparing it with the length of plastic region;

(4) The failure of cylinder edge is controlled by "plastic collapse mechanism" based on the proposed criterion;

(5) The simplification of Mises' yield condition for axisymmetrically loaded revolutional

shells with perfectly-plastic material is proposed and then validated by comparing it with relevant FEA result; and

(6) Easy-to-use formula for predicting full plastic strength is derived by limit analysis. The collapse and general yield strength of the experimental specimens is proposed based on the results of full plastic strength. Their precision is proved by comparing them with previous ones and the effective FEA results.

CHAPTER 4 STRENGTH OF METAL TOUCH CONNECTIONS WITH TAPERED RING FAILURE

4.1 Introduction

Rings are often employed to strengthen cylindrical shell structures when cylindrical walls sustain compression or tension in hoop direction (Teng et al. 1991, Chen el al. 1998). Welding is usually added between ring and cylindrical wall, in which the ring is subjected not only to radial expansion or contraction, but also to axial bending. In this study, it is interesting that the ring is metal-touched with cylindrical wall. A failure mechanism was proposed by Kuwamura et al.(2005a) based on the assumption of uniaxial stress state. Fujimoto and Kuwamura (2009) updated it by considering the contact of the bottom edge of ring with cylindrical wall. But the ultimate behavior of ring was not investigated clearly. Moreover, the influence of axial stress resultant on the failure mechanism was also not considered.

In this chapter, the effectiveness of FEA models is first validated by comparing their strength and deformation with experiments. The friction property in the contact region between cone and cylinder is determined. The influence of friction coefficient in the contact region between ring and cylinder on the strength of connections is analyzed. Then, the changing distributions of stress resultants in cylindrical wall and tapered ring under increasing load are studied. The ultimate deformation of connections is investigated. The failure mode is judged by the proposed criteria for both cylindrical shell and tapered ring. Finally, the full plastic strength is derived based on limit analysis. The prediction of collapse strength and general yield strength is undertaken based on the formula for full plastic strength. Their precision is validated by comparing them with the experimental

and FEA results and previous equation.

4.2 FE Modeling

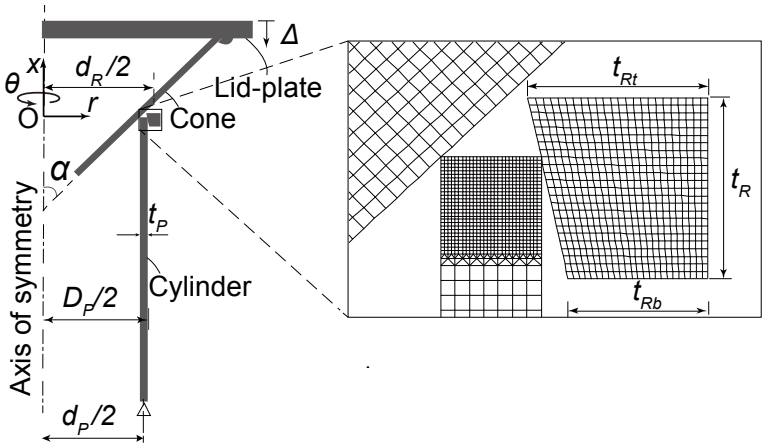

Fig. 4-1 Details of FEA axisymmetric model with tapered ring failure

4.2.1 General

The details of FEA axisymmetric model are shown in Fig. 4-1. Mesh sizes in cylindrical and conical walls are the same as those in Chapter 3. Setting the mesh size of ring to be 0.25mm, twice that in the contact region of cylindrical wall, convergent ultimate strength of the connection can be obtained. Figure 4-2 shows stress-strain curves of mild steel used in tapered rings based on the results of coupon test. Tapered rings with thicknesses of 6, 9, and 12mm were produced from the plates with thicknesses of 9, 12, and 16mm respectively. The s~e_p curves of the material are shown in Fig. 4-3. Perfectly-elastic plastic material is also defined for the following FE analysis, in order to verify the precision of proposed formula for full plastic strength of models.

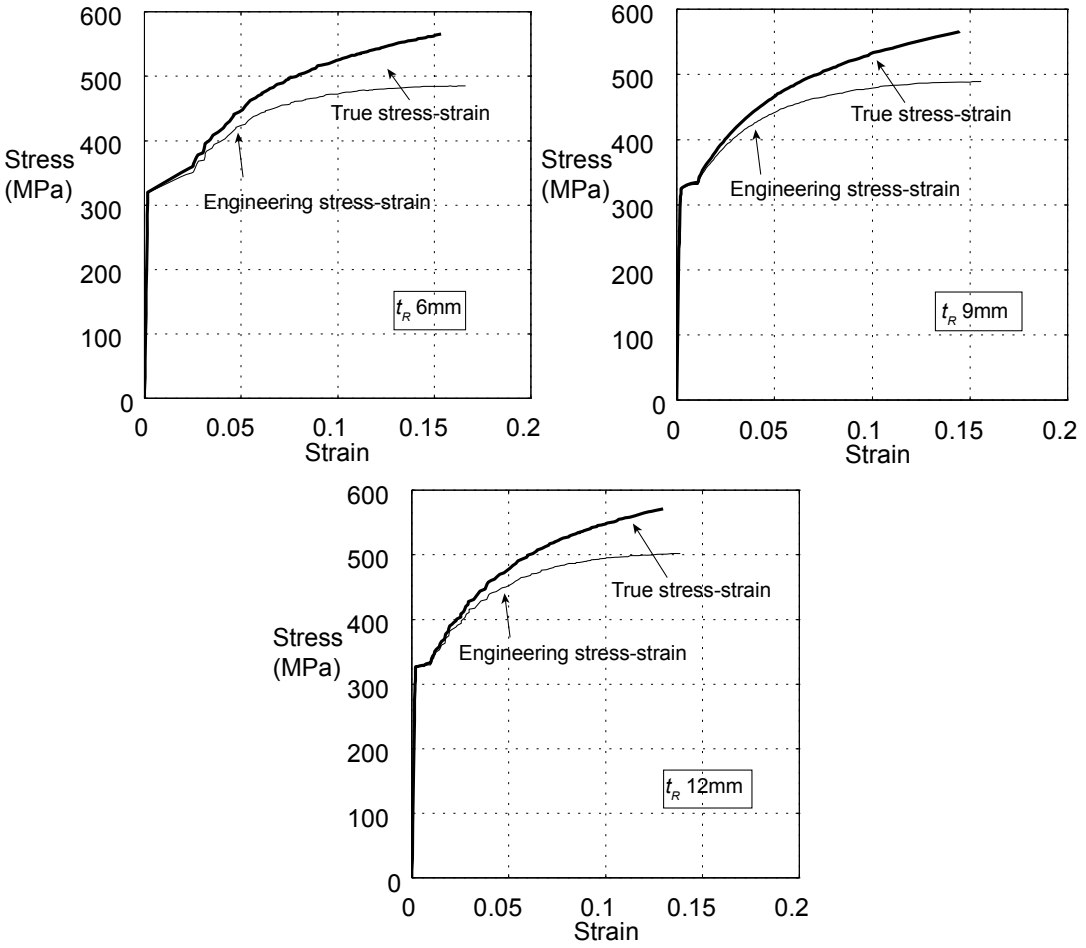

Fig. 4-2 True stress-strain curves for material SM490 of tapered rings

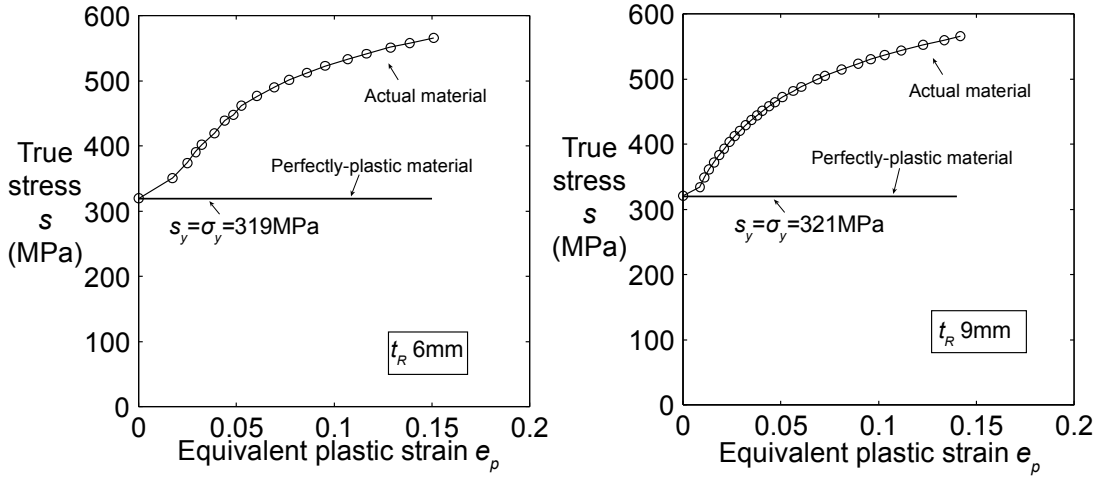

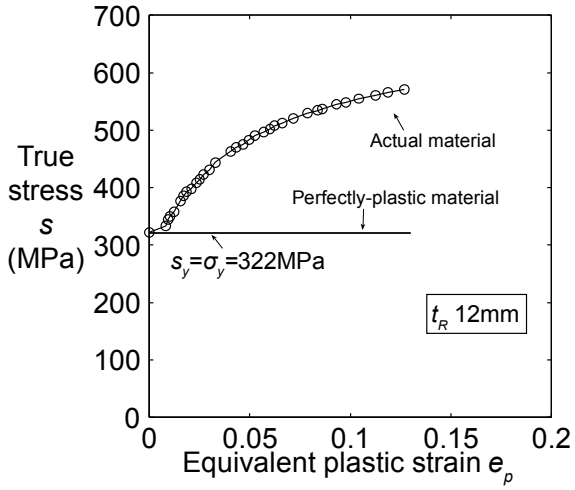

Fig. 4-3 s~e_p curves input in ABAQUS for materials of tapered rings

4.2.2 Effectiveness of FE Models

Amontons-Coulomb's friction law with formulation of Penalty is adopted and friction coefficient μ is assumed to be a constant during the whole deformation process. The variation of collapse strength in FEA along with the increase of μ_1, which is between conical wall and cylinder edge, is shown in Fig. 4-4. It can be seen that as μ_1 increases, collapse strength of taper ring failure increases quickly. The collapse strength of FE model becomes about equal to that of experimental specimen by calibrating the value of μ_1. As a result, the average of μ_1 is 0.28, with a COV of 0.39, as shown in Table 4-1. It is a little greater than that of models with cylinder edge failure shown in Table 3-1. The reason might be the contact surface between cone and cylinder becomes a little rougher due to the confinement effect of tapered ring. The μ_2 in the contact region between ring and cylinder, has no influence on the strength of connection, as shown in Fig. 4-5. But if μ_2 is set to be 0.0, the iteration is difficult to become convergent before ultimate load arrives, even if the minimum increment size is defined as 10^{-50}. Thus, μ_2 is set to be 0.2 for all the models. The full plastic strength and general yield strength of models are then compared with those of experimental specimens. It is found that the averages of ratios are 1.02 for full plastic strength and 0.99 for general yield strength, with small COV of 0.11 and 0.06, respectively.

Then, the maximum strength P_{max} of models with perfectly-plastic material is compared with the full plastic strength P_p of models with actual material, as shown in Fig. 4-6. The average of the ratios is 0.98, with a small standard deviation of 0.05. It is found that the method of "K_0/6 slope factor" proposed by Tateyama (1988) is effective to determine the full plastic strength of models with tapered ring failure.

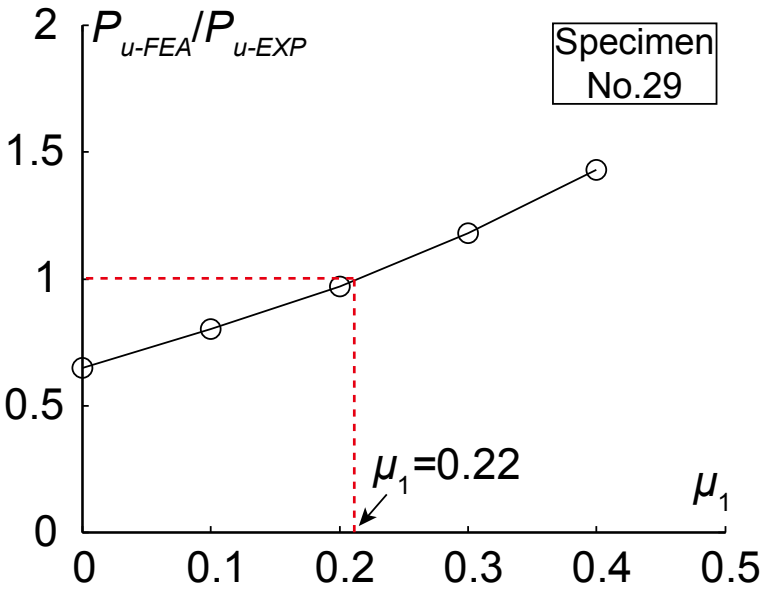

Fig. 4-4 Variation of collapse strength of models with tapered ring failure along with the increase of friction coefficient between conical wall and cylinder edge

Table 4-1 Comparison of strength between FEA and experiments for models in series II

Model NO.	Experiments			FEA					Comparison		
	Collapse strength	Full plastic strength	General yield strength	COF		Collapse strength	Full plastic strength	General yield strength	$P_{u\text{-}FEA}/P_{u\text{-}EXP}$	$P_{p\text{-}FEA}/P_{p\text{-}EXP}$	$P_{y\text{-}FEA}/P_{y\text{-}EXP}$
	$P_{u\text{-}EXP}$ (kN)	$P_{p\text{-}EXP}$ (kN)	$P_{y\text{-}EXP}$ (kN)	μ_1	μ_2	$P_{u\text{-}FEA}$ (kN)	$P_{p\text{-}FEA}$ (kN)	$P_{y\text{-}FEA}$ (kN)			
26	182.4	165.2	160.1	0.16	0.20	189.0	170.5	160.0	1.04	1.03	1.00
27	342.3	287.5	260.0	0.23		328.6	273.5	242.4	0.96	0.95	0.93
28	420.0	333.3	293.3	0.26		413.8	395.0	309.3	0.99	1.19	1.05
29	277.0	257.0	230.4	0.22		270.1	257.0	244.6	0.97	1.00	1.06
30	509.0	417.9	356.4	0.35		503.3	467.3	359.7	0.99	1.12	1.01
35	530.6	484.5	428.6	0.50		432.6	400.0	388.2	0.82	0.83	0.91
37	472.7	432.0	338.0	0.27		469.0	431.4	328.8	0.99	1.00	0.97
Avg.				0.28					0.97	1.02	0.99
COV				0.39					0.07	0.11	0.06

Note: μ_1 is the friction coefficient in the contact region between cone and cylinder.
μ_2 is the friction coefficient in the contact region between cylinder and ring.

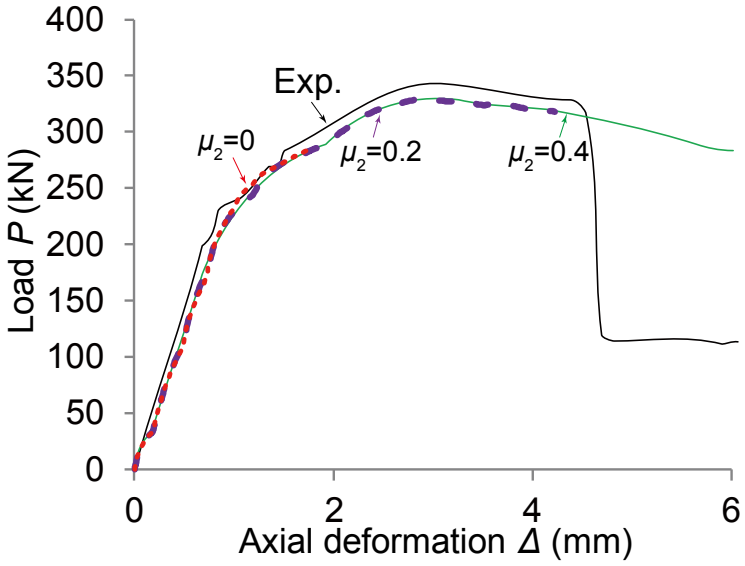

Fig. 4-5 Comparison of load versus axial deformation curves for model No.27 with different friction coefficients μ_2 in the contact region between ring and cylinder

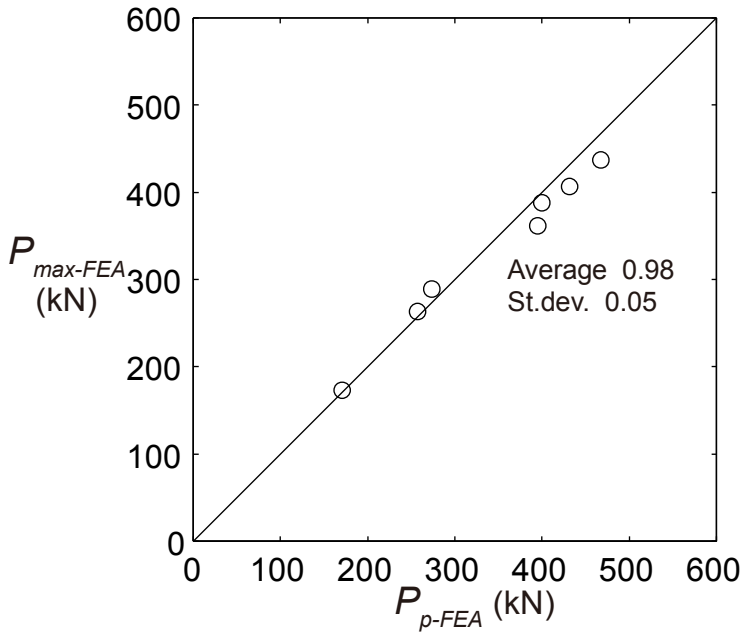

Fig. 4-6 Comparison of maximum strength to full plastic strength of models with tapered ring failure

Fig. 4-7 Ultimate behavior of tapered ring in experimental specimen No. 35

In addition, the load versus axial deformation curves and ultimate deformation of FE models are compared with the relevant experimental results, as shown in Appendix B. The effectiveness of FE models is validated. However, it should be mentioned that the strength of model No.35 obtained by FEA are much smaller than those from experiment even if μ_1 is set to be 0.5, which is already a quite large value for general surface made of mild steel. The ultimate behavior of tapered ring in experimental specimen No. 35 is shown in Fig. 4-7. It can be seen that tapered ring upward rotated to contact with conical wall finally. The confinement effect of ring simulated in FE model No. 35 might be

smaller than that in experimental specimen.

4.2.3 Discussion on Friction Coefficient for Practical Design

As stated in section 4.2.2, the friction coefficient between cone and cylinder is somewhat greater than that of models with cylinder edge failure. The latter is advised to be 0.2 for practical design. In order to make the design work a little simpler and more convenient, it is also assumed that $\mu_1 = 0.20$ for models with tapered ring failure.

The strength in FEA is then compared with experimental results. The ratios are listed in Table 4-2. It is found that the averages of ratios are 0.84, 0.87 and 0.92, for collapse strength, full plastic strength and general yield strength respectively. The values of COV are all about 0.2, because the ratios of model No. 35 are much smaller than others. The prediction of strength by assuming $\mu_1 = 0.20$ can be acceptable in practical design.

Table 4-2 Comparison of strength between FEA and experiments by assuming $\mu_1 = 0.20$ for models with tapered ring failure

Model NO.	Experiments			FEA					Comparison		
	Collapse strength	Full plastic strength	General yield strength	COF		Collapse strength	Full plastic strength	General yield strength	$P_{u\text{-}FEA}/P_{u\text{-}EXP}$	$P_{p\text{-}FEA}/P_{p\text{-}EXP}$	$P_{y\text{-}FEA}/P_{y\text{-}EXP}$
	$P_{u\text{-}EXP}$	$P_{p\text{-}EXP}$	$P_{y\text{-}EXP}$	μ_1	μ_2	$P_{u\text{-}FEA}$	$P_{p\text{-}FEA}$	$P_{y\text{-}FEA}$			
	(kN)	(kN)	(kN)			(kN)	(kN)	(kN)			
26	182.4	165.2	160.1	0.20	0.20	203.5	186.2	181.0	1.12	1.13	1.13
27	342.3	287.5	260.0			305.9	260.0	236.8	0.89	0.90	1.01
28	420.0	333.3	293.3			357.3	313.8	287.5	0.85	0.94	0.91
29	277.0	257.0	230.4			260.0	252.6	236.5	0.94	0.98	1.03
30	509.0	417.9	356.4			369.3	319.7	300.0	0.73	0.77	0.84
35	530.6	484.5	428.6			276.9	250.0	240.7	0.52	0.52	0.56
37	472.7	432.0	338.0			407.1	381.2	307.8	0.86	0.88	0.92
Avg.									0.84	0.87	0.92
COV									0.18	0.19	0.18

Note: μ_1 is the friction coefficient in the contact region between cone and cylinder.
μ_2 is the friction coefficient in the contact region between cylinder and ring.

4.3 FE Analysis Results

4.3.1 Distributions of Stress Resultants

Model No.27 is taken as a typical case to investigate the changing distributions of stress resultants. Based on the results in Chapter 3, it has been known that for cylindrical wall, n_x can be assumed to be distributed uniformly along axial direction at each load, but the changing distributions of n_θ are a little difficult to assimilate due to the interaction among it with other stress resultants. Thus in this chapter, changing distributions of axial bending moment m_x and shear stress resultant q_{rx} in cylindrical wall, at general yield load P_y, full plastic load P_p and ultimate load P_u respectively, are focused. Then, the hoop stress distribution in tapered ring is also analyzed.

The definitions of Sects. A and B are the same as those introduced in section 3.3.2. As shown in Fig. 4-8(a), $|m_x|$ in each section increases as load increases, especially near Sect. B. As shown in Fig. 4-8(b), the values of q_{rx} at P_y and P_p decreases almost in a straight line from Sect. A to Sect. B. But its distribution at P_u has a quite different type. The value of q_{rx} at P_u in Sect. A is much larger than those at P_y and P_p. It decreases rapidly to a value which turns to be smaller than those at P_y and P_p. The reason is explained as follow.

Figure 4-9 shows the changing distributions of resistance zone by ring under increasing load. It can be found that for the cases of both P_y and P_p, the resistance zones by ring are almost at the top of cylindrical wall and a little higher than Sect. A. But it becomes a little lower than Sect. A when Pu arrives. Thus, shear stress resultant in Sect. A at P_y or P_p only includes the value produced in cylindrical wall. While, when P_u arrives, it also includes the radial resistance by tapered ring. In addition, it can be seen that the bottom edge of tapered ring does not contact with cylindrical wall when P_u arrives because the radial stress s_r is very small.

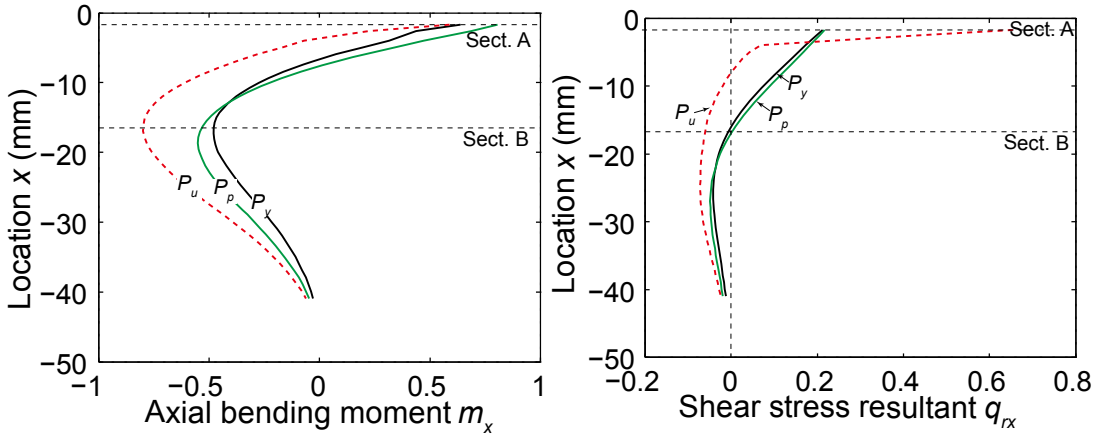

(a) Axial bending moment (b) Shear stress resultant

Fig. 4-8 Changing distributions of stress resultants under increasing load for model No.27

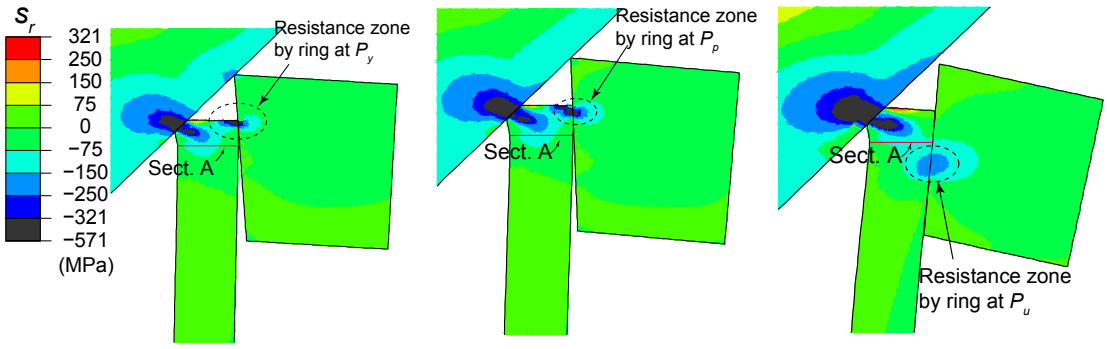

(a) At P_y (b) At P_p (c) At P_u

Fig. 4-9 Changing distributions of resistance zone by the ring under increasing load for model No.27

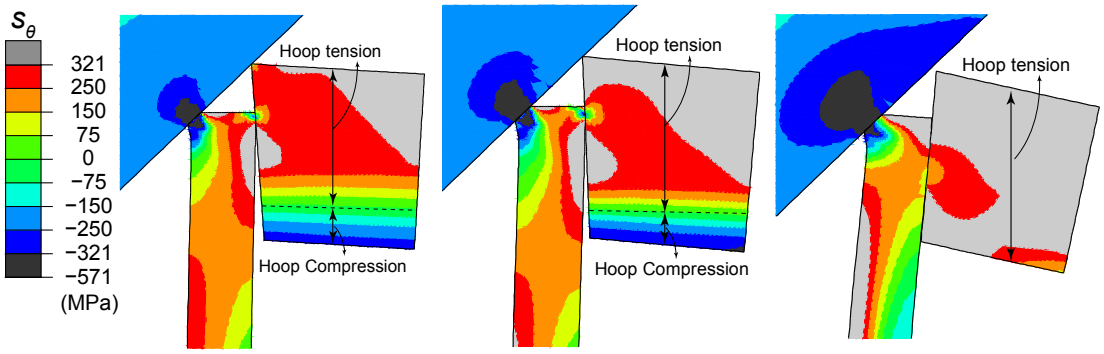

(b) At P_y (b) At P_p (c) At P_u

Fig. 4-10 Changing distributions of hoop stress in the ring under increasing load for model No.27

Figure 4-10 shows the changing distributions of hoop stress in the tapered ring under

increasing load. It is seen that at both P_y and P_p, the region near to bottom edge is under hoop compression, because it rotates downward when expanding outward. However, when P_u arrives, the whole section becomes under hoop tension.

4.3.2 Distributions of Ultimate Deformation

The ultimate behavior of the top edge of cylinder and tapered ring in model No.27 is illustrated in Fig. 4-11. It can be found that the out of plane bending deformation of cylinder edge makes the tapered ring rotate downward.

The ultimate radial deformation in the region AB for model Nos. 26, 27 and 28 are shown in Fig. 4-12. Model No. 4 without the confinement by ring is employed as a comparison. It is found as the thickness of ting increases, the radial deformation will become greater. But the ratios of w_{ruA} in sect. A to the length L of region AB are smaller than 0.1, the rotation of cylinder edge could be analyzed based on the assumption of small deformation theory.

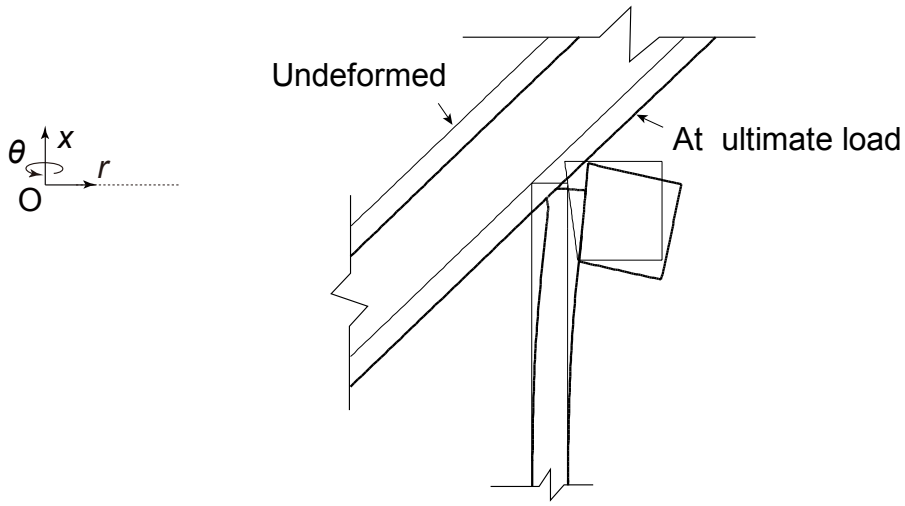

Fig. 4-11 Ultimate deformation of cylinder edge and tapered ring in model No.27

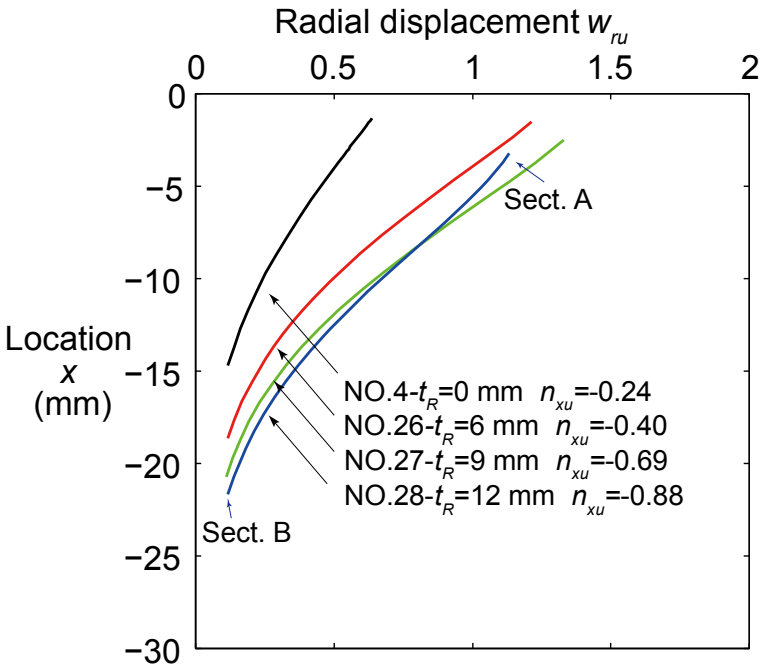

Fig. 4-12 Ultimate radial displacement distribution along *x* direction for models with different kinds of ring

4.4 Judgement of Failure Modes

4.4.1 Definition of the Criteria of Failure Mode

The proposed criterion for plastic collapse of cylindrical wall is the same as that introduced in section 3.4.1. For tapered ring, another way for defining the failure mode is employed.

When the open mouth of cylinder expands like a trumpet, the ring mainly sustains hoop tension. The ratio of its average hoop stress $\bar{s}_{\theta R}$ to yield stress σ_{yR} is defined as

$$k = \frac{\bar{s}_{\theta R}}{\sigma_{yR}} \tag{4-1}$$

If $k \approx 1.0$, hoop tension failure is assumed to occur in tapered ring. It should be noted that

(1) Because of strain hardening effect of materials, k_u at ultimate load is possible to exceed 1.0.

(2) From the engineering point of view, $k_u \geq 0.8$ at ultimate load is acceptable for the determination of hoop tension failure.

4.4.2 Failure Mode of Models

Figure 4-13 shows the changing distributions of ratio r at P_y, P_p and P_u in the cylindrical wall of model No.27. It is found that r increases as the load increases for each section. The r in Sect. B at P_u becomes a little larger than 1.0. It indicates that a plastic hinge forms there.

The values of r in Sect. B for all the models with tapered ring failure are listed in Fig. 4-14. It is seen that all the data are close to 1.0. Therefore, the failure of cylinder edge can be assumed to be controlled by "plastic collapse mechanism".

In addition, Fig. 4-15 shows the values of ratio k_u at ultimate load defined in Eq. (4-1) for all the models. It is seen that most of them are larger than 1.0 except for model No. 28, which is 0.88. The hoop stress distribution in tapered ring of model No. 28 is shown in Fig. 4-16. It is found that the region near to the bottom edge of ring is still under hoop compression, even if P_u arrives. It is the reason why k_u of No. 28 is smaller than 1.0. But as the k_u of No. 28 is greater than 0.80, it can be assumed that the failure of tapered rings is controlled by "Hoop tension mechanism". The proposed failure mode for models with tapered ring failure is shown in Fig. 4-17.

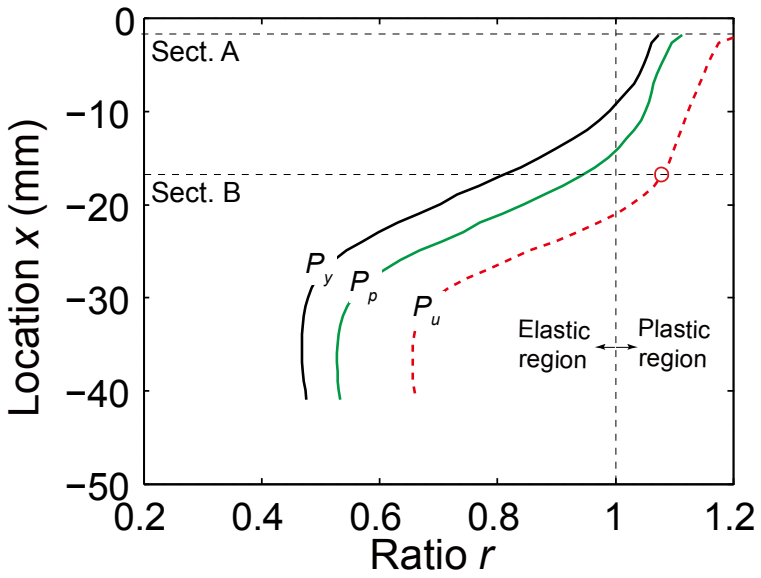

Fig. 4-13 Changing distributions of average equivalent stress in cylindrical walls under increasing load for model No. 27

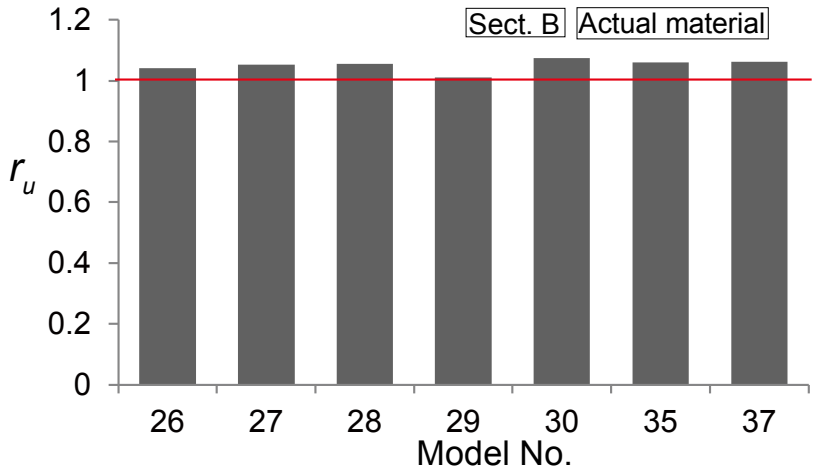

Fig. 4-14 Ratios of average equivalent stress to yield stress at ultimate load in Sect. B of models with actual material

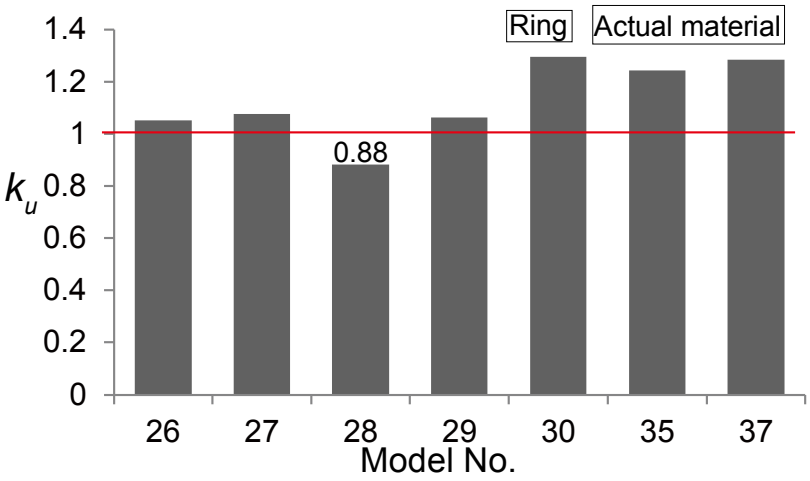

Fig. 4-15 Ratios of average hoop stress to yield stress at ultimate load in the rings of models with actual material

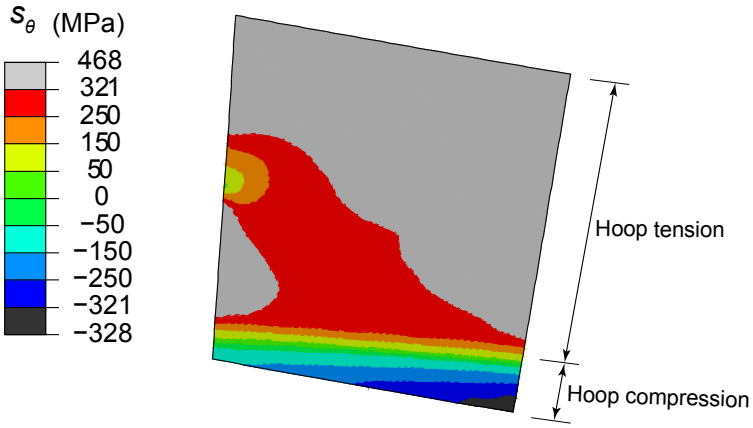

Fig. 4-16 Hoop stress distribution in the ring of model No.28 at ultimate load

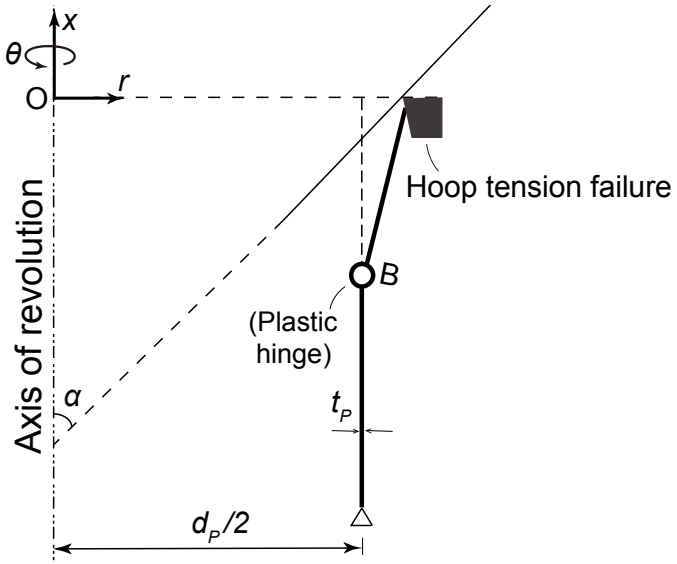

Fig. 4-17 Proposed failure mode for models with tapered ring failure

4.5 Predictions of Strength

4.5.1 Prediction of Full Plastic Strength

4.5.1.1 Proposed Plastic Collapse Mechanism

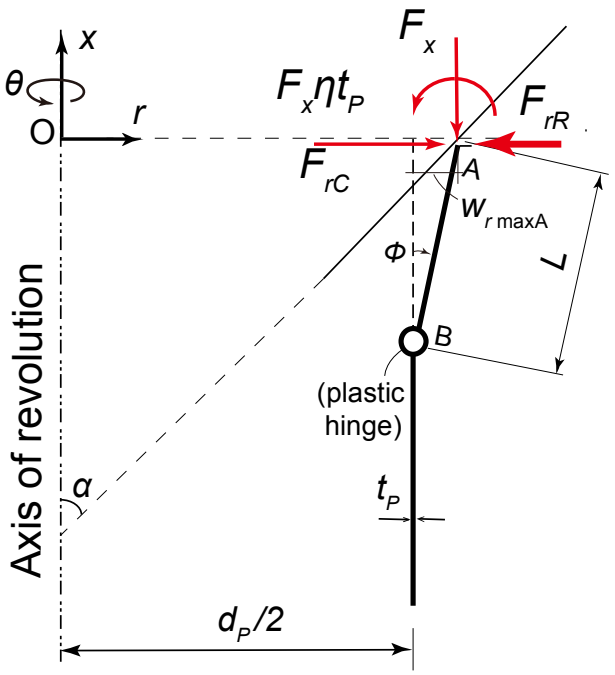

Fig. 4-18 External forces in plastic collapse mechanism for models with tapered ring failure

The external forces in plastic collapse mechanism for models with tapered ring failure is shown in Fig. 4-18. The limit analysis for models with perfectly plastic material is undertaken to derive the maximum strength. The resistance of tapered ring is simplified to be radial reaction force F_{rC}. The external forces of $\{F_{rC}, F_{rR}, F_x, F_x\eta t_P\}$ are assumed to be applied in Sect. A. It should be noted they are defined to be acted in 360 degrees in hoop direction. The distance between Sect. A and the resistance zone by ring is neglected. A plastic hinge with a rotation angle ϕ is assumed to occur in Sect. B. The F_{rC} and F_x are the radial force and axial force transmitted from conical wall respectively. The $F_x\eta t_P$ is the axial bending moment because of the eccentricity of F_x. The value of eccentricity

ratio η is simplified to be a constant of -0.20, which is the same as that in section 3.5.2.

The equilibrium for external forces is given by

$$F_{rC} = -\frac{1-\mu\tan\alpha}{\tan\alpha+\mu}F_x \tag{4-2}$$

The F_{rR} is obtained by

$$F_{rR} = \frac{2\sigma_{\theta\max R}A_R}{d_R} \tag{4-3}$$

Herein, d_R is the center-to-center diameter of ring, A_R is the sectional area of ring, and $\sigma_{\theta\max R}$ is assumed to be equal to σ_{yR}.

4.5.1.2 Proposed Formula for Full Plastic Strength

Based on the principle of virtual work, the equilibrium of external work $\mathrm{d}W$ and dissipation of internal energy $\mathrm{d}U$ for the whole mechanism in 360 degrees in hoop direction during a virtual change of rotation $\mathrm{d}\phi$ is given by

$$\mathrm{d}U=\mathrm{d}W \tag{4-4}$$

where

$$dU = dU_1 + dU_2 + dU_3$$

$$dW = dW_1 + dW_2 + dW_3$$

Herein, for internal energy, dU_1 is done by hoop stress resultant $n_{\theta\max\mathrm{AB}}\sigma_{yP}t_P$ in segment AB, dU_2 is done by axial stress resultant $n_{x\max}\sigma_{yP}t_P$ in segment AB and dU_3 is done by axial bending moment $m_{x\max\mathrm{B}}\frac{1}{4}\sigma_{yP}t_P^2$ at plastic hinge B; For external work, dW_1 is done by radial forces F_{rC} and F_{rR}, dW_2 is done by axial force F_x, and dW_3 is done by axial bending moment $F_x\eta t_P$.

The derivation process for Eq. (4-4) is the same as that introduced in section 3.5.2

and is omitted here. Based on small deformation theory, $\sin\phi=\phi$ and $\cos\phi=1$. The general equation based on Eq. (4-4) can be obtained.

$$\left(F_{rC}-F_{rR}\right)L-F_xL\phi-F_x\eta t_P=\pi n_{\theta\max\mathrm{AB}}\sigma_{yP}t_PL^2-\pi d_Pm_{x\max\mathrm{B}}\frac{1}{4}\sigma_{yP}t_P^2 \qquad (4\text{-}5)$$

Dividing the both sides of Eq. (4-5) by L and substituting $F_x=-P_{\max}$ into Eq. (4-5), F_{rC} can be expressed as

$$F_{rC}=\pi n_{\theta\max\mathrm{AB}}\sigma_{yP}t_PL+\frac{-\pi d_Pm_{x\max\mathrm{B}}\sigma_{yP}t_P^2-4\eta F_xt_P}{4L}-\phi P_{\max}+F_{rR} \qquad (4\text{-}6)$$

Based on upper bound theorem, F_{rC} can be obtained by $\frac{\mathrm{d}F_{rC}}{\mathrm{d}L}=0$. Thus,

$$F_{rC}=\sqrt{-m_{x\max\mathrm{B}}-4\eta n_{x\max}}\sqrt{n_{\theta\max\mathrm{AB}}}\sqrt{\frac{t_P}{d_P}}\sigma_{yP}t_P-\phi P_{\max}+F_{rR} \qquad (4\text{-}7)$$

where, $\eta=-0.20$.

The length of plastic region L is given by

$$L=\sqrt{\frac{-m_{x\max\mathrm{B}}-4\eta n_{x\max}}{4n_{\theta\max\mathrm{AB}}}}\sqrt{d_Pt_P} \qquad (4\text{-}8)$$

The interaction of stress resultants is assumed as follow, which is the similar to that in the failure mechanism of cylinder edge failure introduced in section 3.5.2.

For segment AB: $$n_{\theta\max\mathrm{AB}}=\frac{1}{2}n_{x\max}+\sqrt{1-\frac{3}{4}n_{x\max}^2} \qquad (4\text{-}9)$$

For plastic hinge B: $$m_{x\max\mathrm{B}}=-\frac{2}{\sqrt{3}}(1-\frac{3}{4}n_{x\max}^2) \qquad (4\text{-}10)$$

Substituting Eqs. (4-2), (4-3), (4-9) and (4-10) into Eq. (4-7) and then dividing the both sides of Eq. (4-7), $n_{x\max}$ can be expressed by two parts, one is induced by cylindrical wall, and the other by tapered ring.

$$n_{x\max}=n_{x\max P}+n_{x\max R}=-\psi\cdot\gamma\cdot\chi-\beta\cdot\gamma\cdot\chi \qquad (4\text{-}11)$$

Herein, the parameters of ψ, γ, and χ are expressed in the same equations as those in section 3.5.2.

$$\psi = \sqrt{\frac{2}{\sqrt{3}}(1-\frac{3}{4}n_{x\max}^2)-0.8n_{x\max}}\sqrt{\frac{1}{2}n_{x\max}+\sqrt{1-\frac{3}{4}n_{x\max}^2}} \tag{4-12}$$

$$\gamma = \frac{\frac{1-\mu\tan\alpha}{\tan\alpha+\mu}}{\frac{1-\mu\tan\alpha}{\tan\alpha+\mu}+\phi} \tag{4-13}$$

$$\chi = \sqrt{\frac{t_P}{d_P}}\frac{\tan\alpha+\mu}{1-\mu\tan\alpha} \tag{4-14}$$

The β is the reinforcement factor of tapered ring on the maximum strength of models.

$$\beta = \frac{d_P}{d_R}\frac{2\sigma_{yR}A_R}{\sigma_{yP}t_P\sqrt{d_P t_P}} \tag{4-15}$$

The ψ is approximated in the following quadratic equation

$$\psi = -0.87n_{x\max}^2 - 0.16n_{x\max} + 1.07 \tag{4-16}$$

In addition, the relationship between γ and ϕ for all the models with tapered ring failure is shown in Fig. 4-19. It can be found that γ almost keeps being constant as ϕ increases. It is simplified to be the average of 0.92 in this study.

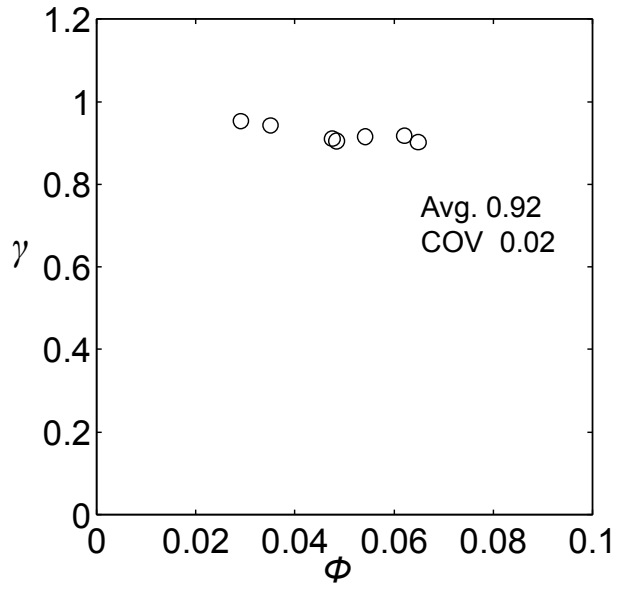

Fig. 4-19 Variation of factor γ with ϕ for models with tapered ring failure

Substituting Eq. (4-16) and $\gamma = 0.92$ into Eq. (4-11), the variation of $n_{x\max}$ with the parameters of β and χ is expressed in a quadratic equation.

$$n_{x\max} = \left(0.80 n_{x\max}^2 + 0.15 n_{x\max} - 0.98\right)\chi - 0.92\beta \cdot \chi \tag{4-17}$$

Its solution is

$$n_{x\max} = \frac{-0.15\chi + 1 - \sqrt{3.16\chi^2 - 0.3\chi + 1 + 2.9\chi^2\beta}}{1.6\chi} \tag{4-18}$$

Prediction of the maximum strength $P_{\max}$ of models is finally obtained as

$$P_{\max\_PRED} = \frac{0.15\chi - 1 + \sqrt{3.16\chi^2 - 0.3\chi + 1 + 2.9\chi^2\beta}}{1.6\chi}\pi d_P t_P \sigma_{yP} \tag{4-19}$$

Comparison of $P_{\max\_PRED}$ expressed in Eq. (4-19) with the maximum strength $P_{\max\_FEA}$ of models is shown in Fig. 4-20. It can be found that the average of ratios is 1.02 with a COV of 0.09. Well prediction of maximum strength is obtained. But it should be mentioned that because the average hoop stress $\sigma_{\theta\max R}$ in tapered ring at maximum load for model No. 28 is smaller than yield stress, assuming $\sigma_{\theta\max R}$ to be equal to σ_{yR} will overestimated the strength of models. It means that the reinforcement effect of tapered ring on the maximum strength of connections would reach the highest limit, even though the thickness of ring in vertical direction increases. It should be noticed in practical design work.

Full plastic strength of models can be obtained as

$$P_{p\_\mathrm{PRED}} = P_{\max\_\mathrm{PRED}} = \frac{0.15\chi - 1 + \sqrt{3.16\chi^2 - 0.3\chi + 1 + 2.9\chi^2\beta}}{1.6\chi}\pi d_P t_P \sigma_{yP} \tag{4-20}$$

Comparison of P_{p_PRED} with the full plastic strength P_{p_EXP} of experimental specimens is shown in Fig. 4-21. It can be found that the average of ratios is 1.02 with a COV of 0.16. Well prediction of full plastic strength for connections with tapered ring

failure is obtained.

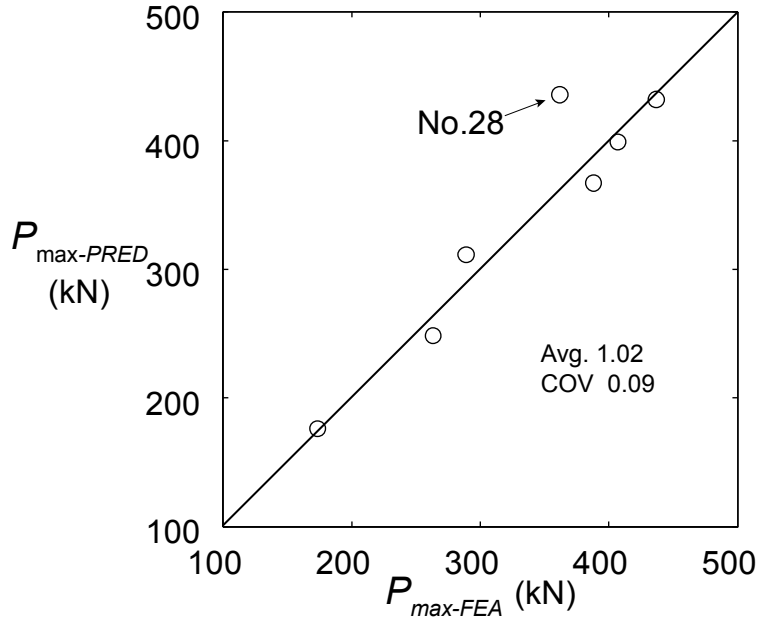

Fig. 4-20 Comparison of predicted maximum strength of models with FEA results

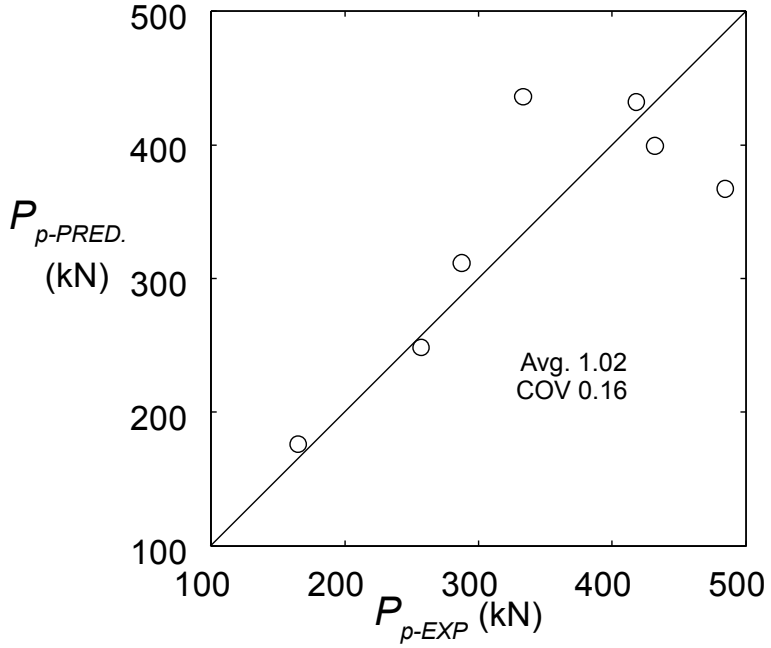

Fig. 4-21 Comparison of predicted full plastic strength of specimens with experimental results

4.5.2 Discussion on Reinforcement Effect of Tapered Ring on Strength of models

Model Nos. 4, 26, 27 and 28 are employed to discuss the reinforcement effect of tapered ring on the maximum strength of models. The thickness of ring is 0mm, 6mm, 9mm, and 12mm, respectively.

Figure 4-22 shows the values of reinforcement factor β and maximum axial stress resultant of them. Especially, for model No. 4, $\beta = 0$, which means tapered ring is not employed. For other models, as the thickness of ring increases, β increases rapidly. Meanwhile, the load carrying capacity of models also becomes greater. The larger the value of β, the greater is $n_{x\max R}$ while the smaller is $n_{x\max P}$. The latter is because of the influence of high axial stress resultant on the failure mechanism of cylindrical wall.

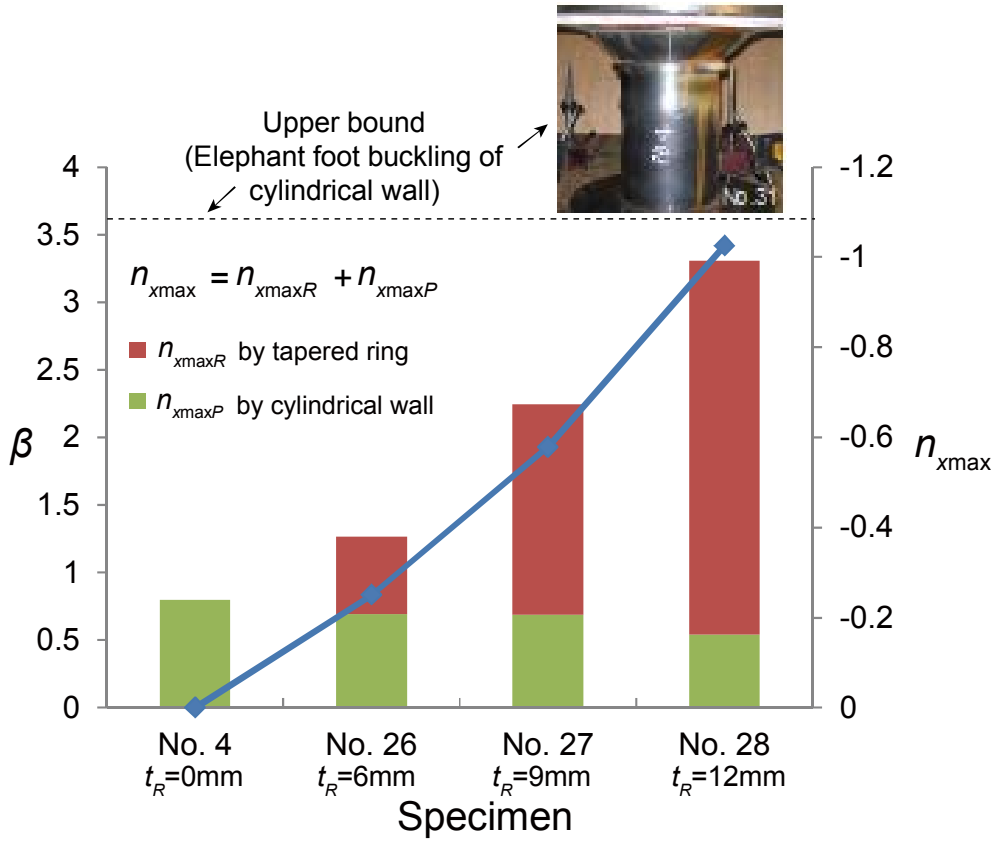

Fig. 4-22 Reinforcement effect of ring on the maximum strength of models with tapered ring failure

However, as stated above, it is found that not the whole section plays a role on the reinforcement effect on strength when the thickness of ring increases to some limit value. In addition, if axial stress resultant in cylindrical wall increases to be very great, unstable phenomenon, for example, the "elephant foot buckling" as observed in experimental specimen No. 31, will occur before tapered ring failure. The prediction of elephant foot buckling of cylindrical wall needs to be studied in future.

4.5.3 Prediction of Collapse Strength

The collapse strength of models is predicted in the same way as that in Chapter 3. The enhancement factor ρ is assumed as the average of the ratios of collapse strength to full plastic strength for both experimental specimens and FEA models. Their average is 1.13 with a small COV of 0.06, as shown in Fig. 4-23. Collapse strength P_u is predicted by

$$P_{u\text{-}PRED} = \rho P_{p-PRED} \tag{4-21}$$

where, $\rho = 1.13$.

The predicted values of collapse strength of P_u in Eq. (4-21) are compared with those by the previous formula (Fujimoto et al. 2005). The ratios of them to the experimental results are shown in Fig. 4-24. It can be found that the average of the ratios in the case of the proposed formula in Eq. (4-21) is 0.99 with a small COV of 0.13, much smaller than that by the previous one. Better prediction is obtained by the proposed method.

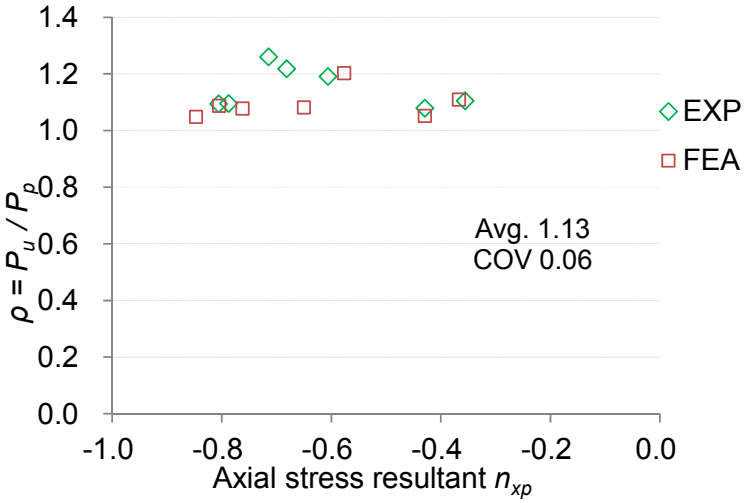

Fig. 4-23 Ratios of P_u to P_p for both experimental specimens and FEA models with tapered ring failure

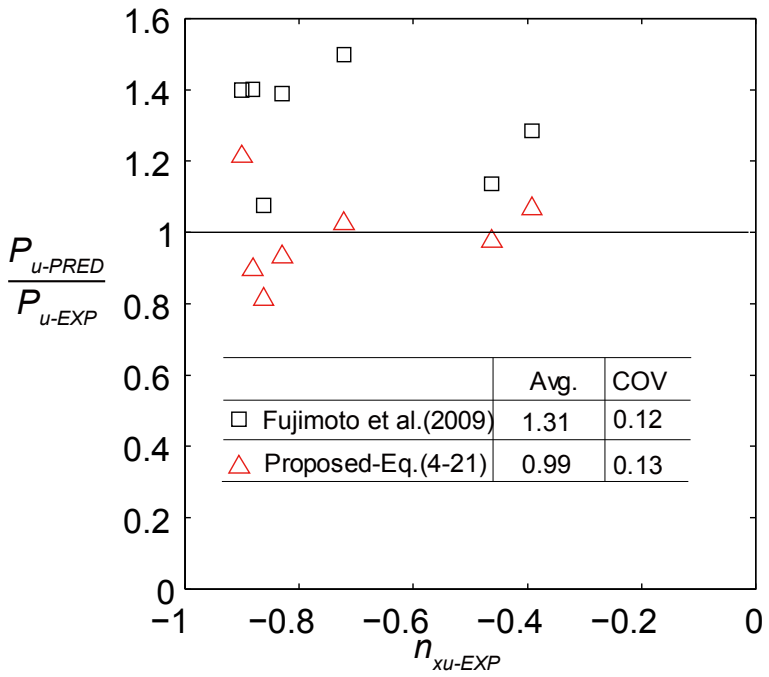

Fig. 4-24 Comparison of collapse strength between the proposed formula with the previous one for models with tapered ring failure

4.5.4 Prediction of General Yield Strength

The general yield strength of models with actual material is also predicted in the same way as that in Chapter 3. The reduction factor ξ is assumed as the ratios of general yield strength P_y to plastic strength P_p for both experimental results and FEA results. The

ratios are listed in Fig. 4-25. It can be found that the average is 0.87 with a small COV of 0.08. The prediction of general yield strength P_y is obtained by

$$P_{y\text{-}PRED} = \xi P_{p-PRED} \tag{4-22}$$

where, $\xi = 0.87$.

The predicted results are compared with those in experiments, as shown in Fig. 4-26. It can be seen that the average of the ratios is 1.00 with a small COV of 0.16. The formula in Eq. (4-22) can predict well the general yield strength of specimens.

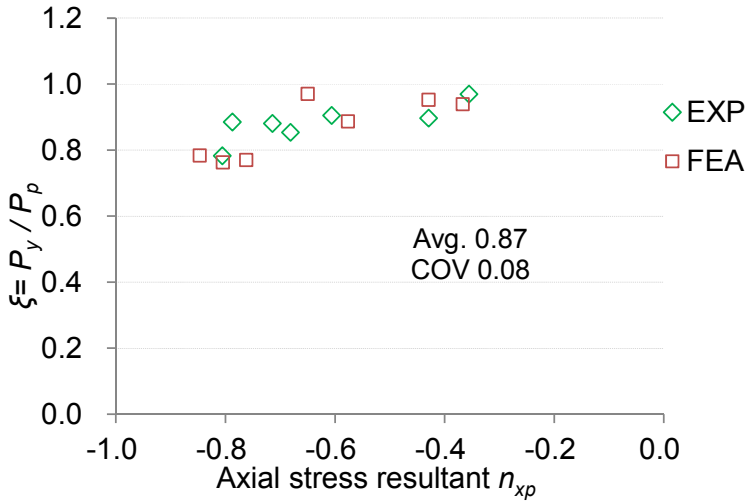

Fig. 4-25 Ratios of P_y to P_p for both experimental and FEA results for models with tapered ring failure

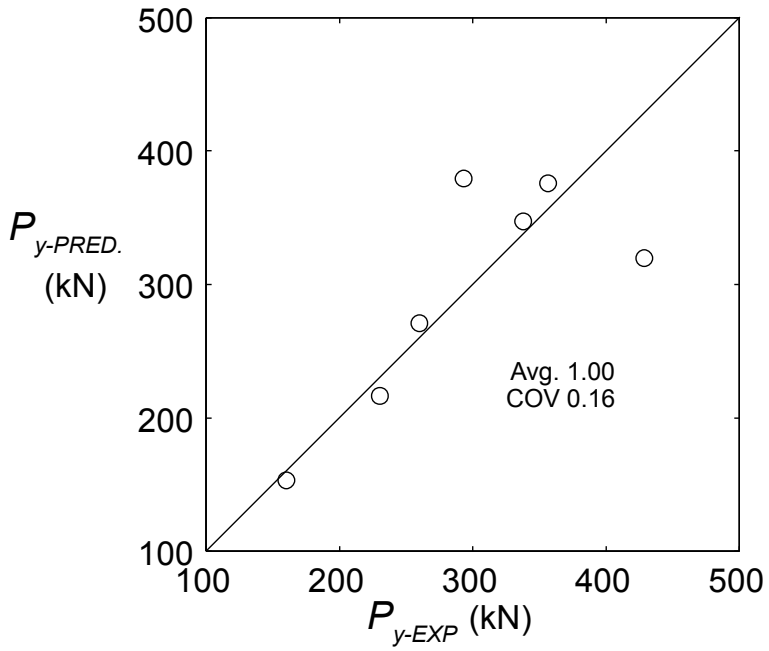

Fig. 4-26 Comparison of predicted general yield strength of specimens with experimental results for models with tapered ring failure

4.6 Summaries

This chapter focuses on the prediction of the strength of models with tapered ring failure. Based on the above analysis, the following conclusions are obtained.

(1) The value of friction coefficient between cone and cylinder can be simplified to be 0.2 for practical design work, like that of models with cylinder edge failure. The friction between cylinder and tapered ring has no effect on the strength of models.

(2) The failure of the models is not only controlled by "hoop tension" of tapered ring, but also by "plastic collapse" of cylindrical shell.

(3) Effective and Easy-to-use formulae for predicting the full plastic strength is derived by limit analysis. The reinforcement effect of tapered ring is found to be obvious, by increasing its thickness. However, it is necessary to be noticed that as the axial stress resultant of cylindrical wall increases to reach some limit value, another failure mechanism, for example, "elephant foot buckling" of cylindrical shell will occur. It was already observed from the experiments.

(4) The prediction of collapse and general yield strength of experimental specimens is proposed based on the formula for full plastic strength. Well agreement is found between them and the experimental results.

CHAPTER 5 STRENGTH OF METAL TOUCH CONNECTIONS WITH CONICAL WALL FAILURE

5.1 Introduction

For the strength of the metal touch connections with conical wall failure, Kuwamura et al. (2005a) proposed a theoretical solution for elastic limit strength of conical wall from bending theory of shells (Timoshenko 1940). The formula is complicated and not suitable in practice. After then, Tomioka (2006) proposed an empirical formula for yield strength based on the experimental results. Multiplying it by some factors, full plastic strength and collapse strength of connections were then predicted. The results were found to be more easy-to-use but the theoretical background is much weaker than previous ones. Moreover, the friction coefficient between cone and cylinder was set to be 1.0, which needs further investigation.

In this chapter, solid axisymmetric FEA models are first created and validated by comparing their strength and deformation with experimental results. The friction property in the contact region between cone and cylinder is discussed. Then, FEA is undertaken to investigate the distributions of stress resultants and deformations. The failure mode is determined by the proposed criterion. Full plastic strength of models is derived by limit analysis. Then, collapse strength and general yield strength are obtained based on the formula for full plastic strength. Finally, their precision is validated by comparing them with the experimental and FEA results.

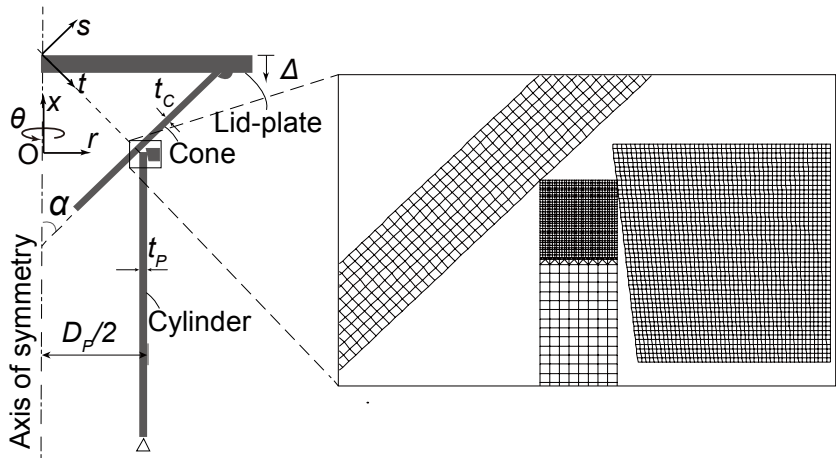

Fig. 5-1 Details of axisymmetric solid FEA models with conical wall failure

5.2 FE Modeling

5.2.1 General

Figure 5-1 illustrates the details of axisymmetric solid model for specimens with conical wall failure. Two coordinates, (r, θ, x) and (t, θ, s), are employed for conical shells, in which t means normal direction and s means meridional direction. The mesh size for conical walls is set to be 0.5mm, which is the same as that in the general region of cylindrical walls. The convergence of analysis results is verified.

Figure 5-2 shows the stress-strain curves of mild steel used in conical wall. The material properties of conical shells with thicknesses of 3.2 and 6mm were not measured in coupon tests. They are assumed to be the same as those of conical shell with thickness of 4.5mm. Figure 5-3 gives true stress s and equivalent plastic strain e_p curves of conical walls with thickness of 4.5 mm and 9.0 mm, for both actual strain-hardening materials and perfectly-elastic plastic material which will be used in the later analysis.

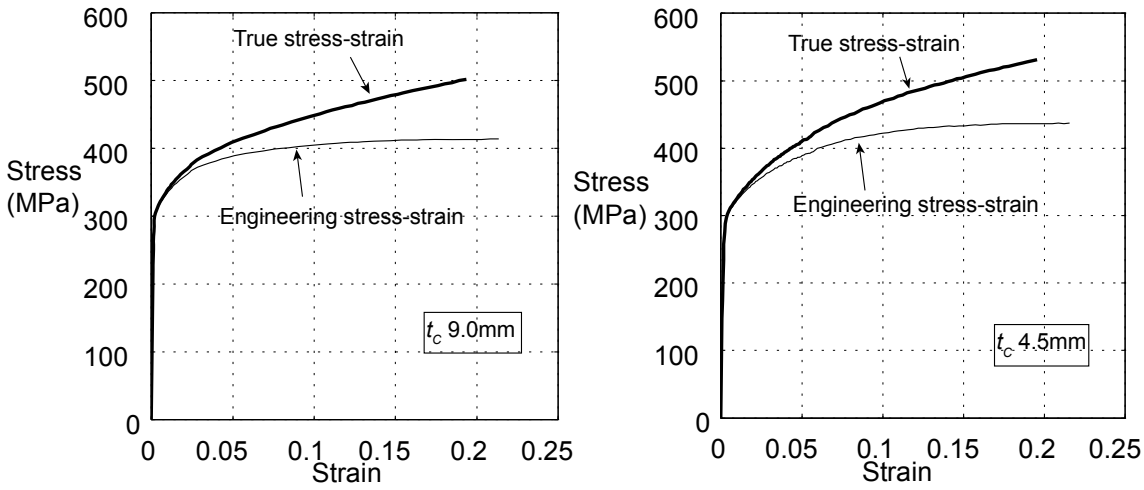

Fig. 5-2 True stress-strain curves for material SS400 of conical shells

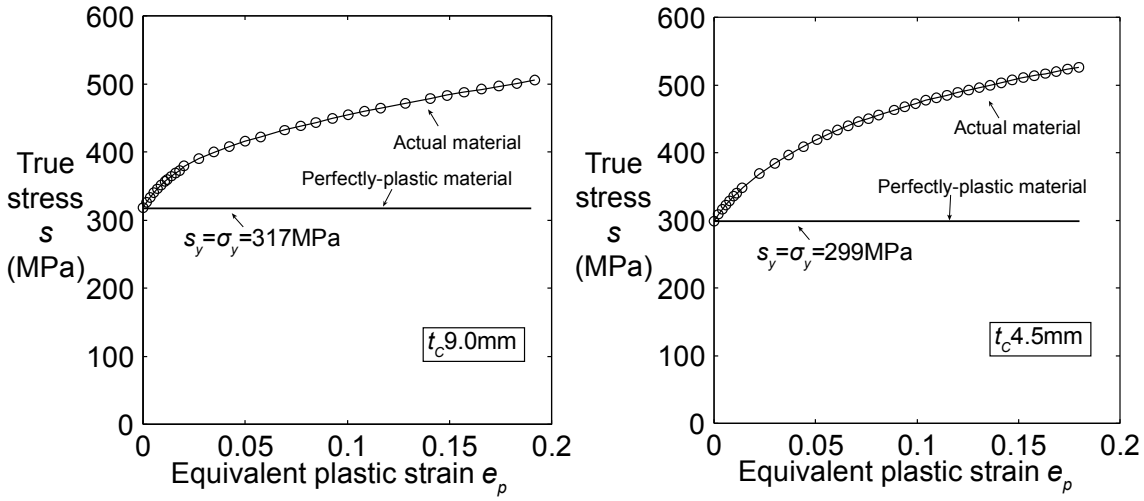

Fig. 5-3 s~e_p curves input in ABAQUS for materials of conical walls

5.2.2 Effectiveness of FE Models

Table 5-1 gives the comparison of the strength of FE models with that of experimental specimens. Friction coefficient μ is assumed to be a constant during the whole deformation process. The value of μ is determined by the following way.

The variation of collapse strength in FEA along with the increase of friction coefficient μ_1 in the contact surface between cone and cylinder is shown in Fig. 5-4. It is found that the correlation between each other is not significant, comparing with those of models with cylinder edge failure and tapered ring failure.

The collapse strength of FE model becomes about equal to that of experimental specimen by calibrating the value of μ_1. It should be noted that the upper bound of the value of μ_1 is set to be 0.50. As a result, the average of μ_1 is 0.43, with a COV of 0.27. It is much larger than those of models with cylinder edge failure and tapered ring failure. The reason might be that large plastic deformation of conical wall destroyed its oxide film and then made the contact surface rougher than those of models with cylinder edge failure and tapered ring failure. In addition, as friction coefficient μ_2 in the contact surface between cylinder and ring has no effect on the strength of specimen, it is set to be 0.20 in order to keep the iteration procedure convergent.

Full plastic strength and general yield strength of FE models are then compared with those of experimental specimens. It is found that the averages of the ratios are 0.94 for full plastic strength and 0.99 for general yield strength, with the COV of 0.09 and 0.14 respectively. The strength of conical wall failure can be predicted well with a constant value of μ_1 for each model.

In addition, the load versus axial deformation curves and ultimate deformation of FE models are compared with the relevant experimental results, as shown in Appendix B. The effectiveness of FE models is verified.

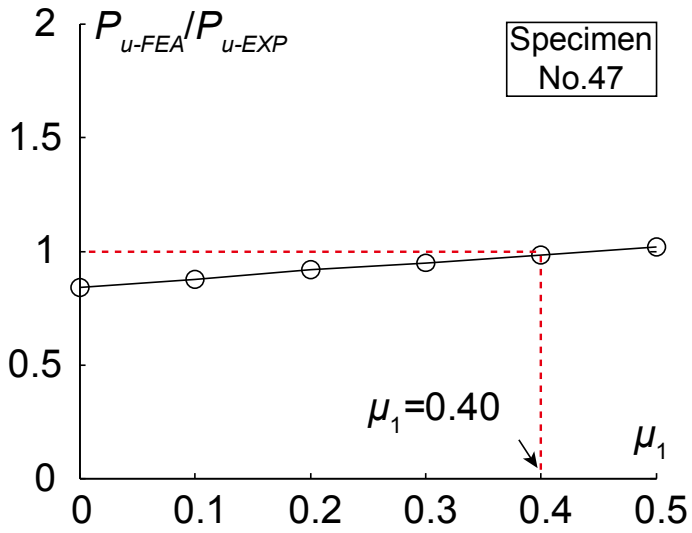

Fig. 5-4 Variation of collapse strength of models with conical wall failure along with the increase of friction coefficient between conical wall and cylinder edge

Table 5-1 Comparison of strength of FE models with those of experimental ones

Model NO.	Experiments			FEA					Comparison		
	Collapse strength	Full plastic strength	General yield strength	COF		Collapse strength	Full plastic strength	General yield strength	$P_{u\text{-}FEA}/P_{u\text{-}EXP}$	$P_{p\text{-}FEA}/P_{p\text{-}EXP}$	$P_{y\text{-}FEA}/P_{y\text{-}EXP}$
	$P_{u\text{-}EXP.}$	$P_{p\text{-}EXP.}$	$P_{y\text{-}EXP.}$	μ_1	μ_2	$P_{u\text{-}FEA}$	$P_{p\text{-}FEA}$	$P_{y\text{-}FEA}$			
	(kN)	(kN)	(kN)			(kN)	(kN)	(kN)			
9	601.2	561.5	482.6	0.18	0.20	614.2	525.4	481.8	1.02	0.94	1.00
34	872.8	620.0	543.8	0.50		873.6	688.9	636.4	1.00	1.11	1.17
36	625.7	527.3	390.9	0.50		581.8	500.0	451.5	0.93	0.95	1.16
43	234.9	153.6	139.1	0.50		206.3	141.9	127.5	0.88	0.92	0.92
44	389.9	294.7	263.0	0.50		358.1	232.6	206.5	0.92	0.79	0.79
46	178.4	158.7	127.5	0.50		161.9	140.5	118.5	0.91	0.89	0.93
47	274.2	218.5	192.6	0.40		265.2	219.6	200.2	0.97	1.01	1.04
48	510.0	400.0	314.8	0.50		435.7	366.1	337.5	0.85	0.92	1.07
49	125.2	123.5	120.9	0.50		122.9	112.2	95.4	0.98	0.91	0.79
50	194.9	190.0	182.8	0.21		190.6	169.6	149.2	0.98	0.89	0.82
51	352.8	336.5	325.0	0.50		337.2	307.0	272.8	0.96	0.91	0.84
52	251.8	208.5	171.1	0.31		246.9	190.6	179.9	0.98	0.91	1.05
53	309.3	254.3	200.0	0.50		287.3	240.4	216.4	0.93	0.95	1.08
Avg.				0.43					0.95	0.94	0.99
COV				0.27					0.06	0.09	0.14

Note: μ_1 is the friction coefficient in the contact region between cone and cylinder. Its upper limit is set to be 0.50.

μ_2 is the friction coefficient in the contact region between cylinder and ring.

The maximum strength $P_{\max}$ of models with perfectly-plastic material is compared with the full plastic strength P_p of models with actual material, as shown in Fig. 5-5. The average of ratios is 1.04, with a small COV of 0.06. It is found that the method of "K_0/6 slope factor" proposed by Tateyama (1988) is also effective to determine the full plastic strength of models with conical wall failure.

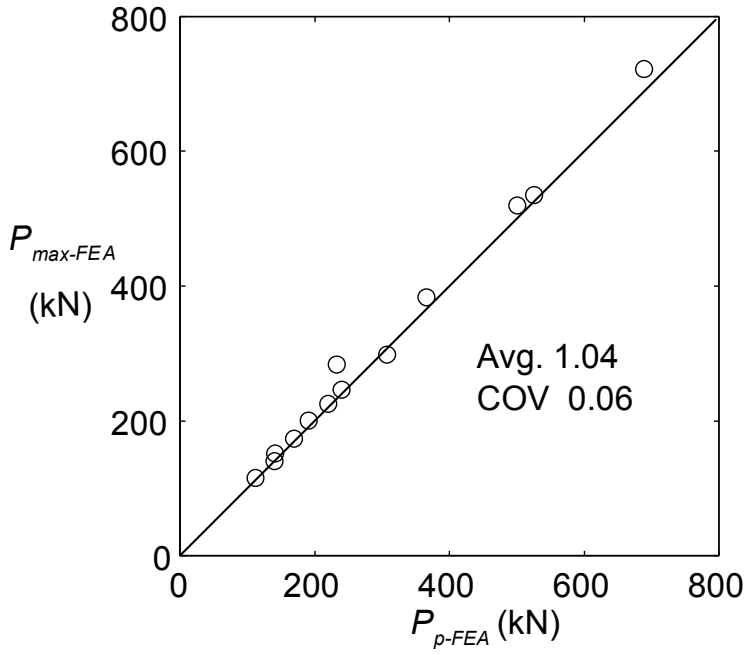

Fig. 5-5 Comparison of maximum strength to full plastic strength of FE models with conical wall failure

5.2.3 Discussion on Friction Coefficient for Practical Design

As stated in section 5.2.2, the friction coefficient between cone and cylinder is greater than those of models with cylinder edge failure and tapered ring failure. The latter two have been suggested to be 0.20 for practical design. Here, it is also assumed that μ_1 = 0.2 for models with conical wall failure.

The results of strength in FEA are then compared with experimental results, as shown in Table 5-2. It is found that the averages of ratios are 0.88, 0.81 and 0.83, for collapse strength, full plastic strength and general yield strength respectively. The values of COV are all about 0.1. The strength by assuming μ_1 = 0.20 has 10~20% under-prediction on a safe side, and can be acceptable in practical design.

Table 5-2 Comparison of strength of FE models with those of experimental ones

Model NO.	Experiments			FEA					Comparison		
	Collapse strength	Full plastic strength	General yield strength	COF		Collapse strength	Full plastic strength	General yield strength	$P_{u\text{-}FEA}/P_{u\text{-}EXP}$	$P_{p\text{-}FEA}/P_{p\text{-}EXP}$	$P_{y\text{-}FEA}/P_{y\text{-}EXP}$
	$P_{u\text{-}EXP}$ (kN)	$P_{p\text{-}EXP}$ (kN)	$P_{y\text{-}EXP}$ (kN)	μ_1	μ_2	$P_{u\text{-}FEA}$ (kN)	$P_{p\text{-}FEA}$ (kN)	$P_{y\text{-}FEA}$ (kN)			
9	601.2	561.5	482.6	0.20	0.20	614.2	525.4	481.8	1.02	0.94	1.00
34	872.8	620.0	543.8			807.5	505.6	473.4	0.93	0.82	0.87
36	625.7	527.3	390.9			554.6	474.5	422.3	0.89	0.90	1.08
43	234.9	153.6	139.1			181.4	110.2	92.4	0.77	0.72	0.66
44	389.9	294.7	263.0			328.5	181.4	165.5	0.84	0.62	0.63
46	178.4	158.7	127.5			143.5	114.9	102.7	0.80	0.72	0.81
47	274.2	218.5	192.6			246.0	190.1	168.6	0.90	0.87	0.88
48	510.0	400.0	314.8			392.0	302.3	265.9	0.77	0.76	0.84
49	125.2	123.5	120.9			110.9	97.3	84.4	0.89	0.79	0.70
50	194.9	190.0	182.8			190.6	169.6	149.2	0.98	0.89	0.82
51	352.8	336.5	325.0			306.0	270.2	234.8	0.87	0.80	0.72
52	251.8	208.5	171.1			239.3	179.8	158.1	0.95	0.86	0.92
53	309.3	254.3	200.0			257.1	203.4	169.5	0.83	0.80	0.85
Avg.									0.88	0.81	0.83
COV									0.08	0.09	0.13

5.3 FE Analysis Results

5.3.1 Definition of Stress Resultants

The internal forces acting on an infinitesimal body cut out from conical wall are defined in Fig. 5-6. Hoop stress resultant N_θ, meridional stress resultant N_s, meridional bending moment M_s, and shear stress resultant Q_{st} are defined as

$$N_\theta = \int_{-t/2}^{t/2} s_\theta dz;\ N_s = \int_{-t/2}^{t/2} s_s dz;\ M_s = \int_{-t/2}^{t/2} s_s z dz;\ \text{and}\ Q_{st} = \int_{-t/2}^{t/2} \tau_{st} dz \qquad (5\text{-}1)$$

Herein, s is normal stress, τ is shear stress, t is the thickness of conical wall, and z is the radially outward distance from its middle surface. The subscript C for conical shells is

omitted in the equations (The same hereinafter in this chapter).

The following dimensionless variables are introduced for stress resultant distributions.

$$n_s = \frac{N_s}{\sigma_y t};\ n_\theta = \frac{N_\theta}{\sigma_y t};\ m_s = \frac{M_s}{M_{sp0}};\ \text{and}\ q_{st} = \frac{\sqrt{3}Q_{st}}{\sigma_y t} \tag{5-2}$$

Where, $M_{sp0} = \sigma_y t^2 / 4$. The σ_y is set to be positive for both tension and compression.

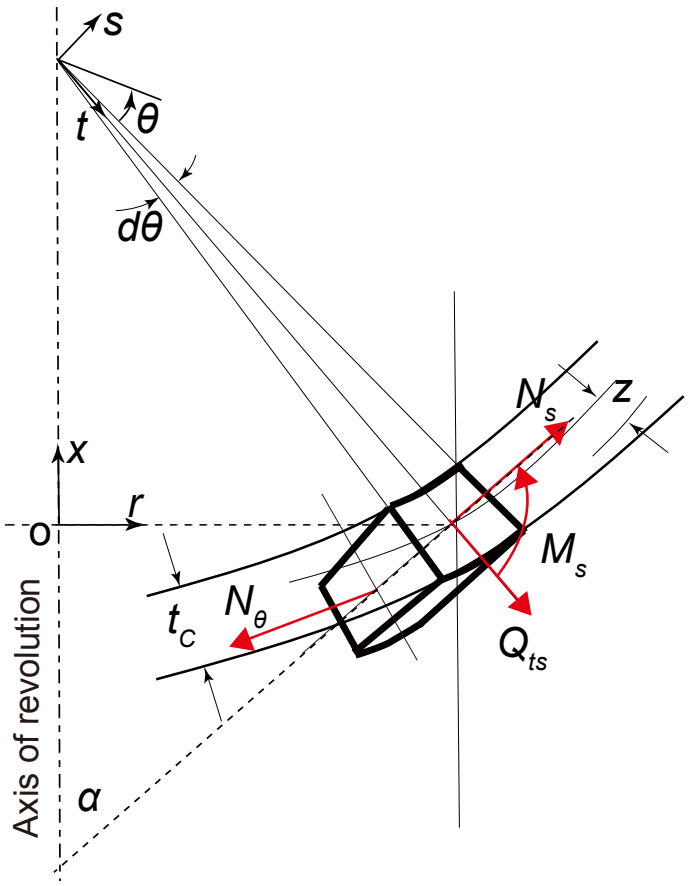

Fig. 5-6 Definition of stress resultants in conical wall

5.3.2 Distributions of Stress Resultants

In order to investigate the failure mechanism of conical wall, the characteristics of stress resultant distribution are discussed. Model No.47 is taken as a typical case.

Figures 5-7(a~e) show the changing distributions of stress resultants n_x, m_s, q_{st}, n_s and n_θ under increasing load, respectively. It can be found that

① For n_x, its absolute values in the upper part increase from top end to the contact section. They are much larger than those in the lower part, as the confinement effect from cylindrical wall is mainly concentrated in the upper part of conical wall.

② For m_s, its distribution type is like the letter of " W ". The $|m_s|$ increases as load increases. The sections where m_{su} reaches local peak value are defined as Sects. E, F and G.

③ For q_{st}, its direction has a sudden change in Sect. F at which reaction force from cylindrical wall is applied. It decreases from Sect. F and reaches about 0 in Sects. E and G respectively.

④ For n_s, its distribution type is a little different from that of n_x. Especially in the upper part of conical wall, the largest value of $|n_s|$ does not occur in Sect. F, but close to Sect. E. The reason might be that the vertical component of n_s in Sect. F is cancelled out partially by q_{st}.

⑤ For n_θ, its distribution is concentrated in the region from Sect. E to Sect. G, where compressive deformation in hoop direction is much larger than that in other regions.

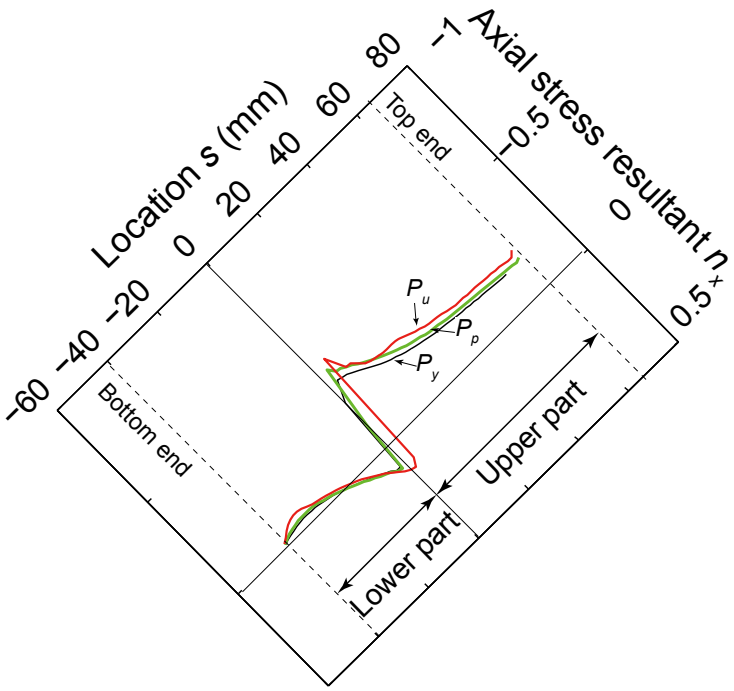

(a) Axial stress resultant n_x

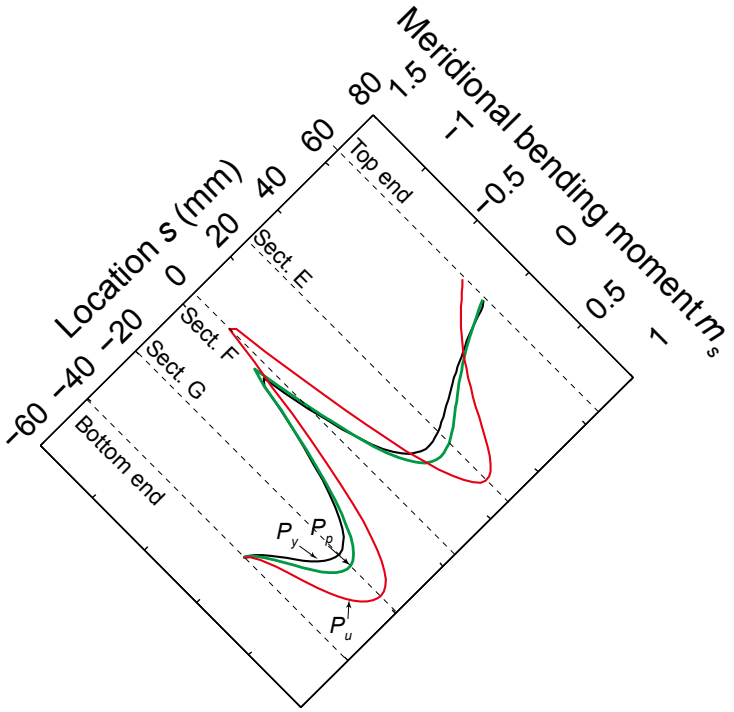

(b) Meridional bending moment m_s

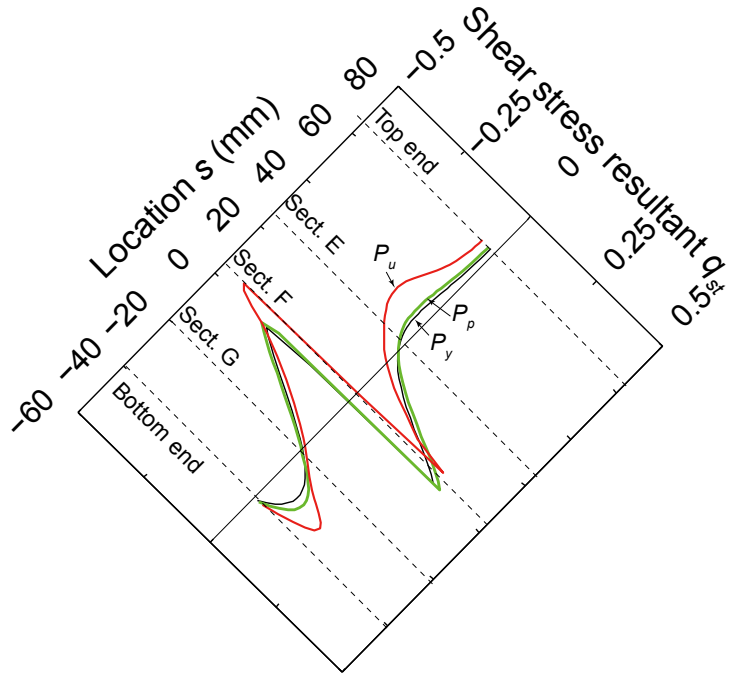

(c) Shear stress resultant q_{st}

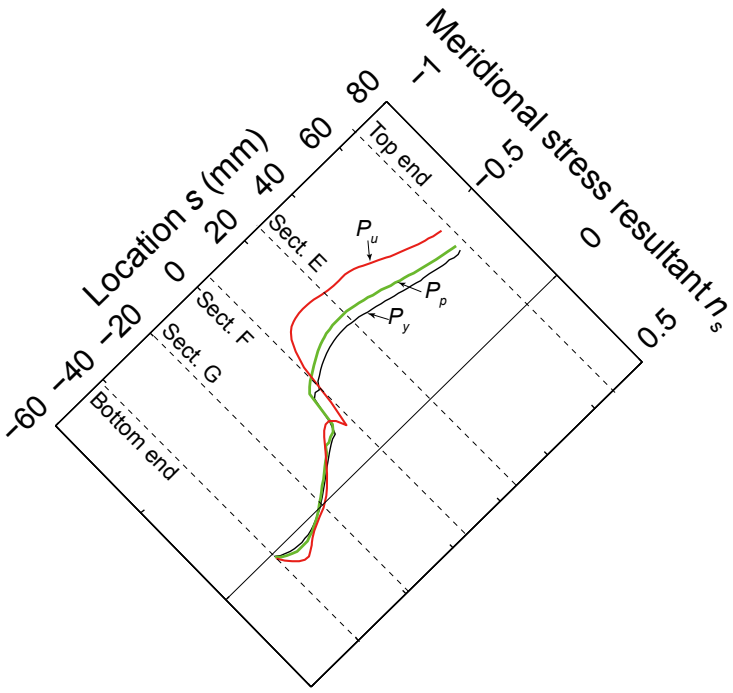

(d) Meridional stress resultant n_s

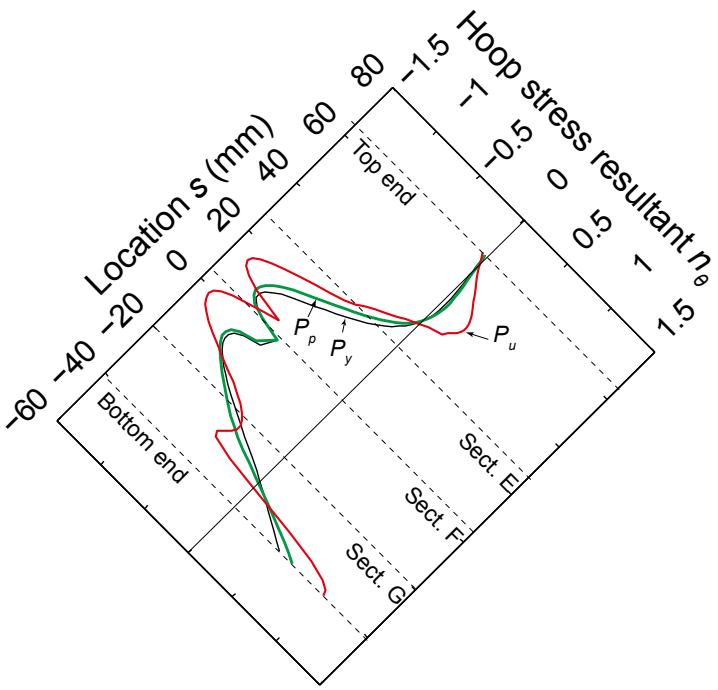

(e) Hoop stress resultant n_θ

Fig. 5-7 Changing distributions of stress resultants in conical wall under increasing load for model No. 47 with actual material

5.3.3 Distribution of Deformation

The ultimate deformation of conical wall in model No. 47 is shown in Fig. 5-8. It is found that the conical wall seems to be symmetric with respect to *t*-axis. Like the upper part, the lower part also takes an important role in failure mechanism. It is not just a free edge of conical wall. In addition, as the normal direction of contact region at ultimate load is close to the one before testing, the upper part does not sit on the cylindrical wall.

Figure 5-9 gives the changing distributions of normal displacement w_t under increasing load. It can be found that w_t at P_u is much larger than those at P_y and P_p, and actually it is not distributed in a perfectly axisymmetric type. The w_t in the upper part is slightly greater than that in the lower part.

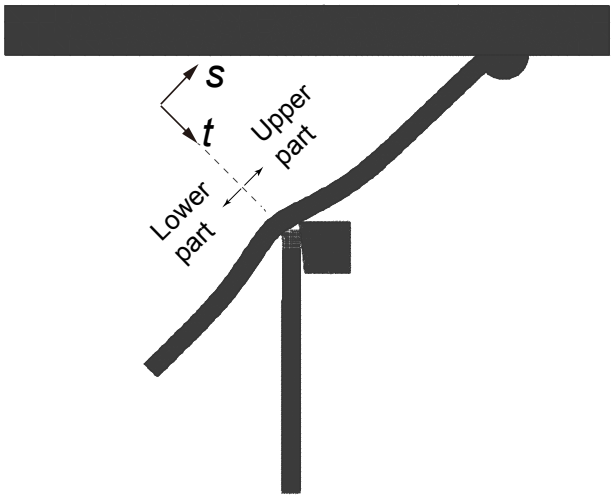

Fig. 5-8 Ultimate behavior of model No.47

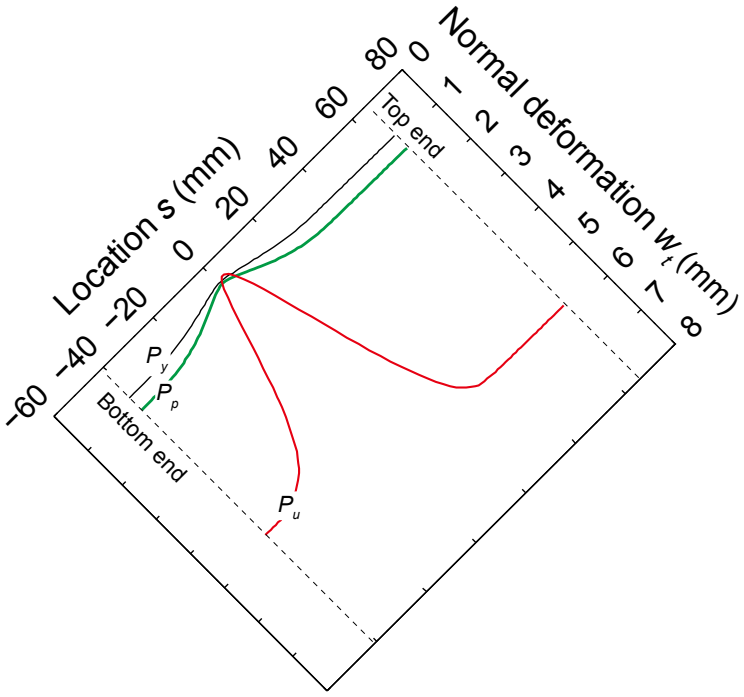

Fig. 5-9 Changing distributions of normal deformation w_t in conical wall under increasing load for model No.47

5.4 Judgement of Failure Mode

5.4.1 Definition of the Criterion of Failure Mode

The criterion of failure mode for cone wall is defined with the similar method to that

for cylinder edge failure. The ratio of average equivalent stress $\bar{s}_{eq}$ in a section to yield stress σ_y is defined as

$$r=\frac{\bar{s}_{eq}}{\sigma_y}=\frac{\int_{-t/2}^{t/2} s_{eq}\mathrm{d}z}{\sigma_y t} \tag{5-3}$$

where, equivalent stress s_{eq} in each small mesh of FE model is obtained by

$$s_{eq}=\sqrt{s_s^2-s_s s_\theta+s_\theta^2+3\tau_{st}} \tag{5-4}$$

If r in the section where meridional bending moment m_s reaches the local peak, satisfies that $r_{(m_s=m_{s,peak})}\approx 1.0$, a plastic hinge is assumed to form there. If the number of plastic hinges becomes sufficient and the kinematically admissible state is reached just prior to or at collapse load, the failure is assumed to be governed by "plastic collapse". It should be noted that

(1) Because of the strain hardening effect of materials, $r_{u(m_{su}=m_{su,peak})}$ at ultimate load is possible to exceed 1.0;

(2) From the engineering point of view, $r_{u(m_{su}=m_{su,peak})}\geq 0.8$ is acceptable for the determination of plastic hinge.

5.4.2 Failure Mode of models

Figure 5-10 shows the changing distributions of ratios r at P_y, P_p, and P_u in the conical wall of model No.47. It is found that r increases as load increases for each section. The r_y near to Sect. F have already exceeded 1.0 as P_y is reached, which means the contact region has entered into plastic as general yield load arrives. Finally, r_u in Sects. E, F and G are all greater than 1.0. It indicates that three plastic hinges form there. Because of the strain hardening effect of material, the nearer a section get to Sect. F where the plastic deformation is the greatest, the larger is r_u.

The r_u in Sects. E, F and G for all the models with actual material are listed in Fig.

5-10. It is seen that all the values are larger than 1.0. Especially the values in Sect. F are much greater than those in Sects. E and G. The failure mode can be assumed to be controlled by "plastic collapse" of conical wall.

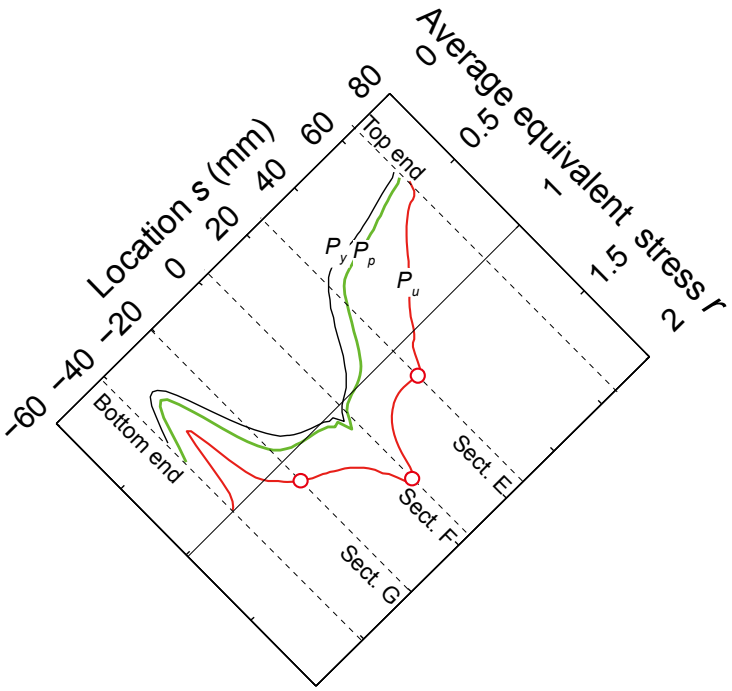

Fig. 5-10 Changing distributions of average equivalent stress in the conical wall under increasing load for model No.47

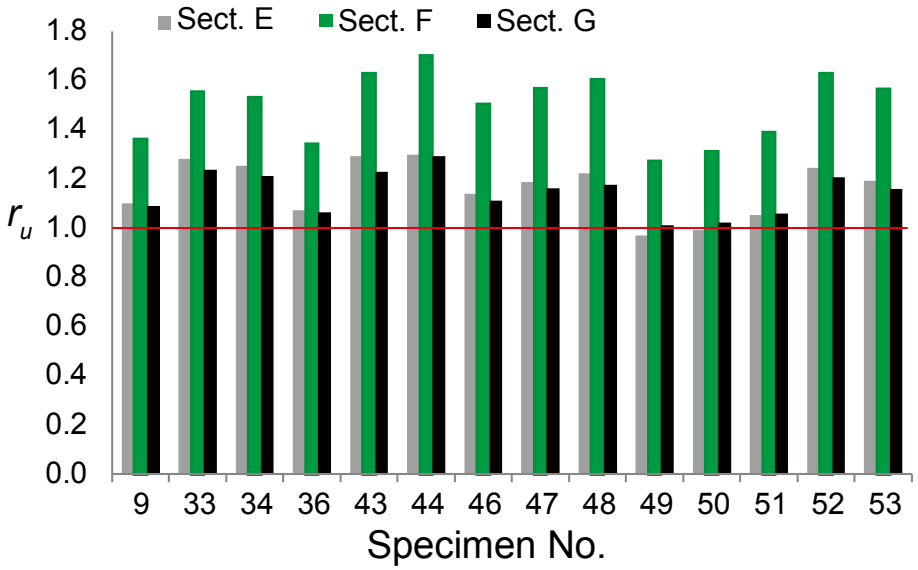

Fig. 5-11 Ratios of average equivalent stress to yield stress at ultimate load for Sects. E, F and G of models with conical wall failure.

5.5 Prediction of Strength

5.5.1 Prediction of Full Plastic Strength

5.5.1.1 Proposed Plastic Collapse Mechanism

The plastic collapse mechanism has been employed successfully for estimating the collapse strength of conical shell fixed in two ends under axisymmetric loading (Panzeri et al. 1999, Chryssanthopoulos et al. 2001). The proposed formula by them predicted well the collapse strength. But it was in complicated implicit form and difficult to be applied in practical design. In this section, a new plastic collapse mechanism is proposed and then limit analysis is undertaken. Finally, a simple and easy-to-use formula is obtained for prediction of full plastic strength.

In the plastic collapse mechanism shown in Fig. 5-12, R and μR are the reaction force and frictional force acted in Sect. F respectively. They are defined to be applied in 360 degrees in hoop direction. The equilibriums for external forces are given by

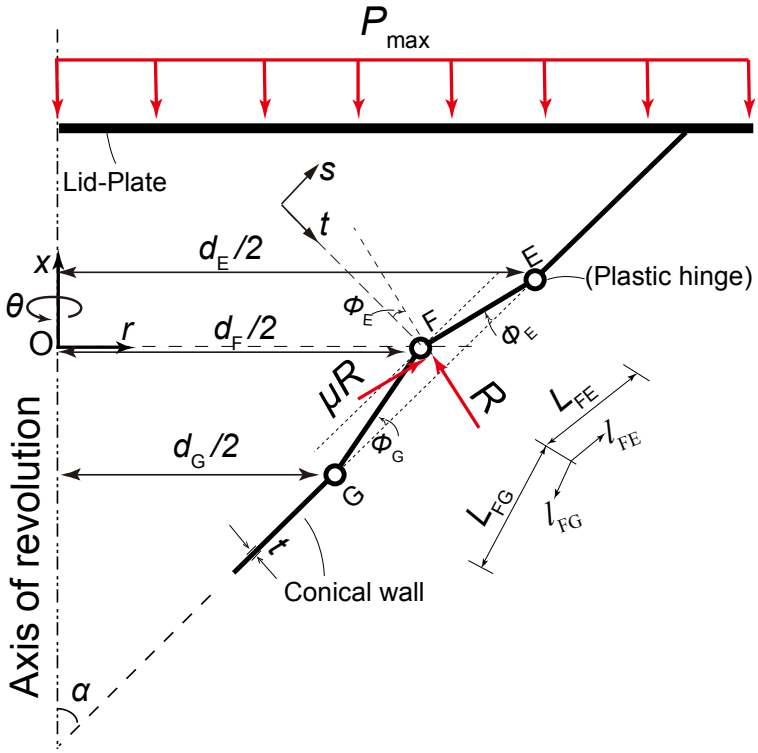

Fig. 5-12 Proposed plastic collapse mechanism for models with conical wall failure

$$P_{\max} = -R\left(\mu\cos\left(\alpha+\phi_{\mathrm{E}}\right)+\sin\left(\alpha+\phi_{\mathrm{E}}\right)\right) \tag{5-5}$$

Like the failure mechanism of cylinder edge failure, it is assumed that stress resultants in plastic hinges are in plane strain state and those in segments are in plane stress state, the interactions of stress resultants are shown as follows:

For plastic hinge E,

$$m_{s\max\mathrm{E}} = \frac{2}{\sqrt{3}}\left(1-\frac{3}{4}n_{s\max\mathrm{E}}^2\right) \tag{5-6a}$$

where $$n_{s\max\mathrm{E}} = \frac{P_{\max}}{\pi d_{\mathrm{E}}\sigma_y t\cos\alpha} \tag{5-6b}$$

and $$d_{\mathrm{E}} = d_{\mathrm{F}} + 2L_{\mathrm{FE}}\sin(\alpha+\phi_{\mathrm{E}}) \tag{5-6c}$$

For plastic hinge F,

$$m_{s\max\mathrm{F}} = \frac{2}{\sqrt{3}}\left(-1+\frac{3}{4}n_{s\max\mathrm{F}}^2\right) \tag{5-7a}$$

where $$n_{s\max\mathrm{F}} = \frac{P_{\max}}{\pi d_{\mathrm{F}}\sigma_y t\cos\left(\alpha+\phi_{\mathrm{E}}\right)} \tag{5-7b}$$

For plastic hinge G, as meridional stress resultant is zero,

$$m_{s\max\mathrm{G}} = \frac{2}{\sqrt{3}} \tag{5-8}$$

In addition, $$d_{\mathrm{G}} = d_{\mathrm{F}} - 2L_{\mathrm{FG}}\sin(\alpha-\phi_{\mathrm{G}}) \tag{5-9}$$

For segment FE, as $n_{s\max}$ varies along with the location in meridional direction, hoop stress resultant $n_{\theta\max(l_{\mathrm{FE}})}$ for an arbitrary section is assumed as

$$n_{\theta\max(l_{\mathrm{FE}})} = \frac{1}{2}n_{s\max(l_{\mathrm{FE}})} - \sqrt{1-\frac{3}{4}n_{s\max(l_{\mathrm{FE}})}^2} \tag{5-10a}$$

where $$n_{s\max(l_{\mathrm{FE}})} = \frac{P_{\max}}{\pi d_{(l_{\mathrm{FE}})}\sigma_y t\cos\left(\alpha+\phi_{\mathrm{E}}\right)} \tag{5-10b}$$

and $$d_{(l_{\mathrm{FE}})} = d_{\mathrm{F}} + 2l_{\mathrm{FE}}\sin(\alpha+\phi_{\mathrm{E}}) \tag{5-10c}$$

For segment FG, as meridional stress resultant $n_{s\max FG}$ is zero, hoop stress resultant $n_{\theta\max FG}$ is assumed to be that

$$n_{\theta\max FG} = -1 \tag{5-11}$$

5.5.1.2 Derivation of Virtual Work Equations

Based on the principle of virtual work, the equilibrium of external work $\mathrm{d}W$ and dissipation of internal energy $\mathrm{d}U$ of the whole mechanism in 360 degrees in hoop direction during a virtual change of rotation $\mathrm{d}\phi_E$ at plastic hinge E, $\mathrm{d}\phi_G$ at plastic hinge G and $(\mathrm{d}\phi_E + \mathrm{d}\phi_G)$ at plastic hinge F, is given by

$$\mathrm{d}U = \mathrm{d}W \tag{5-12}$$

where

$$\mathrm{d}U = \mathrm{d}U_1 + \mathrm{d}U_2 + \mathrm{d}U_3$$

$$\mathrm{d}W = \mathrm{d}W_1 + \mathrm{d}W_2$$

Herein, for internal energy, $\mathrm{d}U_1$ is done by hoop stress resultant $n_{\theta\max}\sigma_y t$, $\mathrm{d}U_2$ is done by meridional stress resultant $n_{s\max}\sigma_y t$, and $\mathrm{d}U_3$ is done by meridional bending moment $m_{s\max}\frac{1}{4}\sigma_y t^2$; For external work, $\mathrm{d}W_1$ is done by reaction force R, and $\mathrm{d}W_2$ is done by meridional force $\frac{-P_{\max}}{\cos\alpha}$ acted in Sect. E because of the shortening of segment FE in meridional direction. The friction energy dissipation produced by frictional force μR is neglected.

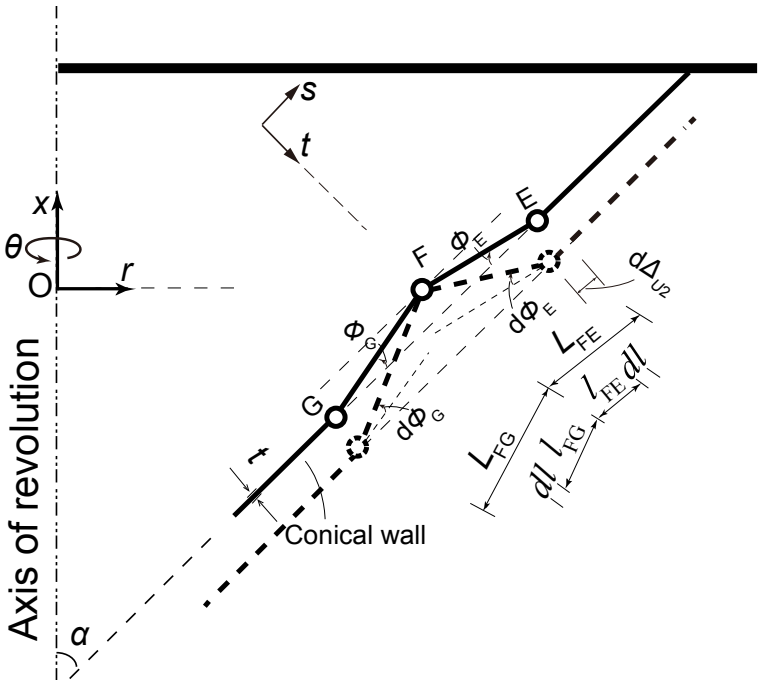

Fig. 5-13 Meridional shortening compatible with the circumferential stretching of the segments in plastic collapse mechanism of conical wall failure

① $\mathrm{d}U_1$

A small segment of length $\mathrm{d}l$ for segments FE and FG is considered respectively, as shown in Fig. 5-13. For segment FE, the increase in length $\mathrm{d}\Delta_{U1\mathrm{FE}}$ in hoop direction after the virtual change of rotation $\mathrm{d}\phi_{\mathrm{E}}$ can be derived as

$$\begin{aligned}\mathrm{d}\Delta_{U1(l_{\mathrm{FE}})} &= -(L_{\mathrm{FE}} - l_{\mathrm{FE}})[\sin(\phi_{\mathrm{E}} + \mathrm{d}\phi_{\mathrm{E}}) - \sin\phi_{\mathrm{E}}]\cos(\alpha + \phi_{\mathrm{E}}) \\ &\approx -(L_{\mathrm{FE}} - l_{\mathrm{FE}})\cos\phi_{\mathrm{E}}\mathrm{d}\phi_{\mathrm{E}}\cos(\alpha + \phi_{\mathrm{E}})\end{aligned} \tag{5-13}$$

The strain rate in hoop direction is given by

$$\dot{\varepsilon}_{\theta\max(l_{\mathrm{FE}})} = \frac{-2(L_{\mathrm{FE}} - l_{\mathrm{FE}})\cos\phi_{\mathrm{E}}\cos(\alpha + \phi_{\mathrm{E}})}{d_{(l_{\mathrm{FE}})}}\mathrm{d}\phi_{\mathrm{E}} \tag{5-14}$$

For segment FG, the increase in length $\mathrm{d}\Delta_{U1\mathrm{FG}}$ in hoop direction after the virtual change of rotation $\mathrm{d}\phi_{\mathrm{G}}$ can be derived as

$$\begin{aligned}\mathrm{d}\Delta_{U1(l_{\mathrm{FG}})} &= -(L_{\mathrm{FG}} - l_{\mathrm{FG}})[\sin(\phi_{\mathrm{G}} + \mathrm{d}\phi_{\mathrm{G}}) - \sin\phi_{\mathrm{G}}]\cos(\alpha - \phi_{\mathrm{G}}) \\ &\approx -(L_{\mathrm{FG}} - l_{\mathrm{FG}})\cos\phi_{\mathrm{G}}\mathrm{d}\phi_{\mathrm{G}}\cos(\alpha - \phi_{\mathrm{G}})\end{aligned} \tag{5-15}$$

The strain rate in hoop direction is given by

$$\dot{\varepsilon}_{\theta(l_{\mathrm{FG}})}=\frac{-2(L_{\mathrm{FG}}-l_{\mathrm{FG}})\cos\phi_{\mathrm{G}}\cos(\alpha-\phi_{\mathrm{G}})}{d_{(l_{\mathrm{FG}})}}\mathrm{d}\phi_{\mathrm{G}} \tag{5-16a}$$

where $$d_{(l_{\mathrm{FG}})}=d_{\mathrm{F}}-2l_{\mathrm{FG}}\sin(\alpha-\phi_{\mathrm{G}}) \tag{5-16b}$$

Thus, $\mathrm{d}U_1$ during the increase in length in hoop direction for segments FE and FG can be obtained as

$$\begin{aligned}\mathrm{d}U_1&=\int_0^{L_{\mathrm{FE}}}\int_0^{\pi d_{(l_{\mathrm{FE}})}} n_{\theta\max(l_{\mathrm{FE}})}\sigma_y t\dot{\varepsilon}_{\theta(l_{\mathrm{FE}})}\mathrm{d}y\mathrm{d}l+\int_0^{L_{\mathrm{FG}}}\int_0^{\pi d_{(l_{\mathrm{FG}})}} n_{\theta\max\mathrm{FG}}\sigma_y t\dot{\varepsilon}_{\theta(l_{\mathrm{FG}})}\mathrm{d}y\mathrm{d}l\\&\approx\int_0^{L_{\mathrm{FE}}}\int_0^{\pi d_{(l_{\mathrm{FE}})}} n_{\theta\max(l_{\mathrm{FE}})}\sigma_y t\dot{\varepsilon}_{\theta(l_{\mathrm{FE}})}\mathrm{d}y\mathrm{d}l+\pi\sigma_y tL_{\mathrm{FG}}^2\cos\left(\alpha-\phi_{\mathrm{G}}\right)\cos\phi_{\mathrm{G}}\mathrm{d}\phi_{\mathrm{G}}\end{aligned} \tag{5-17}$$

Herein, $\mathrm{d}y$ is differential in hoop direction. The integral of $n_{\theta\max(l_{\mathrm{FE}})}$ is not expressed because of the quite complicated form.

② $\mathrm{d}U_2$

Since the deformations in segment FE take place under Mises' yield condition as shown in Eq. (5-18), a flow rule must be adopted to determine the change in the strain rate (Save, 1997).

$$f=n_{s\max(l_{\mathrm{FE}})}^2+n_{\theta\max(l_{\mathrm{FE}})}^2-n_{s\max(l_{\mathrm{FE}})}n_{\theta\max(l_{\mathrm{FE}})}-1=0 \tag{5-18}$$

Thus,

$$\dot{\varepsilon}_{s\max(l_{\mathrm{FE}})}=\lambda\frac{\partial f}{\partial n_{s\max(l_{\mathrm{FE}})}}=\lambda(2n_{s\max(l_{\mathrm{FE}})}-n_{\theta\max(l_{\mathrm{FE}})}) \tag{5-19}$$

and $$\dot{\varepsilon}_{\theta\max(l_{\mathrm{FE}})}=\lambda\frac{\partial f}{\partial n_{\theta\max(l_{\mathrm{FE}})}}=\lambda(2n_{\theta\max(l_{\mathrm{FE}})}-n_{s\max(l_{\mathrm{FE}})}) \tag{5-20}$$

where λ is a positive scalar factor.

Combining Eqs. (5-19) and (5-20) gives

$$\dot{\varepsilon}_{s\max(l_{\mathrm{FE}})}=\frac{2n_{s\max(l_{\mathrm{FE}})}-n_{\theta\max(l_{\mathrm{FE}})}}{2n_{\theta\max(l_{\mathrm{FE}})}-n_{s\max(l_{\mathrm{FE}})}}\dot{\varepsilon}_{\theta\max(l_{\mathrm{FE}})} \tag{5-21}$$

Substituting Eq. (5-14) into Eq. (5-21) and integrating $\dot{\varepsilon}_{s\max(l_{\mathrm{FE}})}$, the shortening in length $\mathrm{d}\Delta_{U2}$ in the meridional direction, as shown in Fig. 5-13, is given by

$$\mathrm{d}\Delta_{U2}=\mathrm{d}\Delta_{U2(l_{\mathrm{FE}})}=\int_0^{L_{\mathrm{FE}}}\dot{\varepsilon}_{s\max(l_{\mathrm{FE}})}\mathrm{d}l$$
$$\approx-\int_0^{L_{\mathrm{FE}}}\frac{2n_{s\max(l_{\mathrm{FE}})}-n_{\theta\max(l_{\mathrm{FE}})}}{2n_{\theta\max(l_{\mathrm{FE}})}-n_{s\max(l_{\mathrm{FE}})}}\frac{2(L_{\mathrm{FE}}-l_{\mathrm{FE}})\cos(\alpha+\phi_{\mathrm{E}})\cos\phi_{\mathrm{E}}}{d_{(l_{\mathrm{FE}})}}\mathrm{d}\phi_{\mathrm{E}}\mathrm{d}l \quad (5\text{-}22)$$

Thus, $\mathrm{d}U_2$ can be obtained by

$$\mathrm{d}U_2=\int_0^{\pi d_{(l_{\mathrm{FE}})}}n_{s\max\mathrm{FE}}\sigma_y t\mathrm{d}\Delta_{U2}$$
$$=-\int_0^{L_{\mathrm{FE}}}\pi d_{(l_{\mathrm{FE}})}n_{s\max(l_{\mathrm{FE}})}\sigma_y t\frac{2n_{s\max(l_{\mathrm{FE}})}-n_{\theta\max(l_{\mathrm{FE}})}}{2n_{\theta\max(l_{\mathrm{FE}})}-n_{s\max(l_{\mathrm{FE}})}}\frac{2(L_{\mathrm{FE}}-l_{\mathrm{FE}})\cos(\alpha+\phi_{\mathrm{E}})\cos\phi_{\mathrm{E}}}{d_{(l_{\mathrm{FE}})}}\mathrm{d}\phi_{\mathrm{E}}\mathrm{d}l \quad (5\text{-}23)$$

③ $\mathrm{d}U_3$

The $\mathrm{d}U_3$ by meridional bending moment in plastic hinges E, F, and G is obtained as:

$$\mathrm{d}U_3=\left(\pi d_{\mathrm{E}}m_{s\max\mathrm{E}}\mathrm{d}\phi_{\mathrm{E}}-\pi d_{\mathrm{F}}m_{s\max\mathrm{F}}(\mathrm{d}\phi_{\mathrm{E}}+\mathrm{d}\phi_{\mathrm{G}})+\pi d_{\mathrm{G}}m_{s\max\mathrm{G}}\mathrm{d}\phi_{\mathrm{G}}\right)\frac{1}{4}\sigma_y t^2 \quad (5\text{-}24)$$

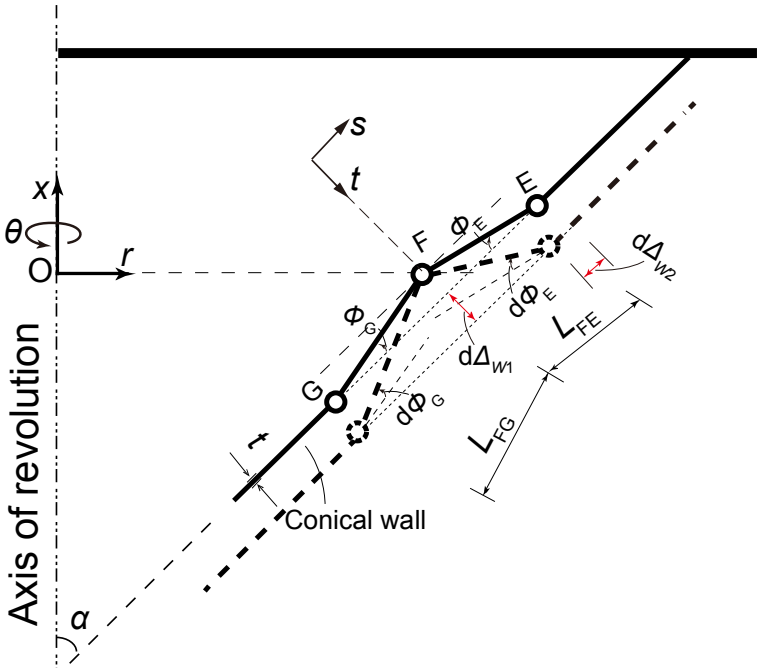

Fig. 5-14 Virtual deformations due to an incremental rotation of plastic hinges

④ $\mathrm{d}W_1$

After the virtual change of rotation $\mathrm{d}\phi_{\mathrm{G}}$, the virtual deformation by reaction force R acted in Sect. F is defined as $\mathrm{d}\Delta_{W1}$ in Fig. 5-14.

$$\mathrm{d}\Delta_{W1} = L_{\mathrm{FG}}\sin\phi_{\mathrm{G}} - L_{\mathrm{FG}}\sin(\phi_{\mathrm{G}} + \mathrm{d}\phi_{\mathrm{G}}) \approx -L_{\mathrm{FG}}\cos\phi_{\mathrm{G}}\mathrm{d}\phi_{\mathrm{G}} \tag{5-25}$$

The work $\mathrm{d}W_1$ is obtained by

$$\mathrm{d}W_1 = -\pi d_{\mathrm{F}} R L_{\mathrm{FG}}\cos\phi_{\mathrm{G}}\mathrm{d}\phi_{\mathrm{G}} \tag{5-26}$$

⑤ $\mathrm{d}W_2$

For segment FE, after the virtual change of rotation $\mathrm{d}\phi_{\mathrm{E}}$, the virtual meridional deformation by meridional force $\dfrac{-P_{\max}}{\cos\alpha}$, excluding the virtual strain deformation $\mathrm{d}\Delta_{U2}$ in Eq. (5-25), is defined as $\mathrm{d}\Delta_{W2}$ in Fig. 5-14.

$$\mathrm{d}\Delta_{W2} = L_{\mathrm{FE}}\cos(\phi_{\mathrm{E}} + \mathrm{d}\phi_{\mathrm{E}}) - L_{\mathrm{FE}}\cos\phi_{\mathrm{E}} \approx -L_{\mathrm{FE}}\sin\phi_{\mathrm{E}}\mathrm{d}\phi_{\mathrm{E}} \tag{5-27}$$

The work $\mathrm{d}W_2$ can be obtained as

$$\mathrm{d}W_2 = \frac{-P_{\max}}{\cos\alpha}\mathrm{d}\Delta_{W2} + \frac{-P_{\max}}{\cos\alpha}\mathrm{d}\Delta_{U2} = \frac{P_{\max}}{\cos\alpha}L_{\mathrm{FE}}\sin\phi_{\mathrm{E}}\mathrm{d}\phi_{\mathrm{E}} + \mathrm{d}U_2 \tag{5-28}$$

herein, $\mathrm{d}U_2$ is expressed in Eq. (5-23).

Substituting Eqs. (5-17), (5-23), (5-24), (5-26), and (5-28) into Eq. (5-12), the following general equation can be obtained.

$$\begin{aligned} &-RL_{\mathrm{FG}}\cos\phi_{\mathrm{G}}\mathrm{d}\phi_{\mathrm{G}} + \frac{P_{\max}}{\cos\alpha}L_{\mathrm{FE}}\sin\phi_{\mathrm{E}}\mathrm{d}\phi_{\mathrm{E}} = \\ &\int_0^{L_{\mathrm{FE}}}\int_0^{\pi d_{(l_{\mathrm{FE}})}} n_{\theta\max(l_{\mathrm{FE}})}\sigma_y t\dot{\varepsilon}_{\theta(l_{\mathrm{FE}})}\mathrm{d}y\mathrm{d}l + \pi\sigma_y t L_{\mathrm{FG}}^2\cos(\alpha-\phi_{\mathrm{G}})\cos\phi_{\mathrm{G}}\mathrm{d}\phi_{\mathrm{G}} + \\ &\left(\pi d_{\mathrm{E}} m_{s\max\mathrm{E}}\mathrm{d}\phi_{\mathrm{E}} - \pi d_{\mathrm{F}} m_{s\max\mathrm{F}}(\mathrm{d}\phi_{\mathrm{E}} + \mathrm{d}\phi_{\mathrm{G}}) + \pi d_{\mathrm{G}} m_{s\max\mathrm{G}}\mathrm{d}\phi_{\mathrm{G}}\right)\frac{1}{4}\sigma_{\mathrm{y}} t^2 \end{aligned} \tag{5-29}$$

5.5.1.3 Proposed Formula for Full Plastic Strength

The general equation (5-29) is difficult to be solved by hand calculation，because the

results of integral of $n_{\theta\max(l_{\mathrm{FE}})}$ is quite complicated. Moreover, the $\mathrm{d}U_3$ in Eq. (5-24) is also difficult to be derived because of the different diameters at the three plastic hinges. In order to obtain simple solution for practical design, Eq. (5-29) is simplified as follow.

First, based on small deformation theory, $\cos\phi_{\mathrm{G}}=\cos\phi_{\mathrm{E}}=1.0$, $\sin\phi_{\mathrm{G}}=\phi_{\mathrm{G}}$, and $\sin\phi_{\mathrm{E}}=\phi_{\mathrm{E}}$. Because $\phi_{\mathrm{E}}, \phi_{\mathrm{G}} \ll \alpha$, $\alpha+\phi_{\mathrm{E}}=\alpha-\phi_{\mathrm{G}}=\alpha$.

Then, $n_{\theta\max(l_{\mathrm{FE}})}$ in Eq. (3-24) is simplified. For segment FE, because $n_{\theta\max\mathrm{F}} \le n_{\theta\max(l_{\mathrm{FE}})} \le n_{\theta\max\mathrm{E}}$, $1 \le \dfrac{n_{\theta\max(l_{\mathrm{FE}})}}{n_{\theta\max\mathrm{F}}} \le \dfrac{n_{\theta\max\mathrm{E}}}{n_{\theta\max\mathrm{F}}}$. The variation of upper bound $\dfrac{n_{\theta\max\mathrm{E}}}{n_{\theta\max\mathrm{F}}}$ along with $n_{\theta\max\mathrm{F}}$ for all the FEA models is listed in Fig. 5-15. The maximum value is 1.18 and the minimum one is 1.00. The average is assumed to be (1.18+1.00)/2=1.09. Based on Eq. (5-10a), $n_{\theta\max(l_{\mathrm{FE}})}$ is simplified to be

$$n_{\theta\max(l_{\mathrm{FE}})}=\overline{n}_{\theta\max\mathrm{FE}}=\frac{1+1.09}{2}n_{\theta\max\mathrm{F}}=1.05\left(\frac{1}{2}n_{s\max\mathrm{F}}-\sqrt{1-\frac{3}{4}n_{s\max\mathrm{F}}^2}\right) \qquad (5\text{-}30)$$

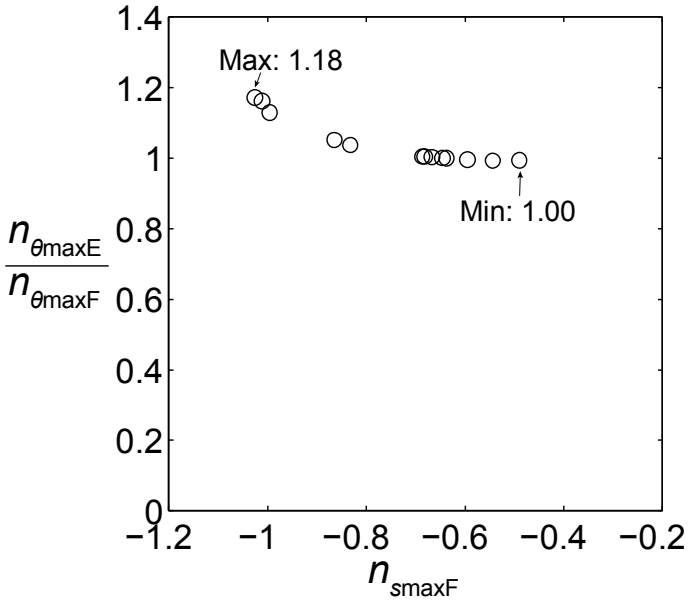

Fig. 5-15 Variation of ratio $\dfrac{n_{\theta\max\mathrm{E}}}{n_{\theta\max\mathrm{F}}}$ along with axial stress resultant $n_{s\max\mathrm{F}}$ for FE models with conical wall failure

Next, $\mathrm{d}U_3$ in Eq. (5-24) simplified. It is defined to be $\mathrm{d}U_3^{exact}$ and approximated to be that

$$\mathrm{d}U_3^{approximated} = \left[-2m_{s\max \mathrm{F}}\mathrm{d}\phi_{\mathrm{E}} + \left(m_{s\max \mathrm{G}} - m_{s\max \mathrm{F}}\right)\mathrm{d}\phi_{\mathrm{G}}\right]\pi d_{\mathrm{F}}\frac{1}{4}\sigma_{\mathrm{y}}t^2 \qquad (5\text{-}31)$$

By assuming that $L_{\mathrm{FE}}\mathrm{d}\phi_{\mathrm{E}} = L_{\mathrm{FG}}\mathrm{d}\phi_{\mathrm{G}}$, $\frac{\mathrm{d}\phi_{\mathrm{E}}}{\mathrm{d}\phi_{\mathrm{G}}} = \frac{L_{\mathrm{FG}}}{L_{\mathrm{FE}}}$. The variation of ratios $\frac{L_{\mathrm{FG}}}{L_{\mathrm{FE}}}$ along with $n_{s\max \mathrm{F}}$ for all the FE models is listed in Fig. 5-16. It is seen that the average is 1.27, with a COV of 0.09. By setting $\frac{\mathrm{d}\phi_{\mathrm{E}}}{\mathrm{d}\phi_{\mathrm{G}}} = 1.27$, the $\mathrm{d}U_3^{approximated}$ in Eq. (5-31) is compared with the $\mathrm{d}U_3^{exact}$ in Eq. (5-24). Variation of their ratios along with $n_{s\max \mathrm{F}}$ for all the models is listed in Fig.5-17. The average of the ratios is assumed to be (1.20+1.01)/2=1.11, as the trend is almost in a straight line. Thus, $\mathrm{d}U_3$ is assumed that

$$\mathrm{d}U_3^{exact} = 1.11\mathrm{d}U_3^{approximated} \qquad (5\text{-}32)$$

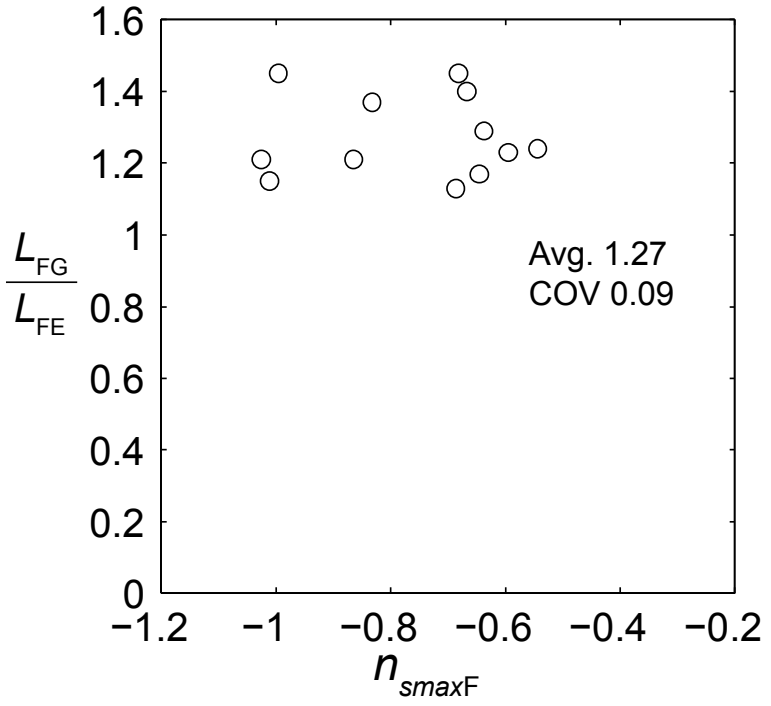

Fig. 5-16 Variation of $\frac{L_{\mathrm{FG}}}{L_{\mathrm{FE}}}$ along with $n_{s\max \mathrm{F}}$ for FE models

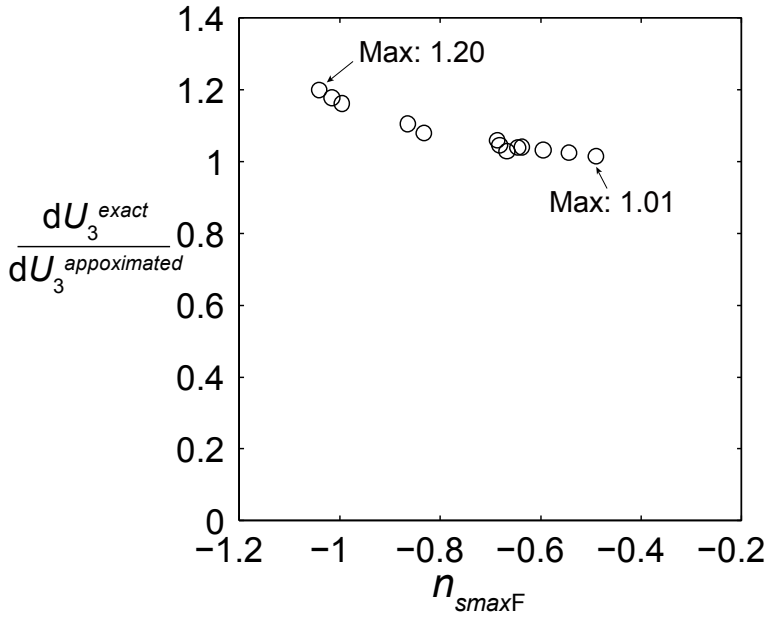

Fig. 5-17 Distribution of $\frac{dU_3^{exact}}{dU_3^{approximated}}$ along with $n_{s\max F}$ for FE models

Finally, by substituting Eqs. (5-30) ~ (5-32) into Eq. (5-29), the general equation is simplified to be that

$$R = -\frac{P_{\max}}{\cos\alpha}\phi_E + 1.05\pi\left(\frac{1}{2}n_{s\max F} - \sqrt{1-\frac{3}{4}n_{s\max F}^2}\right)\sigma_y t L_{FE}\cos\alpha - \pi\sigma_y t L_{FG}\cos\alpha$$
$$+1.11\left(\frac{2m_{s\max F}}{L_{FE}} + \frac{m_{s\max F} - m_{s\max G}}{L_{FG}}\right)\pi d_F\frac{1}{4}\sigma_y t^2$$

(5-33)

Based on upper bound theory, the true value of R is obtained by $\frac{\partial R}{\partial L_{FE}} = 0$, and $\frac{\partial R}{\partial L_{FG}} = 0$. Thus,

$$R = -1.05\left(\sqrt{-2.1m_{s\max F}\left(\frac{1}{2}n_{s\max F} - \sqrt{1-\frac{3}{4}n_{s\max F}^2}\right)} + \sqrt{\frac{2}{\sqrt{3}} - m_{s\max F}}\right)\sqrt{\frac{t}{d_F}}\pi d_F\sigma_y t\sqrt{\cos\alpha}$$
$$+\frac{P_{\max}}{\cos\alpha}\phi_E$$

(5-34)

The lengths of segments FE and FG are obtained as

$$L_{\mathrm{FE}} = \sqrt{\frac{0.53 m_{s\max \mathrm{F}}}{\left(\frac{1}{2} n_{s\max \mathrm{F}} - \sqrt{1-\frac{3}{4} n_{s\max \mathrm{F}}^2}\right)\cos\alpha}} \sqrt{d_{\mathrm{F}} t} \tag{5-35}$$

$$L_{\mathrm{FG}} = \sqrt{\frac{0.31 - 0.26 m_{s\max \mathrm{F}}}{\cos\alpha}} \sqrt{d_{\mathrm{F}} t} \tag{5-36}$$

respectively.

Substituting Eqs. (5-5), (5-7a) and (5-11) into Eq. (5-34), and Dividing both sides of Eq. (5-34) by $\pi \sigma_y t d_{\mathrm{F}}$, the following equation for $n_{s\max \mathrm{F}}$ can be obtained.

$$n_{s\max \mathrm{F}} = -\psi \cdot \chi \cdot \gamma \tag{5-37}$$

where,

$$\psi = 1.05\left[\sqrt{\frac{4.2}{\sqrt{3}}\left(-1+\frac{3}{4} n_{s\max \mathrm{F}}^2\right)\left(\frac{1}{2} n_{s\max \mathrm{F}} - \sqrt{1-\frac{3}{4} n_{s\max \mathrm{F}}^2}\right)} + \sqrt{\frac{4}{\sqrt{3}} - \frac{\sqrt{3}}{2} n_{s\max \mathrm{F}}^2}\right] \tag{5-38}$$

$$\chi = \frac{\sqrt{\frac{t}{d_{\mathrm{F}}}}\sqrt{\cos\alpha}}{\sqrt{\frac{\cos\alpha}{\mu\cos\alpha + \sin\alpha}}} \tag{5-39}$$

and

$$\gamma = \frac{\sqrt{\frac{\cos\alpha}{\mu\cos\alpha + \sin\alpha}}}{\frac{\cos\alpha}{\mu\cos\alpha + \sin\alpha} + \phi_{\mathrm{E}}} \tag{5-40}$$

The variation of ψ along with $n_{s\max \mathrm{F}}$ is listed in Fig. 5-18. It can be approximated in a quadratic equation as follow

$$\psi = -1.76 n_{s\max \mathrm{F}}^2 - 0.68 n_{s\max \mathrm{F}} + 3.22 \tag{5-41}$$

The values of γ for all the FE models are shown in Fig. 5-19. It can be found that the average is 0.92, with a small COV of 0.01. Thus, γ is simplified to be 0.92.

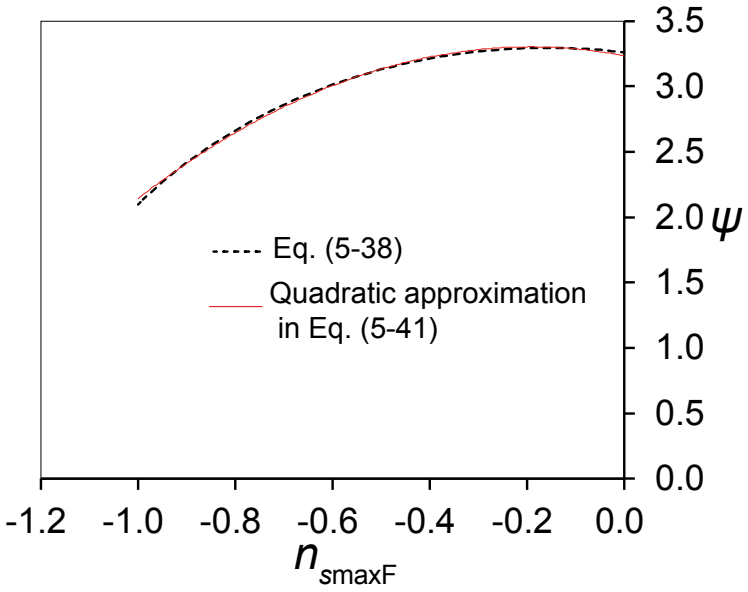

Fig. 5-18 Variation of factor ψ along with axial stress resultant $n_{s\max F}$ for models with conical wall failure

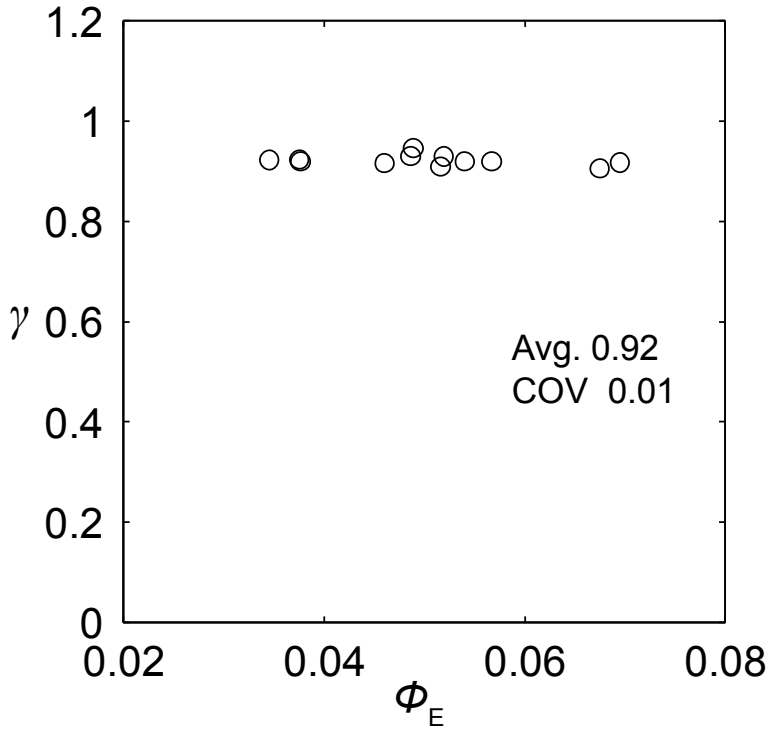

Fig. 5-19 Variation of factor γ along with rotational angle ϕ_E for FE models with conical wall failure

Substituting Eq. (5-41) and $\gamma = 0.92$ into Eq. (5-37), $n_{s\max F}$ can be expressed as

$$n_{s\max F} = 0.92\left(1.76n_{s\max F}^2 + 0.68n_{s\max F} - 3.22\right)\chi \tag{5-42}$$

The solution is

$$n_{s\max F} = \frac{-0.63\chi + 1 - \sqrt{19.58\chi^2 - 1.26\chi + 1}}{3.24\chi} \tag{5-43}$$

Prediction of the maximum strength of models can be finally obtained as

$$P_{\max - PRED} = \frac{0.63\chi - 1 + \sqrt{19.58\chi^2 - 1.26\chi + 1}}{3.24\chi}\pi d_F t\sigma_y \cos\alpha \tag{5-44}$$

The comparison of $P_{\max - PRED}$ in Eq. (5-44) with the maximum strength $P_{\max - FEA}$ is undertaken, as shown in Fig. 5-20. The average of ratios is 0.91 with a small COV of 0.08. The predicted values of model Nos. 9, 34 and 36 are found to be a little smaller than the FEA results. Their diameter-to-thickness ratios at Sect. F are only about 15.5, and the height-to-thickness ratios of the upper part of conical walls are only about 5.6. Thus, the influence of the confinement effect of boundary on the strength of models will be great. The maximum strength will be under-predicted based on the proposed plastic collapse mechanism.

Full plastic collapse of models can be predicted by

$$P_{p-PRED} = P_{\max - PRED} = \frac{0.63\chi - 1 + \sqrt{19.58\chi^2 - 1.26\chi + 1}}{3.24\chi}\pi d_F t\sigma_y \cos\alpha \tag{5-45}$$

The comparison of P_{p-PRED} with the full plastic strength P_{p-EXP} of experimental specimens is undertaken, as shown in Fig. 5-21. The average of ratios is found to be 0.89 with a small COV of 0.08. Well prediction on full plastic strength of specimens with conical wall failure is obtained.

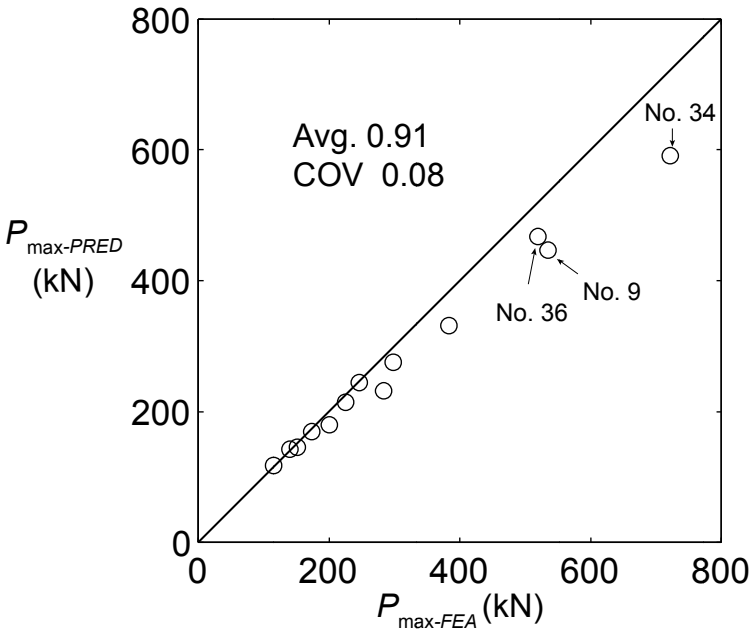

Fig. 5-20 Comparison of predicted maximum strength with FEA results for models with conical wall failure

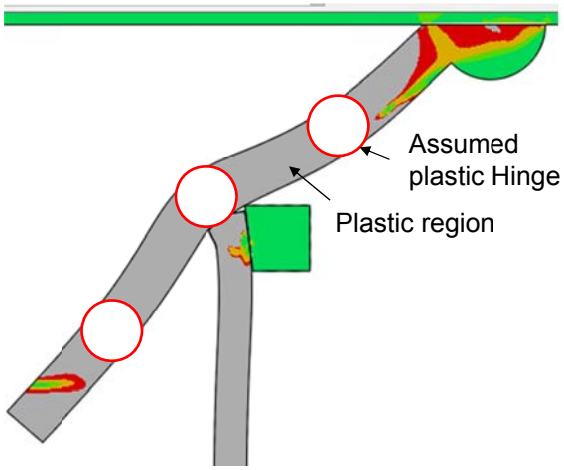

Fig. 5-21 Mises stress distribution in conical and cylindrical walls at ultimate load for model No.9

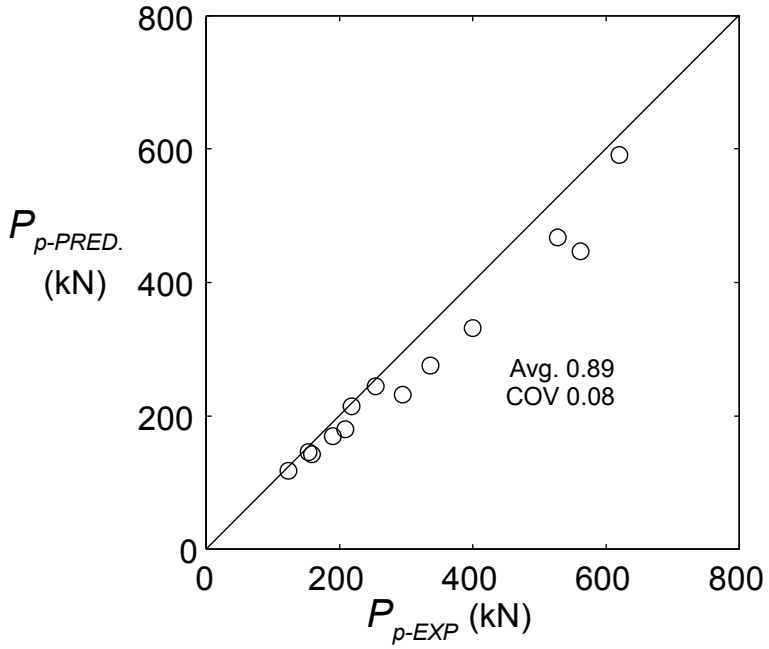

Fig. 5-22 Comparison of predicted full plastic strength with experimental results for specimens with conical wall failure

5.5.2 Prediction of Collapse Strength

The enhancement factor ρ is assumed as the average of the ratios of collapse strength to full plastic strength for both experimental specimens and FEA models. Their average is 1.23 with a COV of 0.11, as shown in Fig. 5-23. Collapse strength P_u is predicted by

$$P_{u\text{-}PRED} = \rho \cdot P_{p-PRED} = 1.23 P_{p-PRED} \tag{5-46}$$

Comparing the predicted collapse strength of P_u in Eq. (5-46) with the P_{u-EXP} of all the models, the ratios are shown in Fig. 5-24. The average is 0.92, with a COV of 0.13. It can be found that the prediction by the proposed formula in Eq. (5-46) can predict well the collapse strength of experimental specimens.

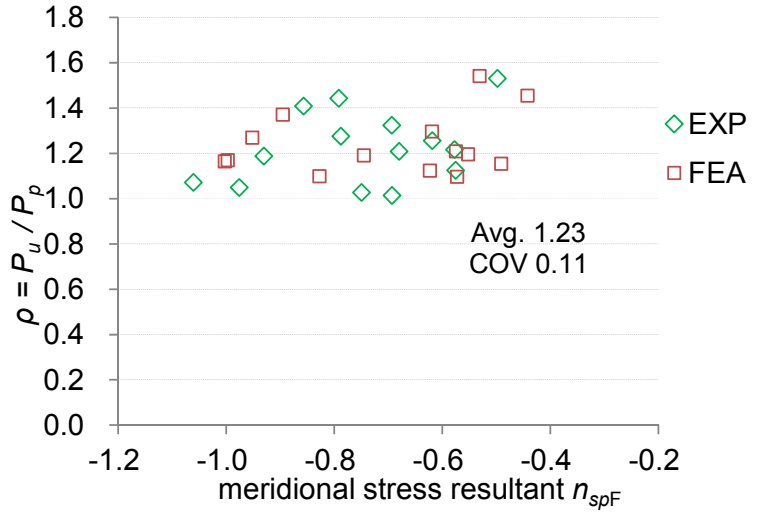

Fig. 5-23 Ratios of collapse strength to full plastic strength for both experimental and FEA results of models with conical wall failure

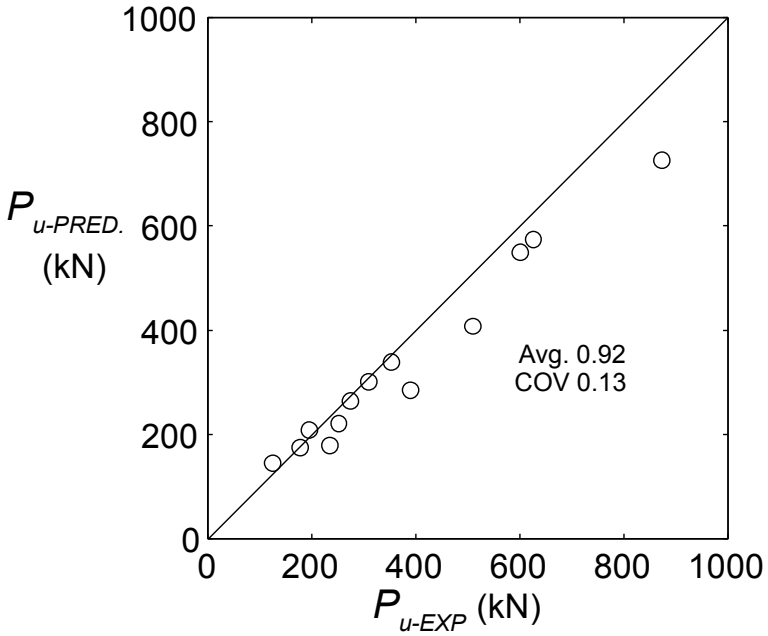

Fig. 5-24 Comparison of predicted collapse strength with experimental results for specimens with conical wall failure

5.5.3 Prediction of General Yield Strength

The ratios of general yield strength P_y to plastic strength P_p for both experimental and FEA results are listed in Fig. 5-25. It can be found that their average is 0.88 with a small COV of 0.06. The prediction of general yield strength P_y, is obtained by

$$P_{y-PRED} = \xi P_{p-PRED} = 0.88 P_{p-PRED} \tag{5-47}$$

The predicted results are compared with those of the experimental specimens, as shown in Fig. 5-26. It is found that the average value is 0.92 with a coefficient of variation of 0.11. The formula in Eq. (5-47) can predict well the general yield strength of experimental specimens.

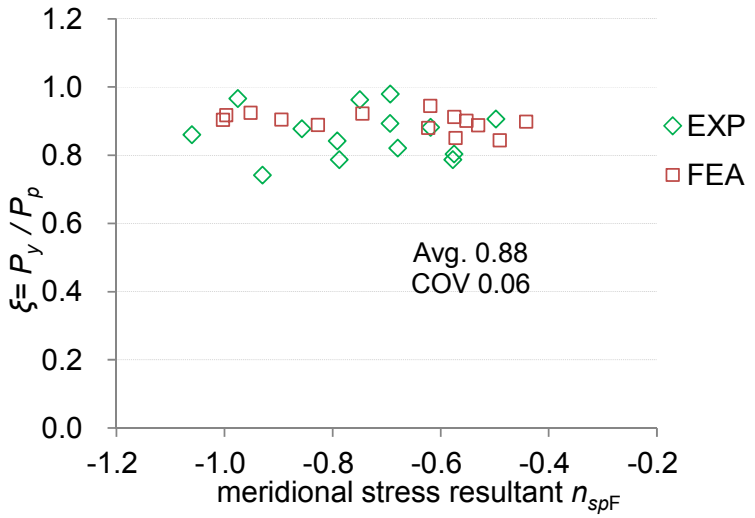

Fig. 5-25 Ratios of general yield strength to full plastic strength for both experimental and FEA results of models with conical wall failure

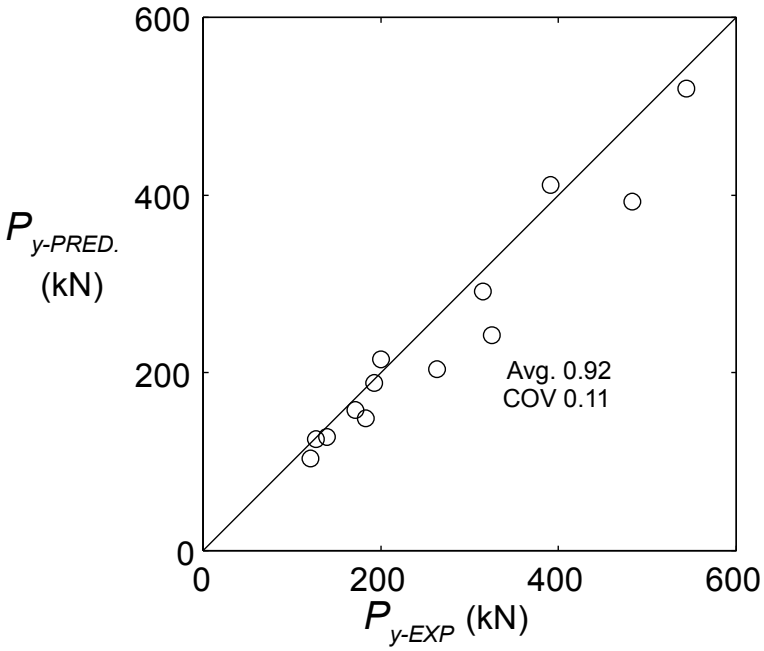

Fig. 5-26 Comparison of predicted general yield strength with experimental results for specimens with conical wall failure

5.6 Summaries

This chapter focuses on prediction of the strength of metal touch connections with conical wall failure. Based on the above analysis, the following conclusions are obtained.

(1) The axisymmetric solid models are effective to simulate conical wall failure of the socket connections. The friction coefficient between cone and cylinder is found to be greater than that of models with cylinder edge failure and tapered ring failure. But in practical design work, setting it to be 0.20 is also acceptable.

(2) The failure of the conical walls is assumed to be controlled by "plastic collapse" based on the proposed criterion.

(3) Easy-to-use formulae for predicting the full plastic strength is derived by limit analysis. Some satisfactory simplification is employed. The predicted values agree well with the effective FEA results, especially for the models with relatively large diameter to thickness ratios. While, for the models Nos. 9, 34 and 36, with quite small diameter-to-thickness ratios and height-to-thickness ratios, under-prediction is obtained.

(4) The collapse strength and general yield strength of experimental specimens are proposed based on the formula for full plastic strength. Their precision is proved by comparing them with the experimental results.

CHAPTER 6 STRENGTH OF WELDED CONNECTIONS WITH JOINT REGION FAILURE

6.1 Introduction

Relatively thick conical shells of low values of the diameter-to-thickness ratio are usually used as structural components in engineering applications, such as pipelines, offshore platforms and transition elements between cylinders of different diameters. If a conical shell is fixed at both ends and then compressed axially, “plastic buckling of cone” is probable to occur (Chryssanthopoulos and Poggi 2001, Blachut et al. 2010, Ifayefunmi 2015). While, it may be not typical in the case of a cone-to-cylinder intersection, because that the slope discontinuity in shell meridian, leading to local high bending and circumferential stresses, makes the joint region become a structural weakness (Teng and Rotter 1991). “Plastic collapse of joint region” is possible to control the failure of intersection.

However, “Plastic collapse” and “plastic buckling”, as two main failure modes for relatively thick shells or intersections under compressive loading, or along with radial pressure, is rather blurred to be distinguished (Kuwamura and Ito 2009). This is partly due to the fact that the onset of buckling in the shell walls is difficult to pinpoint experimentally (Wilbert, et al. 2011). Collapse load is usually defined as the peak load of load-deformation curves. But how to determine eigenvalue plastic buckling (bifurcation) load is difficult even by finite element analysis (FEA) because of the limitation of some commercial software, such as ABAQUS FE package (Hibbitt et al. 2011), in which the inelastic material properties are ignored during eigenvalue buckling analysis. Riks method algorithm (Riks 1979) based on a Lagrangean formulation for moderately large

deflections is implemented in ABAQUS to simulate nonlinear post-buckling and collapse behaviors. But it cannot obtain bifurcation load directly and rigorously.

For the welded cone-to-cylinder socket connections in this study, it was observed that the failure occurred close to the joint region between cone and cylinder. Kuwamura et al. (2005) proposed a formula for plastic buckling strength of conical wall based on the assumptions that cylindrical wall is rigid and conical wall is in membrane stress condition. Tomioka (2006) found that it overestimated the collapse strength of experimental specimens. The reason might be the actual boundary and stress conditions at ultimate load are different from the assumption. Plastic collapse of the intersection may be another possibility. For example, Teng and Rotter (1991) proposed a plastic collapse mechanism for steel silo transition junctions under internal pressure and frictional downward drag on the hopper and predicted the strength effectively. Therefore, the failure mechanism and strength of the welded connections are necessary to be discussed in further.

In the first half of this chapter, FEA models are created and their effectiveness is validated. Distributions of deformation and stress resultants in conical and cylindrical walls are analyzed. The failure mode is judged based on the proposed criteria. It should be noted that no further discussion is given on plastic buckling of cone in this chapter; instead the effort is concentrated on the plastic collapse mechanism of welded connections.

In the second half of this chapter, the strength of connections is predicted by limit analysis. And then, the precision of the proposed formulae is validated by comparing them with the experimental results.

6.2 FE Modeling

6.2.1 General

Figure 6-1 shows the details of FEA models in ABAQUS (Hibbitt et al. 2011). Two coordinates, (r, θ, x) and (t, θ, s), are employed, in which t means normal direction and s

means meridional direction. The location of origin "O" in x direction is defined to coincide with the middle point of Sect. F, which is at the top edge of weld. The weld is simulated by the quadrilateral and triangular axisymmetric solid element CAX4R and CAX3. For all the parts in the model, mesh size is set to be 0.5mm, which is about equal to 1/6 of the smallest thickness of conical wall. The convergence of analysis results is verified.

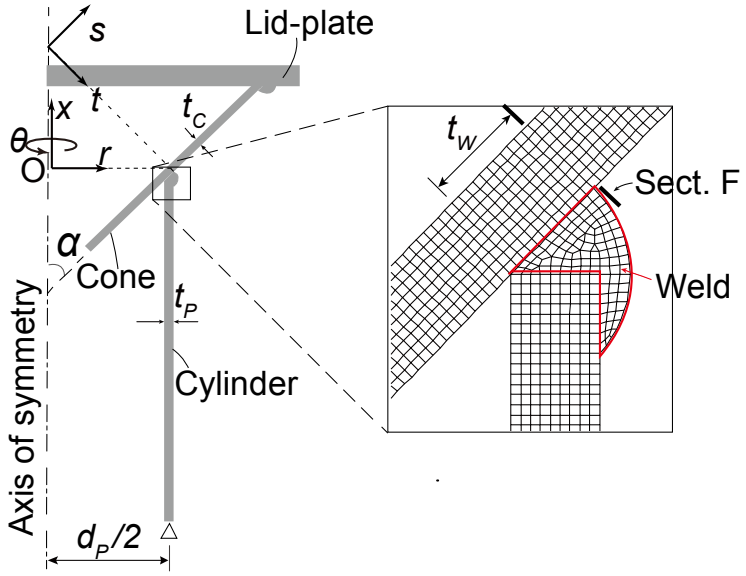

Fig. 6-1 Details of welded FE models

6.2.2 Influence of Weld Length on Collapse Strength of Connections

The material of weld is assumed to be the same as that of cylindrical wall. The softening of heat-affected zone and residual stress due to welding are not considered in this study. In this section, the influence of weld length on collapse strength of connections is investigated by FEA. Model No. 68 is taken as a typical case. The variation of collapse strength along with the ratio of weld length t_W to the thickness of cylindrical wall t_P is shown in Fig. 6-2. It is found that positive linear correlation occurs between them. As weld length t_W increases from t_P to $2t_P$, collapse strength P_{u-FEA} increases by about 20%. The influence of weld length on collapse strength is obvious. But for the weld

connections in this study, the weld length is difficult to be measured exactly. Moreover, it is usually just a little greater than base metal. In this study, weld length t_W in cone-to-cylinder joint is assumed to be $\sqrt{3}\,t_P$ for all the connections. As the thickness t_P of cylindrical wall is about 4.3mm, weld length t_W is 7.4mm and about 3mm longer than t_P, which is satisfactory in this study.

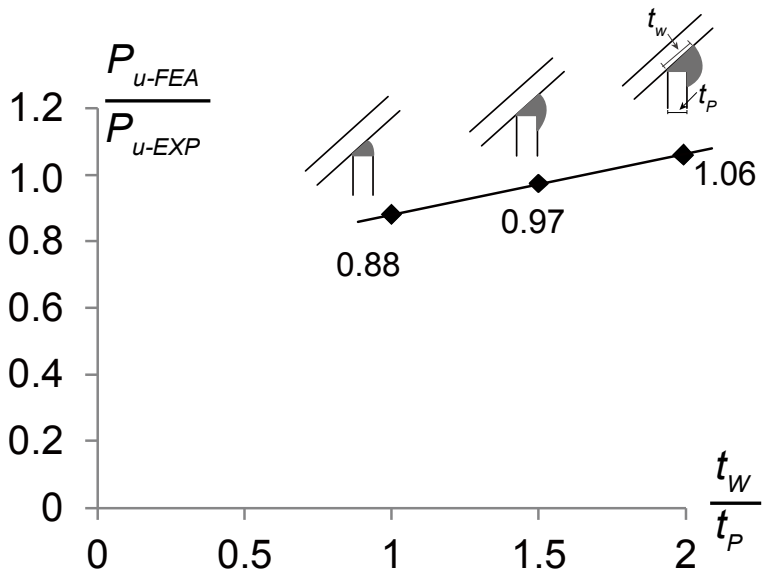

Fig. 6-2 Variation of collapse strength of connections along with the increase of weld length in cone-to-cylinder joint (Model No.68 is taken as a typical case)

6.2.3 Effectiveness of FE Models

Table 6-1 gives the comparisons of collapse strength P_u, full plastic strength P_p and general yield strength P_y obtained by FEA with those from experiments. Their definitions are the same as those shown in Chapter 3. It can be found that the averages of ratios are 1.01 for P_u, 0.95 for P_p and 0.94 for P_y respectively. The coefficients of variation (COV) for them are all very small.

In addition, the load versus axial deformation curves and ultimate deformation of FE models are compared with the relevant experimental results, as shown in Appendix B. Figure 6-2 shows the comparison of load versus axial deformation curves between FEA

and experiment for the typical model No. 68. It can be seen strength agrees well with each other. While, the degradation of load-axial deformation curve after collapse of FE model seems a little slower than that of experimental result. The reason might be that the residual stress, weld size, and the actual boundary condition in the welding region are not simulated precisely. But the FE models are effective for this study.

Maximum strength P_{max} of models with perfectly-plastic material is compared with Full plastic strength P_p of models with actual material, as shown in Fig. 6-4. The average of the ratios is 1.00, with a small COV of 0.02. It is found that the method of "K_0/6 slope factor" proposed by Tateyama (1988) is also effective to determine the full plastic strength of welded models with joint region failure.

Table 6-1 Comparison of strength between FEA and experiments for the welded connections with joint region failure

Model NO.	Experiments			FEA			Comparison		
	Collapse strength	Full plastic strength	General yield strength	Collapse strength	Full plastic strength	General yield strength	$P_{u\text{-}FEA}/P_{u\text{-}EXP}$	$P_{p\text{-}FEA}/P_{p\text{-}EXP}$	$P_{y\text{-}FEA}/P_{y\text{-}EXP}$
	$P_{u\text{-}EXP}$ (kN)	$P_{p\text{-}EXP}$ (kN)	$P_{y\text{-}EXP}$ (kN)	$P_{u\text{-}FEA}$ (kN)	$P_{p\text{-}FEA}$ (kN)	$P_{y\text{-}FEA}$ (kN)			
64	409.0	390.0	365.0	403.1	369.2	344.7	0.99	0.95	0.94
65	576.7	547.7	519.0	581.4	514.1	481.8	1.01	0.94	0.93
67	305.0	294.4	276.9	307.0	286.0	256.2	1.01	0.97	0.93
68	460.0	450.0	418.4	463.1	419.1	388.1	1.01	0.93	0.93
69	641.4	581.5	546.2	639.8	563.1	524.3	1.00	0.97	0.96
70	220.7	216.1	209.7	216.5	201.4	187.5	0.98	0.93	0.89
71	322.7	316.1	291.3	335.4	305.8	290.1	1.04	0.97	1.00
72	474.7	460.8	435.9	462.5	422.1	385.7	0.97	0.92	0.88
73	409.0	394.1	361.8	414.0	375.2	340.2	1.01	0.95	0.94
74	497.2	467.5	413.0	520.5	466.3	411.6	1.05	1.00	1.00
Avg.							1.01	0.95	0.94
COV							0.02	0.03	0.04

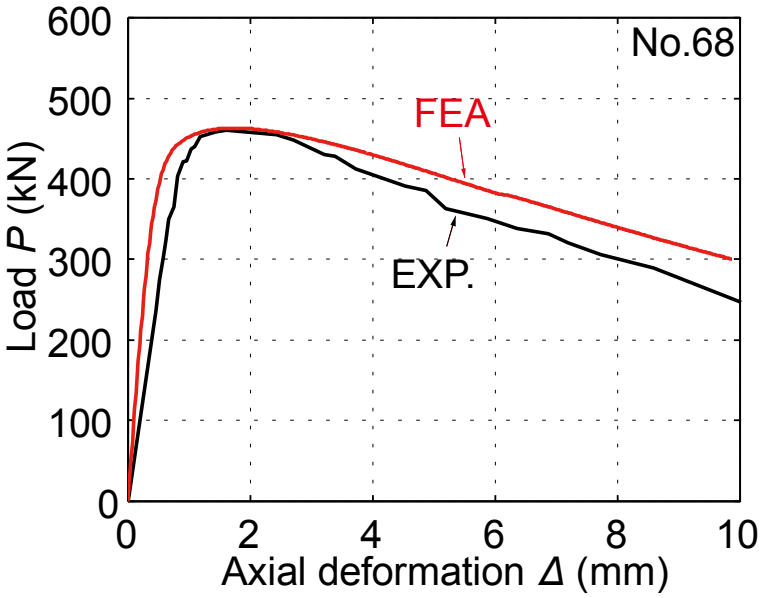

Fig. 6-3 Comparison of load versus axial deformation curves of model No. 68 between FEA and experiment

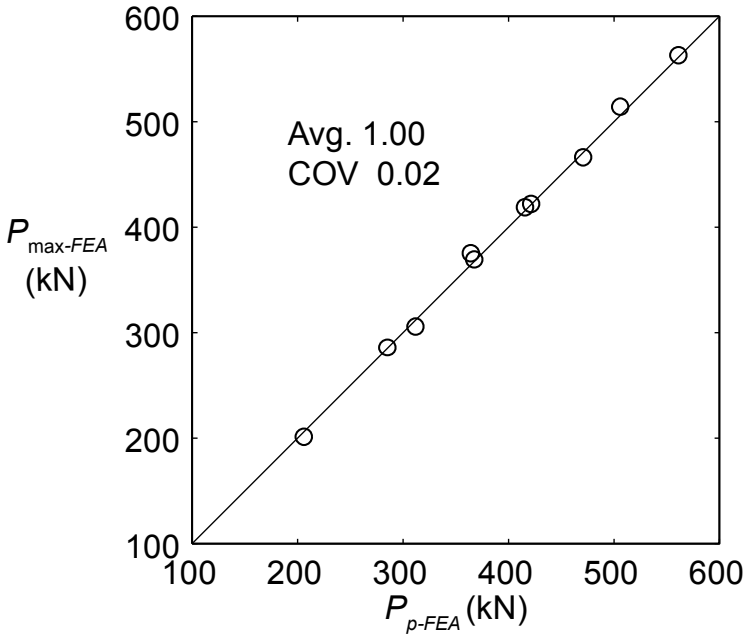

Fig. 6-4 Comparison of maximum strength to full plastic strength for welded models with joint region failure

6.3 FE Analysis Results

6.3.1 Distribution of Stress Resultants

In order to make clear the failure mechanism of models, the stress resultant

distributions are analyzed. It is noted that the definitions of stress resultants in conical and cylindrical walls are omitted here because they are the same as those in Chapters 3 and 5. Model No.68 with actual material is taken as a typical case.

Figure 6-5 shows the changing distributions of shear stress resultant τ_{st} in conical wall and τ_{xr} in cylindrical wall under increasing load. It can be found that τ_{st} at Sect. F decreases rapidly from the upper part of conical wall. The τ_{xr} at cylinder edge is the greatest in cylindrical wall.

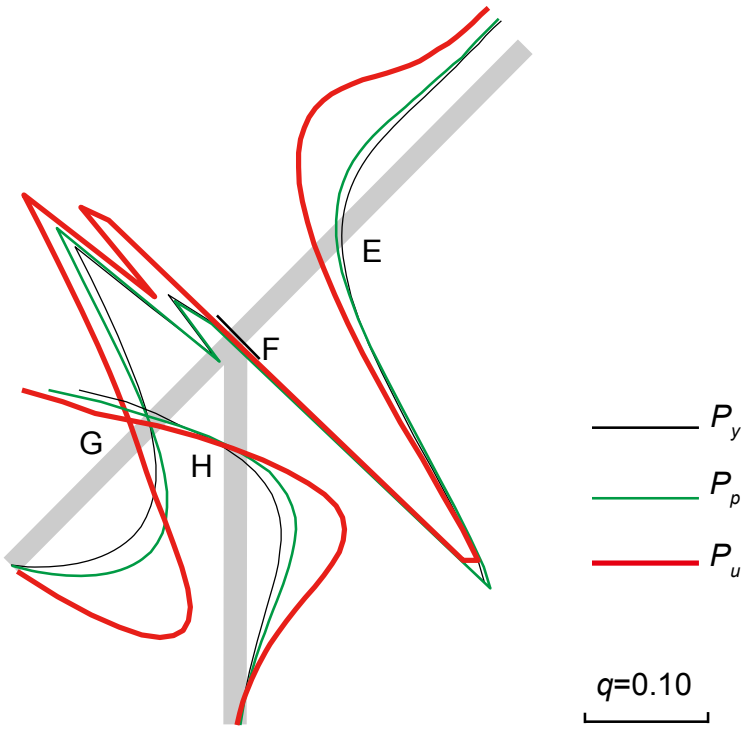

Fig. 6-5 Changing distributions of shear stress resultant in both conical and cylindrical walls under increasing load for model No.68

Figure 6-6 shows the changing distributions of meridional bending moment m_s in conical wall and axial bending moment m_x in cylindrical wall under increasing load. It can be found that for m_s in conical wall, its distribution type is the letter of " W ", which is similar to that of models with conical wall failure in Chapter 5. The $|m_s|$ increases as

load increases. The sections where m_{su} reaches local peak value are defined as Sects. E, F and G. It is found that m_{su} reaches peak value in negative direction in Sect. F, which is located at the top edge of welding. For m_x in cylindrical wall, it reaches local peak value at Sect. H. The nearer a section get to the top end of cylinder wall, the smaller is m_x. Finally, it becomes close to zero at the top end.

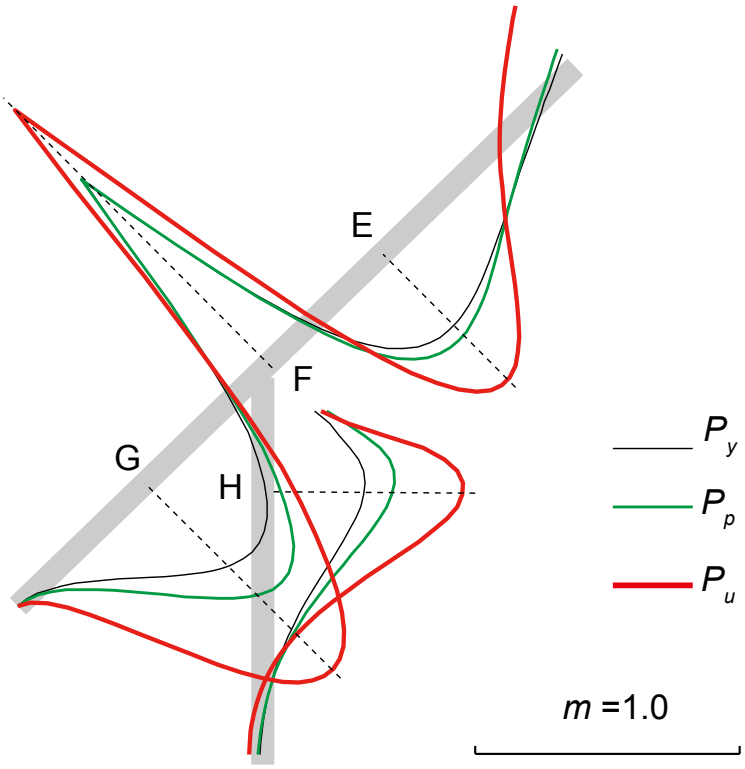

Fig. 6-6 Changing distributions of bending moment in both conical and cylindrical walls under increasing load for model No.68

Figure 6-7 shows the changing distributions of hoop stress resultant n_θ in conical and cylindrical walls under increasing load. Their distribution is concentrated in two regions. One is from Sect. E to Sect. G in conical wall; the other is from the top end of cylinder wall to Sect. H. Thus, the joint region will be weak because local high bending moment and hoop stress occur there.

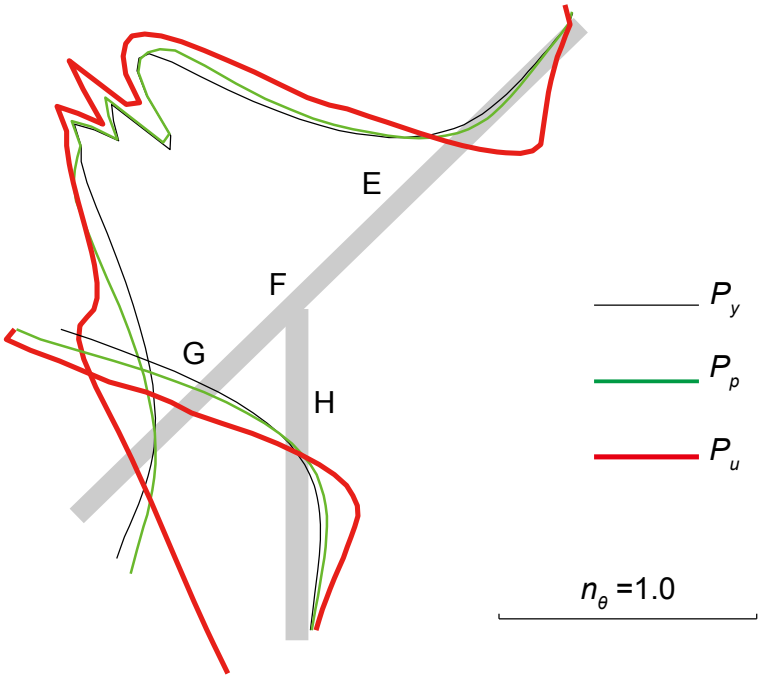

Fig. 6-7 Changing distributions of hoop stress resultant in conical and cylindrical walls under increasing load for model No.68

6.3.2 Distribution of Deformation

Model No.68 with actual material is taken as a representative case to introduce the deformation characteristics of models. Its behavior with the increase of loading is shown in Fig. 6-8, where the deformation scale factor is set to be 10. It can be found that the deformation is concentrated in the joint region. Not only in the upper part of conical shell, but also in the lower part of it and in the top edge of cylindrical shell, bending behavior is obvious.

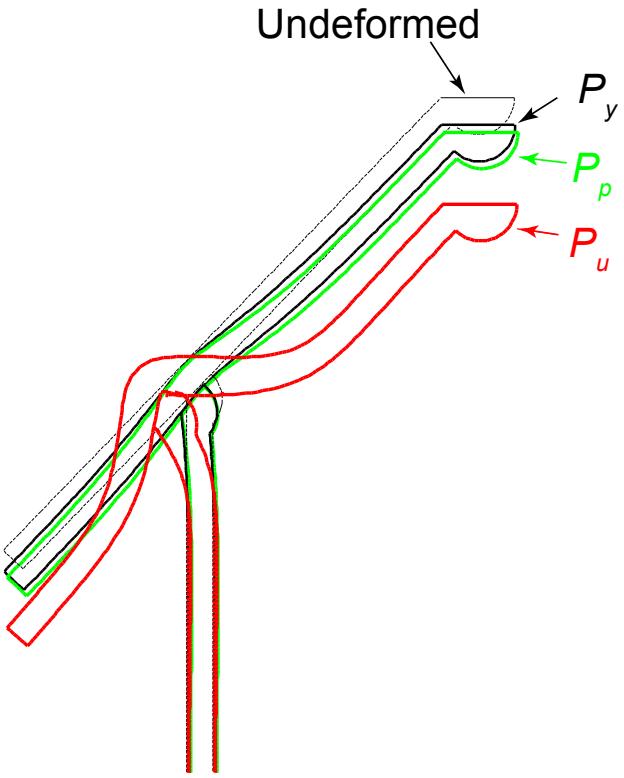

Fig. 6-8 Changing distributions of deformation in conical and cylindrical walls under increasing load for model No.68
(Deformation scale factor is set to be 10)

6.4 Judgement of Failure Mode

6.4.1 Definition of the Criteria of Failure Mode

The criterion of "plastic collapse" is defined as follow. The ratio of average equivalent stress $\overline{s}_{eq}$ in a section to yield stress σ_y is defined as

$$r=\frac{\overline{s}_{eq}}{\sigma_y}=\frac{\int_{-t/2}^{t/2} s_{eq}\mathrm{d}z}{\sigma_y t} \tag{6-1}$$

where, equivalent stress s_{eq} in each small mesh is obtained by

$$s_{eq}=\sqrt{s_s^2-s_s s_\theta+s_\theta^2+3\tau_{st}}$$

herein, s is true normal stress, τ is true shear stress, and σ is engineering normal stress.

If r in a section with peak meridional bending moment m_s satisfies that $r_{(m_s=m_{s,peak})}$

$\approx$1.0, a plastic hinge is assumed to form there. If the number of plastic hinges becomes sufficient and the kinematically admissible state is reached just prior to or at collapse load, the failure is assumed to be governed by "plastic collapse". It should be noted that

(1) Because of the strain hardening effect of materials, $r_{(m_s=m_{s,peak})}$ in some section where plastic deformation is great, is possible to exceed 1.0;

(2) Some section with peak meridional bending moment does not enter into plastic range at ultimate load. From the engineering point of view, $r_{u(m_{su}=m_{su,peak})} \geq 0.8$ is acceptable for the determination of plastic hinge.

6.4.2 Failure mode of Models

Figure 6-9 shows the changing distributions of r in conical and cylindrical walls under increasing load for model No.68. It is found that the region near to Sect. F enters into plastic when general yield load arrives. The r_u in Sects. E, F, G and H are all greater than 1.0 when collapse load arrives. It indicates that four plastic hinges will form there.

The r_u in Sects. E, F, G and H for all the welded models with joint region failure are listed in Fig. 6-10. It is found that all the values of r_u are close to or larger than 1.0. Therefore, the failure mode can be assumed to be controlled by "plastic collapse of joint intersection".

Based on the above analysis, it is known that for each model, the number of plastic hinges is sufficient and the kinematically admissible state is reached at ultimate load. Therefore, the failure of welded cone-to-cylinder connections in this study is assumed to be controlled by "plastic collapse of joint region".

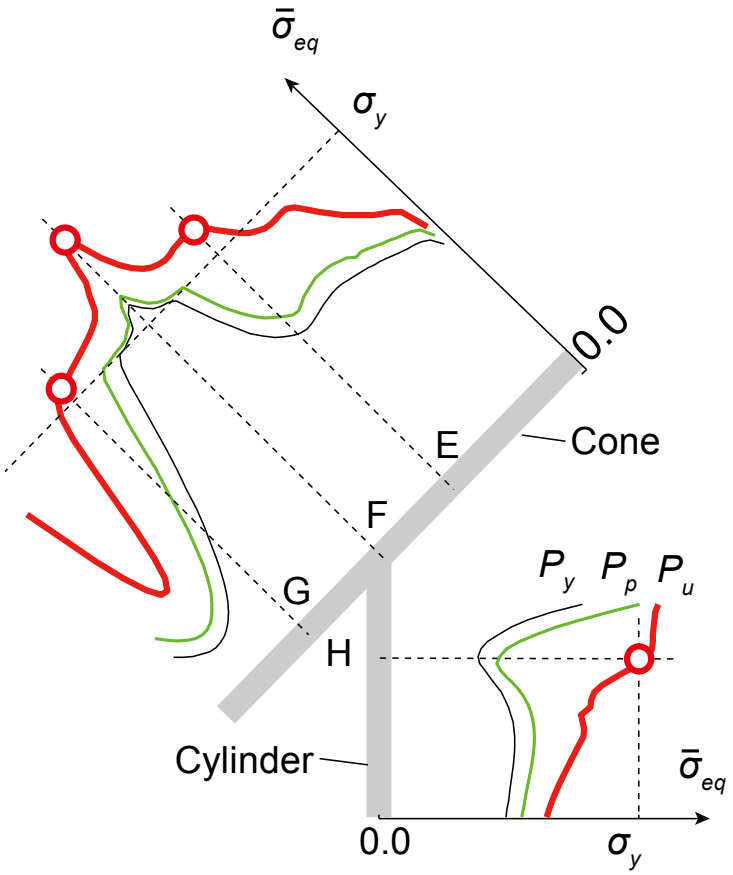

Fig. 6-9 Changing distributions of average equivalent stress in both conical and cylindrical walls under increasing load for model No.68

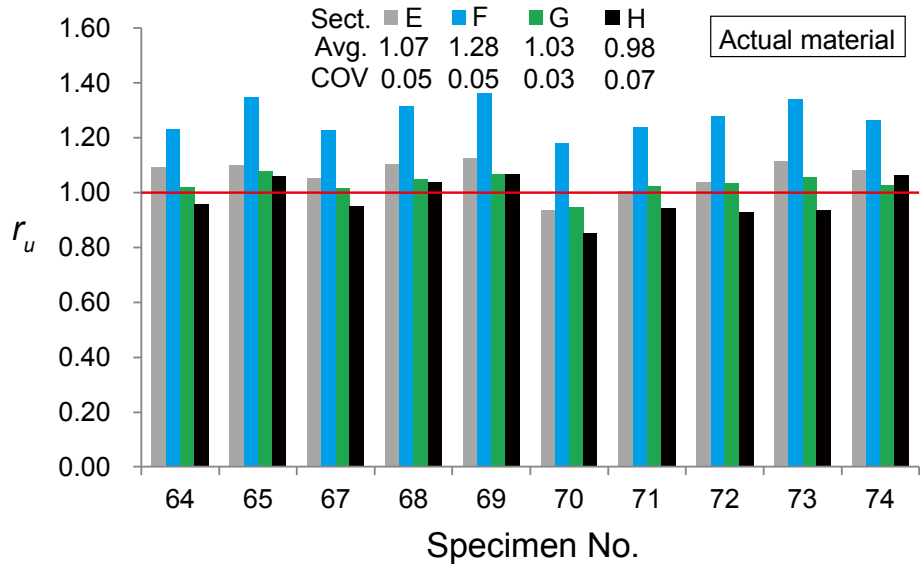

Fig. 6-10 Ratio r_u of average equivalent stress to yield stress in Sects. E, F, G and H for welded models with joint region failure

6.5 Prediction of Strength

6.5.1 Prediction of Full Plastic Strength

A plastic collapse mechanism shown in Fig. 6-11 is proposed. The dissipation of internal energy is absorbed by plastic hinges E, F_1, F_2, G and H, and segments EF_1, F_2G, and F_3H. It totally includes two parts: one is absorbed by conical wall and the other by cylindrical wall. It should be noted that the distance among Sects. F_1, F_2 and F_3 is defined to be zero. The location of Sects F_1, F_2 and F_3 is the same as Sect. F in the model. The welding region is neglected in the failure mechanism and the top edge of cylinder wall is assumed to coincide with Sect. F

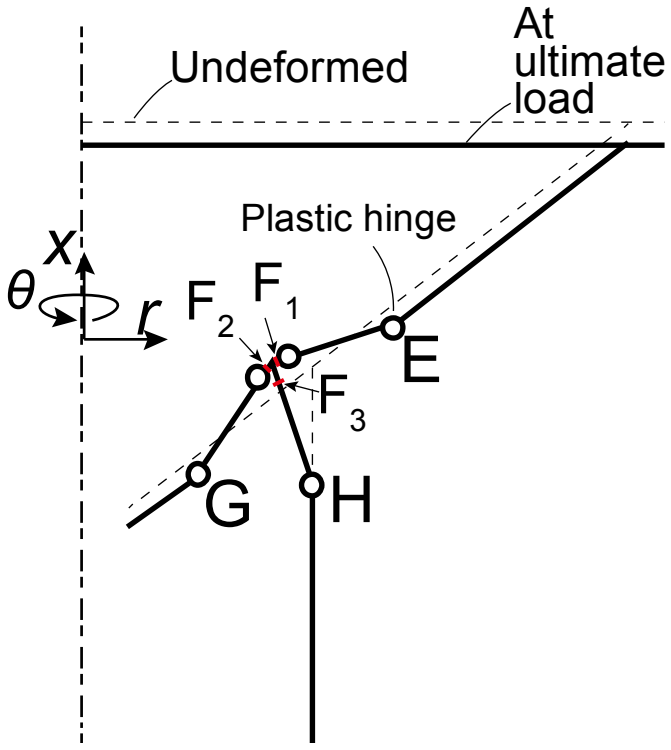

Fig. 6-11 Proposed plastic collapse mechanism for welded models with joint region failure mode

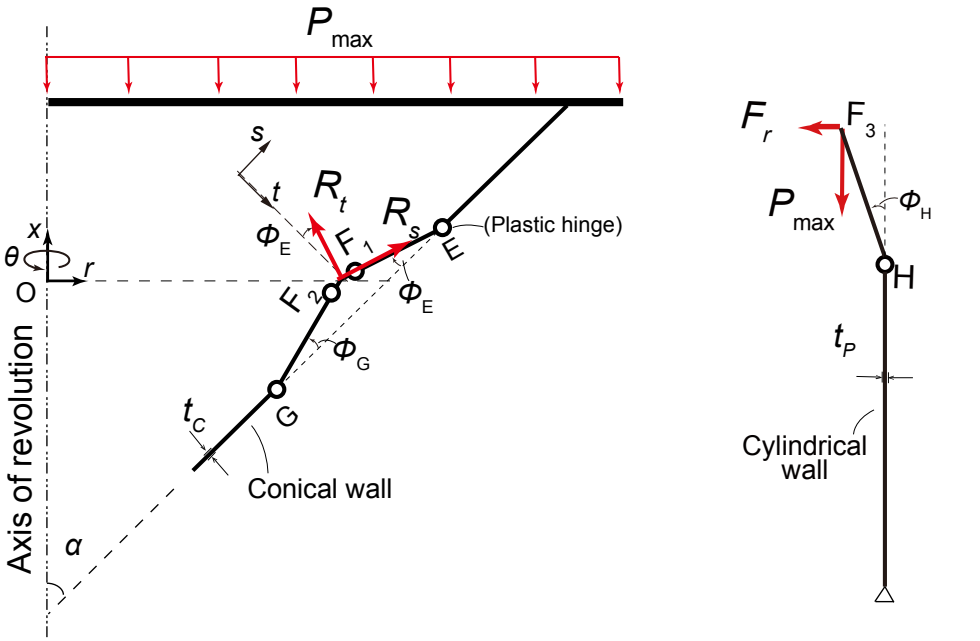

(a) In conical wall (b) In cylindrical wall

Fig. 6-12 External forces applied in conical and cylindrical walls

For conical wall, reaction forces R_t and R_s from cylindrical wall are assumed to be applied in Sect. F_1, as shown in Fig. 6-12(a). For cylindrical wall, external forces $P_{\max}$ and F_r from conical wall are assumed to be applied in Sect. F_3, as shown in Fig. 6-12(b). It is noted that all the external forces are defined to be acted in the whole model in 360 degrees in hoop direction. Their equilibriums are given by

$$-R_t \sin(\alpha+\phi_E) - R_s \cos(\alpha+\phi_E) = P_{\max} \tag{6-2a}$$

$$-R_t \cos(\alpha+\phi_E) + R_s \sin(\alpha+\phi_E) = F_r \tag{6-2b}$$

Combining Eqs. (6-2a) and (6-2b) by eliminating R_s, the relationship among $P_{\max}$, R_t and F_r is expressed as

$$P_{\max} = \frac{-R_t}{\sin(\alpha+\phi_E)} + \frac{-F_r}{\tan(\alpha+\phi_E)} \tag{6-3}$$

It indicates that ultimate strength includes two parts: the former one induced by conical shell, and the latter one by cylindrical shell. They are assumed to be independent

with each other.

For the one induced by conical wall, R_t can be derived based on the principle of virtual work as introduced in section 5.5.1. From Eq. (5-34), it can be obtained. The derivation procedure is omitted here.

$$R_t = -1.05\left(\sqrt{-2.1m_{s\max \mathrm{F1}}\left(\frac{1}{2}n_{s\max \mathrm{F_1}} - \sqrt{1-\frac{3}{4}n_{s\max \mathrm{F_1}}^2}\right)} + \sqrt{\frac{2}{\sqrt{3}} - m_{s\max \mathrm{F_2}}}\right)\sqrt{\frac{t}{d_{\mathrm{F_1}}}}\pi d_{\mathrm{F_1}}\sigma_y t\sqrt{\cos\alpha} + \frac{P_{\max}}{\cos\alpha}\phi_{\mathrm{E}} \tag{6-4a}$$

Herein, the stress resultants are assumed as follow:

$$m_{s\max \mathrm{F_1}} = m_{s\max \mathrm{F_2}} = \frac{2}{\sqrt{3}}\left(-1+\frac{3}{4}n_{s\max \mathrm{F_1}}^2\right) \tag{6-4b}$$

For the other induced in cylindrical wall, F_r can be derived based on virtual work principle as introduced in section 3.5.2. It should be mentioned that the top edge of cylindrical shell is under hoop compression, and no axial bending moment is acted in Sect. $\mathrm{F_3}$. These are two key points different from models with cylinder edge failure. The F_r can be obtained from Eq. (3-44). The derivation procedure is also omitted here.

Because the direction of F_r is opposite to that in Eq. (3-44),

$$F_r = -\sqrt{-m_{x\max \mathrm{H}}n_{\theta\max \mathrm{F_3H}}}\sqrt{d_P t_P}\sigma_{yP}t_P\pi + P_{\max}\phi_{\mathrm{H}} \tag{6-5a}$$

Herein, the stress resultants are assumed as follow.

$$n_{\theta\max \mathrm{F_3\,H}} = \frac{1}{2}n_{x\max \mathrm{F_3H}} - \sqrt{1-\frac{3}{4}n_{x\max \mathrm{F_3\,H}}^2} \tag{6-5b}$$

$$m_{x\max \mathrm{H}} = \frac{2}{\sqrt{3}}\left(1-\frac{3}{4}n_{x\max \mathrm{H}}^2\right) \tag{6-5c}$$

Substituting Eqs. (6-4) and (6-5) into Eq. (6-3), assuming that $\alpha+\phi_{\mathrm{E}} = \alpha$ based on the small deformation theory, and then dividing the both sides of Eq. (6-3) by

$\sigma_{yC} t_C d_{CF_1} \pi \cos\alpha$, the follow equation for meridional stress resultant $n_{s\max CF_1}$ is obtained.

$$n_{s\max CF1} = -(\psi_C + \psi_P \beta)\gamma \cdot \chi \tag{6-6a}$$

Herein,

$$\psi_C = 1.05\left(\sqrt{-\frac{4.2}{\sqrt{3}}\left(1-\frac{3}{4}n_{s\max CF_1}^2\right)\left(\frac{1}{2}n_{s\max CF_1} - \sqrt{1-\frac{3}{4}n_{s\max CF_1}^2}\right)} + \sqrt{\frac{4}{\sqrt{3}} - \frac{\sqrt{3}}{2}n_{s\max CF_1}^2}\right) \tag{6-6b}$$

$$\psi_P = \sqrt{\frac{2}{\sqrt{3}}\left(-1+\frac{3}{4}n_{x\max H}^2\right)\left(\frac{1}{2}n_{x\max H} - \sqrt{1-\frac{3}{4}n_{x\max H}^2}\right)} \tag{6-6c}$$

$$\beta = \frac{\sigma_{yP} t_P \sqrt{t_P}}{\sigma_{yC} t_C \sqrt{t_C}} \sqrt{\cos\alpha} \tag{6-6d}$$

$$\chi = \sqrt{\frac{t_C}{d_{CF_1}}} \frac{\sqrt{\cos\alpha}}{\cos\alpha \sin\alpha} \tag{6-6e}$$

$$\gamma = \frac{\cos\alpha \sin\alpha}{\cos\alpha\left(\sin\alpha + \phi_H \cos\alpha\right) + \phi_E} \tag{6-6f}$$

A quadratic approximation of ψ_C is obtained as

$$\psi_C = -1.76 n_{s\max CF_1}^2 - 0.68 n_{s\max CF_1} + 3.22 \tag{6-7}$$

The variation of ψ_P in Eq. (6-6c) along with axial stress resultant $n_{x\max H}$ is shown in Fig. 6-13. A quadratic approximation is obtained as

$$\psi_P = -0.92 n_{x\max H}^2 - 0.42 n_{x\max H} + 1.06 \tag{6-8a}$$

Herein

$$n_{x\max H} = \kappa \cdot n_{s\max CF_1} \tag{6-8b}$$

where

$$\kappa = \frac{\sigma_{yC} t_C}{\sigma_{yP} t_P} \cos\alpha \tag{6-8c}$$

Then the variation of factor γ in Eq. (6-6e) along with the rotational angle ϕ_E in

Sect. E is shown in Fig. 6-14. It can be seen the average is 0.92, with a small COV of 0.01.Thus, the γ is assumed to be a constant of 0.92 for all the models.

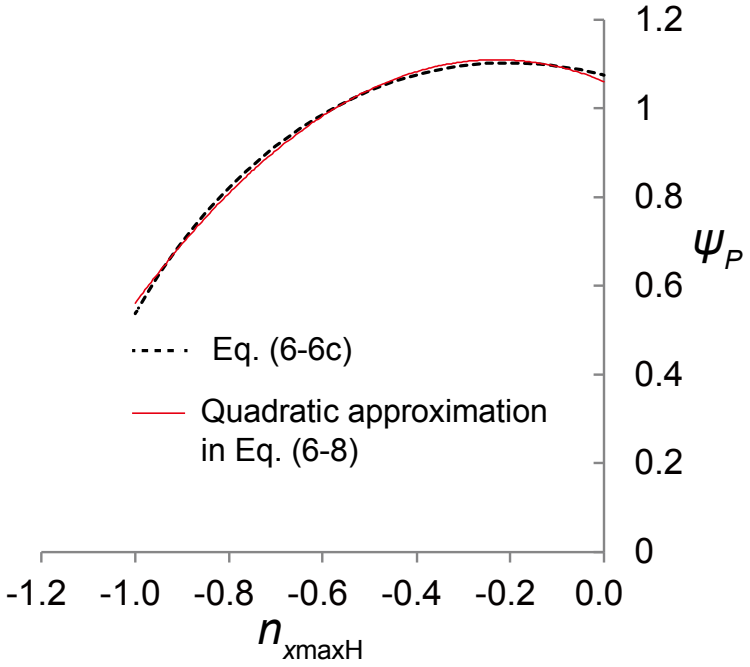

Fig. 6-13 Plot of ψ_P along with $n_{x\max H}$ and the quadratic approximation

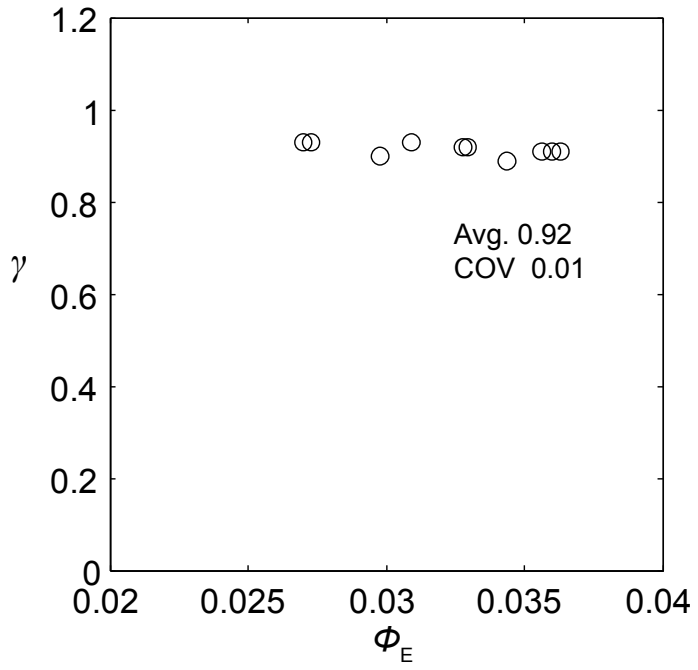

Fig. 6-14 Variation of factor γ along with rotational angle ϕ_E for all the welded models with joint region failure

Substituting Eqs. (6-6), (6-7) and $\gamma = 0.92$ into Eq. (6-5a), the simplified equation for $n_{s\max F_1}$ is obtained as

$$\left(1.62\chi + 0.85\kappa^2\beta\chi\right) n_{s\max CF_1}^2 + \left(0.63\chi + 0.39\kappa\beta\chi - 1\right) n_{s\max CF_1} - 2.96\chi - 0.98\beta\chi = 0 \tag{6-9}$$

The solution of $n_{s\max F_1}$ is

$$n_{s\max CF_1} = -\frac{0.63\chi + 0.39\kappa\beta\chi - 1 + \sqrt{19.58\chi^2 - 1.26\chi + 1 + (10.06\kappa + 6.35\frac{\chi}{\kappa} + 3.48\kappa\beta\chi + 0.49\chi - 0.78)\kappa\beta\chi}}{3.24\chi + 1.70\kappa^2\beta\chi} \tag{6-10}$$

The prediction of maximum strength $P_{\max}$ of models can be finally obtained as

$$P_{\max-PRED} = -n_{s\max CF_1}\pi d_{CF_1} t_C \sigma_{yC}\cos\alpha \tag{6-11}$$

The predicted values of $P_{\max}$ in Eq. (6-11) are compared with those of FEA results. The results are shown in Fig. 6-15. The average of ratios is 0.92 with a COV of 0.06. A good agreement with each other can be found. Thus, full plastic strength P_p of models is predicted by

$$P_{p-PRED} = -n_{s\max CF_1}\pi d_{CF_1} t_C \sigma_{yC}\cos\alpha \tag{6-12}$$

herein, $n_{s\max F_1}$ is obtained by Eq. (6-10).

The predicted values of P_p are compared with those of experimental results. The results are shown in Fig. 6-16. The average of ratios is 0.88 with a COV of 0.06. The full plastic strength of connections with joint region failure can be predicted well by the proposed mechanism.

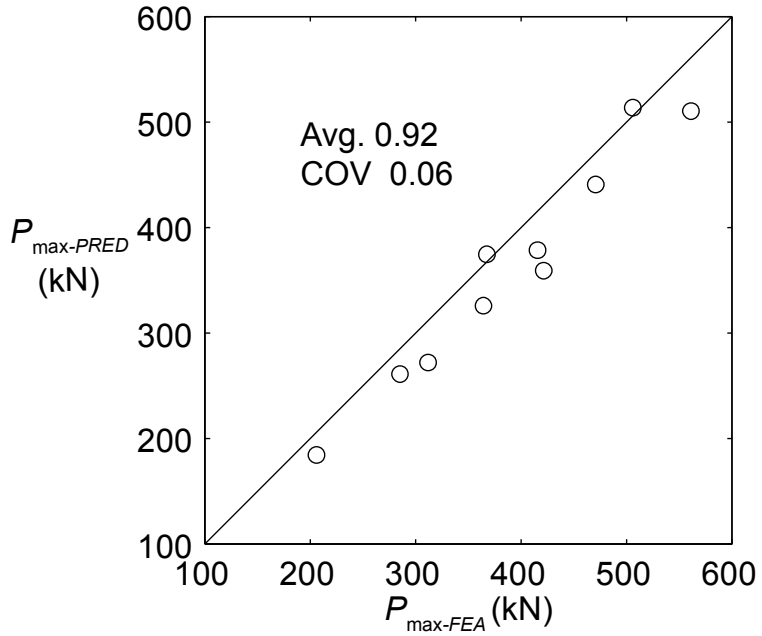

Fig. 6-15 Comparison of predicted maximum strength with FEA results for welded models with joint region failure

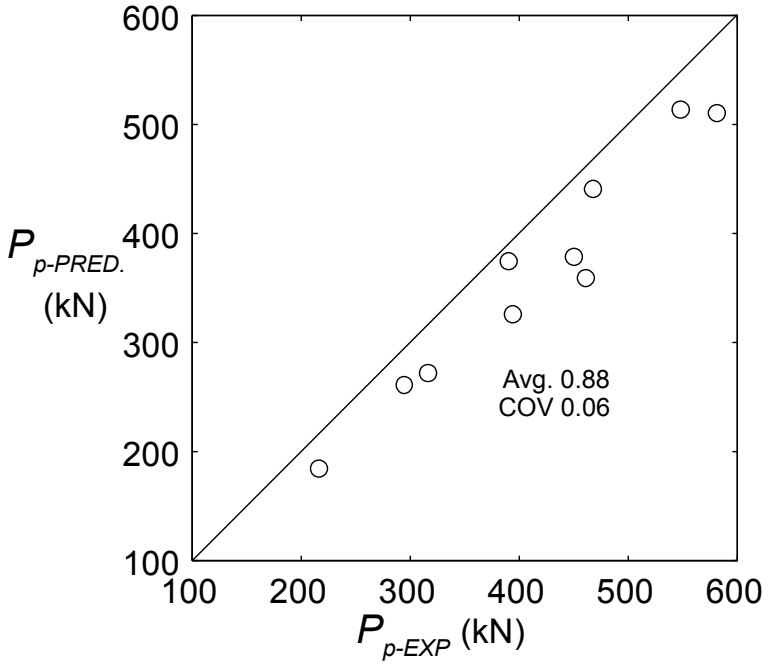

Fig. 6-16 Comparison of predicted full plastic strength with experimental results for welded models with joint region failure

6.5.2 Prediction of Collapse Strength

The enhancement factor ρ is assumed as the average of the ratios of collapse strength to full plastic strength for both experimental specimens and FEA models. Their

average along with axial stress resultant n_{spF} is 1.07 with a COV of 0.04, as shown in Fig. 6-17. Collapse strength P_u is predicted by

$$P_{u\text{-}PRED} = \rho P_{p-PRED} = 1.07 P_{p-PRED} \tag{6-13}$$

The predicted values of collapse strength P_u by formula in Eq. (6-13) are compared with those by the plastic buckling equation of cone in Kuwamura et al. (2005b). The ratios of them to the experimental results are shown in Fig. 6-18. It is seen that the average in the case of the proposed formula in this study is 0.88. While, that in the case of plastic buckling equation is 1.28. It indicates that the proposed plastic collapse mechanism in the joint region can predict the collapse strength of welded models better than the plastic buckling mode of conical wall.

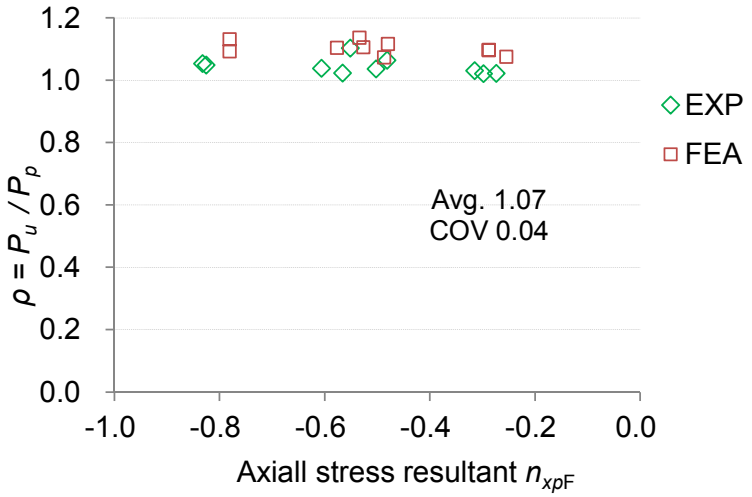

Fig. 6-17 Ratios of collapse strength to full plastic strength of both experiments and FEA for welded models with joint region failure

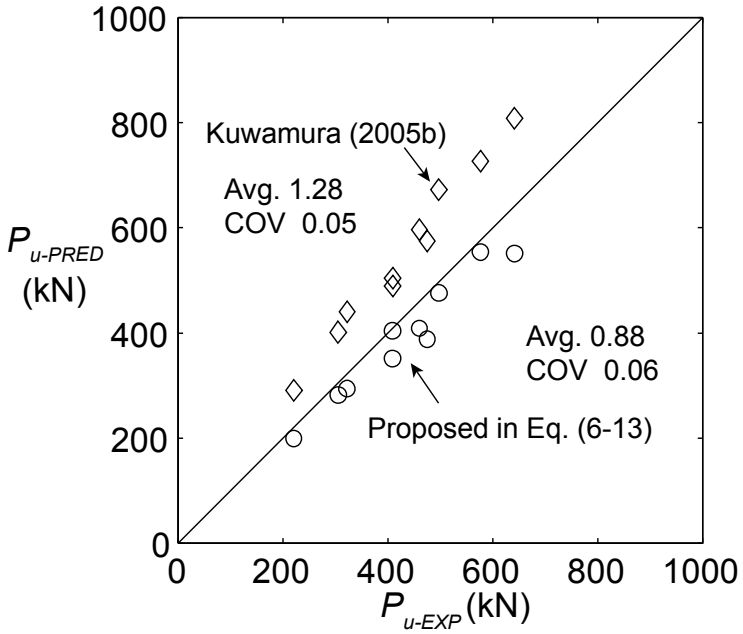

Fig. 6-18 Comparison of proposed formula and previous one for collapse strength with experimental results for welded models with joint region failure

6.5.3 Prediction of General Yield Strength

The ratios ξ of general yield strength P_y to plastic strength P_p for both experimental and FEA results are listed in Fig. 6-19. It can be found that their average is 0.93 with a small COV of 0.02. The prediction of general yield strength $P_{y.}$ is obtained by

$$P_{y\text{-}PRED} = \xi P_{p-PRED} = 0.93 P_{p-PRED} \tag{6-14}$$

The predicted results are compared with those of experimental specimens, as shown in Fig. 6-20. It is found that the average value is 0.87 with a COV of 0.08. The proposed formula in Eq. (6-14) can predict well the general yield strength of experimental speicmens.

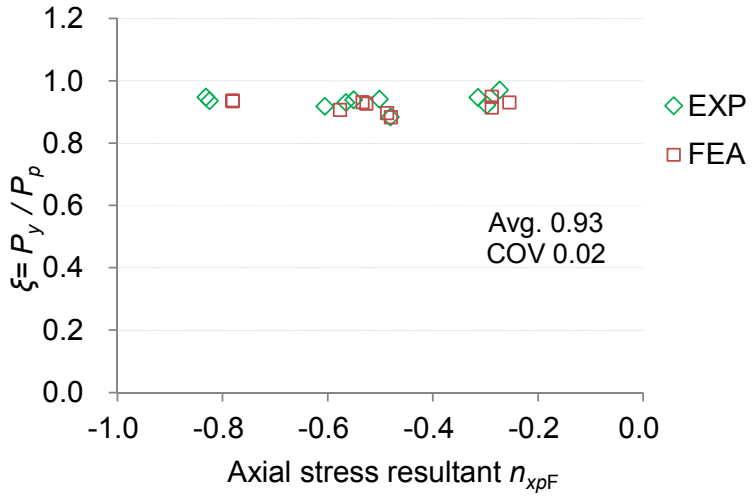

Fig. 6-19 Ratios ξ of general yield strength to full plastic strength of both experiments and FEA for welded models with joint region failure

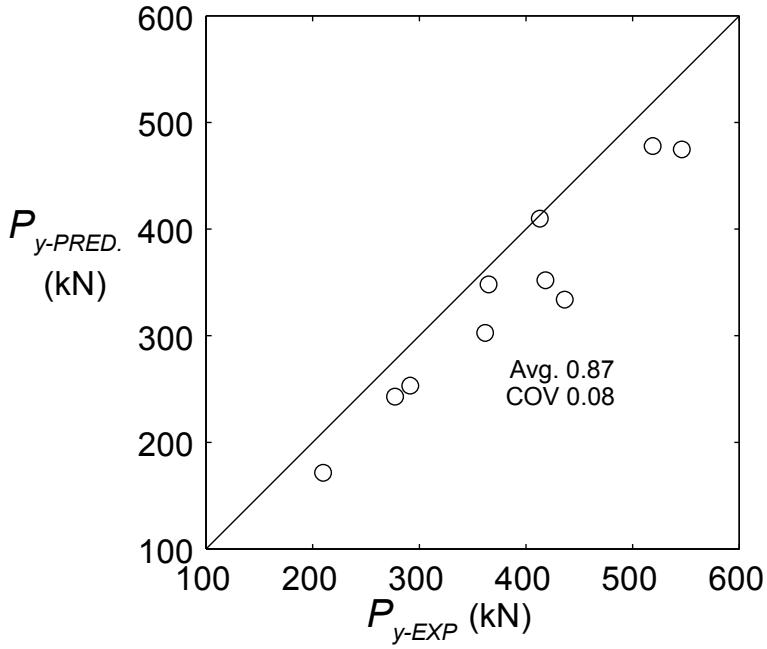

Fig. 6-20 Comparison of predicted general yield strength with experimental results for welded models with joint region failure

6.6 Summaries

This chapter focuses on prediction of the strength of welded cone-to-cylinder socket connections with joint region failure. Based on the above analysis, the following

conclusions are obtained.

(1) The distributions of deformation and stress resultant in conical and cylindrical walls are made clear. The intersection of cone and cylinder is weak because meridional bending moment, hoop stress resultant and radial deformation are all greater than those in other regions.

(2) The failure of the specimens is assumed to be governed by “plastic collapse of joint region” based on the proposed criteria, because the number of plastic hinges is sufficient and the kinematically admissible state is reached at ultimate load.

(3) The proposed plastic collapse mechanism can predict well the full plastic strength of experimental specimens. In addition, the prediction of collapse strength and general yield strength of models is also proposed and validated by the experimental specimens. The proposed formula can predict the collapse strength of models better than the previous plastic buckling equation for conical shells.

(4) The rigorous eigenvalue plastic buckling analysis needs to be undertaken in future to study the plastic buckling behavior of conical and cylindrical shells under axial compression.

CHAPTER 7 CONCLUSIONS AND FUTURE RESEARCH

7.1 Main Conclusions

For metal touch connections, the characteristics of frictional contact between conical and cylindrical walls are investigated. A satisfactory value of friction coefficient for practical design work is proposed. For both metal touch and welded connections, stress and deformation behaviors during the whole loading process are clarified. Their failure modes are determined based on the proposed criterion. The Mises' yield condition expressed by stress resultants for axisymmetrically loaded revolutional shells with perfectly-plastic material is simplified and validated by effective finite element (FE) analysis. Full plastic strength is effectively predicted by limit analysis, in which the influence of the correlation of stress resultants on failure mechanisms is considered. Collapse strength and general yield strength are also well predicted based on the formula for full plastic strength. The detailed findings are given in the following.

7.1.1 Metal Touch Connections

Based on the experimental, numerical and theoretical studies on metal touch connections with cylinder edge failure, tapered ring failure, and conical wall failure, the following main conclusions can be drawn.

(1) Failure mechanisms of connections with different kinds of boundary condition between conical wall and cylinder edge are determined by the proposed criterion. For the connections with cylinder edge failure, failure mode is controlled by plastic collapse of cylindrical shell; For the connections with tapered ring failure, failure mode is not only controlled by hoop tension of ring but also by plastic

collapse of cylindrical shell; and For the connections with conical wall failure, failure mode is controlled by plastic collapse of conical shell.

(2) The simplification of Mises' yield condition for axisymmetrically loaded revolutional shells with perfectly-plastic material, as shown in Eq. (7-1), can be employed as the basis of plastic analysis of shell structures.

$$\left|\frac{2n_{\theta\max}-n_{s\max}}{\sqrt{4-3n_{s\max}^2}}\right|^{2.5}+\left(\frac{2\sqrt{3}m_{s\max}}{4-3n_{s\max}^2}\right)^2=1 \qquad (7\text{-}1)$$

where, $n_{\theta\max}$, $n_{s\max}$, $m_{s\max}$ are the normalization of hoop stress resultant, meridional stress resultant and meridional bending moment in shell walls.

(3) The full plastic strength of connections is predicted well by plastic collapse mechanism, in which the correlation of stress resultants is considered. The prediction of collapse strength and general yield strength of connections, based on the formula for full plastic strength, are also in good agreement with experimental and FE analysis results.

(4) In practical design, conical shell, employed as pile head, is desirable to fail before the edge of cylindrical pile in order to protect the pile from damage. When conical shell bends inward, friction coefficient μ between conical wall and cylinder edge will be greater than 0.20 due to the breakdown of oxide film. Therefore, setting $\mu=0.20$ can be acceptable because it gives an obvious under-prediction for the strength of pile.

(5) In order to make sure that conical shell fails before the edge of cylindrical pile, it is necessary to know the collapse strength of connections with all the failure modes. The predicted collapse strength by the proposed formula for each mode is listed in Table 7-1. The failure mode with minimum collapse strength is assumed to occur. It is found that predicted mode coincides well with actual one. Taking specimen Nos. 34 and 36 for example, the expected failure mode before experiments is tapered ring failure. But actually they failed in conical wall

failure, which is the same as the prediction. It should be noted that the actual mode of specimen No.9 is conical wall failure, while prediction is cylinder edge failure. The reason is that the collapse strength of cylinder edge failure is underestimated when friction coefficient μ is set to be 0.20.

Table 7-1 Comparison of predicted failure mode with actual one for metal touch connections with different kinds of boundary condition

Boundary condition (cone-cylinder)	Specimen No.	Cone			Cylinder			Tapered ring		Predicted collapse strength (μ=0.20)			$P_{u\text{-min}}$	Predicted mode	Actual mode	Coincide or not
		Semi-angle	Thick-ness	Yield stress	External diameter	Thick-ness	Yield stress	Thick-ness	Yield stress	P_{u1}	P_{u2}	P_{u3}				
		α	t_C	σ_{yC}	D_P	t_P	σ_{yP}	t_R	σ_{yR}	Cylinder edge failure	Tapered ring failure	Conical wall failure				
		°	mm	mm	mm	mm	mm	mm	mm	kN	kN	kN				
"Metal touch"	1	31.97	8.74	317	139.80	3.32	331	-	-	75.0	-	640.8	P_{u1}	cylinder	cylinder	*yes*
	2	32.26	8.77	317	139.80	4.20	343	-	-	111.1	-	640.0	P_{u1}	cylinder	cylinder	*yes*
	3	32.64	8.67	317	140.50	6.03	361	-	-	202.0	-	623.0	P_{u1}	cylinder	cylinder	*yes*
	4	46.81	8.56	317	139.80	3.32	331	-	-	125.9	-	644.4	P_{u1}	cylinder	cylinder	*yes*
	5	45.91	8.53	317	140.00	4.30	343	-	-	184.1	-	637.8	P_{u1}	cylinder	cylinder	*yes*
	6	46.45	8.53	317	140.00	6.06	361	-	-	322.8	-	624.8	P_{u1}	cylinder	cylinder	*yes*
	7	59.26	8.63	317	140.05	3.33	331	-	-	209.2	-	575.9	P_{u1}	cylinder	cylinder	*yes*
	8	59.52	8.62	317	139.90	4.20	343	-	-	302.0	-	566.6	P_{u1}	cylinder	cylinder	*yes*
	9	59.97	8.64	317	140.00	6.03	361	-	-	526.5	-	552.5	P_{u1}	cylinder	cone	*no*
	10	32.72	8.46	317	114.50	4.24	369	-	-	110.8	-	532.4	P_{u1}	cylinder	cylinder	*yes*
	11	32.74	8.51	317	165.60	5.58	343	-	-	187.7	-	681.9	P_{u1}	cylinder	cylinder	*yes*
	12	47.34	8.50	317	114.30	4.23	369	-	-	181.5	-	542.0	P_{u1}	cylinder	cylinder	*yes*
	13	45.69	8.64	317	165.50	5.64	343	-	-	296.5	-	722.9	P_{u1}	cylinder	cylinder	*yes*
	14	59.71	8.64	317	114.40	4.25	369	-	-	292.1	-	481.4	P_{u1}	cylinder	cylinder	*yes*
"Metal touch +weak ring"	26	46.28	8.74	317	139.85	3.27	331	6.11	319	-	227.5	664.2	P_{u2}	ring	ring	*yes*
	27	46.25	8.77	317	139.75	3.34	331	9.16	321	-	347.5	666.4	P_{u2}	ring	ring	*yes*
	28	45.03	8.67	317	139.90	3.28	331	11.99	322	-	462.9	659.9	P_{u2}	ring	ring	*yes*
	29	46.64	8.56	317	139.75	4.13	343	6.01	319	-	282.3	639.3	P_{u2}	ring	ring	*yes*
	30	45.86	8.53	317	139.80	4.17	343	9.05	321	-	390.2	638.1	P_{u2}	ring	ring	*yes*
	34	46.08	8.64	317	139.85	5.99	361	12.00	322	-	663.8	636.2	P_{u3}	cone	cone	*yes*
	35	33.38	8.46	317	139.85	4.21	343	9.07	321	-	264.8	614.9	P_{u2}	ring	ring	*yes*
	36	62.39	8.51	317	139.90	4.14	343	9.06	321	-	673.1	528.8	P_{u3}	cone	cone	*yes*
	37	49.02	8.50	317	114.30	4.24	369	9.07	321	-	416.0	536.4	P_{u2}	ring	ring	*yes*
"Metal touch +strong ring"	43	33.27	3.05	299	139.90	4.21	343	12.07	322	-	366.7	136.2	P_{u3}	cone	cone	*yes*
	44	33.51	4.24	299	139.95	4.23	343	11.99	322	-	367.2	220.1	P_{u3}	cone	cone	*yes*
	46	46.03	3.05	299	139.90	4.24	343	11.98	322	-	535.6	145.5	P_{u3}	cone	cone	*yes*
	47	46.68	4.27	299	139.85	4.21	343	12.01	322	-	545.6	234.2	P_{u3}	cone	cone	*yes*
	48	48.01	5.74	299	139.95	4.19	343	12.02	322	-	567.0	351.4	P_{u3}	cone	cone	*yes*
	49	61.37	3.05	299	139.80	4.19	343	12.05	322	-	847.4	130.6	P_{u3}	cone	cone	*yes*
	50	60.56	4.25	299	139.85	4.20	343	11.98	322	-	823.3	208.1	P_{u3}	cone	cone	*yes*
	51	59.58	5.64	299	139.90	4.17	343	11.96	322	-	795.4	308.5	P_{u3}	cone	cone	*yes*
	52	44.80	4.29	299	114.50	4.26	369	12.01	322	-	493.3	207.2	P_{u3}	cone	cone	*yes*
	53	46.24	4.20	299	165.80	5.62	343	12.04	322	-	674.1	252.0	P_{u3}	cone	cone	*yes*

Note: specimen Nos. 15, 32, 33, 38, and 45 failed in asymmetric modes, and specimen No. 31 failed in cylindrical wall with elephant foot buckling mode. Their failure modes are outside the scope of this study and not included in this table.

(6) The reinforcement effect of tapered ring on the strength of connections is found to be obvious and can be predicted well by the proposed formulae. However, tapered ring failure does not always occur along with the increase of the thickness of ring. The failure mode would be turned into plastic collapse of conical wall or elephant foot buckling of cylindrical wall. The lateral one is necessary to be studied in future.

7.1.2 Welded Connections

(1) The strength of intersection of conical wall and cylinder edge is weak because the meridional bending moment, hoop stress resultant and radial deformation are all much greater than those in other regions.

(2) The failure mechanism of welded connections in this study is assumed to be governed by "plastic collapse of joint region" based on the proposed criteria, because the number of plastic hinges is sufficient and the kinematically admissible state is reached at ultimate load.

(3) The proposed plastic collapse mechanism can predict the full plastic strength of models more precisely than the previously proposed plastic buckling equation for conical shell.

(4) Plastic buckling strength of conical and cylindrical shells needs to be studied in order to make clear the bound of plastic collapse mechanism of joint region.

7.2 Future work

In future, the following items require further study on the steel cone-to-cylinder socket connections.

(1) The elastic stiffness of connections under compression needs to be studied.

(2) Plastic bifurcation buckling analysis needs to be undertaken to judge plastic buckling failure mode of shell structures. Some computer codes (eg. Bushnell,

1976; Teng and Rotter, 1989), which have been employed successfully in shell structures (Blachut, et al. 2010; Teng 1994a, b) will be studied.

(3) The gap between conical wall and cylinder edge will occur inescapably when conical wall rotates. Appendix D gives a qualitative study on the influence of gap on collapse strength of metal touch connections by finite element analysis. The relevant study is necessary to be undertaken in further.

(4) This study focuses on the strength of steel cone-to-cylinder socket connections under axial compression. Actually, shear force and bending moment are also transformed from upper structure due to earthquake or wind load. The socket connection will be compressed under eccentric loading. The corresponding strength and behavior of connections have not been clarified. Appendix E gives a qualitative study on the influence of eccentricity ratio of compressive loading on collapse strength of connections by finite element analysis. The relevant study needs to be undertaken in further.

(5) The seismic performance of structure with metal touch cone-to-cylinder socket connections is interesting to be studied.

REFERENCES

Architectural Institute of Japan (2002). “Design Standard for Steel Structures”.

ABAQUS Standard Manual (Version 6.11). Hibbitt, Karlsson & Sorensen, Inc., Pawtucket, RI, USA, 2011.

Alexander, J.M. (1960). “An Approximate Analysis of the Collapse of Thin Cylindrical Shells under Axial Loading”. *Quart.J. Mech. Appl. Math.* Vol. VIII. Pt.1, pp. 10-15

Andronicou, A. and Walker, A.C. (1981). “A Plastic Collapse Mechanism for Cylinders under Uniaxial End Compression”. *J. Constr. Steel Res.* Vol.1, No.4, pp. 23-34.

Blachut, J. and Ifayefunmi, O. (2010). “Plastic Buckling of Conical Shells”. *J. offshore Mech. and Arctic Eng.*, ASME. 132/041401

Building Research Institute and Japan Iron and Steel Federation. (2002). “Report of Study on Experimental Methods for Performance Evaluation of Steel Structural Buildings”.

Bushenell, D. (1976). “Bosor5: Program for Buckling of Elastic-Plastic Complex Shells of Revolution Including Large Deflections and Creep”. *Comput. Struct.*, 6(3), pp. 221-239.

Cao, J.J., Packer, J.A., Yang, G.J. (1998). “Yield Line Analysis of RHS Connections with Axial Loads”. *J. Constr. Steel Res.* 48, pp.1-25.

Chen, J. F. and Rotter, J. M. (1998). “ Effective Cross Sections of Asymmetric Rings on Cylindrical Shells”. *J. Struct. Eng.*, ASCE. 124. pp. 1074-1080.

Chryssanthopoulos, M.K. and Poggi, C. (2001). “Collapse Strength of Unstiffened Conical Shells under Axial Compression”. *J. Constr. Steel Res.* 57, pp.165-184.

Drucker, D.C. (1954). “Limit Analysis of Cylindrical Shells under Axially-Symmetric Loading”. *Proceedings First Midw. Conf. Solid Mech.* (Urbana, 1953), Eng. Exp. Sta., Univ. of Illinois, pp. 158-163.

Eason, G and Shield, R.T. (1955). “The Influence of Free Ends on the Load Carrying Capacities of Cylindrical Shells”. *J. Mech. Phys. Solids*, Vol. 4, pp. 17-27.

Ehara, Y., Ito, T. and Kuwamura, H. (2007). “Study on Steel Cone-to-Cylinder Socket Connections Part 9 Effect of Imperfection and Friction Coefficient on Cylinder Edge Failure”. *Summaries of Tech. Papers of Annual Meeting of Arch. Ins. Japan*. pp. 843-844. (in Japanese)

Fujimoto, T and Kuwamura, H. (2009). “Study on Steel Cone-to-Cylinder Socket Connections Part 8 Yield Compression Strength in case of Ring Tension Failure”. *Summaries of Tech. Papers of Annual Meeting of Arch. Ins. Japan*. pp. 787-788. (in Japanese)

Fujimoto, T and Kuwamura, H. (2010). “Study on Steel Cone-to-Cylinder Socket Connections Part 9 Formulae for Strength of Ring Tension Failure”. *Proc. 81st Arch. Res. Meeting of Kanto Chapter AIJ*: 305-308. (in Japanese).

Hayashi, Y., Tamura, K., Mori, M. and Takahashi, I. (1999). “ Simulation Analysis of Buildings Damaged in the 1995 Kobe, Japan, Earthquake considering Soil-structure Interaction”. *Earthquake Eng. Struct. Dyn.* 284: pp. 371-391.

Hibbitt, Karlson, Sorensen, ABAQUS-Theory and Standard User’s Manual, Version 6.12, *Pawtucket, RI*, USA, 2012

Hodge, P.G. (1961). “The Mises Yield Condition for Rotationally Symmetric Shells”. *Quart. Appl. Math.* No.4, pp. 305-311.

Ifayefunmi, O. (2015). “Plastic Buckling of Axially Compressed Thick Unstiffened Steel Cones”. *Ocean Eng.* 103, pp. 1-9.

Ito, T., Ehara, Y. and Kuwamura, H. (2008). “Cylinder Edge Failure of Steel Cone-to-Cylinder Socket Connections under Compression”. *J. Struct. and Constr. Eng.*, AIJ, No.630, pp. 1377-1384. (in Japanese).

Iwashita, K., Taniguchi, H., Kimura, H. and Kasuga, Y. (2003). “Effect of Uplift on Earthquake Response of Building”. *J. Struct. and Constr. Eng.*, AIJ, No.567, pp. 33-40. (in Japanese).

Ishizaki, S., Majima, M., Nagao, T., Funahara, H. and Aoshima, K. (2006). “Shaking Table Tests on Soil-Pile-Structure Models with Semi-Rigid Pile Head Connections”. *J.*

Struct. and Constr. Eng., AIJ, No.602, pp. 171-177. (in Japanese).

Johnston, B.G. (1939a). "The Structural Significance of Stress". *Civil Engineering* 9 (5), pp.291-294.

Johnston, B.G. (1939b). "Pin Connected Plate Links". *Trans. ASCE.*, 104, pp. 314-339.

Kamba T. and Taclendo C. (1998). "CHS Column Connections without Stiffeners". *Proc. Eighth International Symposium on Tubular Struct.,* Singapore; pp. 67-76.

Kurobane Y., Makino Y. and Ochi K. (1984). "Ultimate Resistance of Unstiffened Tubular Joints". *J. Struct. Eng.*, ASCE; 110(2): pp. 385-400.

Kuwamura (2001). "Performance and Design of Steel Structure". *Kyoritsu Press.*

Kuwamura, H., Ito, T. and Tomioka, Y. (2005a). "Study on Steel Cone-to-Cylinder Socket Connections Part 1 Outline of Feasibility Assessment Test/ Part 2 Strength of Cylinders/ Part 3 Strength of Cones". *Summaries of Tech. Papers of Annual Meeting of Arch. Ins. Japan*. pp. 887-892. (in Japanese)

Kuwamura, H., Ito,T. and Tomioka,Y. (2005b). "Study on Steel Cone-to-Cylinder Socket Connection". *J. Struct. and Constr. Eng.*, AIJ, No.598, pp. 155-162. (in Japanese).

Kuwamura, H. and Ito, T. (2007): "Study on Steel Cone-to-Cylinder Socket Connections Part 2 Frictional Rotation Resistance of Steel Cone-to-Cylinder Socket Connections". *J. Struct. and Constr. Eng.*, AIJ, No.622, pp. 169-176. (in Japanese).

Kuwamura, H. and Ito, T. (2009): "Cone-shaped Socket Connections for Cylindrical Members". *Proc. of Nordic Steel Constr. Conf.*, Sep. 2-4, 2009, Malmo, Sweden. Pp. 247-254.

Kuwamura, H. and Sato, Y. (2015). "Local Strength and Stiffness of Non-diaphragm Connection of CHS Column to Beam Flange". *J. Struct. and Constr. Eng.*, AIJ, No. 710, pp. 703-713. (in Japanese).

Nishimura, Y., Miyazaki, M. and Sugawara, T. (2004). "Development of Pile-top Isolation System (Part 1) Concept and Mechanism of Pin-supported Slider". *Summaries of Tech. Papers of Annual Meeting of Arch. Ins. Japan*. pp. 383-384. (in Japanese)

Onat, E.T. (1955). "Plastic Collapse of Cylindrical Shells under Axially Symmetric

Loading". *Quart. Appl. Math.* 13, pp. 63-72.

Packer J. A., Davies G, and Coutie M.G. (1980). "Yield Strength of Gapped Joints in Rectangular Hollow Section Trusses". *Proc.-Inst. of Civil Engineers, Part 2;* 69. pp 995-1013.

Panzeri, N. and Poggi C. (1999). "Stability and Strength of Conical Shells Subject to Axial Load and External Pressure". *In: Chan SL, Teng J. G, editors. Advances in Steel Struct.* Oxford, UK: Elsevier, 1999, 6, pp. 21-30.

Prager. W. (1952). " The General Theory of Limit Design". *Proc. 8th Int. Conr. Theor. Appl. Mech.*, Istanbul, vol. II, pp. 65-72.

Rasmussen, K. J.R and Hancock, G. J. (1998). "Buckling Analysis of Thin-walled Structures: Analytical Developments and Applications". *Struc. Analysis and CAD*. pp.316-322.

Riks, E. (1979). "An Incremental Approach to the Solution of Snapping and Buckling". *Int. J. Solid. Struct.* 15(7). pp. 529-551.

Rutenberg, A., Jennings, P.C. and Housner, G.W. (1982). "The Response of Veterans Hospital Building 41 in the San Fernando Earthquake". *Earthquake Eng. Struct. Dyn.* 103: pp. 359-379.

Save, M.A and Masonnet, C. E. (1997). "Plastic Analysis and Design of Plates, Shells and Disks". *Amsterdam, North Holland Publishing Co.*, pp. 12-28.

Sawczuk, A., and Hodge, P., 1960, "Comparison of Yield Conditions for Circular Cylindrical Shells," *J. Franklin Inst*., 269(5), pp. 362-374.

Schey (1983). "Tribology in Metalworking: Friction, Lubrication and Wear". *Asm. Intl.*

Seide, P. (1956). "Axisymmetrical Buckling of Circular Cones under Axial Compression". *J. Appl. Mech.* No.56-APM-36. Pp. 625-628.

Tateyama, E., Inoue K., Sugimoto, S., and Matsumura, H. (1988). "Study on Ultimate Bending Strength and Deformation Capacity of H-Shaped Beam Connected to RHS Column with Through Diaphragms". *J. Struct. and Constr. Eng.*, AIJ, No. 389, pp. 109-121. (in Japanese).

Teng, J.G. and Rotter, J.M. (1989). “Non-symmetric bifurcation of geometrically nonlinear elastic-plastic axisymmetric shells under combined loads including torsion”. *Comput. Struct.* 32(2), 453-475.

Teng, J.G. and Rotter, J.M. (1991). “Collapse Behavior and Strength of Steel Silo Transition Junction. Part I: Collapse Mechanics”. *J. Struct. Eng.*, ASCE,117 (8): pp. 3587-3604.

Teng, J.G. (1994a). “Plastic Collapse at Lap Joints in Pressurized Cylinder under Axial Load”. *J. Struct. Eng.*, ASCE,120 (1): pp. 23-45.

Teng, J.G. (1994b). “Cone-Cylinder Intersection under Pressure: Axisymmetric Failure”. *J. Struct. Eng.*, ASCE,120 (9): pp. 1896-1912.

Teng, J.G. (2000). “Intersections in Steel Shell Structures”. “*Prog.Struct. Engng. Mater.* 2; pp. 459-471.

Timoshenko, S. (1940). “Theory of Plates and Shells”. *McGraw-Hill Book Company,* New York, N.Y.

Tomioka, Y. (2006). “Compressive Strength of Steel Cone-to-Cylinder Socket Connections ”. *Master thesis. The University of Tokyo.* (in Japanese).

Tomioka, Y., Ito, T. and Kuwamura, H. (2006). “Study on Steel Pipe Joints with an Inserted Cone Part 4”. *Proc. 77th Arch. Res. Meeting of Kanto Chapter AIJ*: pp. 145-148. (in Japanese).

Tsang, S.K. and Harding, J.E. (1984). “A mechanism Approach for the Prediction of the Collapse Strength of Ring-stiffened Cylinders under Axial Compression and External Pressure”. *Thin Wall Struct*. 2, pp. 325-353.

Wardenieer, J. (1982). “Hollow Section Joints”. *Delft Univ. Pre*ss.

Wilbert, A., Jang, W.-Y., Kyriakides, S. and Floccari, J.F. (2011). “Buckling and Progressive Crushing of Laterally Loaded Honeycomb”. *Int. J. Solid. Struct*. 48. pp. 803-816.

Zhao, X.L. and Hancock G.J. (1991). “T-joints in Rectangular Hollow Sections Subject to Combined Actions”. *J. Struct. Eng.*, ASCE,117 (8): pp. 58-77.

Zhao, X.L. and Hancock G.J. (1993). "A Theoretical Analysis of the Plastic Moment Capacity of an Inclined Yield Line under Axial Force". *Thin-walled Struct.,* 15(3): pp. 185-208.

APPENDIX

Appendix A Coupon Test Results of Connections

A.1 Coupon Test Results of Cylindrical Shell

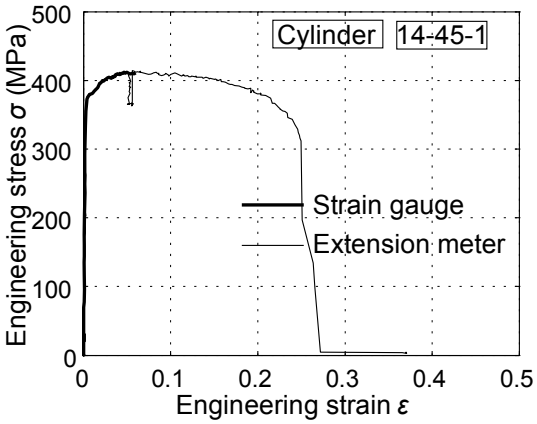

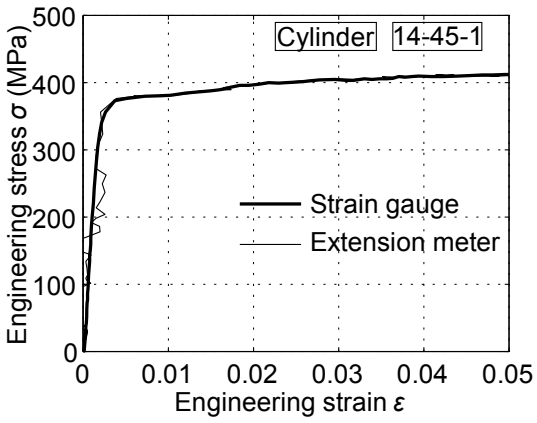

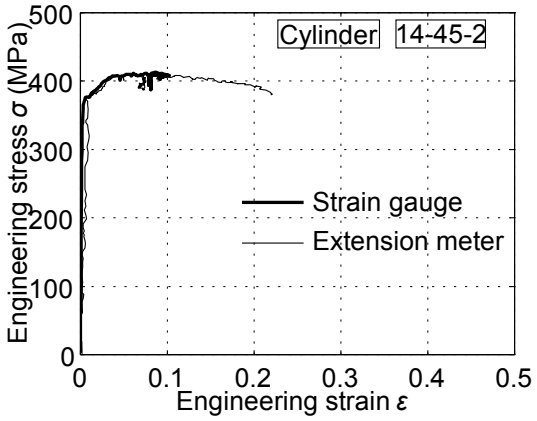

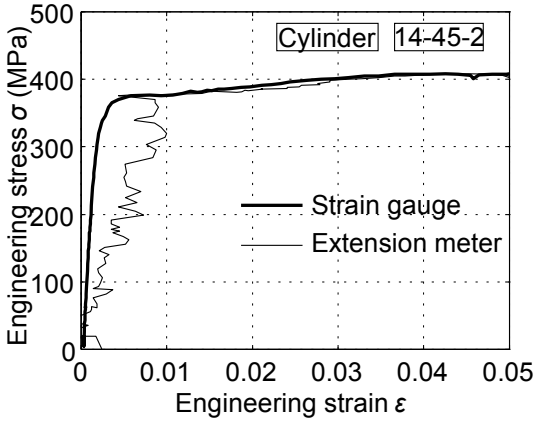

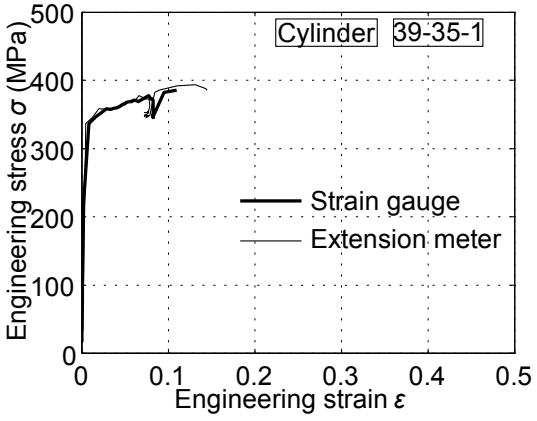

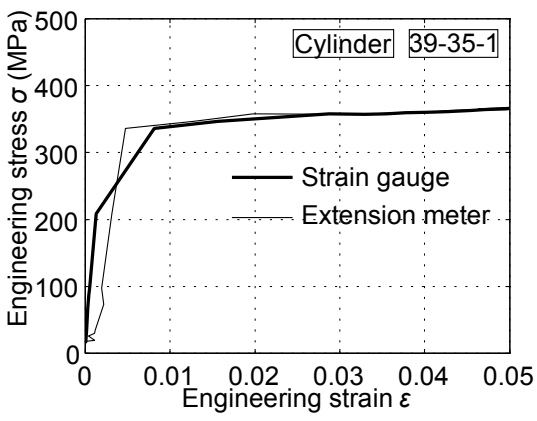

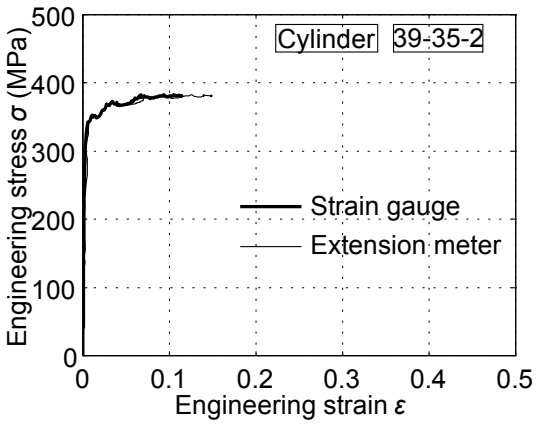
Cylinder 39-35-2
Strain gauge
Extension meter
Engineering stress σ (MPa)
Engineering strain ε
0
100
200
300
400
500
0.1
0.2
0.3
0.4
0.5

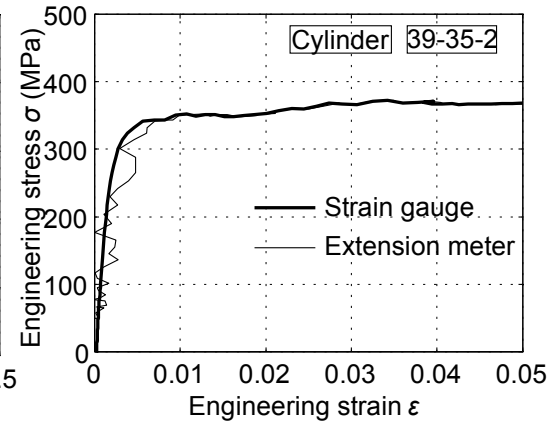
Cylinder 39-35-2
Strain gauge
Extension meter
Engineering stress σ (MPa)
Engineering strain ε
0
100
200
300
400
500
0.01
0.02
0.03
0.04
0.05

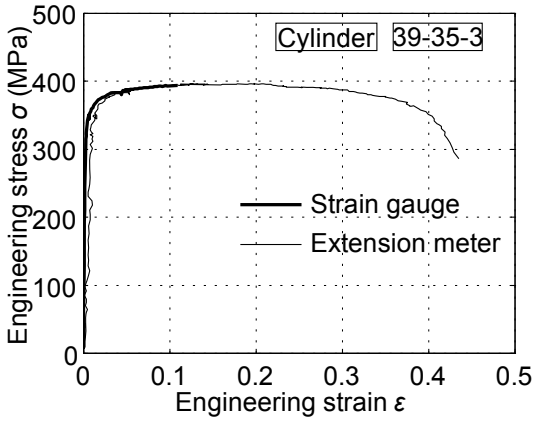
Cylinder 39-35-3
Strain gauge
Extension meter
Engineering stress σ (MPa)
Engineering strain ε
0
100
200
300
400
500
0.1
0.2
0.3
0.4
0.5

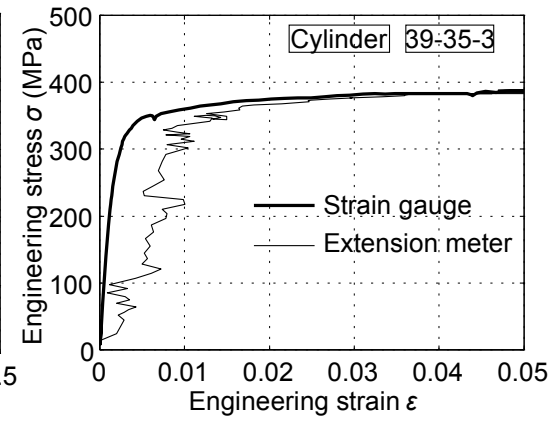
Cylinder 39-35-3
Strain gauge
Extension meter
Engineering stress σ (MPa)
Engineering strain ε
0
100
200
300
400
500
0.01
0.02
0.03
0.04
0.05

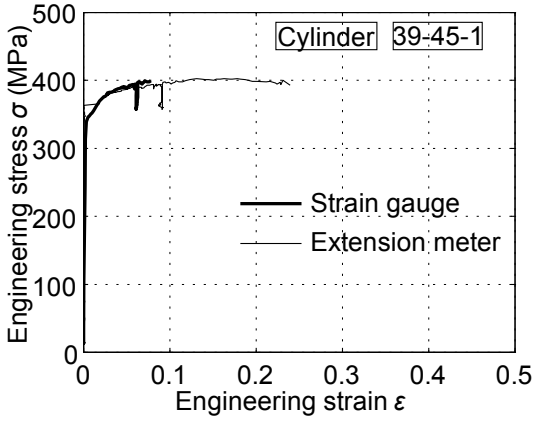
Cylinder 39-45-1
Strain gauge
Extension meter
Engineering stress σ (MPa)
Engineering strain ε
0
100
200
300
400
500
0.1
0.2
0.3
0.4
0.5

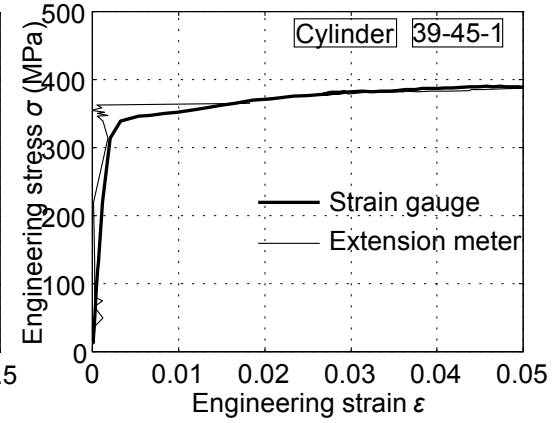
Cylinder 39-45-1
Strain gauge
Extension meter
Engineering stress σ (MPa)
Engineering strain ε
0
100
200
300
400
500
0.01
0.02
0.03
0.04
0.05

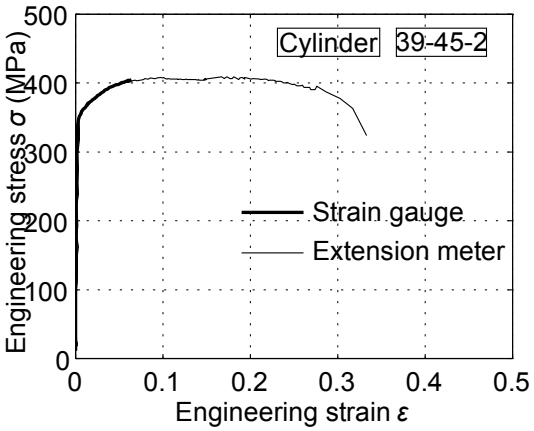
Cylinder 39-45-2
Strain gauge
Extension meter
Engineering stress σ (MPa)
Engineering strain ε
0
100
200
300
400
500
0
0.1
0.2
0.3
0.4
0.5

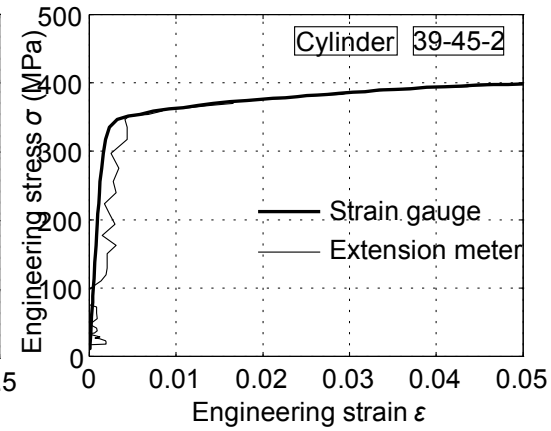
Cylinder 39-45-2
Strain gauge
Extension meter
Engineering stress σ (MPa)
Engineering strain ε
0
100
200
300
400
500
0
0.01
0.02
0.03
0.04
0.05

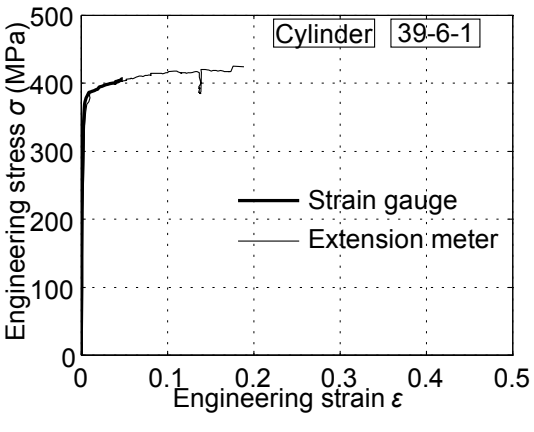
Cylinder 39-6-1
Strain gauge
Extension meter
Engineering stress σ (MPa)
Engineering strain ε
0
100
200
300
400
500
0
0.1
0.2
0.3
0.4
0.5

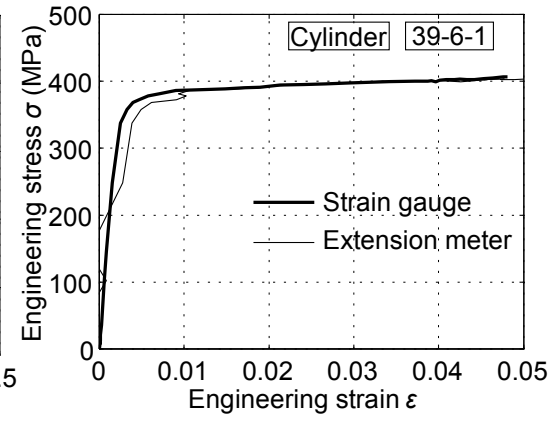
Cylinder 39-6-1
Strain gauge
Extension meter
Engineering stress σ (MPa)
Engineering strain ε
0
100
200
300
400
500
0
0.01
0.02
0.03
0.04
0.05

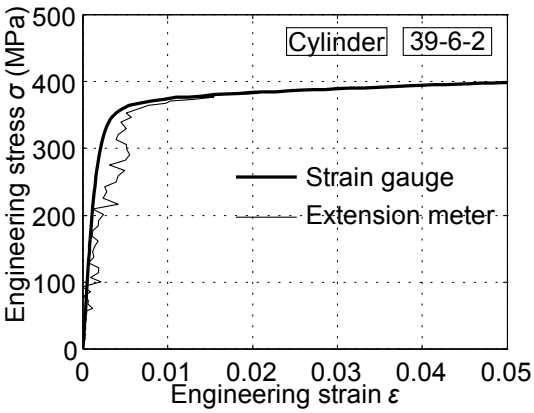
Cylinder 39-6-2
Strain gauge
Extension meter
Engineering stress σ (MPa)
Engineering strain ε
0
100
200
300
400
500
0
0.01
0.02
0.03
0.04
0.05

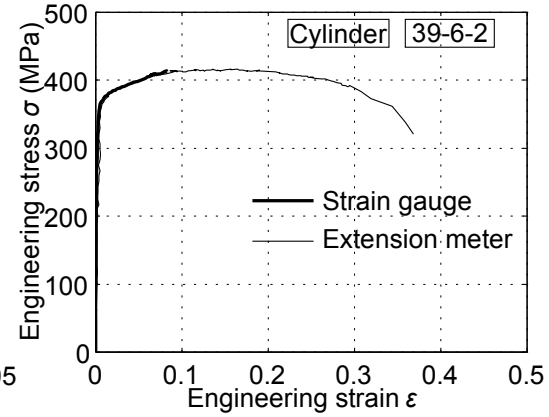
Cylinder 39-6-2
Strain gauge
Extension meter
Engineering stress σ (MPa)
Engineering strain ε
0
100
200
300
400
500
0
0.1
0.2
0.3
0.4
0.5

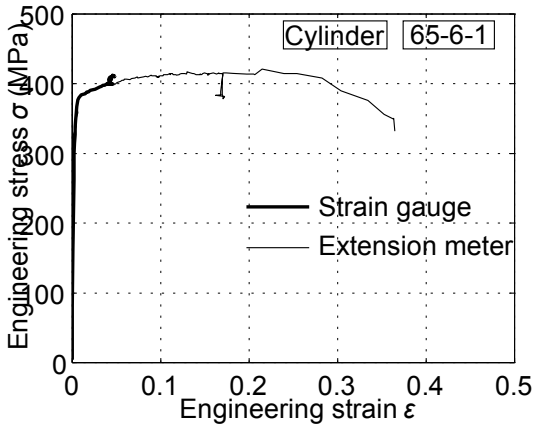
Cylinder 65-6-1
Strain gauge
Extension meter
Engineering stress σ (MPa)
Engineering strain ε
0
100
200
300
400
500
0.1
0.2
0.3
0.4
0.5

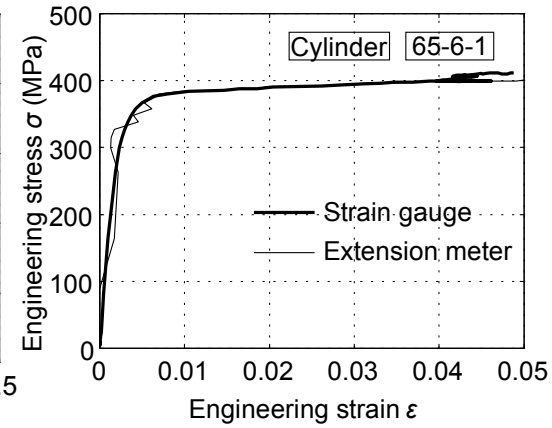
Cylinder 65-6-1
Strain gauge
Extension meter
Engineering stress σ (MPa)
Engineering strain ε
0
100
200
300
400
500
0.01
0.02
0.03
0.04
0.05

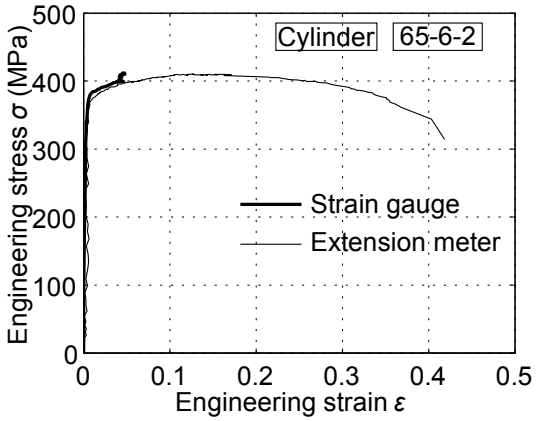
Cylinder 65-6-2
Strain gauge
Extension meter
Engineering stress σ (MPa)
Engineering strain ε
0
100
200
300
400
500
0.1
0.2
0.3
0.4
0.5

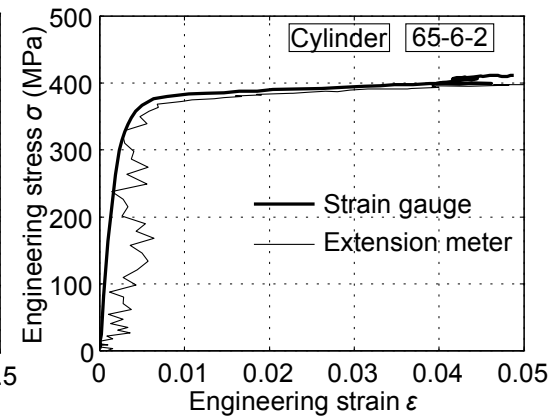
Cylinder 65-6-2
Strain gauge
Extension meter
Engineering stress σ (MPa)
Engineering strain ε
0
100
200
300
400
500
0.01
0.02
0.03
0.04
0.05

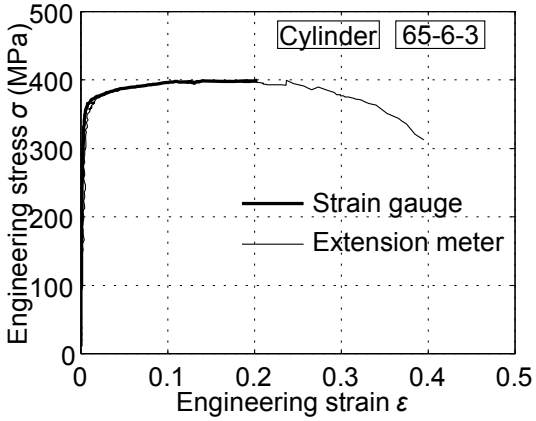
Cylinder 65-6-3
Strain gauge
Extension meter
Engineering stress σ (MPa)
Engineering strain ε
0
100
200
300
400
500
0.1
0.2
0.3
0.4
0.5

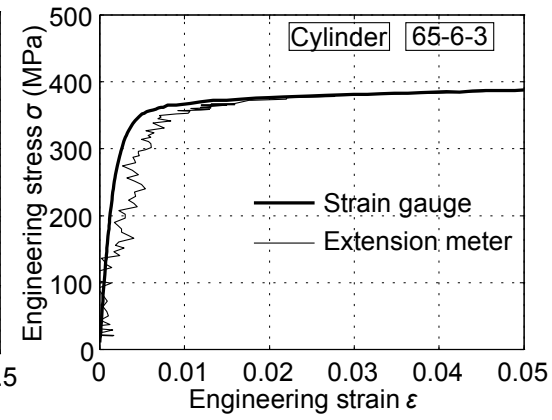
Cylinder 65-6-3
Strain gauge
Extension meter
Engineering stress σ (MPa)
Engineering strain ε
0
100
200
300
400
500
0.01
0.02
0.03
0.04
0.05

A.2 Coupon Test Results of Conical Shell

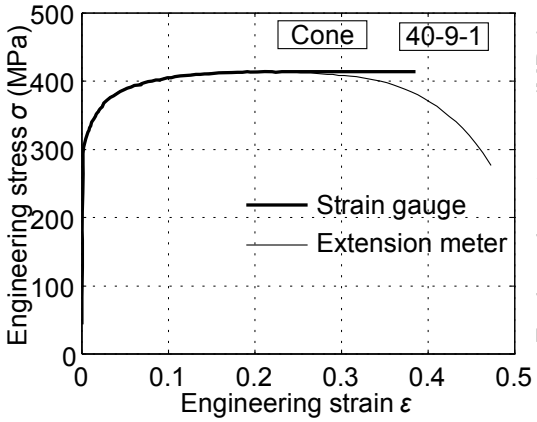

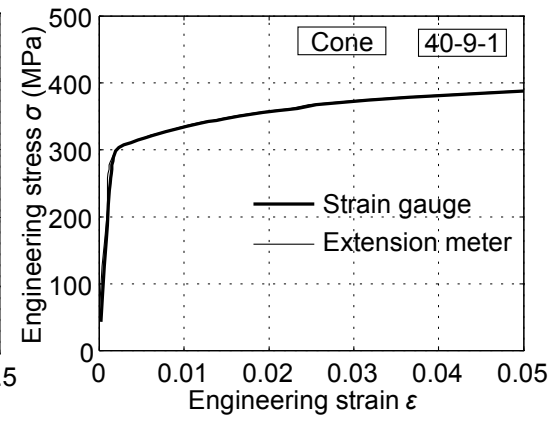

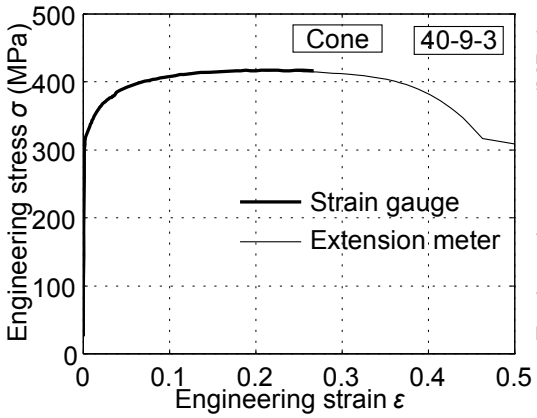

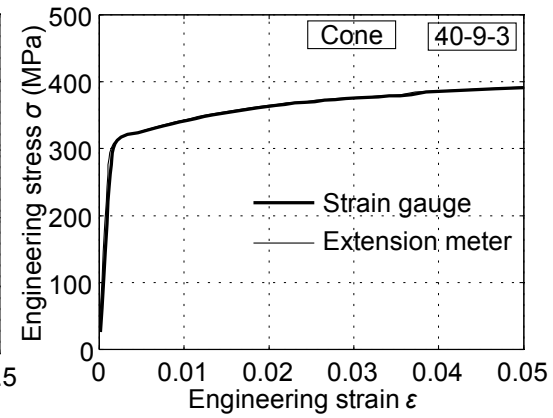

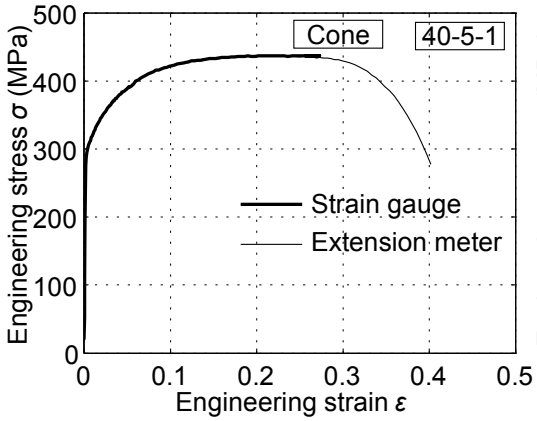

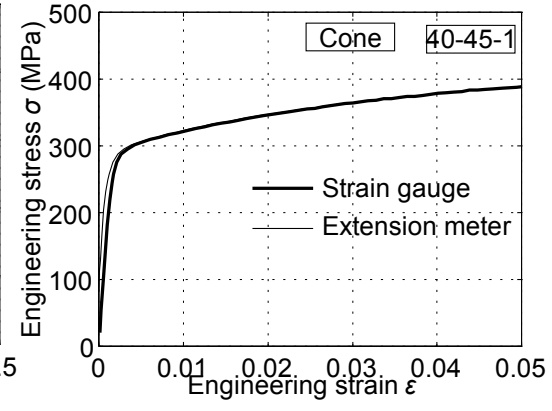

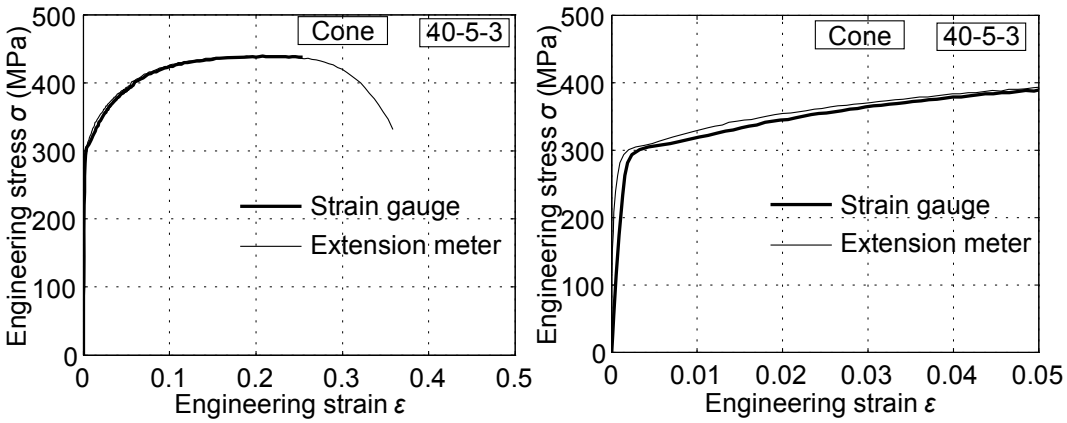

A.3 Coupon Test Results of Lid Plate

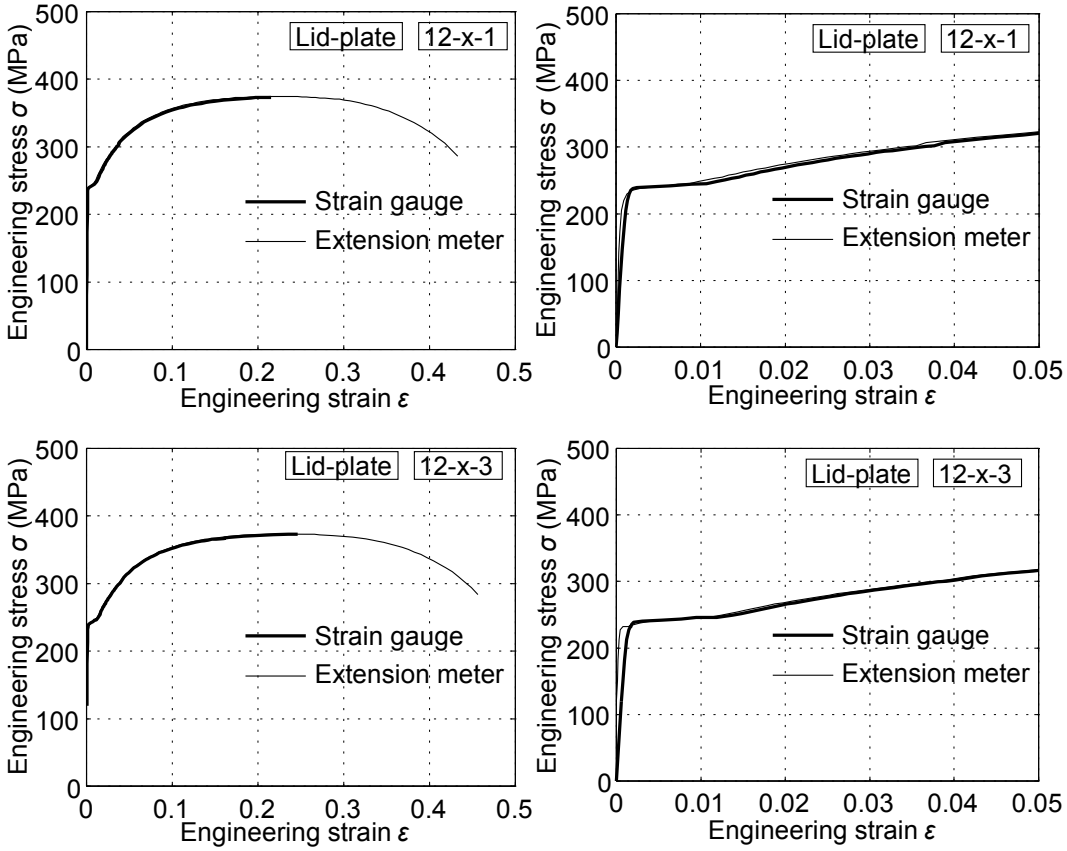

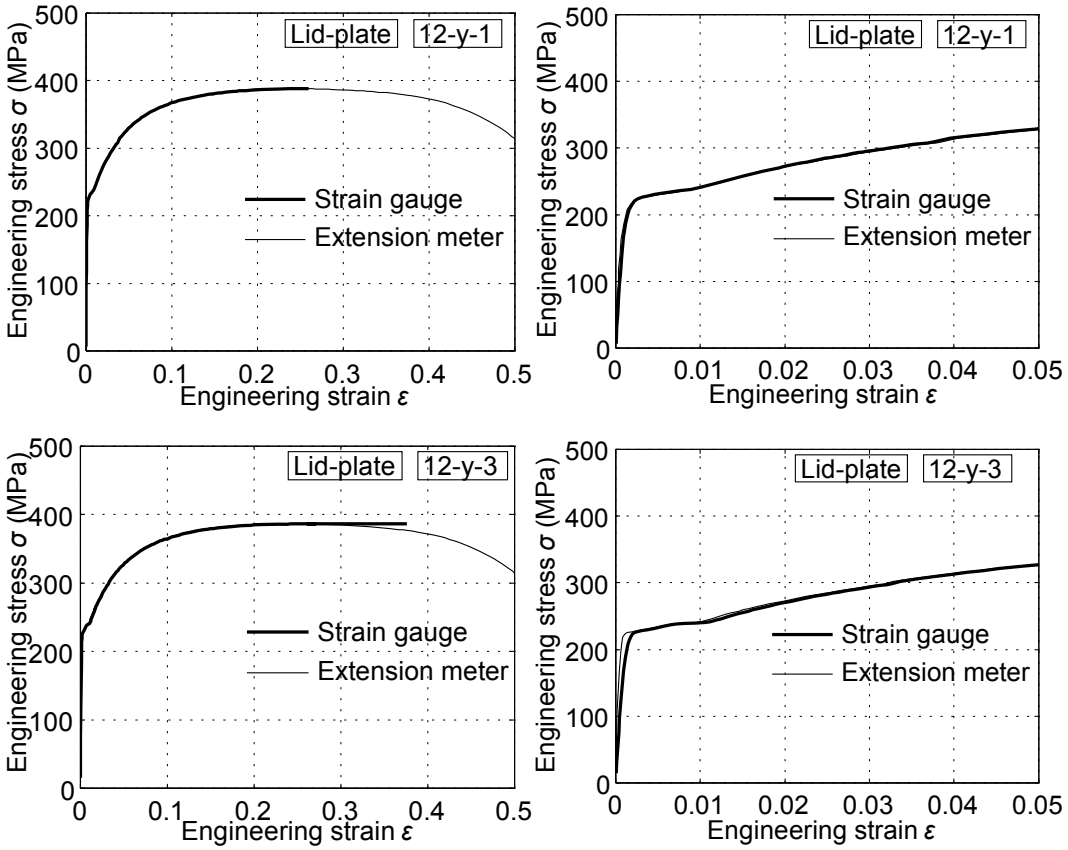

A.4 Coupon Test Results of Tapered Ring

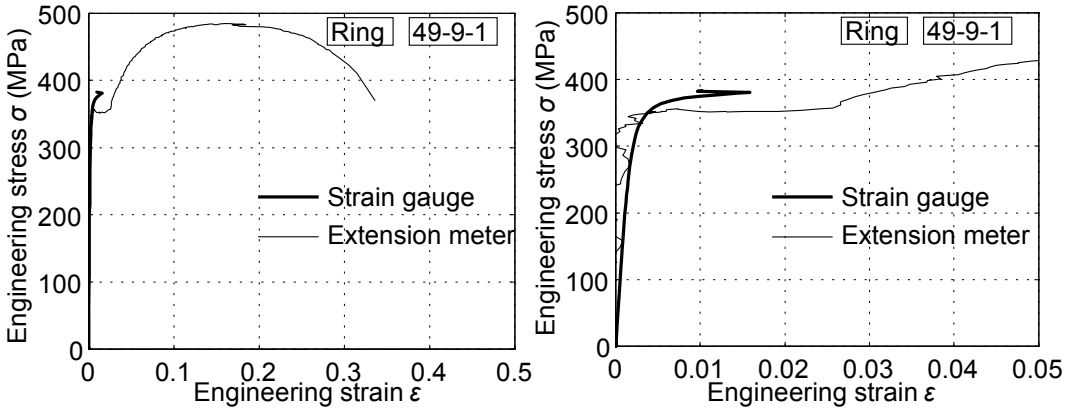

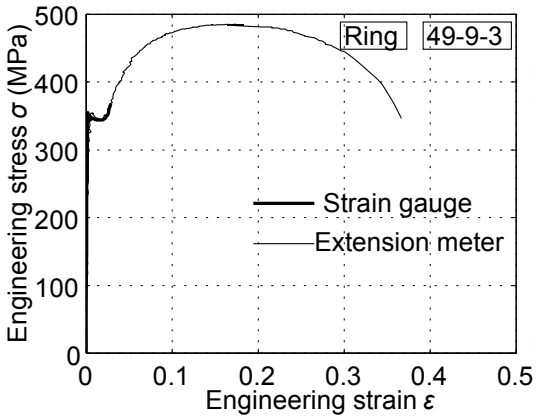
Ring 49-9-3
Strain gauge
Extension meter
Engineering stress σ (MPa)
Engineering strain ε
0
100
200
300
400
500
0.1
0.2
0.3
0.4
0.5

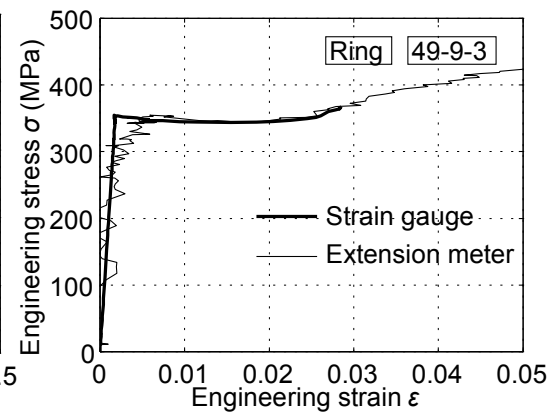
Ring 49-9-3
Strain gauge
Extension meter
Engineering stress σ (MPa)
Engineering strain ε
0
100
200
300
400
500
0.01
0.02
0.03
0.04
0.05

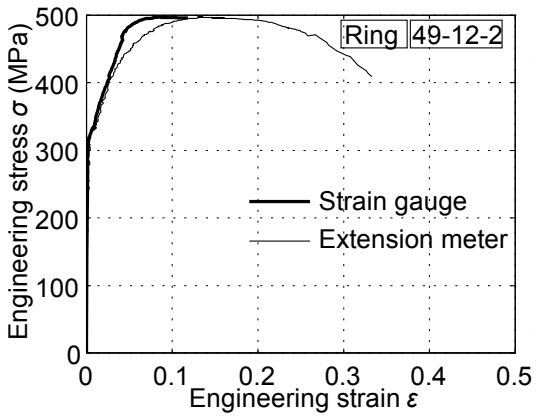
Ring 49-12-2
Strain gauge
Extension meter
Engineering stress σ (MPa)
Engineering strain ε
0
100
200
300
400
500
0.1
0.2
0.3
0.4
0.5

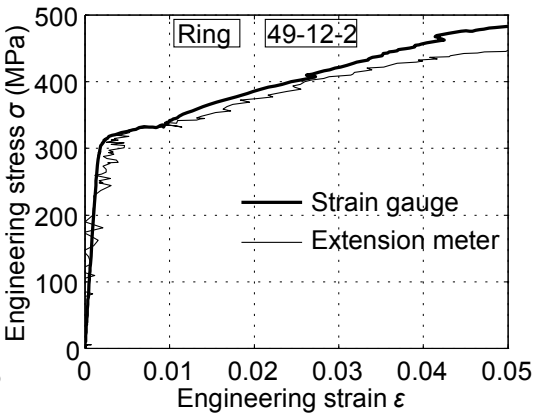
Ring 49-12-2
Strain gauge
Extension meter
Engineering stress σ (MPa)
Engineering strain ε
0
100
200
300
400
500
0.01
0.02
0.03
0.04
0.05

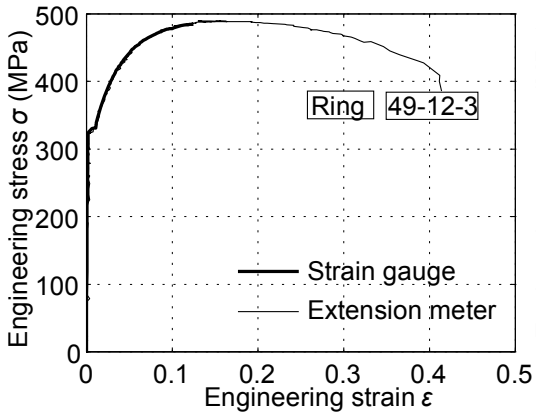
Ring 49-12-3
Strain gauge
Extension meter
Engineering stress σ (MPa)
Engineering strain ε
0
100
200
300
400
500
0.1
0.2
0.3
0.4
0.5

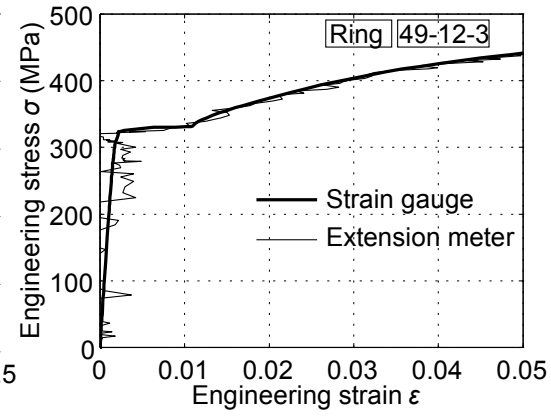
Ring 49-12-3
Strain gauge
Extension meter
Engineering stress σ (MPa)
Engineering strain ε
0
100
200
300
400
500
0.01
0.02
0.03
0.04
0.05

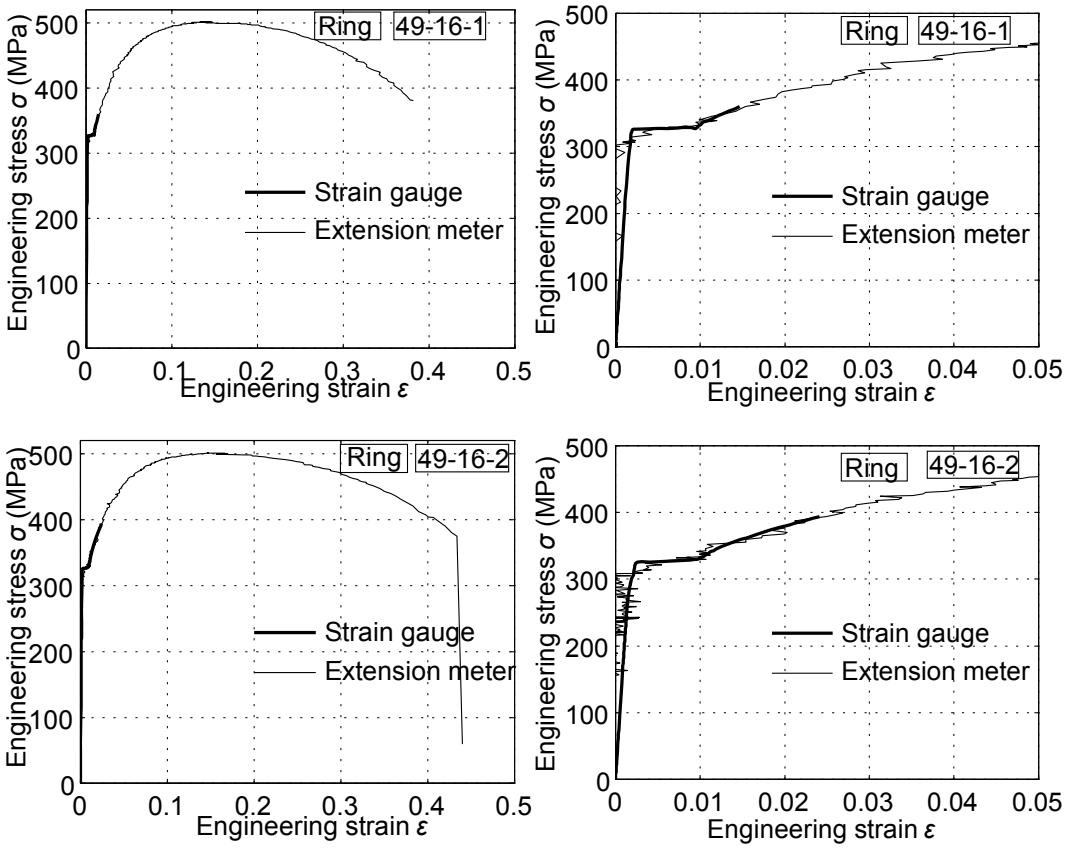
Ring 49-16-1
Strain gauge
Extension meter
Engineering stress σ (MPa)
Engineering strain ε
0
100
200
300
400
500
0.1
0.2
0.3
0.4
0.5
0.01
0.02
0.03
0.04
0.05
Ring 49-16-2

Appendix B Load versus Axial Deformation Curves of All the Experimental Specimens

B.1 Connections with Boundary of "Metal touch"

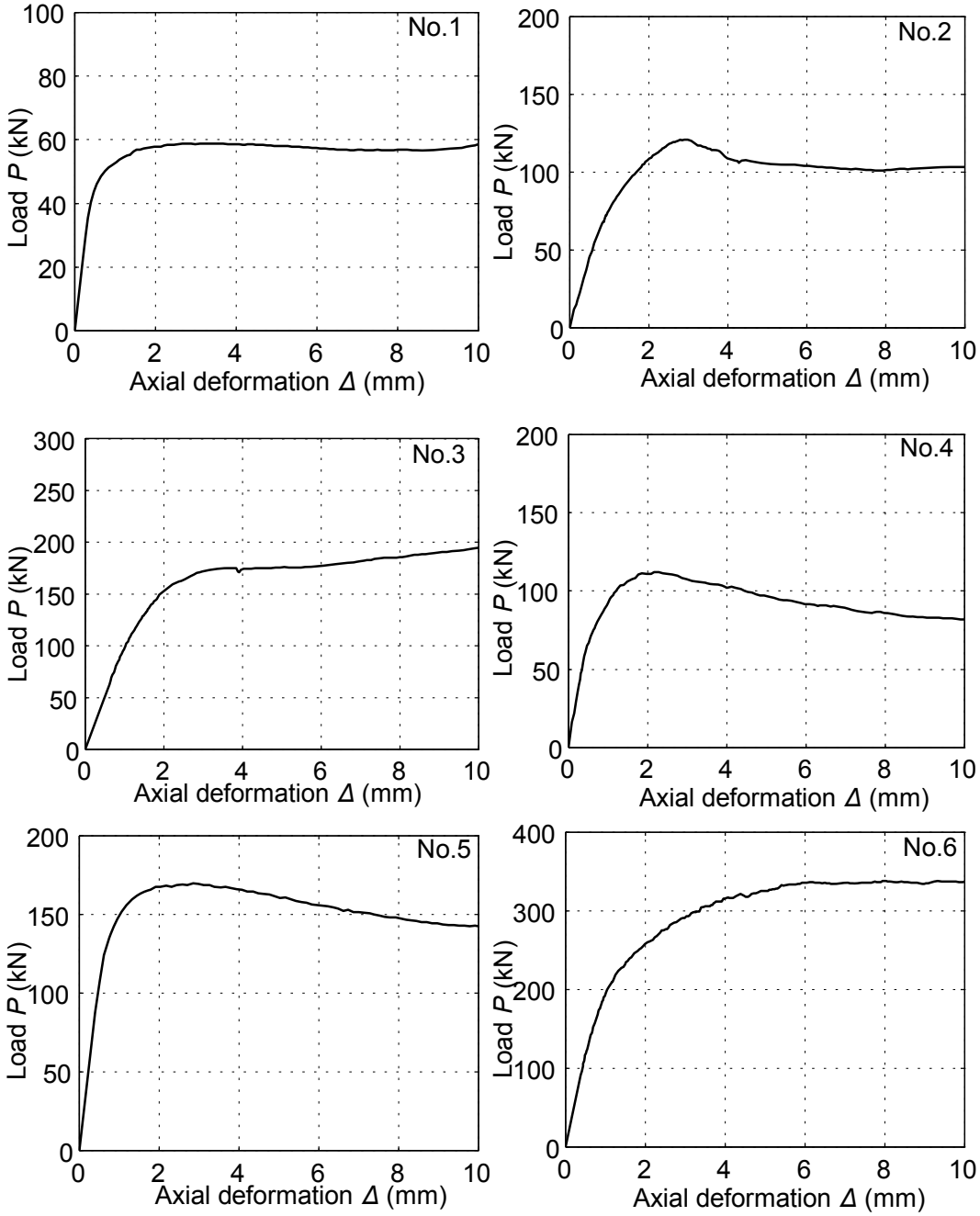

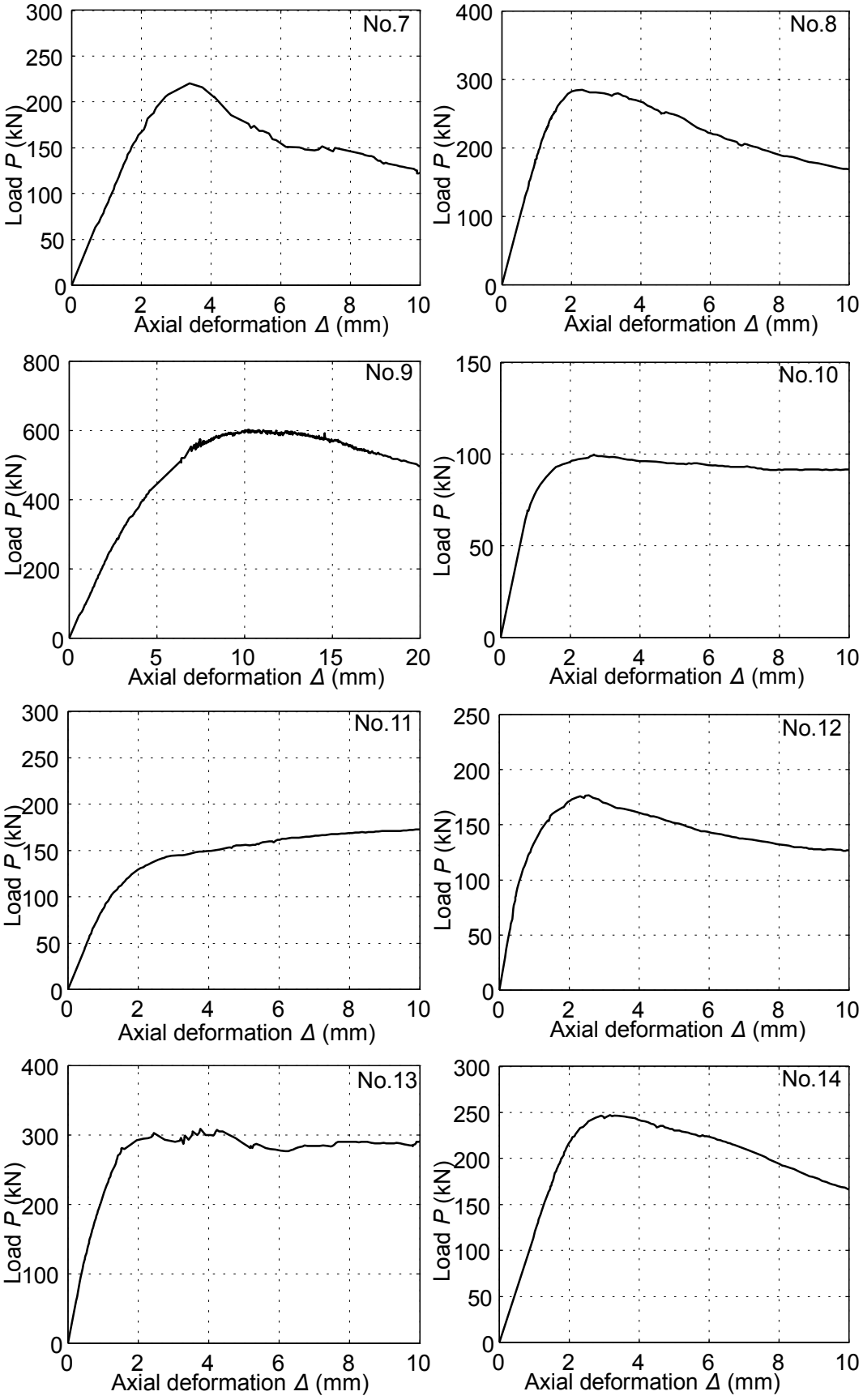
No.7
Load P (kN)
Axial deformation Δ (mm)
No.8
Load P (kN)
Axial deformation Δ (mm)
No.9
Load P (kN)
Axial deformation Δ (mm)
No.10
Load P (kN)
Axial deformation Δ (mm)
No.11
Load P (kN)
Axial deformation Δ (mm)
No.12
Load P (kN)
Axial deformation Δ (mm)
No.13
Load P (kN)
Axial deformation Δ (mm)
No.14
Load P (kN)
Axial deformation Δ (mm)

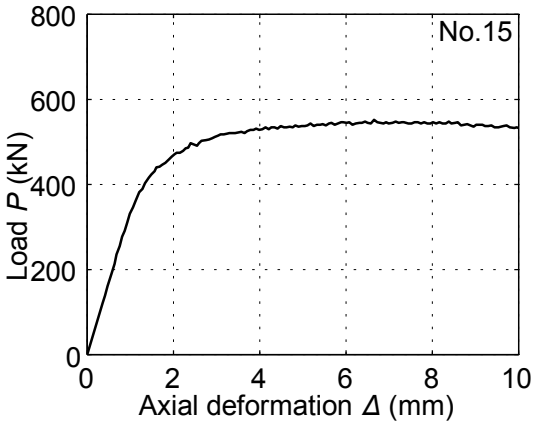

B.2 Connections with Boundary of "Metal touch +thin ring"

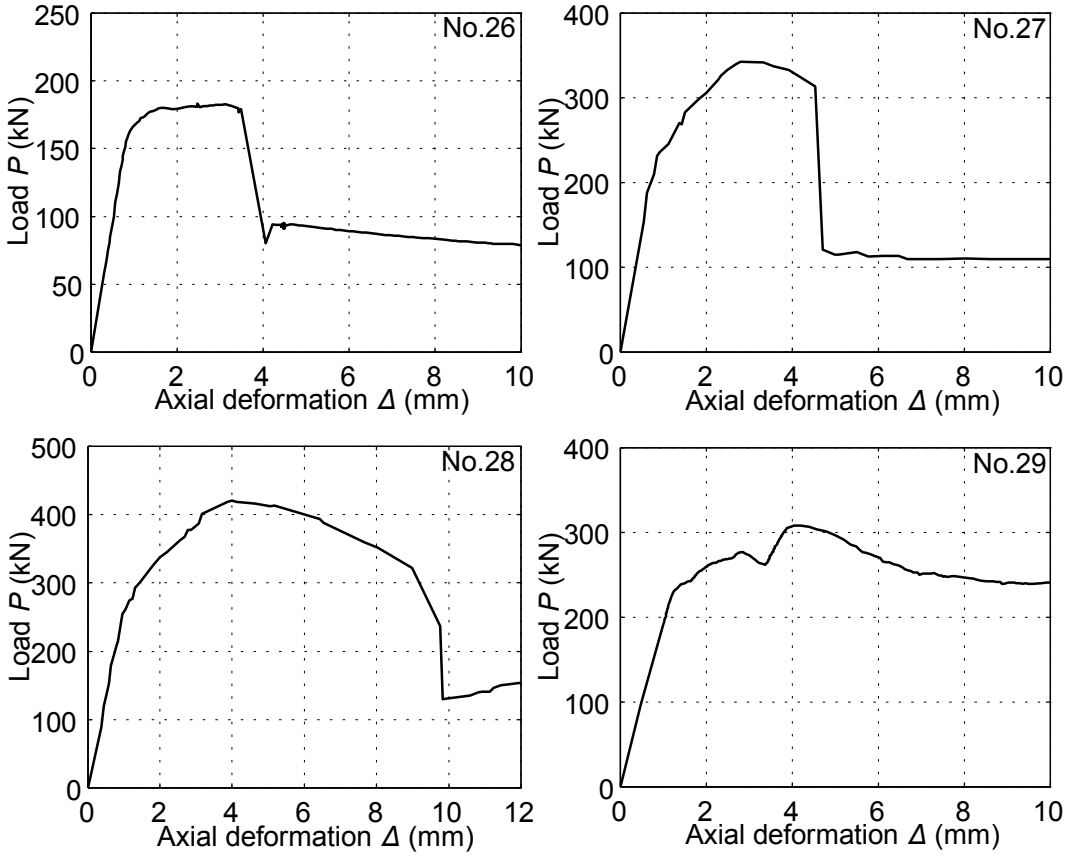

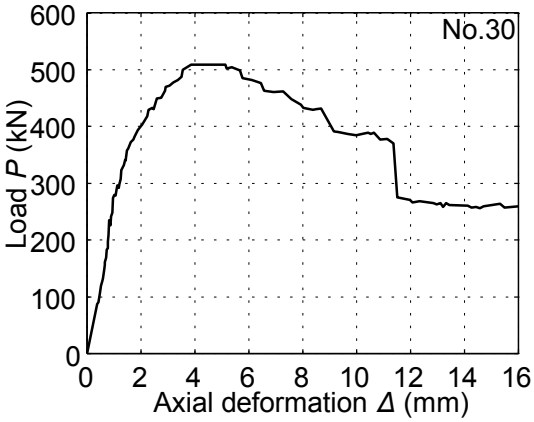
No.30
Load P (kN)
Axial deformation Δ (mm)

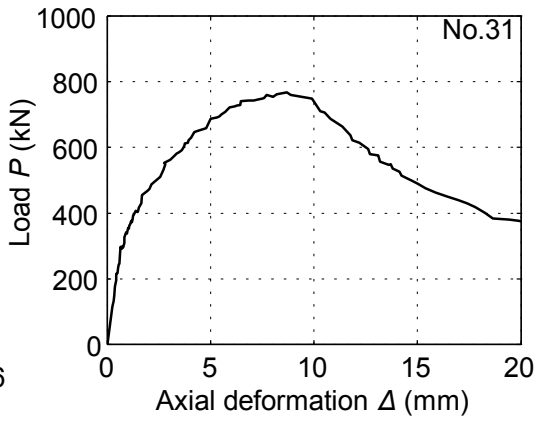
No.31
Load P (kN)
Axial deformation Δ (mm)

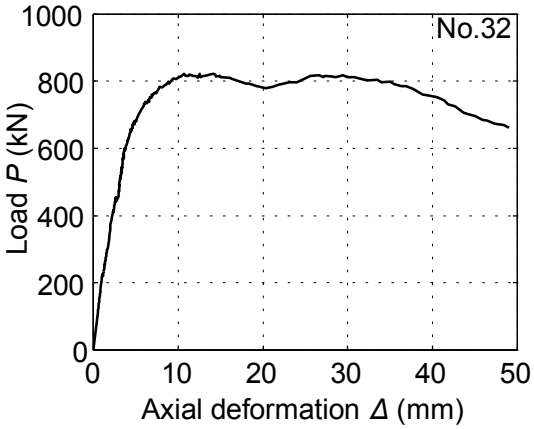
No.32
Load P (kN)
Axial deformation Δ (mm)

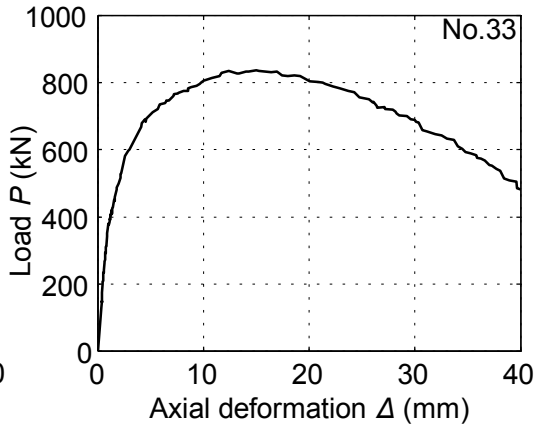
No.33
Load P (kN)
Axial deformation Δ (mm)

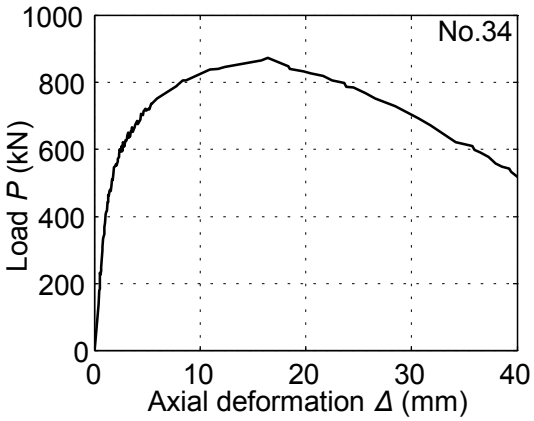
No.34
Load P (kN)
Axial deformation Δ (mm)

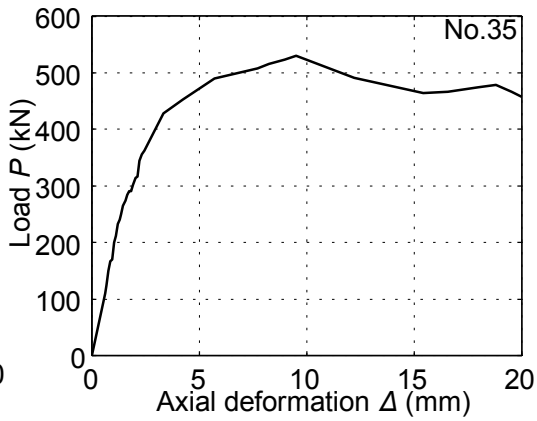
No.35
Load P (kN)
Axial deformation Δ (mm)

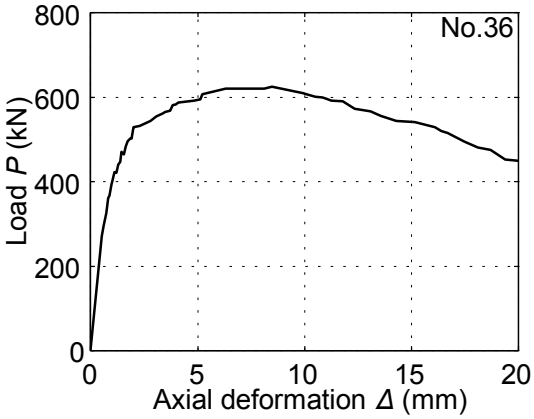
No.36
Load P (kN)
Axial deformation Δ (mm)

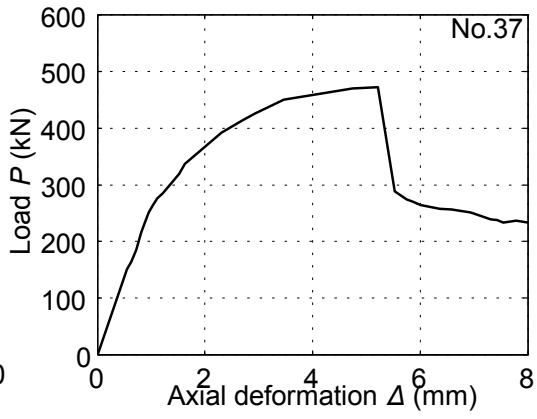
No.37
Load P (kN)
Axial deformation Δ (mm)

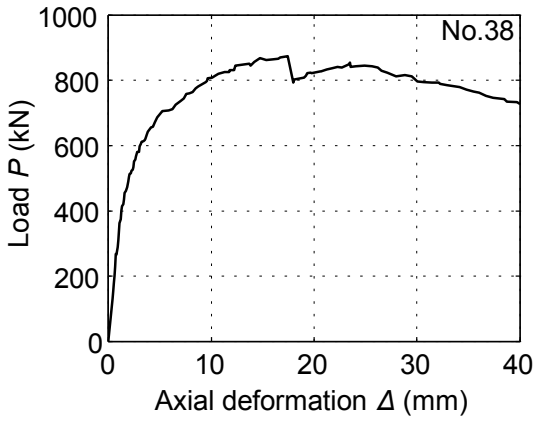

B.3 Connections with Boundary of "Metal touch +thick ring"

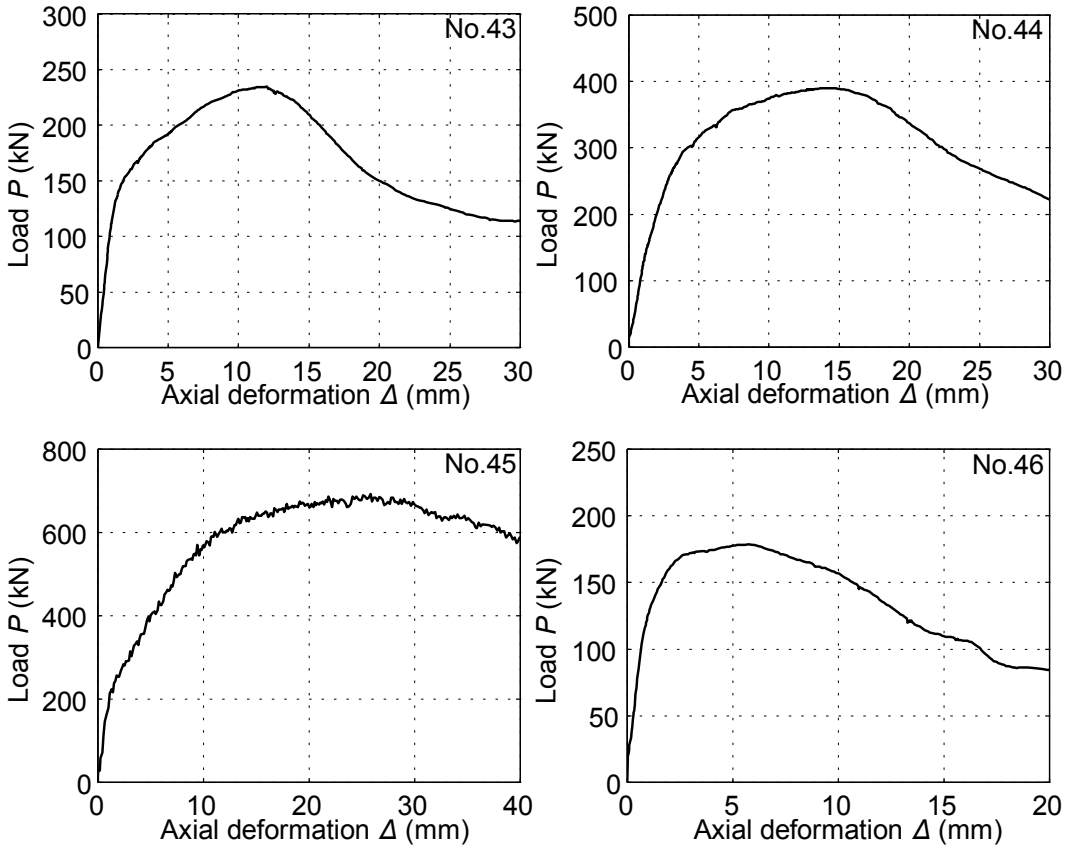

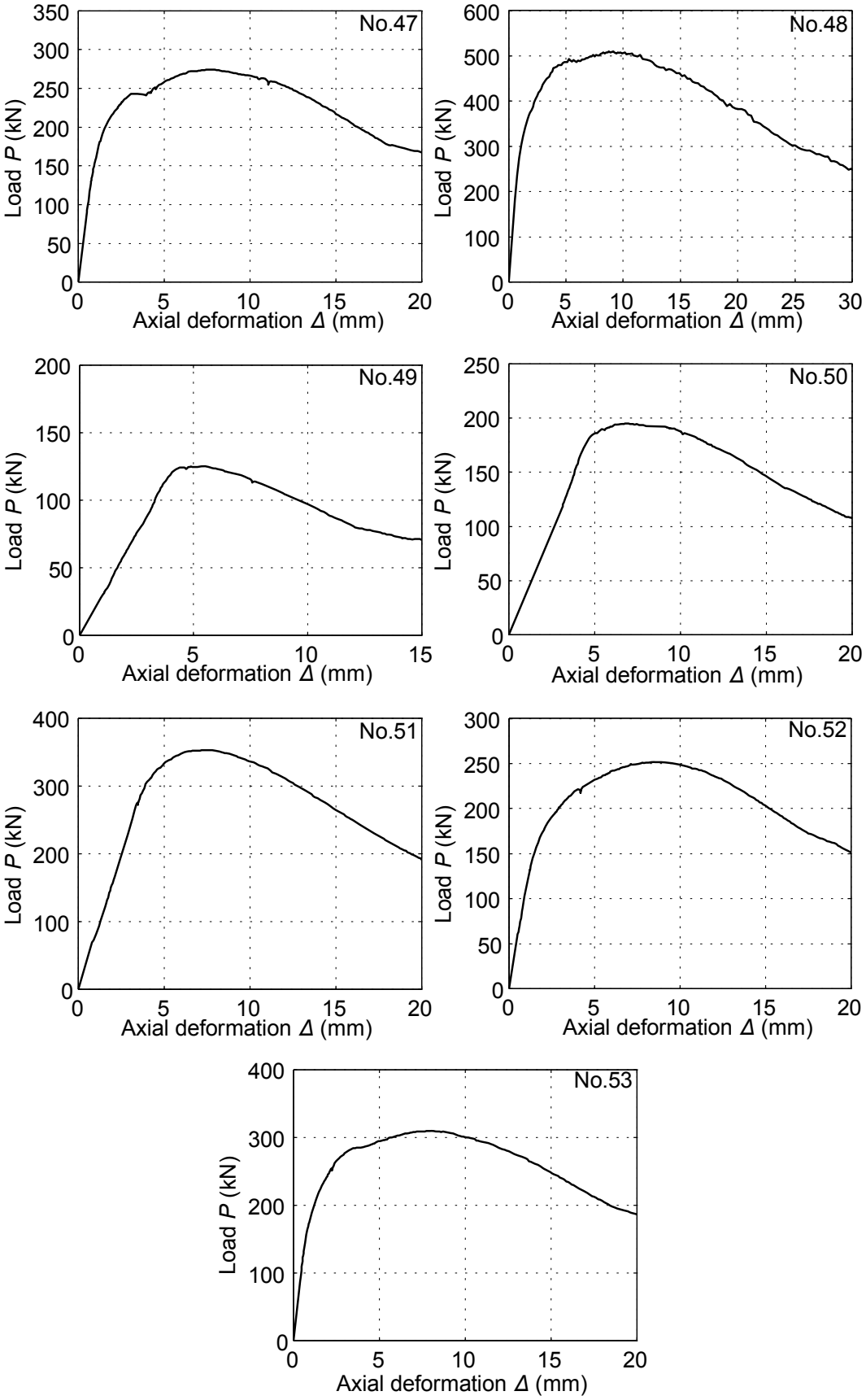
No.47
Load P (kN)
Axial deformation Δ (mm)
No.48
Load P (kN)
Axial deformation Δ (mm)
No.49
Load P (kN)
Axial deformation Δ (mm)
No.50
Load P (kN)
Axial deformation Δ (mm)
No.51
Load P (kN)
Axial deformation Δ (mm)
No.52
Load P (kN)
Axial deformation Δ (mm)
No.53
Load P (kN)
Axial deformation Δ (mm)

B.4 Connections with Boundary of "Welding"

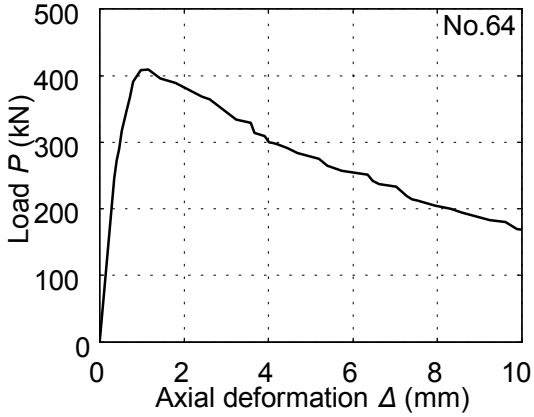

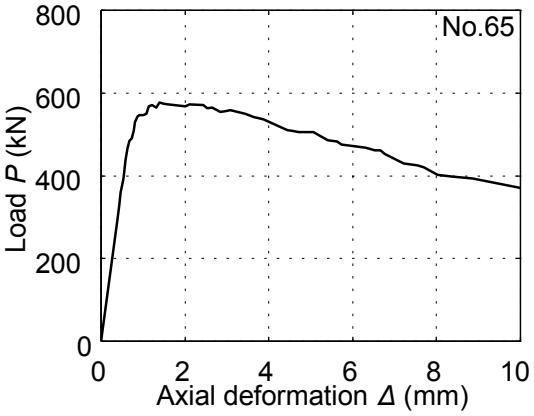

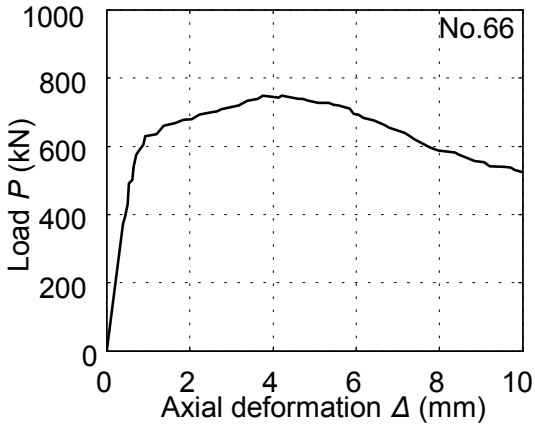

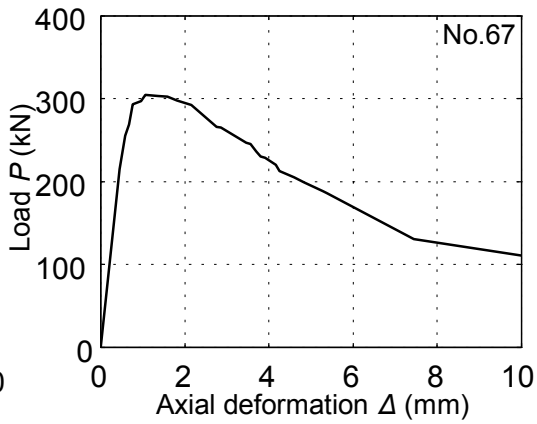

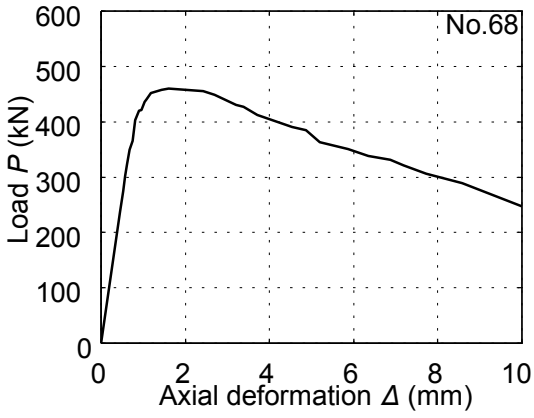

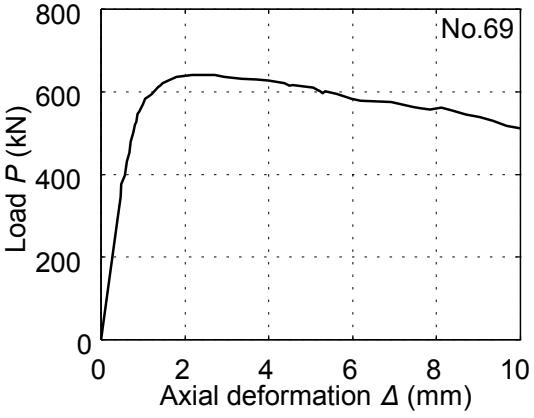

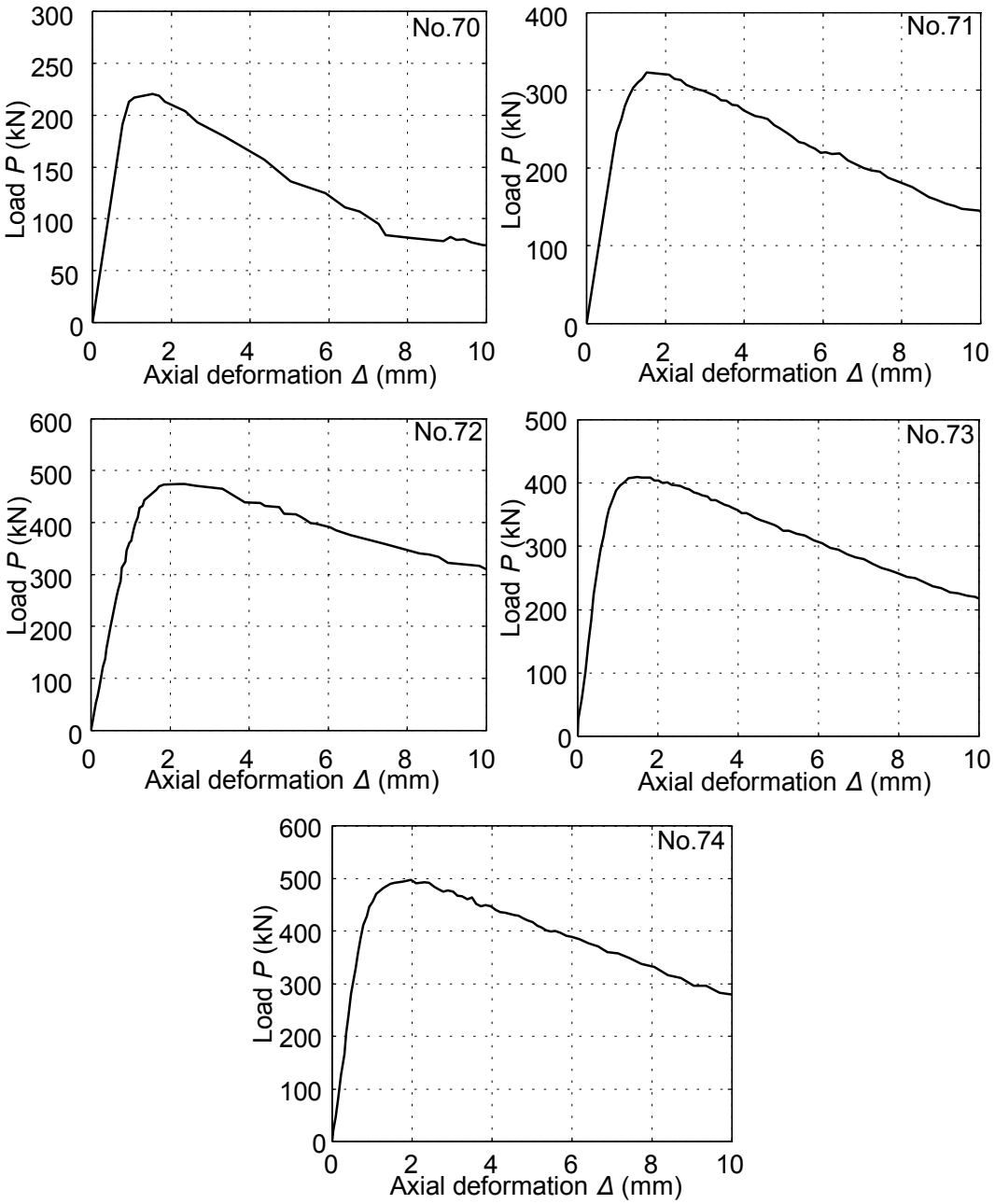
No.70
Load P (kN)
Axial deformation Δ (mm)
No.71
Load P (kN)
Axial deformation Δ (mm)
No.72
Load P (kN)
Axial deformation Δ (mm)
No.73
Load P (kN)
Axial deformation Δ (mm)
No.74
Load P (kN)
Axial deformation Δ (mm)

Appendix C Comparison of Load versus Axial Deformation Curves and Deformation between Experiments and FEA

C.1 Metal Touch Connections with Cylinder Edge Failure

No.	*P-Δ* curves	Deformation after collapse	
		EXP.	FEA
1	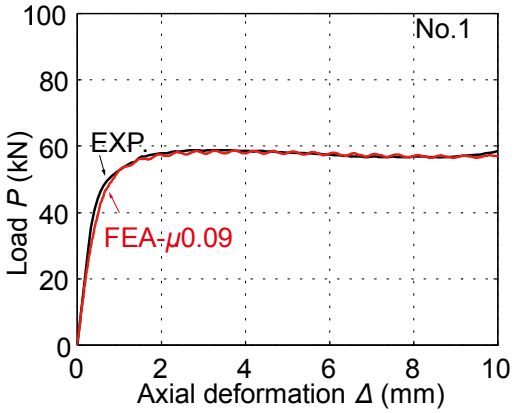		
2	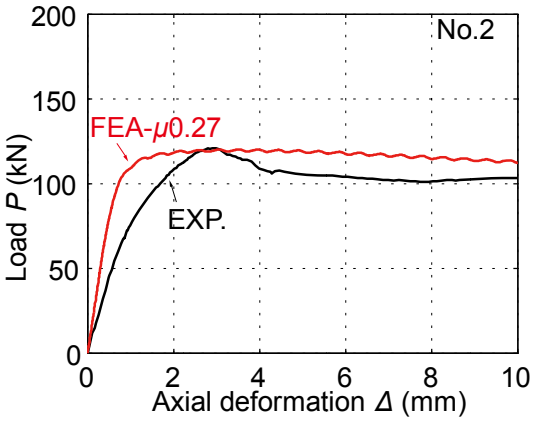		
3	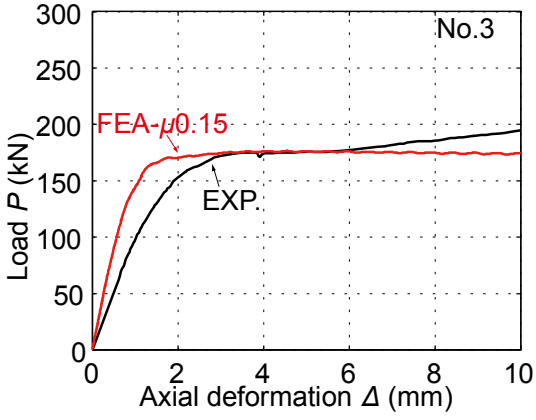		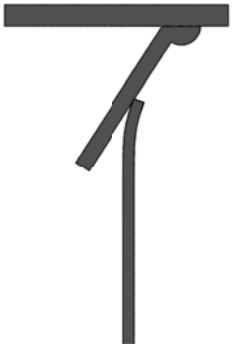

4	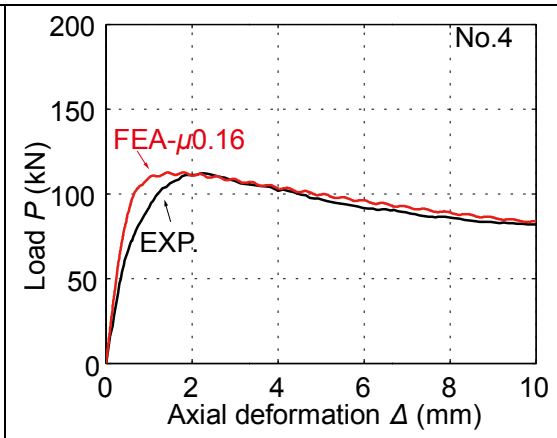 No.4 FEA-μ0.16 EXP. Load P (kN) Axial deformation Δ (mm)		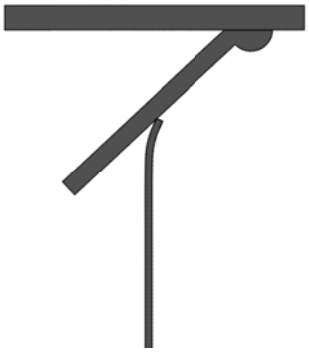
5	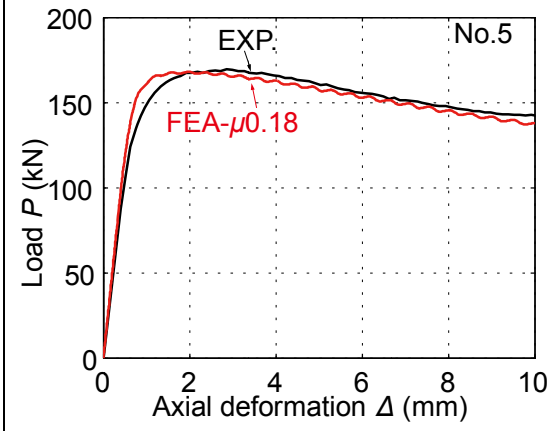 No.5 EXP. FEA-μ0.18 Load P (kN) Axial deformation Δ (mm)		
6	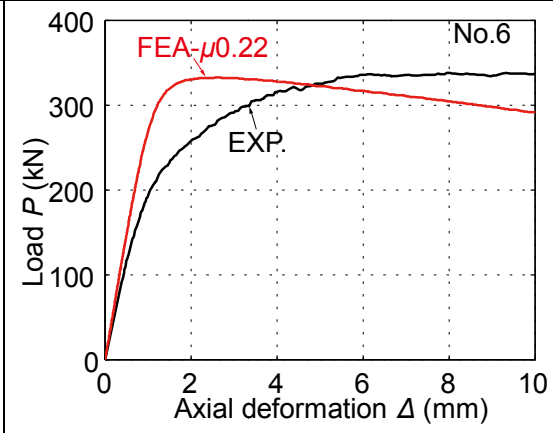 No.6 FEA-μ0.22 EXP. Load P (kN) Axial deformation Δ (mm)		
7	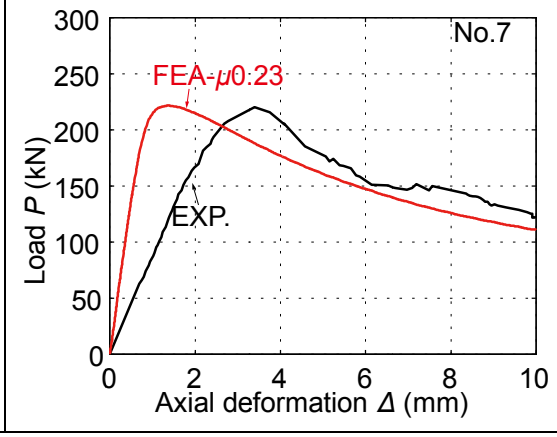 No.7 FEA-μ0.23 EXP. Load P (kN) Axial deformation Δ (mm)		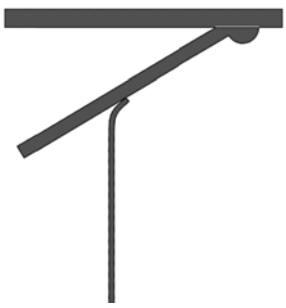

8	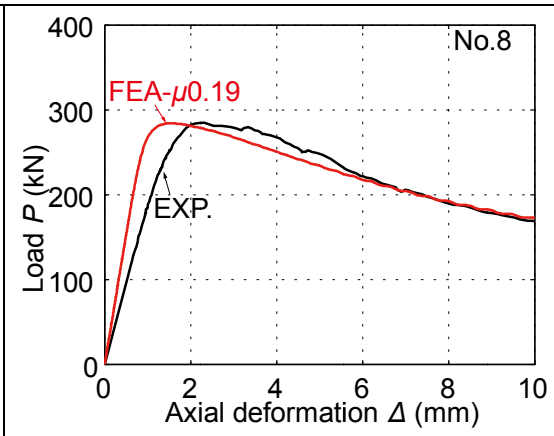 No.8 FEA-μ0.19 EXP. Load P (kN) Axial deformation Δ (mm) 0 100 200 300 400 0 2 4 6 8 10		
10	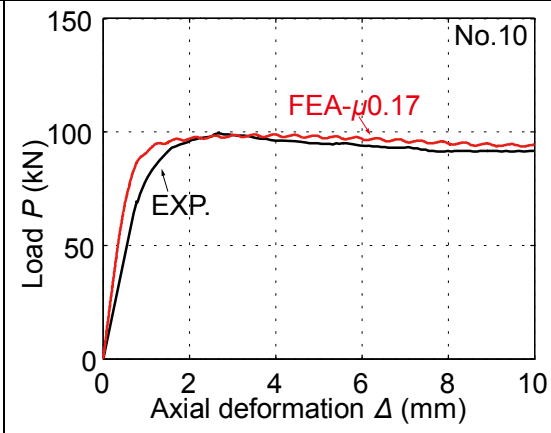 No.10 FEA-μ0.17 EXP. Load P (kN) Axial deformation Δ (mm) 0 50 100 150 0 2 4 6 8 10	 PA4-1	
11	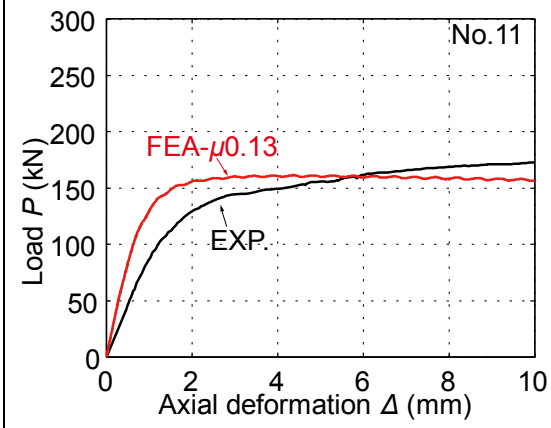 No.11 FEA-μ0.13 EXP. Load P (kN) Axial deformation Δ (mm) 0 50 100 150 200 250 300 0 2 4 6 8 10	 PC6-1	
12	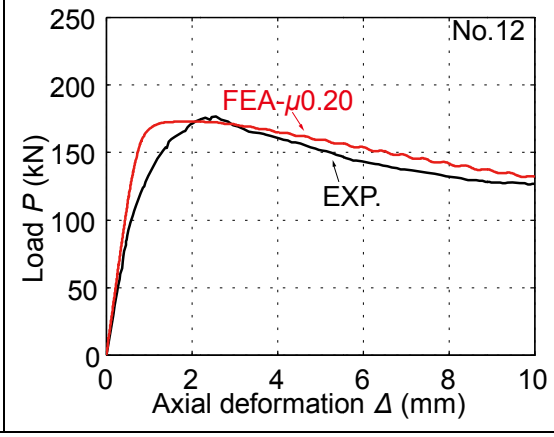 No.12 FEA-μ0.20 EXP. Load P (kN) Axial deformation Δ (mm) 0 50 100 150 200 250 0 2 4 6 8 10	 PA4-2	

13	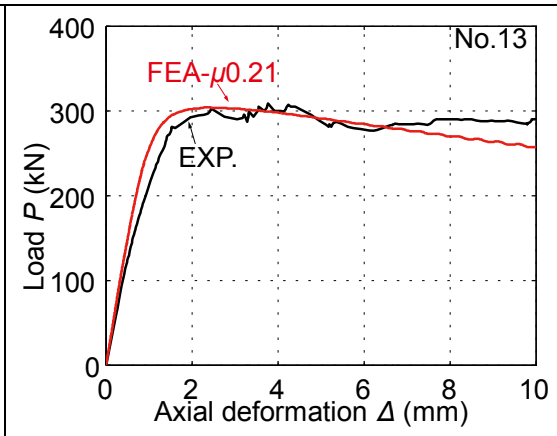 No.13 FEA-μ0.21 EXP. Load P (kN) Axial deformation Δ (mm)		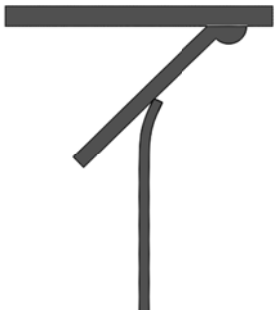
14	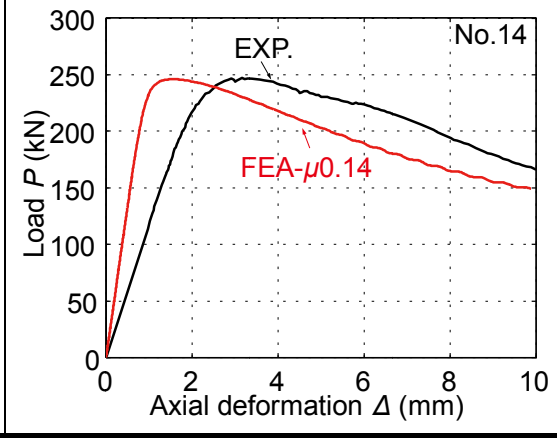 No.14 EXP. FEA-μ0.14 Load P (kN) Axial deformation Δ (mm)		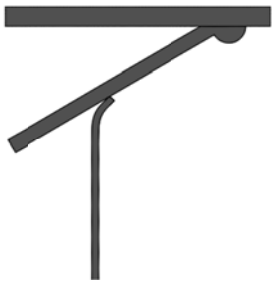

C.2 Metal Touch Connections with Tapered Ring Failure

No.	*P-Δ* curves	Deformation at collapse load	
		EXP.	FEA
26	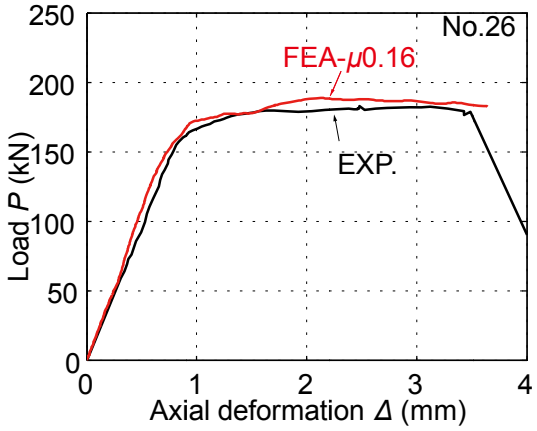		
27	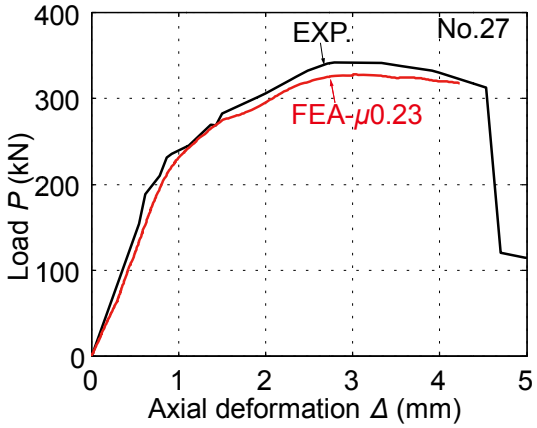		
28	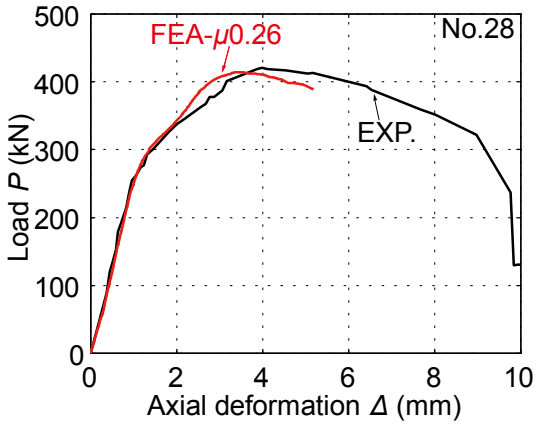		

29	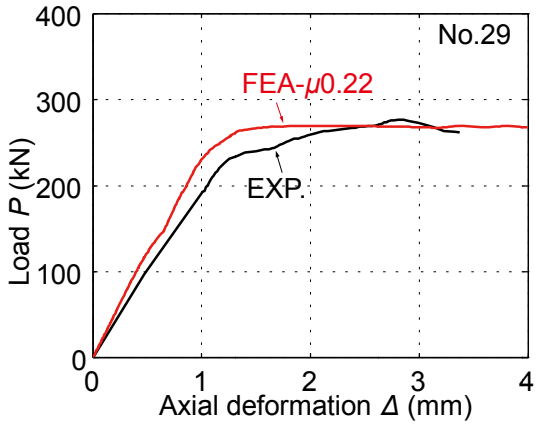 No.29 FEA-μ0.22 EXP. Load P (kN) Axial deformation Δ (mm)		
30	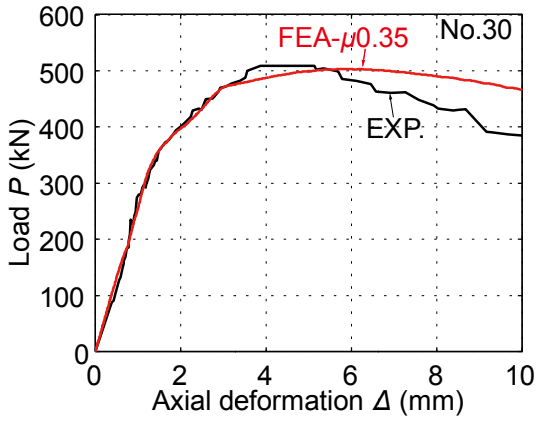 No.30 FEA-μ0.35 EXP. Load P (kN) Axial deformation Δ (mm)		
35	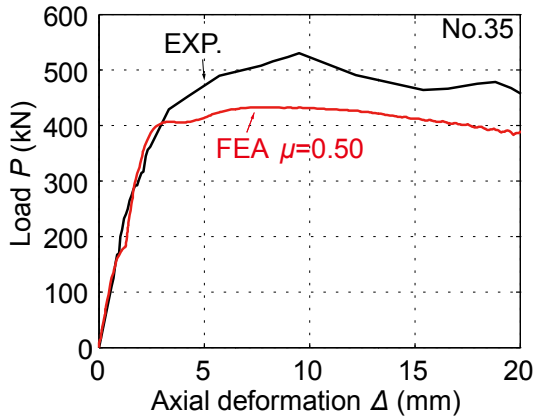 No.35 EXP. FEA μ=0.50 Load P (kN) Axial deformation Δ (mm)		
37	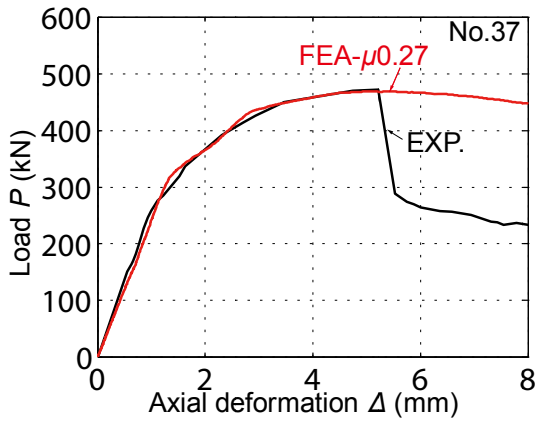 No.37 FEA-μ0.27 EXP. Load P (kN) Axial deformation Δ (mm)		

C.3 Metal Touch Connections with Conical Wall Failure

No.	*P-Δ* curves	Deformation after collapse	
		EXP.	FEA
9	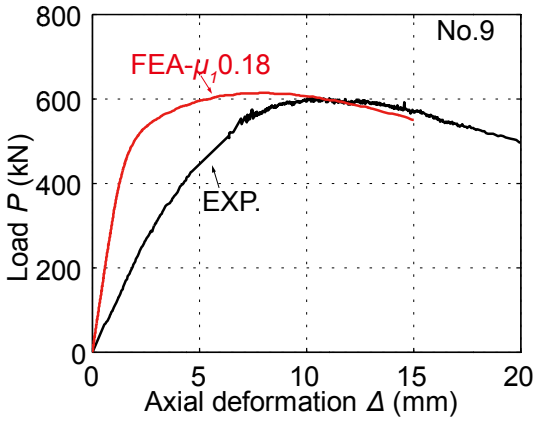		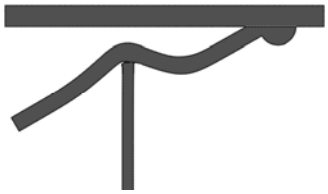
34	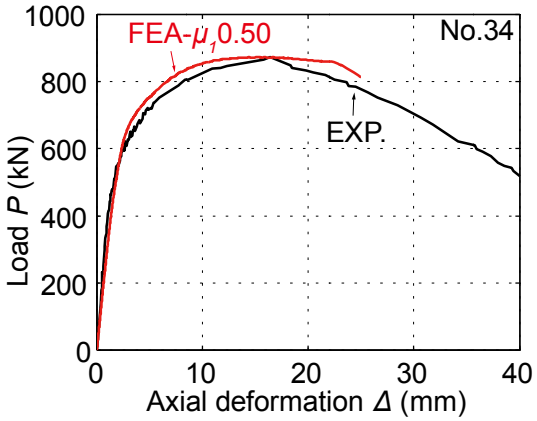		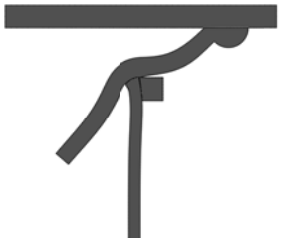
36	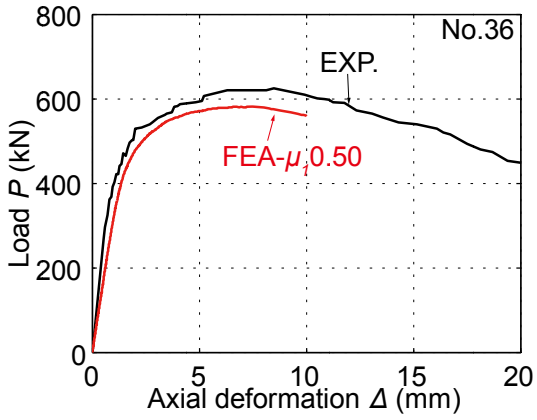		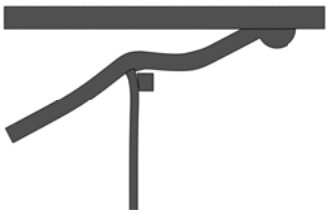

43	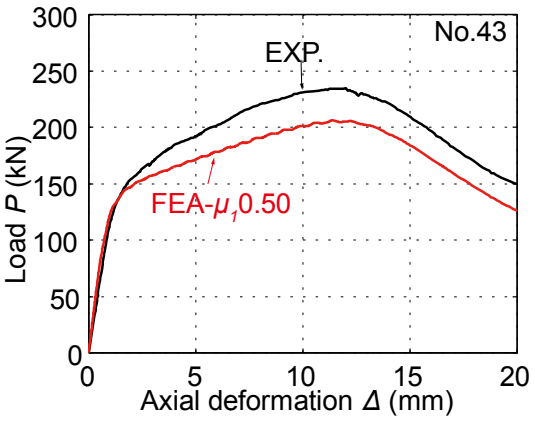 No.43 EXP. FEA-$\mu_1$0.50 Load P (kN) Axial deformation Δ (mm)	 PB-4	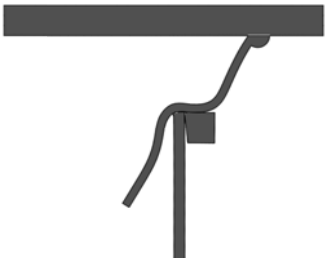
44	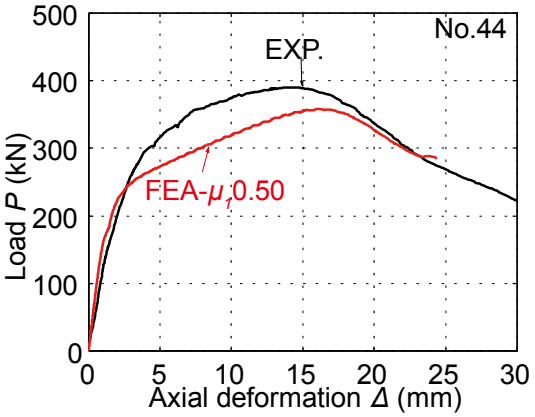 No.44 EXP. FEA-$\mu_1$0.50 Load P (kN) Axial deformation Δ (mm)	 PB4	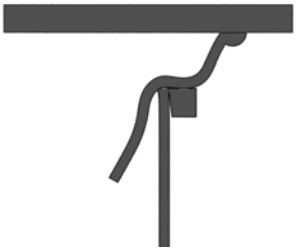
46	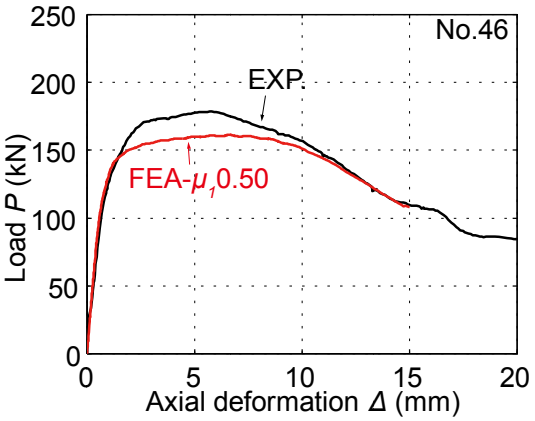 No.46 EXP. FEA-$\mu_1$0.50 Load P (kN) Axial deformation Δ (mm)	 PB4	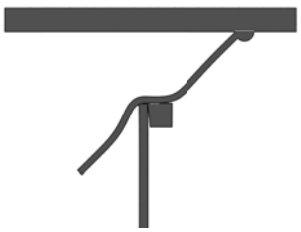
47	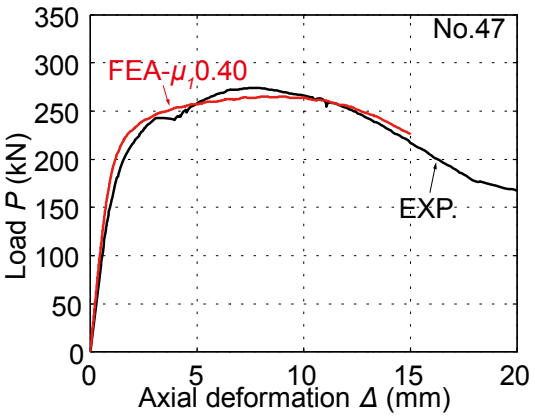 No.47 FEA-$\mu_1$0.40 EXP. Load P (kN) Axial deformation Δ (mm)	 PB4	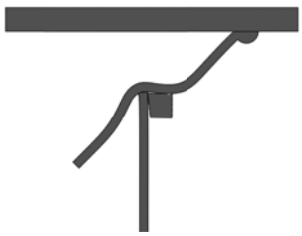

48	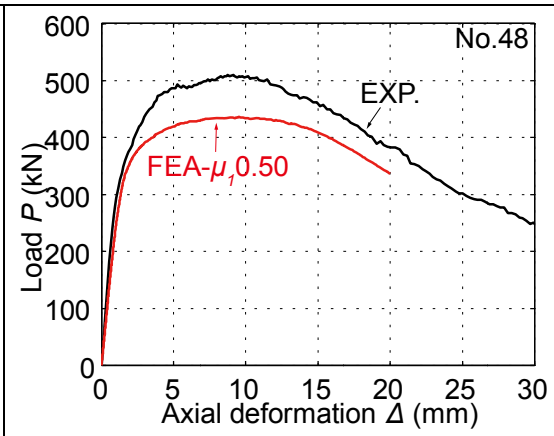 No.48 EXP. FEA-$\mu_1$0.50 Load P (kN) Axial deformation Δ (mm)		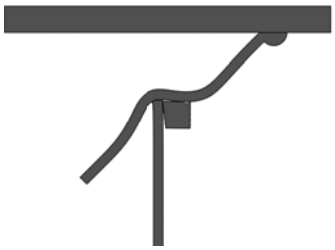
49	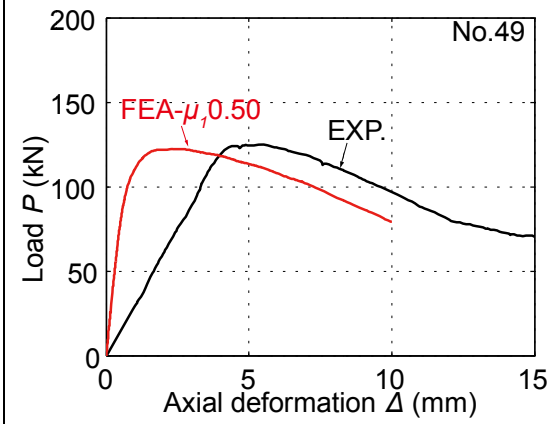 No.49 FEA-$\mu_1$0.50 EXP. Load P (kN) Axial deformation Δ (mm)		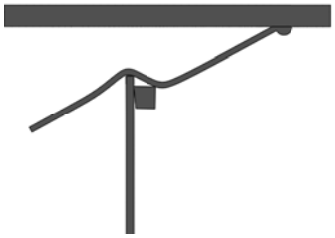
50	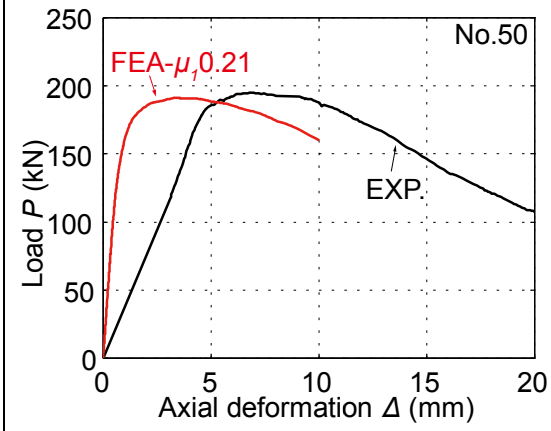 No.50 FEA-$\mu_1$0.21 EXP. Load P (kN) Axial deformation Δ (mm)		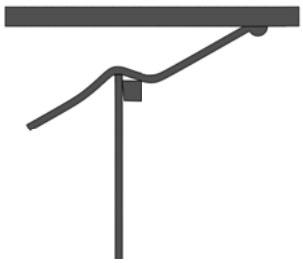
51	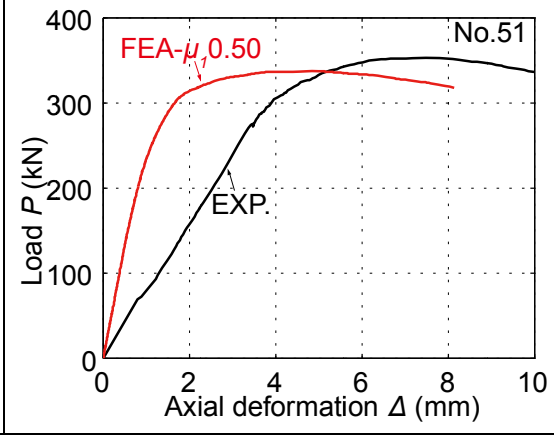 No.51 FEA-$\mu_1$0.50 EXP. Load P (kN) Axial deformation Δ (mm)		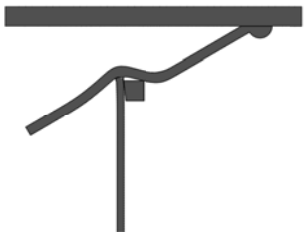

52	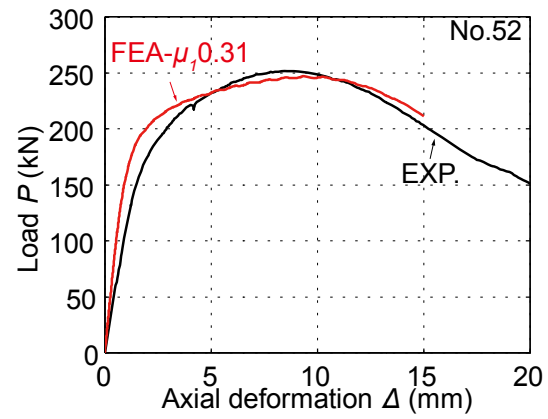 No.52 FEA-$\mu_1$0.31 EXP. Load P (kN) Axial deformation Δ (mm)		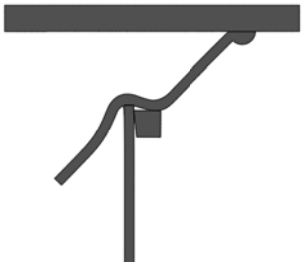
53	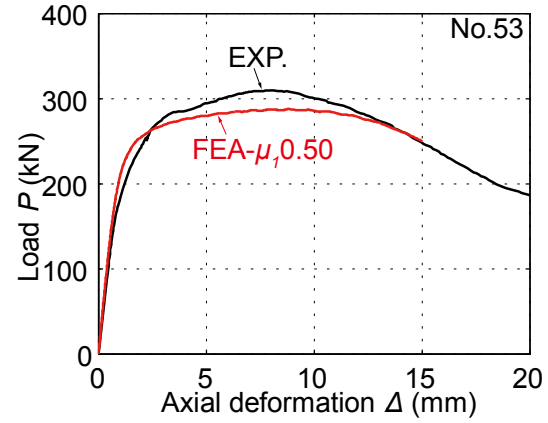 No.53 EXP. FEA-$\mu_1$0.50 Load P (kN) Axial deformation Δ (mm)		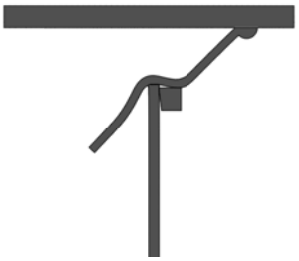

C.4 Welded Connections with Joint Region Failure

No.	*P-Δ* curves	Deformation after collapse	
		EXP.	FEA
64	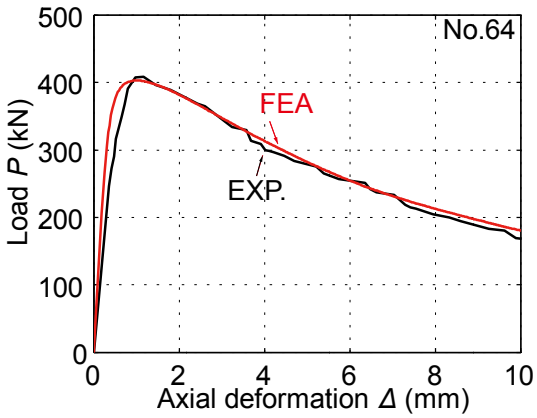		
65	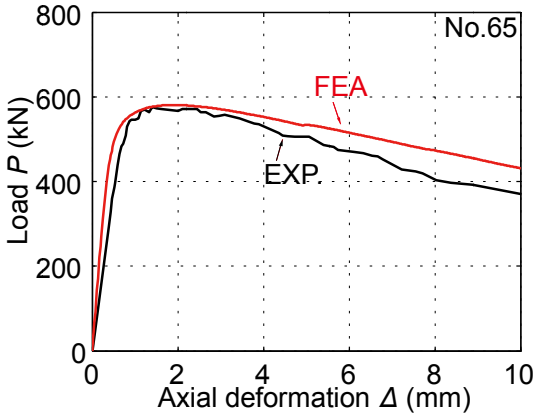		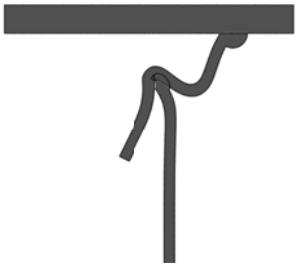
67	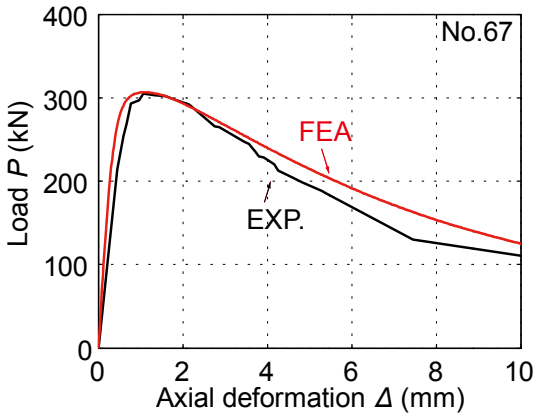		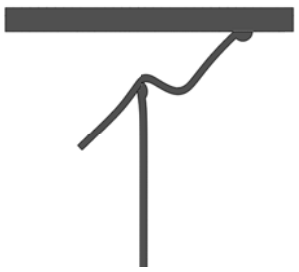

68	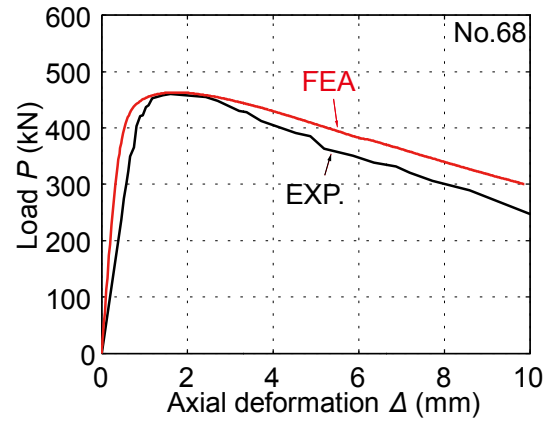 No.68 FEA EXP. Load P (kN) Axial deformation Δ (mm)		
69	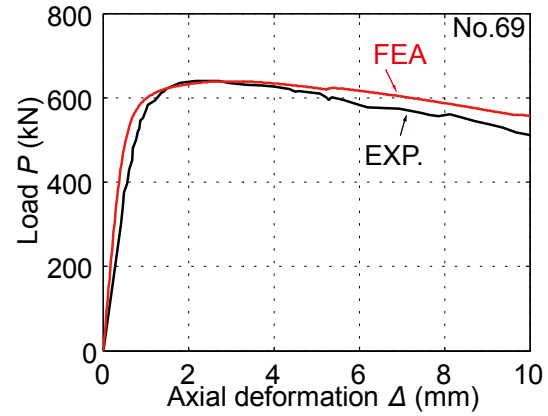 No.69 FEA EXP. Load P (kN) Axial deformation Δ (mm)		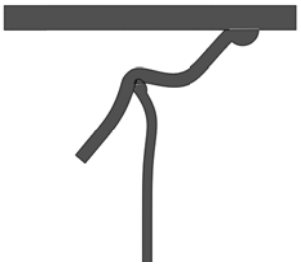
70	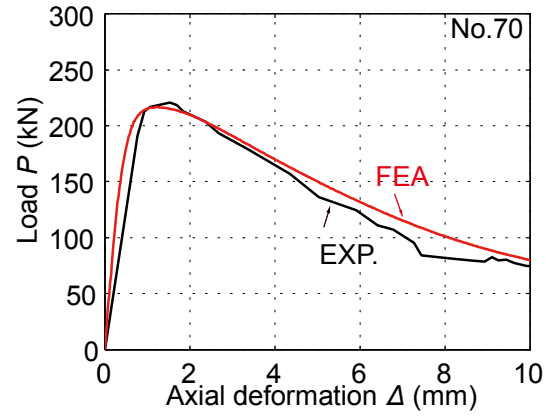 No.70 FEA EXP. Load P (kN) Axial deformation Δ (mm)	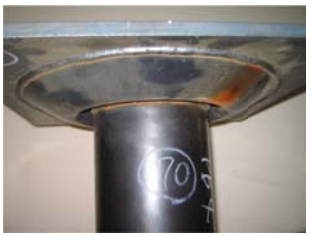	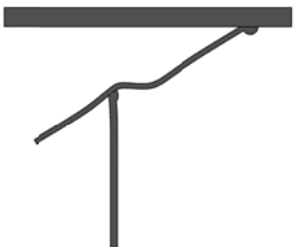
71	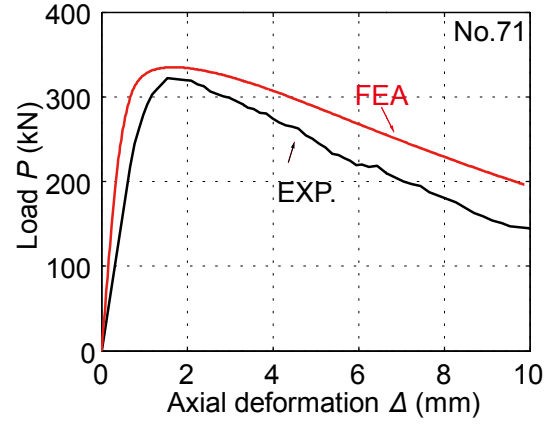 No.71 FEA EXP. Load P (kN) Axial deformation Δ (mm)		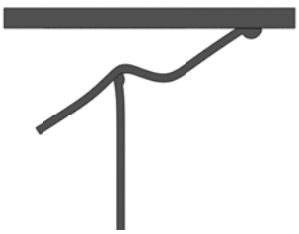

72	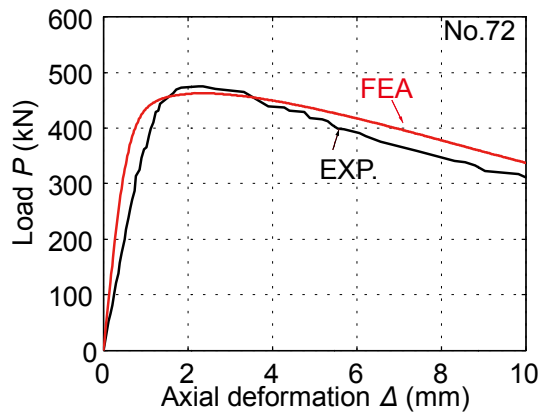 No.72 FEA EXP. Load P (kN) Axial deformation Δ (mm)		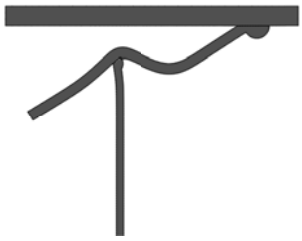
73	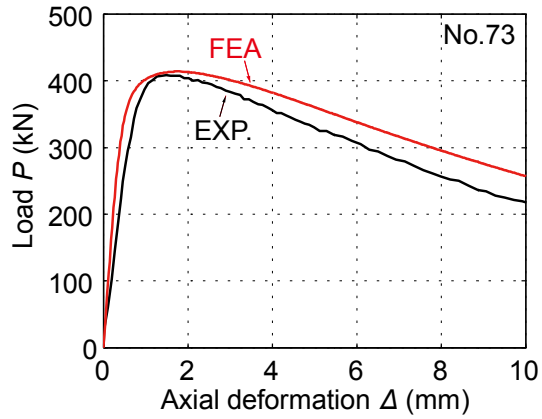 No.73 FEA EXP. Load P (kN) Axial deformation Δ (mm)		
74	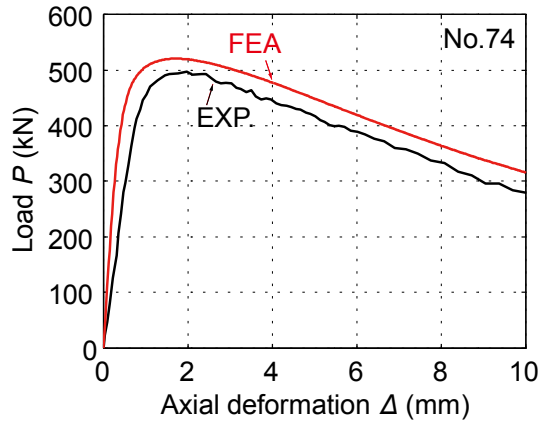 No.74 FEA EXP. Load P (kN) Axial deformation Δ (mm)		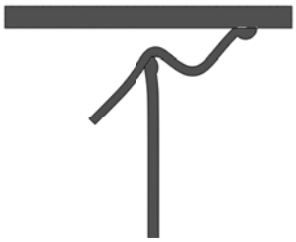

Appendix D Influence of Gap between Conical Wall and Cylinder Edge on Collapse Strength of Metal Touch Connections

D.1 Introduction

For metal touch cone-to-cylinder socket connections, perfect contact between conical wall and cylinder edge is quite difficult to be realized in practice because of the rotation of conical wall. As shown in Fig. D-1, when conical wall rotates at an angle of θ, the contact surface of conical wall is turned into an ellipse. Gap with maximum length g will occur between conical wall and cylinder edge. The stress in the contact region will not be distributed uniformly any more. The corresponding behavior and strength of connections have not been made clear. In this appendix, the variation of gap length with the increase of rotational angle is first analyzed. And then, Finite element (FE) analysis is employed to investigate the influence of gap on strength of connections qualitatively.

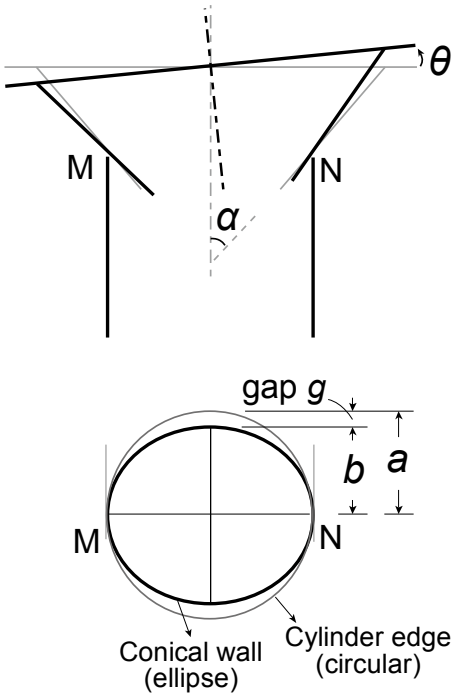

Fig. D-1 Gap between conical wall and cylinder edge after rotation of conical wall

D.2 Variation of Gap Length along with Rotation of Conical Wall

The relationship between gap length and rotational angle of conical wall is derived based on geometry theorem. The result is expressed in Eq. (D-1).

$$g \equiv a - b = \left(1 - \cos\theta\sqrt{1 - (\tan\alpha\tan\theta)^2}\right) \cdot a \qquad \text{(D-1)}$$

where, g is the maximum length of gap, a is the radius of cylindrical wall, b is the minor axis of ellipse, α is semi-vertex angle of conical wall, and θ is rotational angle of conical wall.

By setting radius a to be 65.72mm, semi-vertex angle α to be 30°, 45°, and 60° respectively, and tangent of rotational angle θ to be 0, 1/20, 1/10 and 1/5 respectively, the variation of gap length g with increase of rotational angle θ is plotted in Fig. D-2. It can be found that when α increases, the increase of gap length g becomes more rapidly along with tangent of rotational angle θ. In the lateral FEA, the representative models with α=45° are employed to investigate the influence of gap length g on the strength of connections.

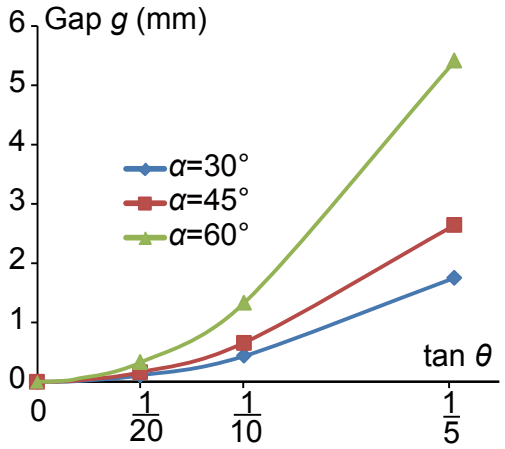

Fig. D-2 Increase of the length of gap along with rotation θ of conical wall

Note: radius a is equal to 65.72mm.

D.3 FE Analysis

D.3.1 FE Modeling

Half three-dimensional solid finite element (FE) model as illustrated in Fig. D-3 is established using ABAQUS 6.11 based on the consideration of geometrical symmetry and computing time. Four-node shell elements with reduced integration, *S4R*, are adopted for conical and cylindrical shells. Eight-node solid element with reduced integration, *C3D8R*, is adopted for tapered ring.

For the top edge of cone, all the freedoms except for the displacement freedom in x direction are fixed. For plane z=0, the symmetric boundary condition as shown in the figure are applied. For the bottom end of cylinder, all the displacement freedoms are fixed.

Displacement loading histories are applied at the top edge of cone. Rotational angle θ of conical wall is shown in Fig. D-3(b). The tangent of θ is set to be 0, 1/20, 1/10, and 1/5 respectively, as shown in Fig. D-4.

In total, 12 models are created. Their dimensions are listed in Table D-1. Friction coefficient in the contact surface between conical wall and cylinder edge is set to be 0.20. Cylindrical wall is tied to ring for tapered ring failure. The displacement in x and z directions of the top edge of cylindrical wall is fixed for conical wall failure, where ring is not employed.

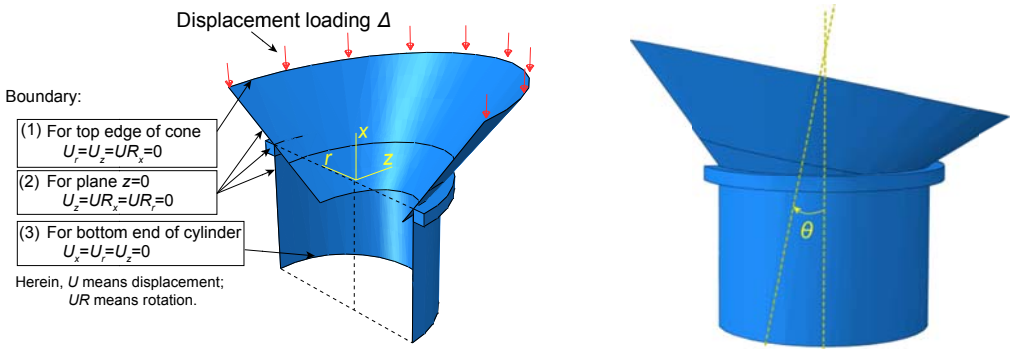

(a) Perspective (b) Elevation

Fig. D-3 Half three-dimensional FE models with rotation of conical wall

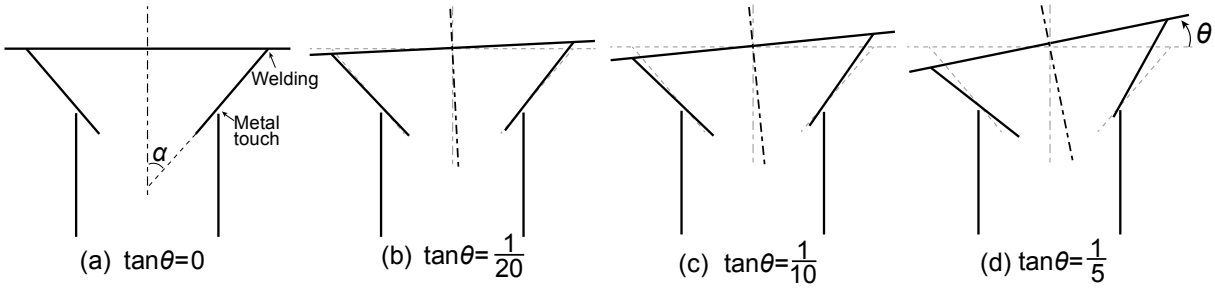

Fig. D-4 Condition of connections with different rotational angles of conical wall (α=45°)

Table D-1 Dimensions of models with different failure modes

Model No.	Failure mode	t_C	t_P	t_R	α	d_P	Boundary between cone and cylinder	Boundary between ring and cylinder	tan θ
		mm	mm	mm	°	mm			
1	Cylinder edge failure	9.00	4.21		45	131.38	Frictional contact μ=0.20		0
2									1/20
3									1/10
4									1/5
5	Tapered ring failure	9.00		9.00				Tie	0
6									1/20
7									1/10
8									1/5
9	Conical wall failure	4.27						Top edge of cylinder: U_x=U_z=0. Ring is not employed.	0
10									1/20
11									1/10
12									1/5

Note: (1) t_C means thickness of conical wall; t_P means thickness of cylindrical wall; t_R means thickness of tapered ring; α means semi-convex angle of conical wall; and d_P means diameter of cylindrical shell.

D.3.2 FE Analysis Results

D.3.2.1 Metal Touch Connection with Cylinder Edge Failure

Fig. D-5 shows the load versus deformation curves of model Nos.1~4 with cylinder edge failure. It can be found that the elastic stiffness and ultimate load keep to be constant until tan θ =1/10. When tan θ =1/5, the elastic stiffness decreases obviously while the ultimate load increases very slightly. The reason might be that the actual semi-vertex angle α of conical wall is obviously increased due to the rotation. The increase of α makes the ultimate strength a litter greater. But it can be neglected even if tan θ reaches 1/5, based on the results in Fig. D-6.

Fig. D-7 illustrates the distribution of Mises stress in cylindrical wall with the increase of load for model No.3 with tan θ=1/10. It can be found that at the beginning of loading, Mises stress close to contact points M and N is much greater than other regions. As load increases, Mises stress in other regions also increases. When ultimate load arrives, the distribution of Mises stress becomes to be uniform. It indicates that because of the deformation capacity of cylinder edge, the gap has been filled and the conical wall has contacted with cylinder edge in 360 degrees.

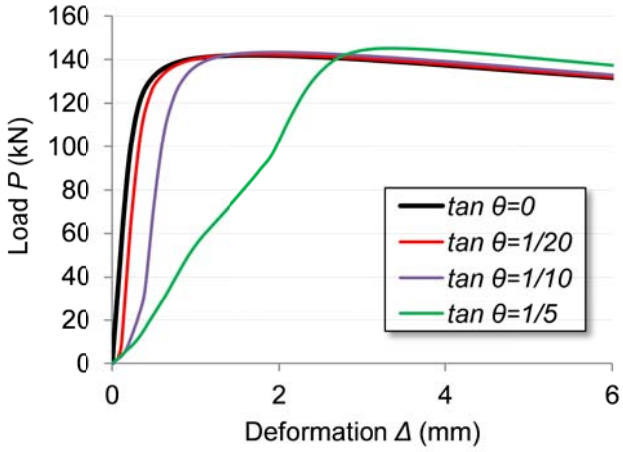

Fig. D-5 Variation of load versus deformation curves along with the increase of rotational angle for models with cylinder edge failure

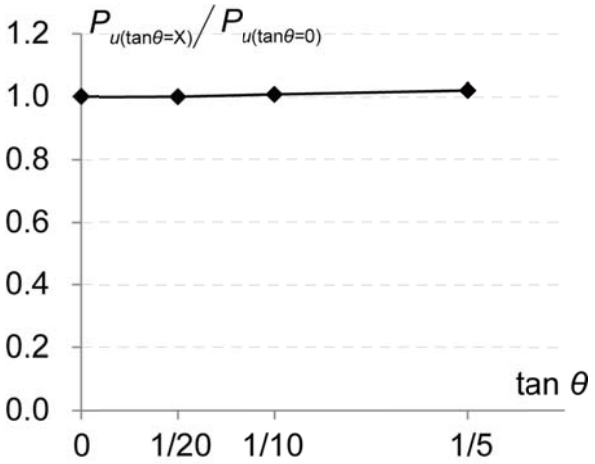

Fig. D-6 Variation of ultimate load along with the increase of rotational angle for models with cylinder edge failure

(tan θ =X means tan θ =0, 1/20, 1/10 and 1/5, the same hereinafter in this appendix)

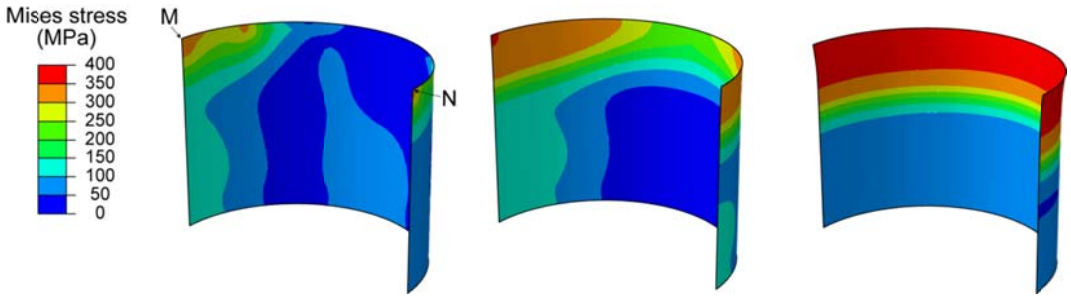

(a) at33.2kN (b) at 105.2kN (c) at 143.2kN (P_u)

Fig. D-7 Mises stress distribution at different load for model No. 3 with tan θ=1/10

D.3.2.2 Metal Touch Connection with Tapered Ring Failure

The results of model Nos. 5~8 with tapered ring failure are shown in Figs. D-8 and D-9. They are similar to those of models No. 1~4 with cylinder edge failure and omitted here.

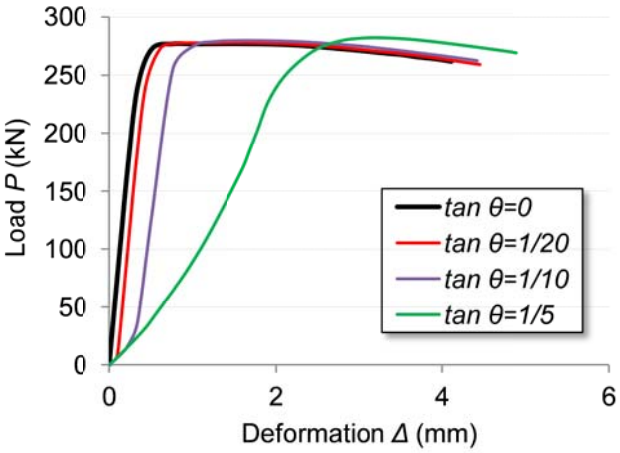

Fig. D-8 Variation of load versus deformation curves along with the increase of rotational angle for models with tapered ring failure

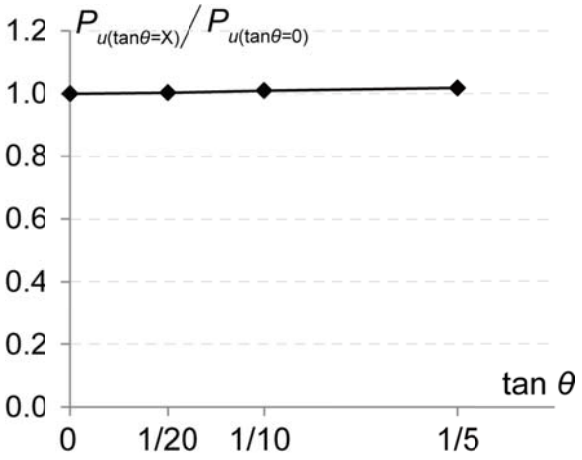

Fig. D-9 Variation of ultimate load along with the increase of rotational angle for models with tapered ring failure

D.3.2.3 Metal Touch Connection with Conical Wall Failure

Fig. D-10 shows the comparison of load versus deformation curves for models with conical wall failure. It can be found the collapse strength almost keeps to be constant until tan θ reaches 1/10. When tan θ=1/5, ultimate load slightly decreases. However, The decrease of ultimate load is so small that can be not considered, based on the result in Fig. D-11.

Fig. D-12 illustrates the distribution of Mises stress at ultimate load for models with different values of tan θ. It can be found that the distribution of Mises stress can be assumed to be uniform until tan θ reaches 1/10.

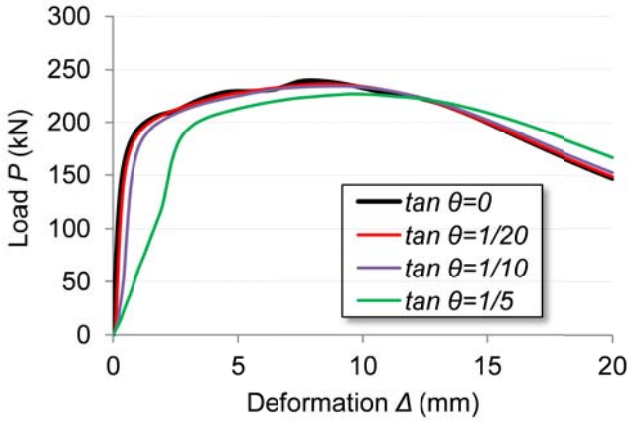

Fig. D-10 Comparison on load versus deformation curves for models with conical wall failure

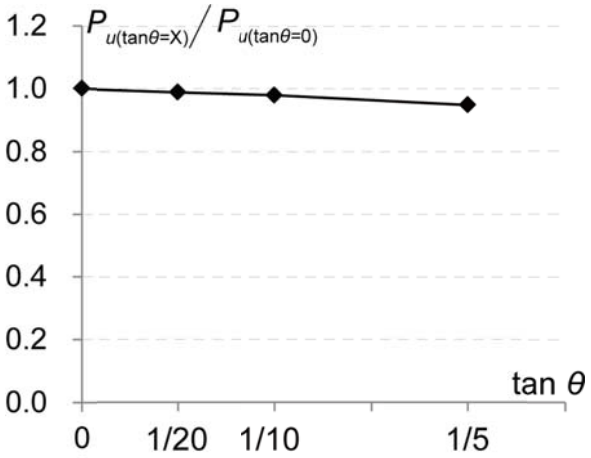

Fig. D-11 Variation of ultimate load along with the increase of rotational angle for models with conical wall failure

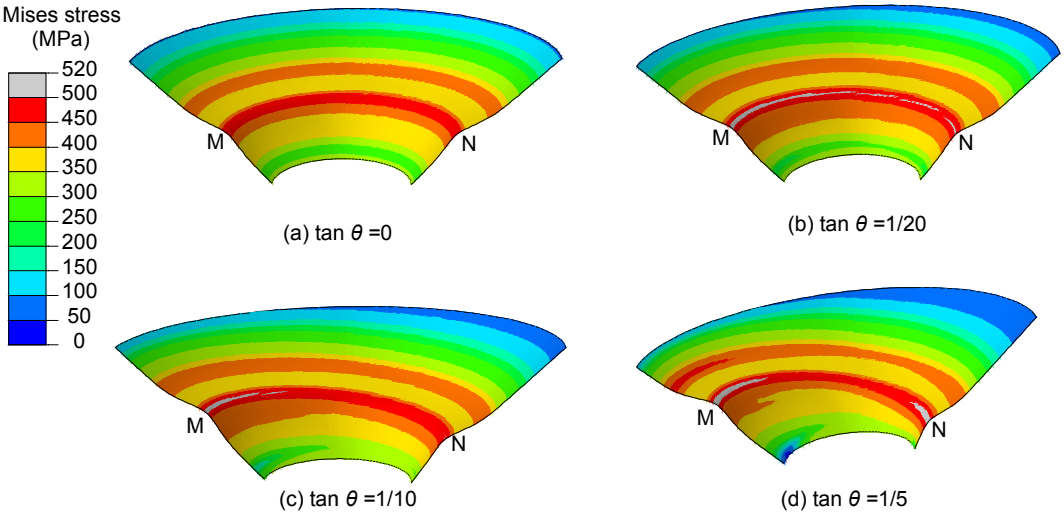

Fig. D-12 Distribution of Mises stress in conical wall at ultimate load for models with conical wall failure

D.4 Summaries

In this appendix, the relationship between gap length and rotational angle of conical wall is derived. And then, the influence of rotational angle on collapse strength of metal touch connections is investigated by FEA. The conclusions are shown as follows:

(1) The gap length g increases as tan θ increases. If semi-vertex angle of conical wall is 45^{o}, diameter of cylindrical shell is 131mm, and tan θ is 1/5, the gap length g will reach about 2.7mm.

(2) Because of the deformation capacity of cylinder edge, the gap can be filled as load increases.

(3) The collapse strength of metal touch connections almost keeps to be constant even if tan θ increases to be 1/10. From the seismic engineering point of view, tan θ of conical wall is similar to that of story drift angle of column, and usually less than 1/50 in practice. Therefore, the influence of gap length or rotational angle of conical wall on collapse strength of metal touch connections can be not considered.

Appendix E Influence of Eccentricity of Compressive Loading on Collapse Strength of Connections

E.1 Introduction

The body part of this thesis focuses on the strength of steel cone-to-cylinder socket connections under axial compression. Actually, shear force and bending moment are also transformed from upper structure due to earthquake or wind load, as shown in Fig. E-1. In this case, the socket connection will be compressed under eccentric loading. The strength and behavior of connections, which are different from those under axial compression, have not been clarified. In this appendix, Finite element (FE) analysis is employed to investigate the influence of eccentricity ratio of load on collapse strength of connections qualitatively.

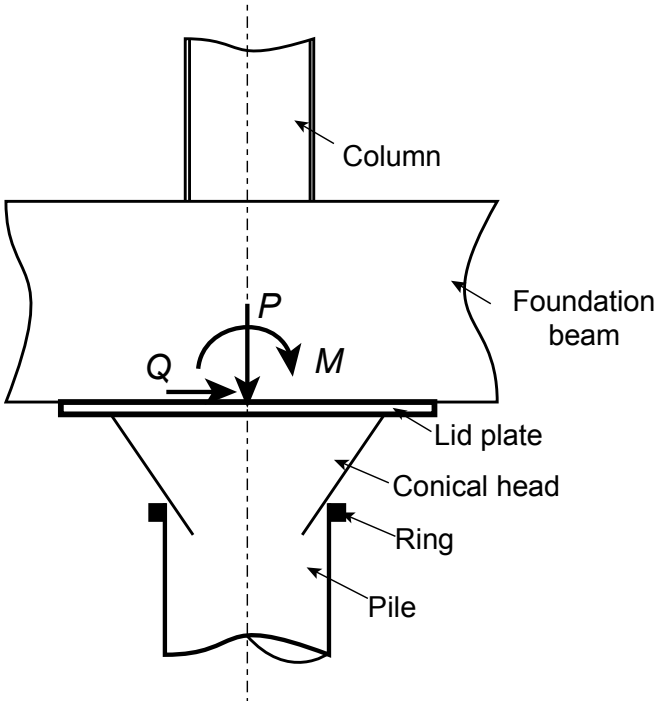

Fig. E-1 Conical pile head model in building structure

E.2 FE Analysis

E.2.1 FE Modeling

Half three-dimensional solid finite element (FE) model as illustrated in Fig. E-2 is established using ABAQUS 6.11 based on the consideration of geometrical symmetry and computing time. Four-node shell elements with reduced integration, *S4R*, are adopted for conical and cylindrical shells, and lid plate. Eight-node solid element with reduced integration, *C3D8R*, is adopted for ring, which is simplified to be rectangular. It should be noted that lid plate is defined to be elastic, with Young's modulus E=205,000MPa and Poisson's ratio v=0.3; conical wall, cylindrical wall and tapered ring are defined to be actual.

For the top edge of cone, it is tied to the bottom surface of lid plate. For plane z=0, the symmetric boundary condition as shown in the figure are applied. For the bottom end of cylinder, all the displacement freedoms are fixed.

Displacement loading histories are applied at the top surface of lid plate. Eccentricity ratio of load is set to be 0, 1/8, 1/4, 3/8, and 1/2 respectively, as shown in Fig. E-3. It should be noted that the influence of loading length h on strength of connections is not considered and defined to be 16mm. The confinement effect of foundation beam on lid plate is also neglected.

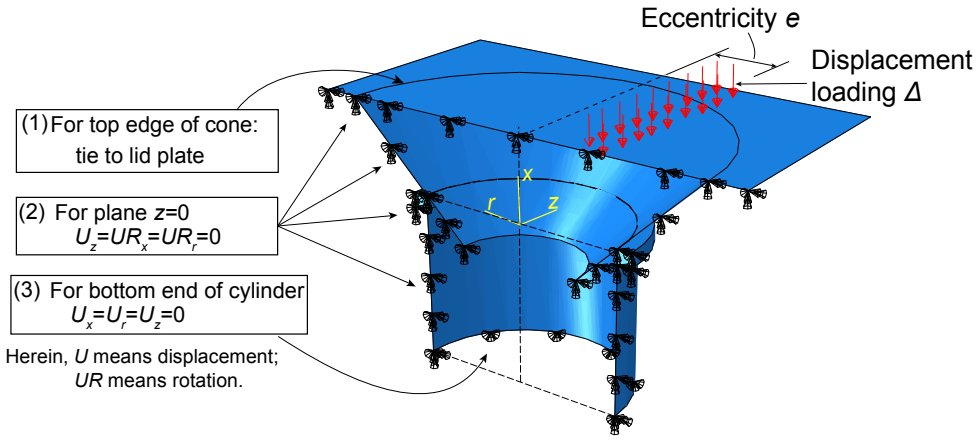

Fig. E-2 Half three-dimensional FE models under eccentric loading

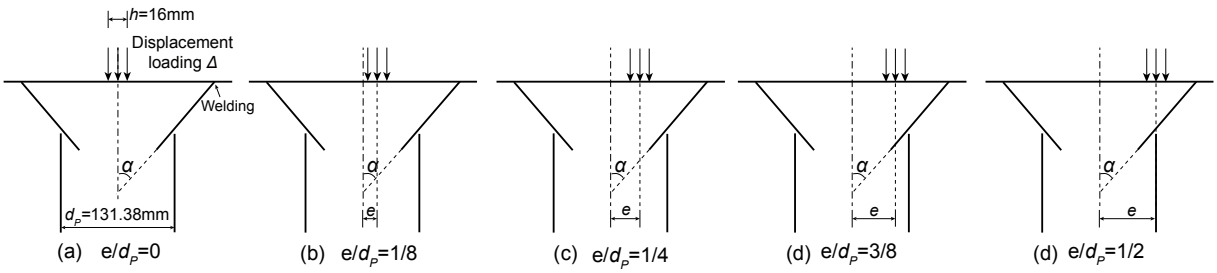

Fig. E-3 Eccentricity ratios of loading employed in FE model

Table E-1 Details of FE models with different modes

Model No.	Failure mode	t_C mm	t_P mm	t_R mm	t_L mm	α °	d_P mm	Boundary between cone and cylinder	Boundary between cylinder and ring	Eccentricity ratio of load
1	Cylinder edge failure	9.00	4.21		12.00	45	131.38	Frictional contact μ=0.20		0
2										1/8
3										1/4
4										3/8
5										1/2
6	Tapered ring failure	9.00		9.00					Tie	0
7										1/8
8										1/4
9										3/8
10										1/2
11	Conical wall failure	4.27							Top edge of cylinder: U_x=U_z=0. Ring is not employed.	0
12										1/8
13										1/4
14										3/8
15										1/2
16	Joint region failure	4.27						Tie		0
17										1/8
18										1/4
19										3/8
20										1/2

Note

t_C : thickness of conical wall; t_P: thickness of cylindrical wall; t_R: thickness of tapered ring; α: semi-convex angle of conical wall; and d_P: diameter of cylindrical shell.

In total, 20 models are created for the four kinds of failure modes. Their dimensions are listed in Table E-1. Friction coefficient in the contact surface between conical wall

and cylinder edge for metal touch models is set to be 0.20. Conical wall is tied to cylinder edge for welded models. Cylindrical wall is tied to ring for tapered ring failure. The displacement in x and z directions of the top edge of cylindrical wall is fixed for conical wall failure, where ring is not employed.

E.2.2 FE Analysis Results

E.2.2.1 Metal Touch Connection with Cylinder Edge Failure

Fig. E-4 gives the comparison of load versus deformation curves among models with different eccentricity ratios of loading. It can be found that the elastic stiffness decreases with the increase of eccentricity ratio of load, while the collapse strength almost keeps constant, as shown in Fig. E-5.

Comparison of Mises stress distribution at ultimate load between models with and without eccentricity ratio of load is shown in Fig. E-6. Because the strength of cylinder edge is much weaker than conical wall, conical wall moves downward almost in parallel even if under eccentric loading. The compression transmitted from conical wall to cylinder edge seems still uniform. As a result, the Mises stress distribution of cylindrical wall in the case of e/t_P=1/2 is quite similar to that in the case of e/t_P=0. It might be the reason why the collapse strength of cylinder edge keeps almost constant.

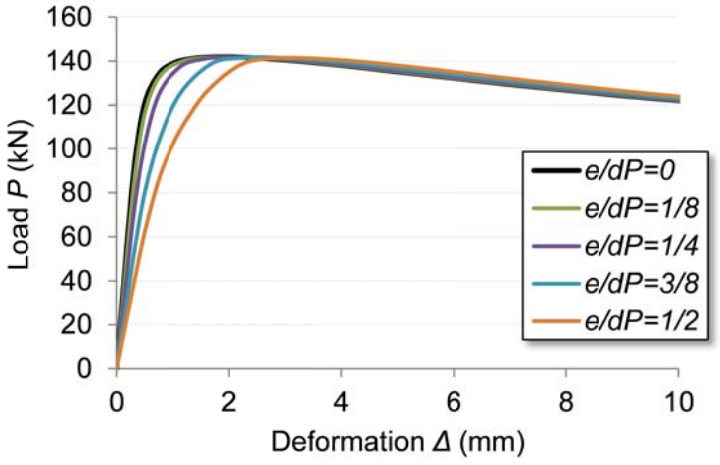

Fig. E-4 Comparison of load versus deformation curves among models with different eccentricity ratios of loading for cylinder edge failure

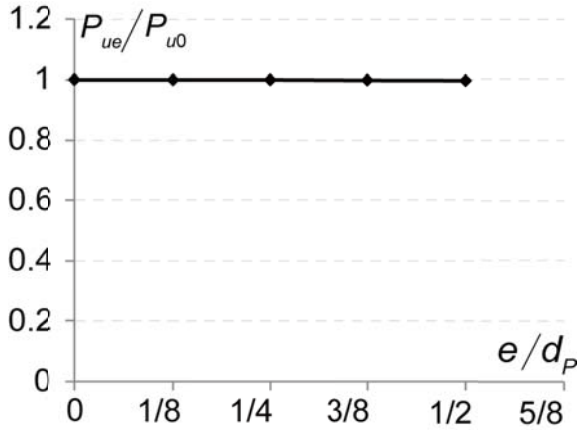

Fig. E-5 Variation of ultimate load along with the increase of eccentricity ratio of load for cylinder edge failure

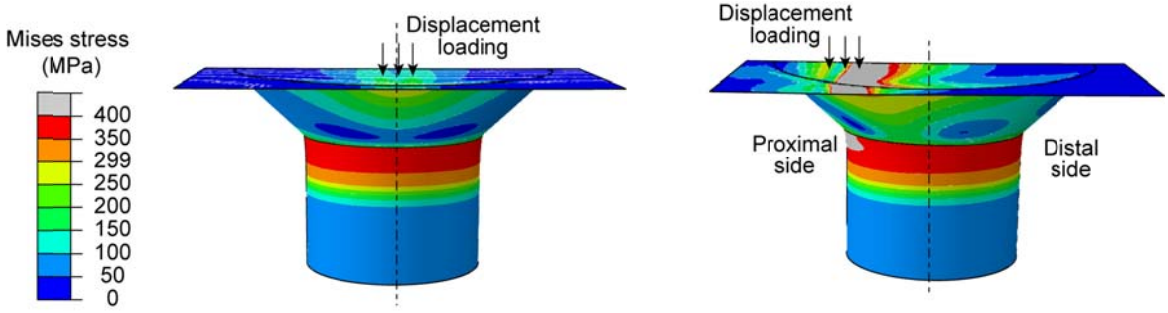

(a) e/d_P=0 (b) e/d_P=1/2

Fig. E-6 Comparison of Mises stress distribution at ultimate load between models with and without eccentricity ratio of load for cylinder edge failure

E.2.2.2 Metal Touch Connection Tapered Ring Failure

Fig. E-7 gives the comparison of load versus deformation curves among models with different eccentricity ratios of loading. It can be found that elastic stiffness decreases as eccentricity ratio of load increases, while collapse strength does not decrease so much. The variation of collapse strength along with eccentricity ratio of load is shown in Fig. E-8. It is seen that collapse strength decreases slightly until eccentricity ratio of load reaches 1/2.

Comparison of Mises stress distribution at ultimate load between models with and without eccentricity ratio of load is shown in Fig. E-9. Because the strength of cylinder edge and ring are weaker than conical wall, the rotation of conical wall and lid plate is not

obvious under eccentric loading. The Mises stress distribution of cylindrical wall in the case of e/t_P=1/2 is a little different from that in the case of e/t_P=0. It might be the reason why collapse strength of cylinder edge decreases slightly when e/t_P=1/2.

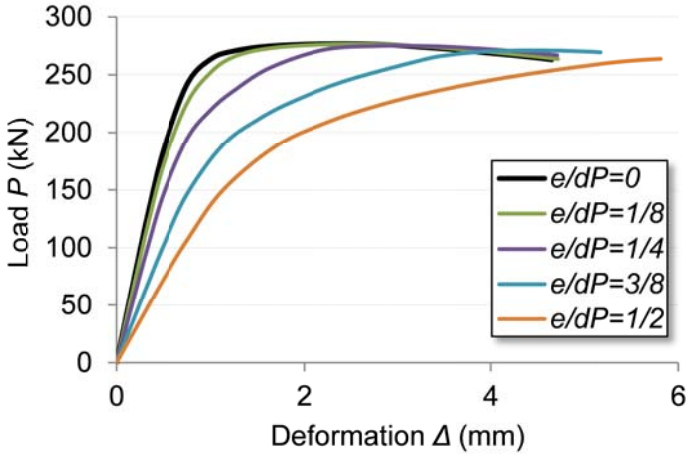

Fig. E-7 Comparison of load versus deformation curves among models with different eccentricity ratios of loading for tapered ring failure

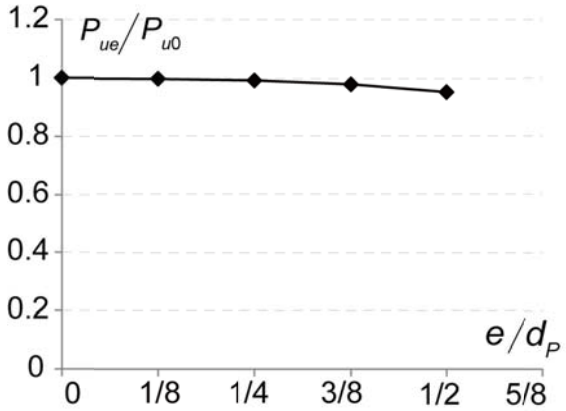

Fig. E-8 Variation of ultimate load along with the increase of eccentricity ratio of load for tapered ring failure

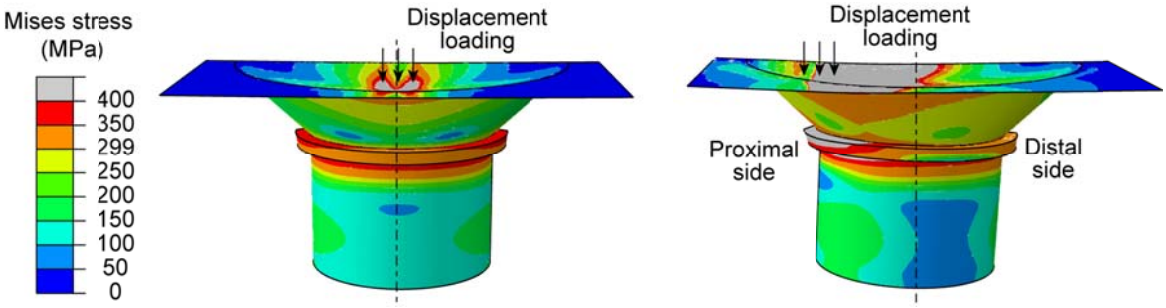

(a) e/d_P=0 (b) e/d_P=1/2

Fig. E-9 Comparison of Mises stress distribution at ultimate load between models with

and without eccentricity ratio of load for tapered ring failure

E.2.2.3 Metal Touch Connection Conical Wall Failure

Fig. E-10 shows the comparison of load versus deformation curves among models with different eccentricity ratios of loading. It can be seen that collapse strength decreases slightly with the increase of eccentricity ratio of load. The variation of collapse strength along with the increase of eccentricity ratio of load is plotted in Fig. E-11. It can be found that collapse strength decreases to be about 0.9 of that under axial compression when eccentricity ratio of load increases to be 1/2.

Fig. E-12 shows the comparison of Mises stress distribution at ultimate load between models with eccentricity ratio of load of 0 and 1/2 respectively. For the case of e/d_P=1/2, the distal side of conical wall uplifts and the proximal side of it descends as loading increases. At the same time, the both sides move downward. When ultimate load arrives, Mises stress distribution in the distal side is close to that in the proximal side. It might be the reason why ultimate load decreases slightly, comparing with the case of e/d_P=0.

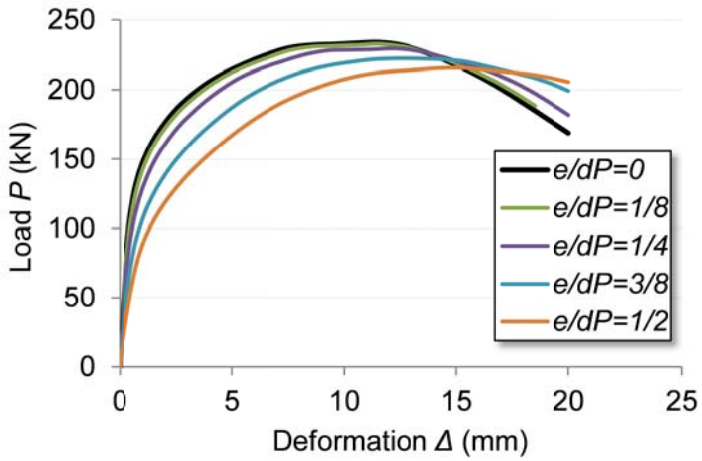

Fig. E-10 Comparison of load versus deformation curves among models with different eccentricity ratios of loading for conical wall failure

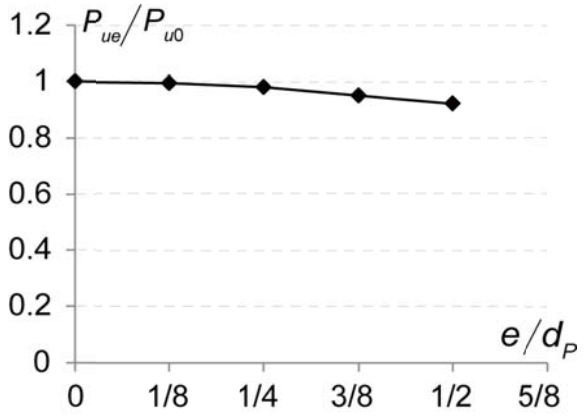

Fig. E-11 Variation of ultimate load along with the increase of eccentricity ratio of load for conical wall failure

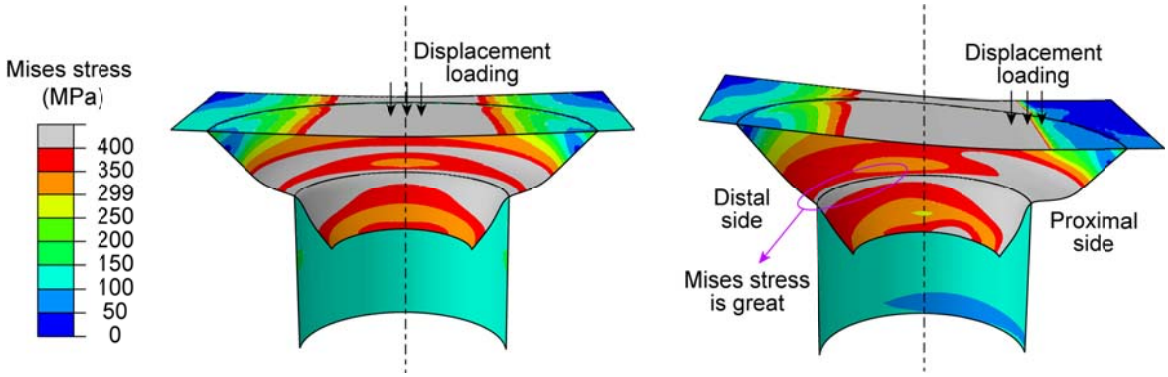

(a) e/d_P=0 (b) e/d_P=1/2

Fig. E-12 Comparison of Mises stress distribution at ultimate load between models with and without eccentricity ratio of load for conical wall failure

E.2.2.4 Welded Connections with Joint Region Failure

Fig. E-13 shows the comparison of load versus deformation curves among models with different eccentricity ratios of loading. It can be seen that collapse strength decreases obviously with the increase of eccentricity ratio of load. The variation of collapse strength along with the increase of eccentricity ratio of load is plotted in Fig. E-14. It can be found that collapse strength decreases to be about 0.7 of that under axial compression, when eccentricity ratio of load increases to be 1/2.

Fig. E-15 shows the comparison of Mises stress distribution at ultimate load between models with eccentricity ratio of load of 0 and 1/2. For the case of e/d_P=1/2, the distal side of conical wall uplifts and the proximal side of it descends as loading increases. The

difference from metal touch model with conical wall failure is that conical wall cannot move downward because of welding. When ultimate load arrives, the Mises stress in the distal side is much smaller than that in the proximal side. It might be the reason why ultimate load decreases quite greatly, comparing with the case of e/d_P=0.

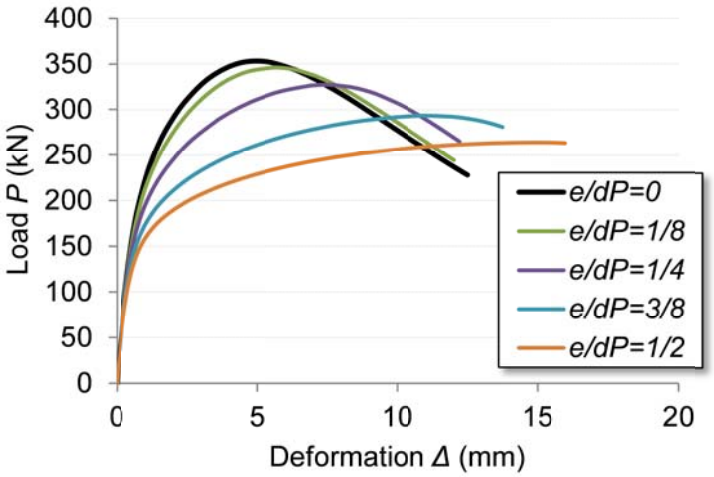

Fig. E-13 Comparison of load versus deformation curves among models with different eccentricity ratios of loading for joint region failure

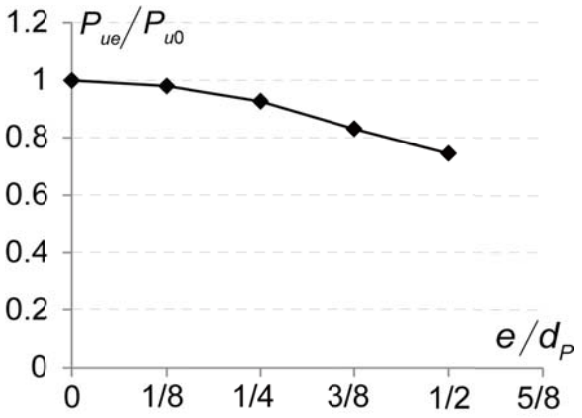

Fig. E-14 Variation of ultimate load along with the increase of eccentricity ratio of load for joint region failure

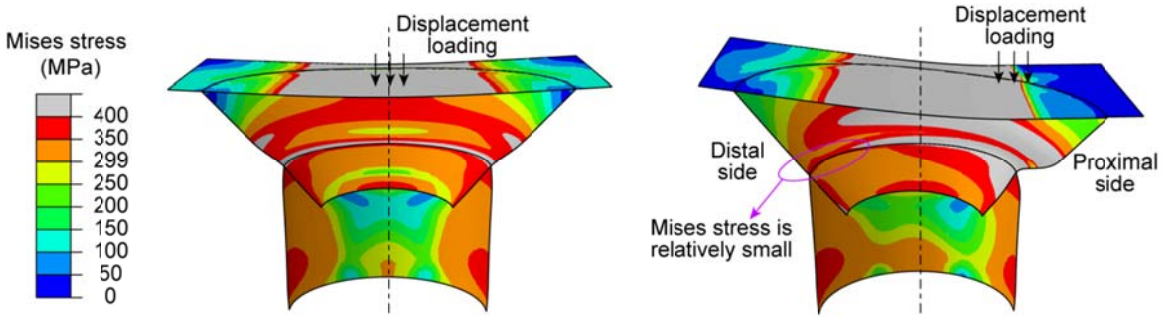

(a) e/d_P=0 (b) e/d_P=1/2

Fig. E-15 Comparison of Mises stress distribution at ultimate load between models with and without eccentricity ratio of load for joint region failure

E.3 Summaries

In this appendix, the influence of eccentricity ratio of load on collapse strength of connections is investigated by FE analysis. The conclusions are listed as follows:

(1) For metal touch connections with cylinder edge failure, the decrease of collapse strength is very slightly even if the eccentricity ratio of load e/d_P reaches 1/2. The reason might be that conical wall is much stronger than cylinder edge and then move downward almost in parallel. It makes Mises stress distribution almost uniform in both distal and proximal sides.

(2) For metal touch connections with tapered ring failure, the decrease of collapse strength is a litter greater than the case of cylinder edge failure. The reason might be that the strength of cylinder edge increases after ring is employed, and then conical wall rotates slightly. It makes the Mises stress distribution in distal side a little smaller than that in proximal side.

(3) For metal touch connections with conical wall failure, the decrease of collapse strength is greater than the cases of both cylinder edge failure and tapered ring failure. It is because that conical wall rotates and moves downward, making the Mises stress distribution in distal side a little smaller than that in proximal side.

(4) For welded connections with joint region failure, the decrease of collapse

strength is much greater than those of metal touch connections with three failure modes. It is because that conical wall only rotates, making the Mises stress distribution in distal side much smaller than that in proximal side.

(5) The length of load region is set to be relatively small in this analysis. Its influence on the collapse strength of connections is necessary to be analyzed in future.

ACKNOWLEDGEMENTS

First and foremost, I would like to express my deepest gratitude to my advisor, Prof. Kuwamura, for his rigorous and constructive guidance during the one year of research student program and the three and a half years of doctoral course I spent at the University of Tokyo. He has not only inspired me how to solve a specific problem, but also often given me insightful comments on how to do research. His strict requirements made me overcome the difficulties in pursuing the truth. The spirit of the Steel Structure Laboratory will encourage me all the time.

I also would like to express my sincere thanks to my associate advisor, Assoc. Prof. Iyama, for his kind and patient discussion and precious advice during seminars and daily life.

I would like to express my sincere thanks to Dr. Koyama, for his kind and continuous assistance and helpful discussion during tough time.

I am grateful to the former students of the laboratory, Dr. Jia, Dr. Araki, Dr. Zhou, Dr. Kim, Mr. Tomioka, Mr. Funabashi, Miss. Kashimoto, Mr. Ikejili, Miss. Kita, Mr. Okuno, Mr. Shimokawa, Mr. Inamoto, and Mr. Su et al., and the students Mr. Wakui, Mr. Fukushima, Mr. Sato, Mr. Saito, Mr. Shiode and Miss. Iba, Mr. Morikawa and Mr. Mori et al., for their kind supports on both research and daily life.

I would like to thank Assoc. Prof. Ito at Tokyo University of Science, for his kind encouragement, patient discussion and helpful comments during study meetings and by email.

I would like to thank Assoc. Prof. Koetaka at Kyoto University and Assoc. Prof. Kishiki at Tokyo Institute of Technology for their patient and helpful discussion and advice.

I would like to thank Chairman Iwakura, Mr. and Mrs. Kawamoto, and all the other members of KIND (Komaba International Friendship Club), for their kind help and

communication during daily life, especially when I just came to Japan.

I also would like to thank the Ministry of Education, Culture, Sports, Science and Technology (MEXT) of Japan for the Japanese government (Monbukagakusho) scholarship, which supported my stay at the University of Tokyo.

I want to express my greatest thanks to my advisor during master course, Prof. Li Yingmin at Chongqing University for his kind and constructive guidance. Without his support, I cannot obtain the chance to study in Japan and pursue a doctoral degree. I also want to thank all the teachers in his research group, for their friendly and continuous guidance and help on both research and daily life.

Acknowledgements are extended to my family, parents and all the friends for their spiritual and economical support and encouragement. Especially, I would like to thank my loving wife, Wang Wei, for her coming to Japan to live with me and supporting me always.

Finally, I would like to express my deep gratitude to the thesis committee: Prof. Aihara, Prof. Kawaguchi, Prof. Noguchi and Assoc. Prof. Iyama, for their precious time and insightful comments.